

**BEHAVIOR, ANALYSIS AND DESIGN OF STEEL-PLATE COMPOSITE  
(SC) WALLS FOR IMPACTIVE LOADING**

by

**Joo Min Kim**

**A Dissertation**

*Submitted to the Faculty of Purdue University*

*In Partial Fulfillment of the Requirements for the degree of*

**Doctor of Philosophy**



Lyles School of Civil Engineering

West Lafayette, Indiana

December 2018

**THE PURDUE UNIVERSITY GRADUATE SCHOOL  
STATEMENT OF COMMITTEE APPROVAL**

Dr. Amit H. Varma, Chair

Lyles School of Civil Engineering

Dr. Robert J. Connor

Lyles School of Civil Engineering

Dr. Sukru Guzey

Lyles School of Civil Engineering

Dr. Weinong Chen

School of Aeronautics and Astronautics

**Approved by:**

Dr. Dulcy M. Abraham

Head of the Graduate Program

*To my parents and my sister*

## ACKNOWLEDGMENTS

First of all, I thank God for always being with me as I walk through the hills and valleys of my life. He knows what I need and provides it at just the right time. Because of Him I am never in short supply and my life is complete.

A special thanks to my advisor Dr. Amit H. Varma for the opportunity he provided. His excellent guidance, patience, and efforts to push me out of my comfort zone allowed me to reach goals that I never thought I could.

Thanks to my committee members: Dr. Robert J. Connor, Dr. Sukru Guzey, and Dr. Weinong Chen. Special thanks to Dr. Weinong Chen for his generosity in allowing me to use his department's gas gun cannon and Mr. Zherui Guo for his assistance for my experimental tests.

Jake Bruhl, thank you for teaching me what I needed to know about all things protective design related and passing along your experiences in LS-DYNA. Kevin Brower and Tom Bradt, thank you for your patience and help in finding an easier and more efficient way to do things involving my experimental tests. I would like to thank my labmates who supported me along this long journey: Jungil Seo, Kadir Sener, Saahas Bhardwaj, Zichao Lai, Rachel Chichi, Hassan Sagheer, and many others with whom I shared time at Bowen Laboratory and in classes. Hassan, thank you for being my study buddy late at night at Bowen Laboratory and it was fun to teach you LS-DYNA.

Love and thanks always to my family. Thanks to my parents for believing in me and encouraging me to go far beyond anything that I used to believe I could do. Special thanks to my sister, Hyunmi; This journey would never have been possible without your amazing sacrifices and support for me and your caring for our parents while I have been away for six and a half years.

Thanks to the Purdue Bible Fellowship International (PBFi) for their friendship and fellowship throughout this journey. They have been my home away from home and my family at Purdue. Special thanks to Matt Scott for his mentoring and help in my English writing.

For fear of leaving someone out by name, I would like to say thank you, from the bottom of my heart, to all of my friends.

The experimental work presented in this dissertation was performed at the Robert L. and Terry L. Bowen Laboratory for Large-Scale Civil Engineering Research at the Lyles School of Civil Engineering at Purdue University. The research presented is based upon work funded by Korea Hydro and Nuclear Power (KHNP) and the United States Nuclear Regulatory Commission (USNRC) Grant No. NRC-HQ-60-14-G-0001. Any opinions, findings, and conclusions are those of the author and do not necessarily reflect the views of the sponsors.

## TABLE OF CONTENTS

LIST OF TABLES .....	11
LIST OF FIGURES .....	13
NOMENCLATURE .....	20
ABBREVIATIONS .....	22
ABSTRACT .....	23
CHAPTER 1. INTRODUCTION .....	25
1.1 Background .....	25
1.2 Motivation .....	27
1.3 Research Goals and Objectives .....	28
1.4 Dissertation Outline .....	29
CHAPTER 2. LITERATURE REVIEW .....	34
2.1 Design Code or Guidance of SC Structures .....	34
2.1.1 AISC N690s1, Appendix N9 .....	34
2.1.2 AISC Design Guide 32 .....	35
2.2 Structural Behavior of SC Walls .....	35
2.2.1 Out-of-plane shear behavior .....	35
2.2.2 Out-of-plane flexural behavior .....	37
2.2.3 In-plane shear behavior .....	38
2.2.4 Cyclic in-plane shear behavior of SC walls with openings .....	38
2.3 Impact Resistance Design .....	39
2.3.1 Walter and Wolde-Tinsae (1984) .....	39
2.3.2 Tsubota et al. (1993) .....	40
2.3.3 Sugano et al. (1993) .....	41
2.3.4 Mizuno et al. (2005) .....	42
2.3.5 Hashimoto et al. (2005) .....	43
2.3.6 Grisaro and Dancygier (2014) .....	44
2.3.7 Bruhl et al. (2015) .....	45
CHAPTER 3. EXPERIMENTAL PROGRAM .....	47
3.1 Introduction .....	47

3.2	Specimen Design and Material Properties .....	47
3.3	Test Matrix.....	51
3.4	Test Setup.....	52
3.5	Instrumentation .....	54
CHAPTER 4. EXPERIMENTAL INVESTIGATIONS .....		74
4.1	Introduction.....	74
4.2	Test Results of Specimens .....	74
4.2.1	Group 1: Test case number 1: 3.7-0.37-50-1.0-1.3-554 .....	74
4.2.2	Group 1: Test case number 2: 3.7-0.37-50-1.0-1.3-677 .....	75
4.2.3	Group 1: Test case number 3: 3.7-0.37-50-1.0-2.0-430 .....	76
4.2.4	Group 1: Test case number 4: 3.7-0.37-50-1.0-2.0-525 .....	77
4.2.5	Group 1: Test case number 5: 3.7-0.53-50-1.5-1.3-660 .....	78
4.2.6	Group 1: Test case number 6: 3.7-0.53-50-1.5-1.3-750 .....	79
4.2.7	Group 1: Test case number 7: 3.7-0.53-50-1.0-2.0-513 .....	80
4.2.8	Group 1: Test case number 8: 3.7-0.53-50-1.0-2.0-626 .....	81
4.2.9	Group 1: Test case number 9: 3.7-1.23-50-1.5-3.5-380 .....	82
4.2.10	Group 1: Test case number 10: 3.7-1.23-50-1.5-3.5-465.....	83
4.2.11	Group 2: Test case number 1: 5.2-0.48-50-1.0-2.0-445.....	84
4.2.12	Group 2: Test case number 2: 5.2-0.48-50-1.0-2.0-544.....	85
4.2.13	Group 2: Test case number 3: 5.2-0.48-50-1.5-3.5-408.....	85
4.2.14	Group 2: Test case number 4: 5.2-0.48-50-1.5-3.5-498.....	86
4.2.15	Group 3: Test case number 1: 3.7-0.37-65-1.0-2.0-443.....	87
4.2.16	Group 3: Test case number 2: 3.7-0.37-65-1.0-2.0-541 .....	88
4.3	Summary of Tests Results .....	89
4.4	Behavior of SC Walls Subjected to Missile Impact.....	92
4.4.1	Damage to exterior surfaces of SC wall specimens.....	92
4.4.2	Damage in the cross-section of SC wall specimens .....	93
4.5	Discussions .....	95
4.5.1	Evaluation of the validity and accuracy of the three-step design method .....	95
4.5.2	Comparison with modified NDRC equations.....	97
4.6	Proposed Local Failure Mechanism of SC Walls Subjected to Missile Impact .....	99

4.7	Conclusions.....	102
CHAPTER 5. NUMERICAL MODEL DEVELOPMENT AND BENCHMARKING.....		150
5.1	Introduction.....	150
5.2	Development of Numerical Models.....	150
5.2.1	Steel Faceplate Modeling .....	151
5.2.2	Tie Bar and Steel-Headed Shear Stud Anchor Modeling.....	151
5.2.3	Concrete Modeling .....	153
5.2.4	Projectile Modeling .....	155
5.2.5	Spacer Plates Modeling .....	155
5.2.6	Other Modeling Details .....	155
5.3	Benchmarking of the Numerical Models.....	157
5.3.1	Representative Analysis Results of Test Case Number 2 in Group 1 .....	157
5.3.2	Representative Analysis Results of Test Case Number 9 in Group 1 .....	158
5.3.3	Representative Analysis Results of Test Case Number 7 in Group 1 .....	159
5.3.4	Summary of Benchmarking Analyses .....	160
5.4	Discussion.....	161
5.5	Conclusions.....	163
CHAPTER 6. NUMERICAL PARAMETRIC STUDIES.....		185
6.1	Introduction.....	185
6.2	Parametric Study to Specify Perforation Velocities .....	185
6.2.1	Parametric study matrix.....	185
6.2.2	Parametric study results.....	188
6.3	Parametric Study to Evaluate the Influence of Parameters.....	192
6.3.1	Parametric study matrix.....	192
6.3.2	Parametric study results.....	193
6.4	Conclusions.....	197
CHAPTER 7. DEVELOPMENT OF MODIFIED DESIGN METHOD.....		212
7.1	Introduction.....	212
7.2	Evaluation on Effectiveness of Penetration Depth Calculation.....	213
7.2.1	Evaluation of modified NDRC equations.....	213
7.2.2	Introduction to modification factor equation, $K_{SC}$ .....	214

7.2.3	Perforation resistance curve generated by applying modification factor equation, $K_{SC}$	216
7.3	Evaluation on Effectiveness of Steel Faceplate Thickness Calculation	216
7.3.1	Analytical model to determine required steel faceplate thickness of SC walls	216
7.3.2	Effect of strain hardening coefficient and strain rate	217
7.4	Development of Modified Design Method	218
7.4.1	Experimental test database	218
7.4.2	Derivation of penetration depth equation for SC walls, $x_{c\_SC\_calc}$	218
7.4.3	Derivation of modification factor equation, $K_{sc}$	220
7.4.4	Proposed modified design method	222
7.5	Evaluation of the proposed modified design method	227
7.5.1	Evaluation of the proposed modified design method - using the small-scale missile impact test data	227
7.5.2	Larger-scale missile impact tests	231
7.5.2.1	Specimen design and material properties	231
7.5.2.2	Test matrix and test results	231
7.5.3	Evaluation of the proposed modified design method - using the larger-scale missile impact test data	234
7.6	Conclusions	235
CHAPTER 8. LOCAL FAILURE MODES OF SC WALLS		270
8.1	Introduction	270
8.2	Development of Numerical Models	270
8.2.1	Steel faceplate modeling	271
8.2.2	Tie bar and steel-headed shear stud anchor modeling	272
8.2.3	Concrete modeling	272
8.2.4	Other modeling details	273
8.3	Numerical Parametric Studies	273
8.4	Influence of Shear Reinforcement Ratio on Local Failure Mode	274
8.5	Influence of Failure Criteria Definition on SC Wall Resistance Function	275
8.6	Summary and Conclusions	278
CHAPTER 9. SUMMARY AND CONCLUSIONS		289

9.1 Research Summary .....	289
9.2 Conclusions.....	293
9.3 Recommendations for Future Work.....	297
APPENDIX.....	300
REFERENCES .....	302
VITA.....	307

## LIST OF TABLES

Table 3-1 Design details of the SC wall specimens.....	56
Table 3-2 Summary of material properties for steel faceplates and stud anchors .....	57
Table 3-3 Best fitted variables for the power law material model (Bruhl 2015).....	57
Table 3-4 Types of projectiles and sabots with their dimensions and material properties .....	58
Table 3-5 Missile impact test matrix for small-scale SC walls .....	59
Table 4-1 Summary of the test results .....	104
Table 4-2 Summary of dimensions of internal damage in the cross-section of the SC wall specimens.....	105
Table 4-3 Summary of the comparison of penetration depth between test results and estimation by the modified NDRC equations.....	106
Table 4-4 Statistical analysis results of the comparison between measured and calculated values .....	106
Table 5-1 Material input parameters for steel faceplates (MAT_24) .....	165
Table 5-2 Material input parameters for tie bars (MAT_24).....	165
Table 5-3 Material input parameters for steel-headed shear stud anchors (MAT_24).....	166
Table 5-4 Material input parameters for connector elements (MAT_74).....	166
Table 5-5 Material input parameters for concrete core (MAT_24) .....	167
Table 5-6 Material input parameters for erosion of concrete core (MAT_ADD_EROSION)...	167
Table 5-7 Material input parameters for projectile (MAT_24) .....	168
Table 5-8 Material input parameters for spacer plates (MAT_20).....	168
Table 5-9 Comparison of results between experimental test and numerical analysis .....	169
Table 5-10 Statistical evaluation of FE models' performance: test cases in group 1 .....	170
Table 5-11 Statistical evaluation of FE models' performance: test cases in group 2 .....	170
Table 5-12 Statistical evaluation of FE models' performance: entire test cases .....	170

Table 6-1 Numerical parametric study matrix (1 <sup>st</sup> ).....	199
Table 6-2 Summary of the numerical parametric study results (1 <sup>st</sup> ).....	201
Table 6-3 Summary of the perforation velocity ranges in the three experimental test groups ...	204
Table 6-4 Summary of the perforation velocity ranges in the three numerical analysis groups	204
Table 6-5 Numerical parametric study matrix (2 <sup>nd</sup> ).....	205
Table 6-6 Summary of the numerical parametric study results (2 <sup>nd</sup> ).....	206
Table 7-1 Summary of penetration depth values from experimental tests and manual calculations .....	238
Table 7-2 Comparison between the three-step design method and the proposed modified design method.....	239
Table 7-3 Comparison of perforation velocity ranges obtained from experimental tests.....	240
Table 7-4 Comparison of perforation velocity ranges obtained from numerical analyses .....	241
Table 7-5 Summary of test matrix and results of larger-scale missile impact tests.....	242
Table 7-6 Comparison of perforation velocity ranges obtained from experimental tests - Larger- scale missile impact tests .....	243
Table 8-1 Parametric analyses matrix (Varma et al. 2017) .....	280

## LIST OF FIGURES

Figure 1-1 Typical SC wall configuration (American Institute of Steel Construction 2015).....	31
Figure 1-2 Comparison of construction schedules (Schlaseman 2004).....	32
Figure 1-3 Impact sequence of missile on SC wall (Bruhl et al. 2015a) .....	33
Figure 2-1 Proposed simplified method to design surface steel plates (Mizuno et al. 2005a) .....	46
Figure 3-1 Three-dimensional rendering and module of SC wall specimen .....	60
Figure 3-2 Representative design drawings of SC wall specimens (all dimensions are in inches) .....	61
Figure 3-3 Representative tensile stress-strain curves (Bruhl 2015) .....	62
Figure 3-4 Photographs of concrete cast.....	64
Figure 3-5 Photographs of the 1.0 in. diameter, 1.3 lbs projectile.....	65
Figure 3-6 Photographs of the projectile and sabot assembly for 1.0 in. diameter, 1.3 lbs projectile .....	65
Figure 3-7 Schematic design of a projectile and sabot assembly .....	65
Figure 3-8 Test cases marked on perforation resistance curves in group 1 .....	66
Figure 3-9 Test cases marked on perforation resistance curves in group 2 .....	67
Figure 3-10 Test cases marked on perforation resistance curve in group 3.....	68
Figure 3-11 Conceptual design of experimental test setup (all dimensions are in inches).....	69
Figure 3-12 Photograph of the installed test setup.....	70
Figure 3-13 Captured images of the inside of the front chamber by a high-speed camera (Test case number 7 in group 1).....	71
Figure 3-14 Bulging depth measurement using a contour gage after test.....	72
Figure 3-15 Representative layout of strain gage rosettes .....	73
Figure 4-1 Photographs of damage in the post-test specimen: Gr.1 #1 .....	107
Figure 4-2 Photographs of damage in the post-test specimen: Gr.1 #2 .....	108

Figure 4-3 Photographs of damage in the post-test specimen: Gr.1 #3 .....	109
Figure 4-4 Photographs of damage in the post-test specimen: Gr.1 #4 .....	110
Figure 4-5 Photographs of damage in the post-test specimen: Gr.1 #5 .....	111
Figure 4-6 Photographs of damage in the post-test specimen: Gr.1 #6 .....	112
Figure 4-7 Photographs of damage in the post-test specimen: Gr.1 #7 .....	113
Figure 4-8 Photographs of damage in the post-test specimen: Gr.1 #8 .....	114
Figure 4-9 Photographs of damage in the post-test specimen: Gr.1 #9 .....	115
Figure 4-10 Photographs of damage in the post-test specimen: Gr.1 #10 .....	116
Figure 4-11 Photographs of damage in the post-test specimen: Gr.2 #1 .....	117
Figure 4-12 Photographs of damage in the post-test specimen: Gr.2 #2 .....	118
Figure 4-13 Photographs of damage in the post-test specimen: Gr.2 #3 .....	119
Figure 4-14 Photographs of damage in the post-test specimen: Gr.2 #4 .....	120
Figure 4-15 Photographs of damage in the post-test specimen: Gr.3 #1 .....	121
Figure 4-16 Photographs of damage in the post-test specimen: Gr.3 #2 .....	122
Figure 4-17 Photograph of damage in a cross-section cut from the post-test specimen: Gr.1 #1 .....	123
Figure 4-18 Photograph of damage in a cross-section cut from the post-test specimen: Gr.1 #2 .....	124
Figure 4-19 Photograph of damage in a cross-section cut from the post-test specimen: Gr.1 #3 .....	125
Figure 4-20 Photograph of damage in a cross-section cut from the post-test specimen: Gr.1 #4 .....	126
Figure 4-21 Photograph of damage in a cross-section cut from the post-test specimen: Gr.1 #5 .....	127
Figure 4-22 Photograph of damage in a cross-section cut from the post-test specimen: Gr.1 #6 .....	128
Figure 4-23 Photograph of damage in a cross-section cut from the post-test specimen: Gr.1 #7 .....	129

Figure 4-24 Photograph of damage in a cross-section cut from the post-test specimen: Gr.1 #8 .....	130
Figure 4-25 Photograph of damage in a cross-section cut from the post-test specimen: Gr.1 #9 .....	131
Figure 4-26 Photograph of damage in a cross-section cut from the post-test specimen: Gr.1 #10 .....	132
Figure 4-27 Photograph of damage in a cross-section cut from the post-test specimen: Gr.2 #1 .....	133
Figure 4-28 Photograph of damage in a cross-section cut from the post-test specimen: Gr.2 #2 .....	134
Figure 4-29 Photograph of damage in a cross-section cut from the post-test specimen: Gr.2 #3 .....	135
Figure 4-30 Photograph of damage in a cross-section cut from the post-test specimen: Gr.2 #4 .....	136
Figure 4-31 Photograph of damage in a cross-section cut from the post-test specimen: Gr.3 #1 .....	137
Figure 4-32 Photograph of damage in a cross-section cut from the post-test specimen: Gr.3 #2 .....	138
Figure 4-33 A representative strain data obtained from the post-test specimen: Gr.1 #3 .....	139
Figure 4-34 A representative strain data obtained from the post-test specimen: Gr.1 #4 .....	139
Figure 4-35 A representative strain data obtained from the post-test specimen: Gr.1 #9 .....	140
Figure 4-36 A representative strain data obtained from the post-test specimen: Gr.1 #10 .....	140
Figure 4-37 A representative strain data obtained from the post-test specimen: Gr.2 #1 .....	141
Figure 4-38 A representative strain data obtained from the post-test specimen: Gr.2 #2 .....	141
Figure 4-39 A representative strain data obtained from the post-test specimen: Gr.2 #4 .....	142
Figure 4-40 Photographs of internal damage progress in a series of post-test SC wall specimens .....	143
Figure 4-41 Schematic of internal damage details in the cross-section of post-test SC wall specimen .....	144
Figure 4-42 Test results marked on the perforation resistance curves in group 1 .....	145

Figure 4-43 Test results marked on the perforation resistance curves in group 2 .....	146
Figure 4-44 Test results marked on the perforation resistance curves in group 3 .....	147
Figure 4-45 Graphical comparison of penetration depth between test result and calculation ....	148
Figure 4-46 Comparison of damage mode between RC and SC walls subjected to missile impact (Hashimoto et al. 2005).....	148
Figure 4-47 Stages in local failure mechanism of SC walls subjected to missile impact.....	149
Figure 5-1 Finite element model developed in LS-DYNA.....	171
Figure 5-2 Dynamic increase factor for the steel faceplates (U.S. Department of Defense 2008) .....	172
Figure 5-3 The average strain softening response (Broadhouse and Attwood 1993).....	173
Figure 5-4 Bulging damage mode in experimental test and numerical analysis: Group 1, test number 2 .....	174
Figure 5-5 Comparison of internal damage behavior between test result and numerical analysis result: Group 1, test number 2.....	174
Figure 5-6 Projectile velocity – time history: Group 1, test number 2 .....	175
Figure 5-7 Splitting damage mode in experimental test and numerical analysis: Group 1, test number 9 .....	176
Figure 5-8 Comparison of internal damage behavior between test result and numerical analysis result: Group 1, test number 9.....	176
Figure 5-9 Projectile velocity – time history: Group 1, test number 9 .....	177
Figure 5-10 Perforation failure in experimental test and numerical analysis: Group 1, test number 7.....	178
Figure 5-11 Comparison of internal damage behavior between test result and numerical analysis result: Group 1, test number 7.....	178
Figure 5-12 Projectile velocity – time history: Group 1, test number 7 .....	179
Figure 5-13 Comparison of experimental tests results and benchmarking analyses results when the 1.0 in. diameter projectiles were used in group 1 .....	180
Figure 5-14 Comparison of experimental tests results and benchmarking analyses results when the 1.5 in. diameter projectiles were used in group 1 .....	181

Figure 5-15 Comparison of experimental tests results and benchmarking analyses results when the 1.0 in. diameter projectiles were used in group 2 .....	182
Figure 5-16 Comparison of experimental tests results and benchmarking analyses results when the 1.5 in. diameter projectiles were used in group 2 .....	183
Figure 5-17 Comparison of experimental tests results and benchmarking analyses results when the 1.0 in. diameter projectiles were used in group 3 .....	184
Figure 6-1 Numerical parametric study results on the perforation resistance curve of analysis group 1 (Benchmarking analyses results are included).....	207
Figure 6-2 Numerical parametric study results on the perforation resistance curve of analysis group 2 (Benchmarking analyses results are included).....	208
Figure 6-3 Numerical parametric study results on the perforation resistance curve of analysis group 3 (Benchmarking analyses results are included).....	209
Figure 6-4 Influence of the shear reinforcement ratio ( $\rho_t$ ) of SC walls on the penetration depth .....	210
Figure 6-5 Influence of the flexural reinforcement ratio ( $\rho$ ) of SC walls on the penetration depth .....	210
Figure 6-6 Influence of the steel faceplate strength of SC walls on the penetration depth .....	211
Figure 7-1 Comparison of penetration depth between measured values and calculated values .	244
Figure 7-2 Comparison of penetration depth between measured values and calculated values by using the modification factor equation $K_{SC}$ .....	244
Figure 7-3 Degree of conservatism in modification factor equation $K_{SC}$ and modified NDRC equations in estimating penetration depth in terms of level of confidence.....	245
Figure 7-4 Perforation resistance curves on the small-scale missile impact tests data: for 1.0 in. diameter projectile in Gr.1 .....	246
Figure 7-5 Perforation resistance curves on the small-scale missile impact tests data: for 1.5 in. diameter projectile in Gr.1 .....	247
Figure 7-6 Perforation resistance curves on the small-scale missile impact tests data: for 1.0 in. diameter projectile in Gr.2 .....	248
Figure 7-7 Perforation resistance curves on the small-scale missile impact tests data: for 1.5 in. diameter projectile in Gr.2 .....	249
Figure 7-8 Perforation resistance curves on the small-scale missile impact tests data: for 1.0 in. diameter projectile in Gr.3 .....	250

Figure 7-9 Comparison of penetration depth between measured value and calculated value by the modified NDRC equations and $x_{c\_SC\_cal}$ equations.....	251
Figure 7-10 Comparison of the degree of conservatism of each penetration depth estimating equation in terms of the level of confidence.....	252
Figure 7-11 Comparison of penetration depth between measured value and calculated value by using the modification factor equation, $K_{SC}$ .....	253
Figure 7-12 Comparison of the degree of conservatism of each modification factor equation in estimating penetration depth in terms of the level of confidence .....	255
Figure 7-13 A failure mechanism proposed based on the experimental investigations on the small-scale missile impact tests results (from Figure 4-47).....	257
Figure 7-14 Calculation procedures of the proposed modified design method .....	258
Figure 7-15 Perforation resistance curves on the small-scale missile impact tests data: for 1.0 in. diameter projectile in Gr.1 .....	260
Figure 7-16 Perforation resistance curves on the small-scale missile impact tests data: for 1.5 in. diameter projectile in Gr.1 .....	261
Figure 7-17 Perforation resistance curves on the small-scale missile impact tests: for 1.0 in. diameter projectile in Gr.2 .....	262
Figure 7-18 Perforation resistance curves on the small-scale missile impact tests data: for 1.5 in. diameter projectile in Gr.2 .....	263
Figure 7-19 Perforation resistance curves on the small-scale missile impact tests data: for 1.0 in. diameter projectile in Gr.3 .....	264
Figure 7-20 Perforation resistance curve and perforation velocity on the larger-scale missile impact tests data of group 1 .....	265
Figure 7-21 Perforation resistance curve and perforation velocity on the larger-scale missile impact tests data of group 2 .....	266
Figure 7-22 Perforation resistance curve and perforation velocity on the larger-scale missile impact tests data of group 3 .....	267
Figure 7-23 Perforation resistance curve and perforation velocity on the larger-scale missile impact tests data of group 4 .....	268
Figure 7-24 Perforation resistance curve and perforation velocity on the larger-scale missile impact tests data of group 5 .....	269
Figure 8-1 A representative quarter finite element model of SC walls (Varma et al. 2017) .....	281

Figure 8-2 The linear strain softening response (Schwer 2011) .....	282
Figure 8-3 Load-displacement curves for analysis numbers from 1 to 8 (Varma et al. 2017) ...	283
Figure 8-4 Detailed local failure behavior of analysis number 2: punching shear failure (concrete core was removed for clarity) (Varma et al. 2017) .....	284
Figure 8-5 Detailed local failure behavior of analysis number 7: plastic mechanism formation (concrete core was removed for clarity) (Varma et al. 2017) .....	284
Figure 8-6 Detailed local failure behavior of analysis number 5: flexural yielding (concrete core was removed for clarity) (Varma et al. 2017) .....	285
Figure 8-7 Load-displacement response from analysis cases of model number 4, 9 and 10 (Varma et al. 2017) .....	286
Figure 8-8 Plastic strain and slip displacement history data for the components of SC walls (Varma et al. 2017) .....	287
Figure 8-9 A representative resistance function on which critical events were marked .....	288

## NOMENCLATURE

$A_t$	Cross-sectional area of the tie bars
$d_1$	Diameter of the cylindrically shaped void
$d_2$	Diameter of the concrete frustum on rear side
$D_p$	Diameter of the projectile
$d_s$	Diameter of the steel-headed shear stud anchors
$D_s$	Outside diameter of the sabot
$d_t$	Diameter of the tie bars
$f_c$	Compressive strength of the material
$f'_c$	Concrete compressive strength at 28 days
$f_u$	Ultimate strength of the material
$f_y$	Yield strength of the material
$f_y^{pl}$	Yield strength of the steel faceplates
$l$	Length of the projectile
$L$	Length of the sabot
$s$	Steel-headed shear stud anchor spacing
$S$	Tie bar spacing
$t$	Thickness of the sabot at the indicated location of the corresponding Figure
$T_c$	Concrete thickness
$t_d$	Depth of the cylindrically shaped void in the concrete core
$t_n$	Penetration depth in the concrete core measured at the tip of the projectile
$t_p$	Thickness of the steel faceplates
$T_{sc}$	Thickness of the SC walls
$V_{des}$	Design velocity of the projectile calculated by the three-step design method
$V_{imp}$	Impact velocity of the projectile
$V_o$	Initial velocity of the projectile
$W_p$	Weight of the projectile
$x_b$	Bulging depth of the rear steel faceplate of the SC wall
$x_{c\_calc}$	Calculated penetration depth of the concrete core of SC walls by the projectile
$x_{c\_test}$	Experimental penetration depth of the concrete core of SC walls by the projectile

$\epsilon_f$	Failure strain of the material
$\epsilon_u$	Ultimate strain of the material
$\epsilon_y$	Yield strain of the material
$\theta$	Inclination angle of the dislodged surface of the concrete frustum
$\rho$	Reinforcement ratio in the SC walls
$\rho_t$	Shear reinforcement ratio in the SC walls

## ABBREVIATIONS

ACI	American Concrete Institute
AISC	American Institute of Steel Construction
ASCE	American Society of Civil Engineers
ASTM	American Society for Testing and Materials
BLS	Blast Load Simulator
COV	Coefficient of variation
DIF	Dynamic increase factor
DOD	U.S. Department of Defense
DOE	U.S. Department of Energy
FE	Finite element
HSLA	High strength, low alloy
IHQ	Hourglass control type in LS-DYNA
JEAG	Japanese Electric Association Guideline
KEPIC-SNG	Korean Electric Power Industry Code - Structural (Nuclear structures) Guideline
NRC	Nuclear Regulatory Commission
PWR	Pressurized water reactor
QM	Hourglass coefficient in LS-DYNA
RC	Reinforced concrete
SC	Steel-plate reinforced concrete
HSC	Half steel-plate reinforced concrete
SDOF	Single-degree-of-freedom dynamic analysis model
SMR	Small modular reactor
TDOF	Two-degree-of-freedom dynamic analysis model
UFC	Unified Facilities Code
USACE	United States Corps of Engineers
DBA	Design basis accident
BDBA	Beyond design basis accident

## ABSTRACT

Author: Kim, Joo Min. PhD

Institution: Purdue University

Degree Received: December 2018

Title: Behavior, Analysis and Design of Steel-Plate Composite (SC) Walls for Impactive Loading

Committee Chair: Amit H. Varma

There is significant interest in the use of Steel-plate composite (SC) walls for protective structures, particularly for impactive and impulsive loading. The behavior of SC walls is fundamentally different from that of reinforced concrete (RC) walls due to the addition of steel plates on the exterior surfaces, which prevent concrete scabbing and enhance local perforation resistance.

Laboratory-scale SC wall specimens were fabricated, cast with concrete, and then tested in an indoor missile impact test-setup specially-built and commissioned for this research. The parameters included in the experimental investigations were the steel plate reinforcement ratio (3.7% - 5.2%), tie bar spacing, size, and reinforcement ratio (0.37% - 1.23%), and the steel plate yield strength (Gr.50 - Gr.65). Additional parameters include the missile diameter (1.0 in., 1.5 in.), weight (1.3 lbs, 2.0, lbs, 3.5 lbs), and velocity (410 - 760 ft/s). A total of sixteen tests were conducted, the results of which are presented in detail including measurements of missile velocity, penetration depth, rear steel plate bulging deformation, and test outcome (stopped or perforated). The test results are further used to illustrate the significant conservatism of a design method developed previously by researchers (Bruhl et al. 2015a), and the sources of this conservatism including differences in the missile penetration mechanism, dimensions of the concrete conical frustum (breaking out), and the penetration depth equations assumed in the design method.

Numerical models were developed to further investigate local damage behavior of SC walls. Three-dimensional finite element models were built using LS-DYNA software and employed to simulate the missile impact tests on the SC wall specimens. The numerical analysis results were benchmarked to the experimental test results for the validation of the models.

Two sets of parametric studies were conducted using the benchmarked numerical models. The first set of the parametric studies was intended to narrow the perforation velocity ranges from the experimental results for use in evaluating the accuracy of a rational design method developed later in this research. The second set of the parametric studies was intended to evaluate the influence of design parameters on the perforation resistance of SC walls. It was found that flexural reinforcement ratio and steel plate strength are significant parameters which affect the penetration depth. However, shear reinforcement ratio has negligible influence.

Results from the experimental investigations and the numerical parametric studies were used to develop a rational design method which modifies the three-step design method. The modified design method incorporates a proposed modification factor applicable to the penetration depth equations and the missile penetration mechanism observed from the experiments. The modified design method was verified using the larger-scale missile impact test data from South Korean tests as well.

Additional research was performed to evaluate the local failure modes when the perforation was prevented from missile impactive loading on SC walls. Through numerical parametric studies, three different local failure modes (punching shear, flexural yielding, and plastic mechanism formation) were investigated. Also, an innovative approach to generating static resistance functions was proposed for use in SDOF or TDOF model analysis.

## CHAPTER 1. INTRODUCTION

This dissertation describes the experimental and numerical study of the local behavior of SC walls subjected to missile impact loads, and design methodology development for them. Sixteen small-scale missile impact tests were conducted to quantify the available perforation resistance of the SC wall specimens. From the results, numerical models were benchmarked and then used to further understand the local behavior of SC walls through a parametric study. A method to design SC walls against missile impact loads was proposed based on the results of these studies.

This dissertation further describes another numerical study which evaluates local failure modes of SC walls when perforation from missile impact loads is prevented. Results of this numerical study were used to propose an innovative approach to generate a static resistance function for use in SDOF or TDOF analysis to evaluate the global response of SC walls.

### *1.1 Background*

Traditionally, reinforced concrete (RC) structures have been preferred as protective structures. Methods to design RC walls against missile impacts are well established and have been validated theoretically and experimentally for decades (American Society of Civil Engineers 1980; ERIN Engineering & Research Inc. 2011). More recently, there has been significant interest in the use of steel-plate composite (SC) walls as a reasonable alternative to RC walls due to advantages such as efficiency in construction and excellent structural performance (Malushte and Varma 2015). SC structures are currently being used as containment internal structures (CIS) of pressurized water reactors (PWRs) as well as being considered for use in small modular reactors (SMRs).

SC walls are composite structures comprised of two steel faceplates, steel-headed shear stud anchors, tie bars, and a concrete infill as shown in Figure 1-1. Steel faceplates create exterior boundaries to serve as formwork during construction. These same faceplates also provide flexural reinforcement for the wall. Steel-headed shear stud anchors are welded to the inner surface of steel faceplates and embedded in the concrete to bond the steel faceplates and the concrete infill. Tie bars maintain the SC wall thickness by connecting the two exterior steel faceplates. They provide stiffness and stability to the empty modules (before the concrete casting) during transportation, handling, and erection. After concrete casting, they serve as out-of-plane shear reinforcement for the composite wall. SC wall structures are well-suited for modular construction and have been demonstrated to reduce construction time since neither formwork nor reinforcing bar cages are needed as shown in Figure 1-2 (Schlaseman 2004). Also, the resistance of SC walls subjected to blast and impact loads has been shown to exceed that of RC walls of the same thickness (Hashimoto et al. 2005; Tsubota et al. 1993).

There have been equations or methodologies to design RC walls against impactive loads for preventing damages such as penetration, scabbing, and perforation for a long time. Design criterion has been determined according to the level of protection required. Typically, scabbing is considered as the most critical damage mode to be prevented because shrapnel from scabbing of the concrete may damage internal equipment or injure personnel. Publicly available codes or standards (ERIN Engineering & Research Inc. 2011; U.S. Department of Energy 2006) provide equations to calculate required wall thicknesses to prohibit damage modes including penetration, scabbing, and perforation. In addition, recommendations for assessing the global response of RC walls against impactive loading is described in ACI 349-06. These recommendations are usually used in SDOF or TDOF models to estimate the maximum deflection and available ductility ratio.

The local failure behavior of SC walls is different from that of RC walls because the rear side (non-impact side) steel faceplate of SC walls prevents scabbing of concrete when impacted by missiles. Experimental tests (Hashimoto et al. 2005; Tsubota et al. 1993; Walter and Wolde-Tinsae 1984) found that the following events may occur in series during impact process as illustrated in Figure 1-3: i) penetration of missile from front side, ii) bulging of rear steel faceplate, iii) splitting of rear steel faceplate, and iv) perforation through the entire thickness. For SC walls, perforation is considered as the most critical damage mode to be prevented since there is no scabbing of the concrete due to the rear steel faceplate on the non-impact side. The global behavior of SC walls is also different from that of RC walls because the rear (non-impact) steel faceplate undergoes biaxial stress status (tension) which affects available ductility ratio.

## *1.2 Motivation*

Currently, there is very limited research in regards to the development of design equations, or methodologies in code provisions, for assessing perforation failure of SC walls subjected to missile impact. Although a variety of experimental and numerical tests of SC walls have been done to evaluate their resistance to missile impact, these tests were typically focused on understanding the behavior rather than developing design methods to prevent perforation against missile impact. AISC N690s1-15 (American Institute of Steel Construction 2015) includes Appendix N9 as the first US industry consensus standard for the design of SC walls. However, it does not contain specific design recommendations or guidance for designing SC walls against impactive loading.

The three-step design approach (Bruhl et al. 2015a) is mentioned in the commentary of AISC N690s1-15 as one of the rational methods to assist in designing individual SC wall for a specific missile. While this design approach was validated using the existing database of tests, it

has not been specifically evaluated and validated by an experimental program designed to confirm its accuracy.

Thus, there is a need for additional systematic research to confirm the three-step design method and to further evaluate the behavior of SC walls against missile impact. This additional research will contribute to design engineers' and regulators' efforts to assess existing or future SC structure designs of safety-related nuclear facilities.

### *1.3 Research Goals and Objectives*

The overall goals of this research project are to develop and confirm: (1) a design method to be used for prevention of perforation failure of steel-plate composite (SC) walls subjected to missile impact, and (2) an innovative approach to generate a static resistance function for use in the analysis of SDOF or TDOF models to evaluate global response to missile impact.

The research objectives of this project are as follows:

- Conduct experimental tests and investigations to evaluate the local penetration and perforation behavior of SC walls subjected to missile impact.
- Develop and benchmark three-dimensional finite element models to numerically simulate experiments which can predict the local penetration and perforation behavior of SC wall specimens subjected to missile impact.
- Conduct numerical parametric studies using benchmarked models to evaluate the influence of SC wall design parameters and missile parameters on the local penetration and perforation behavior of SC walls.
- Develop a design methodology for preventing local perforation failure based on findings from experimental and numerical tests results.

- Conduct numerical parametric studies to evaluate the load-displacement response and local failure mode of SC walls when local perforation failure was prevented.
- Develop a methodology to generate a static resistance function for SC walls using a numerical analysis approach.

#### *1.4 Dissertation Outline*

The outline of this dissertation is as follows:

- Chapter 2 is the literature review. The review addresses research in two categories: (1) SC structures design, and (2) impact resistance design.
- Chapter 3 describes the experimental program of this research project. It contains details of specimen design, development of test matrix, configuration of test set up, and so on.
- Chapter 4 presents results and observations from the experimental investigation of missile impact tests.
- Chapter 5 presents the development of the finite element models, and their benchmarking analyses using the experimental test results from chapter 4.
- Chapter 6 describes numerical parametric studies, with benchmarked models from chapter 5, which evaluate the influence of design parameters on the impact response of SC walls and generate additional simulation data points.
- Chapter 7 discusses the development of methodology proposed to design SC walls against missile impact
- Chapter 8 describes numerical parametric studies to evaluate local failure modes of SC walls when perforation failure was prevented and to generate static resistance function for use in SDOF or TDOF models.

- Chapter 9 summarizes the research presented in this dissertation, describes the conclusions drawn, and provides recommendations for future work.

The preliminary versions of some results in this dissertation were partially presented at a few conferences as follows:

- Chapter 3 & 4:

Kim, J. M., Varma, A., Seo, J., Bruhl, J., Lee, K., and Kim, K. (2017). “Resistance of SC Walls Subjected to Missile Impact: Part 3. Small-Scale Tests” *Transactions of the 24th International Conference of Structural Mechanics in Reactor Technology (SMiRT-24)*, Busan, South Korea.

Kim, J. M., Bruhl, J., Seo, J., and Varma, A. (2017). “An Overview of Missile Impact Tests on Steel- Plate Composite (SC) Walls.” *Proceedings of Structures Congress 2017*, Denver, Colorado.

- Chapter 8:

Varma, A., Kim, J. M., Seo, J., and Bruhl, J. (2017). “Local Failure Modes of SC Walls Subjected to Impactive Loading” *Transactions of the 24th International Conference of Structural Mechanics in Reactor Technology (SMiRT-24)*, Busan, South Korea.

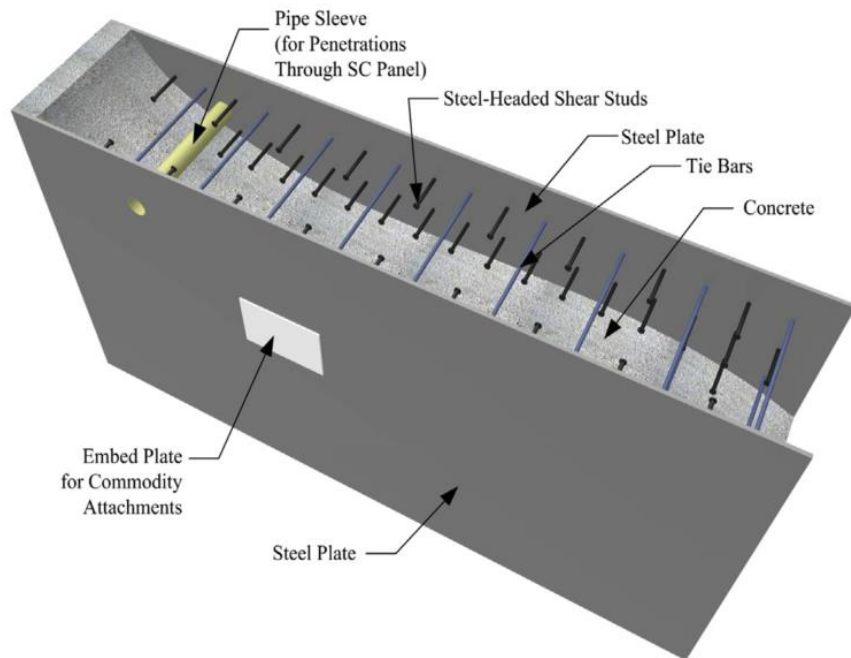


Figure 1-1 Typical SC wall configuration (American Institute of Steel Construction 2015)

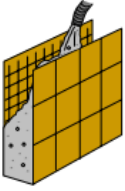
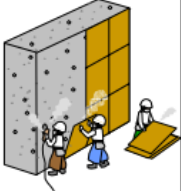
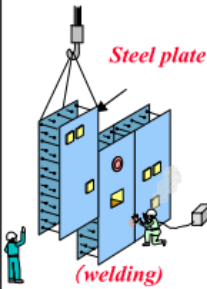
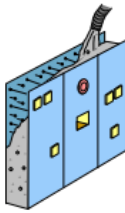
<i>Work Structure</i>	<i>Rebar arrangement</i>	<i>Form work (assembling)</i>	<i>Placing concrete</i>	<i>Form work (removal)</i>
<i>RC</i>		<i>Wooden form</i> 		
<b>28days</b>	13days	7days	4days	4days
<i>SC</i>	—	<i>Steel plate</i>  <i>(welding)</i>		—
<b>14days</b>	—	10days	4days	—

Figure 1-2 Comparison of construction schedules (Schlaseman 2004)

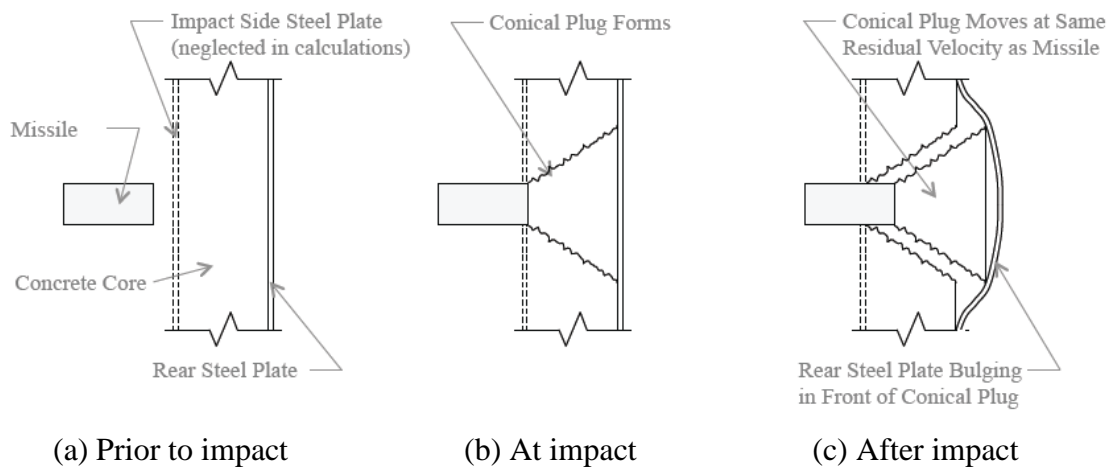


Figure 1-3 Impact sequence of missile on SC wall (Bruhl et al. 2015a)

## CHAPTER 2. LITERATURE REVIEW

This research project focusses on improving understanding of the behavior and failure mechanism of SC walls under impactive loading and developing knowledge to design these walls against missile impact. The literature review is divided into three sections which summarize the state-of-the-art for (1) general guidance of SC structures design, (2) Structural behavior of SC structures and (2) impact resistance design.

### *2.1 Design Code or Guidance of SC Structures*

#### 2.1.1 AISC N690s1, Appendix N9

AISC N690s1-15 is intended to be used in the design, fabrication, and erection of safety-related steel structures for nuclear facilities. Especially, Appendix N9 addresses design requirements of steel-plate composite (SC) walls in safety-related structures for nuclear facilities. SC walls, herein, are limited to the walls “consisting of two steel faceplates composite with structural concrete between them, where the faceplates are anchored to concrete using steel anchors and connected to each other using ties” (American Institute of Steel Construction 2015). This appendix is not applicable to half SC walls which have only one steel faceplate. This appendix is not applicable to SC wall piers which have no flange plates. This appendix applies to SC walls designed by the general requirements of section N9.1.1. Section detailing provisions related to SC wall specific limit states including local buckling, interfacial shear, and delamination of the section are addressed. Commentary is non-mandatory and gives background information and references so that engineers can further understand the derivation and limits of the specification.

This appendix describes the provisions pertaining to:

- Design requirements (N9.1)

- Analysis requirements (N9.2)
- Design of SC walls (N9.3)
- Design of SC wall connections (N9.4)

### 2.1.2 AISC Design Guide 32

AISC Design Guide 32 (Bhardwaj and Varma 2017) was developed to make it easier to design SC walls for safety-related nuclear facilities. Design procedures in the design guide are prepared based on AISC N690s1 (American Institute of Steel Construction 2015).

This design guide:

- Describes SC walls which satisfy requirements of Appendix N9
- Provides additional recommendations for the design of modular SC structures based on Appendix N9
- Presents details of SC wall connection design with design philosophies
- Discusses tolerance requirements for construction and fabrication of SC walls

A design example of an SC wall structure is provided at the end of this design guide. An SC wall from a compartment of a typical safety-related nuclear facility is employed in the design example and design procedures are discussed with all the design aspects considered.

## 2.2 *Structural Behavior of SC Walls*

### 2.2.1 Out-of-plane shear behavior

Sener and Varma (2014) compiled an experimental database of out-of-plane shear tests conducted on SC wall specimens in Japan, South Korea, China, and US. Out-of-plane shear capacities from the tests in the experimental database were summarized and compared with shear strengths calculated based on available design code equations from in US, Japan, and South Korea.

The major parameters considered in the experimental database were: i) specimen depths (225 - 914 mm), ii) shear span-to-depth ratios (0.5 - 3.6), and iii) steel faceplate reinforcement ratio (2.0 - 5.0%). The behavior of the SC wall specimens in the experimental database was divided into two categories based on their failure modes: i) shear failure, or ii) flexural-shear failure. SC wall specimens with other failure modes such as flexural yielding of the steel faceplates or interfacial shear failure of the stud anchors were not included in the experimental database. Thus, the final database had 39 experimental tests with either shear failure or flexural-shear failure for evaluation of the code equations.

The nominal out-of-plane shear strengths of the SC wall specimens in the experimental database were calculated using ACI 349 code equations for RC beams, Japanese code (JEAC) equations for SC beams, and South Korean code (KEPIC-SNG) equations for SC beams. These calculated out-of-plane shear strengths were compared with shear capacity from the tests in the experimental database with respect to the shear span-to-depth ratio and the section depth.

Results of the comparison indicated that ACI 349 code equations provide conservative out-of-plane shear strength of SC wall specimens. These equations reasonably calculated the lower bound out-of-plane shear strength of SC wall specimens with larger shear span-to-depth ratio and section depth. Strength reduction factor ( $\phi$ ) of 0.67 was obtained to be used with the ACI 349 code equations to calculate out-of-plane shear strength of SC walls. However, results of the comparison presented that JEAC and KEPIC-SNG code equations provide unconservative out-of-plane shear strength of SC wall specimens. These equations overestimated the lower bound out-of-plane shear strength of SC wall specimens with larger shear span-to-depth ratio and section depth.

### 2.2.2 Out-of-plane flexural behavior

Sener et al. (2014, 2015) conducted a research project to evaluate the out-of-plane structural response of SC walls including shear and flexural behavior. As a part of the research, the experimental database of out-of-plane tests on SC wall specimens conducted in Japan, South Korea, China, and US was compiled. Out-of-plane tests in the experimental database were categorized into two groups which indicated either shear behavior or flexural behavior. The out-of-plane shear behavior of SC wall specimens in the experimental database was presented in different literature (Sener and Varma 2014b). This research Sener et al. (2015) focuses on the out-of-plane flexural behavior of SC wall specimens in the experimental database. Measured displacements and strains of steel faceplates and ties, and photographs of post-test specimens were employed to discuss the out-of-plane flexural behavior.

The experimental database included a variety of SC wall specimens with varied parameters such as i) specimen depths (400 – 1219 mm), ii) shear span-to-depth ratios (1.0 – 5.5), iii) steel faceplate reinforcement ratios (1.33 – 5.0%), and iv) presence or absence of stiffeners (ribs). Tests of SC wall specimens were classified according to their out-of-plane behavior and failure mode with i) flexural failure mode or ii) flexural-shear failure mode. Final database with 29 SC wall specimen tests was used to evaluate code equations for estimating flexural strengths of SC walls.

This research presented that JEAC code equations predict the flexural strengths of SC wall specimens with reasonable accuracy and conservatism. The faceplate stiffeners are not taken into account in JEAC code equations. This research also indicated that ACI 349 and KEPIC-SNG predict the flexural strengths of SC wall specimens more accurately, however, less conservatively. These code equations can account for the contribution of the faceplate stiffeners, however, provided overestimated flexural strengths for several tests. As a result, it is recommended to use flexural strength equations from ACI 349, JEAC, and KEPIC-SNG codes with strength reduction

factor ( $\phi$ ) of 0.9, 1.0, and 0.9, respectively. For AISC N690, strength reduction factor ( $\phi$ ) of 1.0 can be used to calculate flexural strengths of SC walls.

### 2.2.3 In-plane shear behavior

Seo et al. (2016) conducted research to investigate the in-plane shear behavior of SC walls with boundary elements. Experimental data was compiled of in-plane shear tests on SC walls. A total of 26 in-plane shear tests of SC walls conducted in Japan, South Korea, and US were included in the experimental database. These tests were classified according to specimens' configuration as i) SC wall specimens with flange walls, and ii) SC wall panel specimens.

It was found that in-plane shear strength is influenced by the steel faceplate yielding, not the ultimate strength, and steel faceplate reinforcement ratio is the most critical design parameter affecting the in-plane shear strength of SC walls. In-plane shear strengths of tests in the experimental database were calculated based on ACI 349, mechanics-based model (MBM), and AISC N690 and compared to the test results. This comparison indicated that ACI 349 code equations estimate the in-plane shear strength slightly unconservatively. However, this unconservatism improved as steel plate reinforcement ratio increases due to dominant contribution of steel faceplate to in-plane shear strength. On the other hand, MBM and AISC N690 code equations present a conservative prediction of the in-plane shear strength of SC walls. Strength reduction factors ( $\phi$ ) of 0.82, 0.95, and 0.92 were derived from reliability analyses and recommended to be used with ACI 349, MBM, and AISC N690 code equations, respectively.

### 2.2.4 Cyclic in-plane shear behavior of SC walls with openings

Ozaki et al. (2004) conducted two experimental research programs to investigate the behavior of SC walls subjected to cyclic in-plane shear loading.

The first experimental research tested 9 specimens to evaluate the influence of axial force and partition web in SC walls. It was found that the cracking strength was affected by the axial force. However, there was no significant effect on yield strength and maximum strength by the axial force. The partition web made the post-cracking shear modulus rigid. But there was no significant influence on yield strength and maximum strength.

For the second experimental research, 6 tests were conducted to investigate the effect of openings on the cyclic in-plane shear behavior of SC walls. Numerical simulation results were supplemented to the experimental data. As the results, reduction ratio equations for circular openings and square openings were proposed. These equations are to be applied in calculating yield strength and ultimate strength of SC walls with circular or square openings.

### 2.3 *Impact Resistance Design*

#### 2.3.1 Walter and Wolde-Tinsae (1984)

Walter and Wolde-Tinsae (1984) summarized the existing formulas and evaluated their accuracy to predict perforation of RC barriers. Then, they proposed modifications to some of the methods which provided better results. Proposed modifications were applicable to RC barriers with a thin steel plate affixed to the back face.

A set of test data which consisted of 45 tests was assembled: 35 turbine fragment tests, conducted at both full and reduced scale (1/11), funded by EPRI; 5 tests, conducted as a part of EPRI's research, using axisymmetric missiles to support numerical simulations and to evaluate the effect of missile shape and size; 5 tests, conducted in France, as examples of normal impacts of turbine type missiles. Some of these tests had RC barriers which had a steel plate attached to their rear side to prevent scabbing.

From the test data, it was confirmed that the reduced scale testing approach is a valid test procedure for impact studies of reinforced concrete structures. This means, it is allowed to use available test data at any scale for impact studies.

It was found that Degen, Kennedy and CEA-EDF formulas provided better results than other formulas from the comparison with the test data. Modifications to these formulas were proposed using missile diameter, based on the perimeter (instead of projected area), and equivalent thickness of the concrete panel, incorporating affixed steel plate, calculated by a proposed equation. As a result, modified formulas were derived to calculate perforation velocity.

They proposed an equation to provide an equivalent thickness of a wall with a steel plate attached, equating Ballistics Research Laboratory (BRL) formula to CEA-EDF formula. Limitation of this method is that it is only applicable when assuming  $f'_c = 3800$  psi and parameters of missile weight and diameter was neglected. There was no consideration of the penetration level in this research: only perforation or no-perforation was referred.

### 2.3.2 Tsubota et al. (1993)

In Tsubota et al. (1993)'s research, extensive experimental tests were conducted to quantitatively evaluate the effect of a rear steel faceplate attached to RC panels to prevent local damage against a rigid missile.

A total of 50 test specimens were prepared with a various combination of concrete thicknesses, steel plate thicknesses and attaching methods of the steel plates. The test specimens were 0.6 m square RC panels with different thicknesses ranging from 5.0 to 16.0 cm. Steel plates with four different thicknesses of 0.8, 1.2, 1.6 and 2.0 mm were attached to the RC panels with two different methods: stud bolts and epoxy adhesive. For comparison purpose, 50 test specimens consisted of: 11 test specimens with no steel liner plates; one test specimen with a steel plate on

the front impacted face; another test specimen with steel plates on both the front and the rear faces; and the others with a steel plate only on the rear face.

Projectile employed in the tests consisted of a head, a body, and a tail. The head was solid mild steel with a flat nose, and its diameter was 35 mm. The body was a mild steel pipe with a diameter of 39.5 mm and a thickness of 0.42 mm. The tail was made of plastic. The projectile was considered as a rigid missile because of its solid mild steel head. The total mass of the projectile was 0.43 Kg, and the total length was 125 mm.

Tsubota et al. concluded that a rear steel faceplate attached to RC walls is a very effective way to prevent scabbing or perforation damage. However, they confirmed that the effect of a front impacted face steel plate is negligible on the local damages. As a result of the quantitative evaluation of the effect of the steel plate, they proposed formulas to calculate the equivalent concrete thickness of the steel plate according to three different damage modes: bulging, splitting, and perforation.

### 2.3.3 Sugano et al. (1993)

Sugano et al. (1993) carried out three sets of experimental tests with different scales to evaluate the local damage of RC structures subjected to aircraft engine missiles: small-scale (1:7.5), intermediate scale (1:2.5), and full scale.

According to the observation of test results, they confirmed that a similarity law works appropriately with the comparison of test results of three different scale test specimens. Reduction factors were newly introduced to incorporate the effect of a deformable missile on the local damage of RC structure, comparing to the local damage by a rigid missile: reduction factor for perforation ( $\alpha_p$ ) is recommended as 0.65 based on the Degan formula; reduction factor for scabbing ( $\alpha_s$ ) is

recommended as 0.6 based on the Chang formula. Also, it was found that there is little effect of the reinforcement ratio of RC structures on their local damage, for the tested reinforcement ratio ranges.

#### 2.3.4 Mizuno et al. (2005)

Mizuno et al. (2005)'s research was done to determine the protective capacity of SC walls against a full-scale aircraft impact by conducting numerical experiments to investigate the fracture behaviors and limit thickness of SC walls. They proposed a simplified design method of SC walls to prevent perforation against full-scale of aircraft engine impact following Morikawa (1997)'s work. Morikawa proposed an empirical method to assess the local damage of reinforced concrete barrier with rear steel plate subjected to a rigid missile. In this study, Mizuno et al. took into account the deformability of the missile based on Sugano et al. (1993)'s work.

The proposed simplified method consists of three steps as illustrated in Figure 2-1: i) determine residual velocity,  $V_r$ , by using Muto-Degan formula, of the aircraft engine after perforating the concrete of an SC wall considering missile deformability factor, ii) calculate perforation velocity of the rear steel plate,  $V_{ps}$ , by using Kar (1979)'s formula, assuming the aircraft engine becomes rigid after pass through the concrete, and iii) compare  $V_r$  and  $V_{ps}$  and determine if the SC wall is perforated or not. However, details of formula for each step of this simplified method were not described in the paper.

A design curve generated by the proposed simplified method was presented to determine a limit thickness of an SC wall. This generated design curve can be a useful design aid. However, there were limitations in applicability such as i) the steel plate thickness of 12 mm, and ii) the aircraft weight of 20tf (196 KN).

Mizuno et al. reported that SC walls with approximately 30% less thickness than RC walls can provide equivalent or better protective capacity. They also confirmed that a front side steel plate is effective to prevent damage against relatively soft missile impacts such as those of aircraft fuselage, compared to half SC walls with only a rear steel plate. That is because the front steel plate has higher strength than the concrete and provides better confinement to the concrete infill of the full SC walls

#### 2.3.5 Hashimoto et al. (2005)

Hashimoto et al. (2005) carried out an experimental study to evaluate the effect of steel faceplate on the local damage of RC panels subjected to missile impact.

A total of 40 specimens were tested consisted of three different types of panels: RC, HSC, and SC. All the specimens were 750 mm square panels. RC and HSC panels included reinforcing bars of 6.35 mm diameter at 100 mm spacing. HSC and SC had steel faceplates attached using stud bolts at 50 mm spacing. The concrete had the nominal compressive strength of 30 MPa with the maximum aggregate size of 10 mm. The specimen was suspended vertically with two steel wires so that it was free to move after missile impact. One type of non-deformable projectile and three types of deformable projectile were used in the category of test 1 and test 2, respectively.

Test 1 was comprised of 8 of RC panels, 16 of HSC panels and 4 of SC panels with five different thicknesses of 60 mm, 80 mm, 100 mm, 120 mm, and 150 mm. Steel faceplates applied to HSC and SC panels had three different thicknesses of 0.5 mm, 0.8 mm, and 1.2 mm. Test 2 was comprised of 4 of RC panels and 8 of HSC panels with a thickness of 80 mm. Steel faceplates applied to HSC had two different thicknesses of 0.5 mm and 0.8 mm.

They evaluated the correlation of bulging height of the rear steel plate and missile velocity from experimental test results. They proposed a formula to calculate bulging height of a rear steel

plate combining energy balance equation, revised scabbing velocity from Chang's formula, and proportional coefficient obtained from the test results as follows:

$$v^2 = \frac{\sqrt{T}}{144.4} \cdot \frac{2\pi}{m} \cdot H \left( t + \frac{d}{2} \right)^2 + v_s^2$$

where,  $m$  is a mass of projectile (Kg),  $v$  is an impact velocity (m/s),  $v_s$  is a scabbing velocity,  $t$  is a thickness of RC panel (mm),  $d$  is a diameter of projectile (mm),  $T$  is a thickness of steel plate (mm), and  $H$  is a bulging height. The scabbing velocity of  $v_s(0.8t)$  was used for adjustment to the test results.

### 2.3.6 Grisaro and Dancygier (2014)

Grisaro and Dancygier (2014) proposed a model to assess the perforation failure of RC barriers with a rear steel faceplate to impactive loading from a rigid projectile. The proposed model was developed integrating existing perforation formulas for concrete and steel plate.

They followed Walter and Wolde-Tinsae (1984)'s approach, which is based on the conversion of steel plate thickness to an equivalent thickness of concrete. However, their model took into account more design parameters such as projectile characteristics, steel thickness and concrete strengths.

With regard to incorporating steel faceplate thickness to their model, BRL perforation model (ALCO Products Inc. 1955) was used for thinner thicknesses, and Rosenberg and Dekel (2009, 2010) perforation model was used for thicker thicknesses. Details of the penetration mechanism of composite RC barriers was not considered in their model. For reinforced concrete thickness, NDRC model and Li & Chen model were used. Test data from Tsubota et al. (1993) and Hashimoto et al. (2005) were used for verification of the proposed model.

### 2.3.7 Bruhl et al. (2015)

Bruhl et al. (2015) compiled an experimental database of 130 missile impact tests conducted on SC and RC walls with rear steel plate and used the database to propose a three-step design method of SC walls against missile impact loading, particularly to prevent local perforation.

The 1<sup>st</sup> step is to decide a concrete wall thickness, which may be limited by existing design or other design restrictions. When design guide for RC walls (ERIN Engineering & Research Inc. 2011; U.S. Department of Defense 2008) is used to calculate the trial concrete thickness, then the calculated value can be reduced by 30% to estimate the initial SC wall concrete thickness. The 2<sup>nd</sup> step is to compute the weight and residual velocity of concrete frustum that is dislodged as the missile penetrates into the SC wall. Failure mechanism supporting this design method assumes that the concrete frustum is formed over the depth of the concrete thickness and dislodged to impact the rear steel faceplate of the SC wall together with the original projectile. For calculating perforation velocity for the concrete of the SC wall, modified NDRC equations (American Society of Civil Engineers 1980) was used combined with statistical variability factor,  $\beta$ , to ensure the level of reliability equal to 95%. This  $\beta$  factor can impose inherent conservatism on the design method. The 3<sup>rd</sup> step is to determine the required thickness of the steel faceplate. Steel plate equations (Børvik et al. 2009) based on cylindrical cavity-expansion theory and quasi-static radial compressive stress are adopted. Projectile mass is calculated from both the original projectile and concrete frustum. Strain-rate effect of the steel plate is not taken into account.

Because this method was developed using existing design equations for steel and RC structures and was validated using a database of previous tests, its applicability is limited to the range of applicability of the original equations and previous tests.

While this method was verified using the comprehensive database of existing tests, it has not been specifically validated by an experimental program designed to evaluate its accuracy.

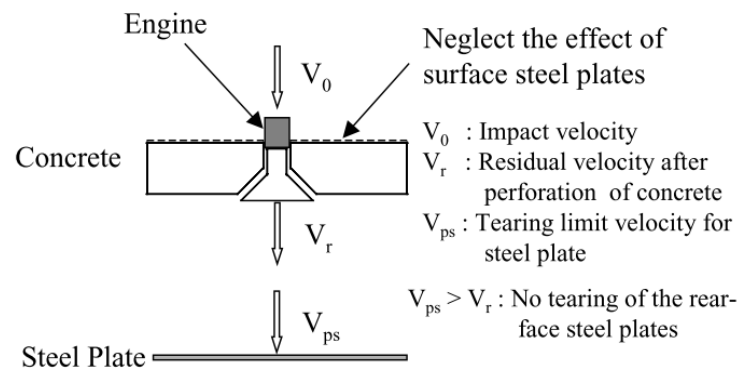


Figure 2-1 Proposed simplified method to design surface steel plates (Mizuno et al. 2005a)

## CHAPTER 3. EXPERIMENTAL PROGRAM

### 3.1 Introduction

This chapter describes an experimental test program to investigate local penetration and perforation behavior of SC wall specimens subjected to missile impact. SC wall specimens were designed in small-scale according to AISC N690s1-15, Appendix N9 with a few limitations. Material properties of components of the SC wall specimen were measured from tensile coupon tests or provided by suppliers. Test matrix was constructed to produce test cases in which the SC wall specimens were to be perforated or not, based on the three-step design method. The test setup was designed to perform missile impact tests in an indoor laboratory with appropriate protection. Damage of SC wall specimens was measured with instrumentation options described herein.

### 3.2 Specimen Design and Material Properties

Each of the SC wall specimens tested in this program was comprised of steel faceplates, steel-headed shear stud anchors, tie bars and a concrete infill as shown in the three-dimensional rendering model in Figure 3-1 (a). A photograph of the specimen before concrete cast in Figure 3-1 (b) depicts how these components were configured in the SC wall section.

For the specimens, two different thicknesses of ASTM A1011 high-strength, low-alloy (HSLA) hot-rolled steel sheet were applied: gage 12 and 14. Thereby, flexural reinforcement ratio ( $\rho = 2t_p/T_{sc}$ ) varied from 3.7% to 5.2% with steel faceplate ranging from 0.0747 in. (1.9 mm) to 0.1046 in. (2.66 mm). For the gage 14 of ASTM A1011 steel faceplate, two different strengths were used: grade 50 and 65. Steel-headed shear stud anchors (or shear studs) with 0.25 in. (6.35 mm) diameter and 1.125 in. (28.58 mm) long were spaced at 2 in. (50.8 mm) on each faceplate. Threaded rods were used as tie bars and secured with hex nuts on both sides of the steel faceplates.

Tie bar spacing varied between 2 in. (50.8 mm) and 4 in. (101.6 mm). Shear reinforcement ratio ( $\rho_t = A_t/S^2$ ) varied from 0.37% to 1.23% with tie bar diameter ranging from 0.138 in. (3.51 mm) to 0.3126 in. (7.94 mm). Normal weight concrete with 0.375 in. (9.53 mm) maximum aggregate diameter (pea gravel) was used as the concrete infill. All the specimens had identical global dimensions of 16 in. (406.4 mm)  $\times$  11 in. (279.4 mm)  $\times$  4 in. (101.6 mm). They were designed as one third scale of practical SC walls so that the missile impact test could be conducted in an indoor scale laboratory. Details of the specimen design are described in Figure 3-2 and Table 3-1.

The specimens in Table 3-1 are identified by the “specimen identifier” which consists of three parts using basic information of their configuration: the first part indicates the flexural reinforcement ratio by percentage; the second part presents the shear reinforcement ratio in percentage; and the third part expresses the grade of the steel faceplates. They were designed in accordance with AISC N690s1-15, Appendix N9 (American Institute of Steel Construction 2015), however, not all provisions were satisfied because of limitations which came mostly from their size:

- Steel faceplate thickness does not satisfy its lower bound requirement: ( $> 0.25$  in. (6.35 mm))
- Specimens of test cases in group 2 (Table 3-5) have marginally greater flexural reinforcement ratio (5.2%) than the upper bound requirement: ( $< 5.0\%$ )
- Specimens of test cases in group 1 and group 3 have slenderness ratios ( $s/t_p$ ) greater than the maximum requirement: ( $< 1.0\sqrt{E_s / f_y}$ )

For design calculations of the SC wall specimens, material properties provided by suppliers were used and the values were summarized in Table 3-2 including the steel faceplates and the steel-headed shear studs. For further use in numerical analysis, the full engineering stress-strain curves were obtained by uniaxial tensile coupon tests except for the steel-headed shear studs. Stress-strain curves for steel faceplates and tie bars are presented in Figure 3-3. These obtained stress-strain curves were converted to power law material model with variables using the equation shown in Equation 3-1 (Varma 2000).

$$\sigma = \sigma_u - (\sigma_u - \sigma_y) \cdot \left( \frac{\varepsilon_u - \varepsilon}{\varepsilon_u - \varepsilon_{sh}} \right)^n \quad \text{Equation 3-1}$$

In Equation 3-1,  $\sigma_u$  is ultimate strength,  $\sigma_y$  is yield strength,  $\varepsilon_u$  is ultimate strain and  $\varepsilon_{sh}$  is the strain when strain hardening is about to occur. Best fitted variables for the power law material model of steel components were summarized in Table 3-3. For steel-headed shear stud anchors, the tensile coupon test was not available.

Two batches of concrete with the same mix design were used to fabricate the specimens. Both concrete batches had nominal specified strength of 5 ksi (34.5 MPa) and measured concrete compressive strength at 28 days ( $f'_c$ ) of 5.31 ksi (36.61 MPa) and 6.28 ksi (43.3 MPa), respectively. Day-of-test strength data varied from 5.89 ksi (40.6 MPa) to 6.53 ksi (45.0 MPa), as described in Table 4-1. Formwork was built for concrete casting in the SC wall specimen modules as shown in Figure 3-4. The SC wall specimen modules were lined up at 3 in. (76.2 mm) spacing on a base plate and two open ends of the module were closed by side plates to support concrete pressure casted. Bracing was installed to maintain the spacing between each module and stabilize

the modules against lateral and vertical movement during casting. The base plate and side plates were made of black phenolic plywood (or film-faced plywood). An immersion (or needle) type electric vibrator was used to compact the concrete infill in the SC wall specimen modules. Figure 3-4 (a) shows the concrete casting of the SC wall specimens. Figure 3-4 (b) shows SC wall specimens in the formwork after casting.

Projectiles were cut from AISI 4340 steel round stock and heat treated to a minimum 42-45 C Rockwell hardness to simulate nondeformable flat-nosed missiles. Material properties of the projectile were obtained from coupon tests with average values of 192 ksi (1324 MPa) yield strength and 205 ksi (1413 MPa) ultimate strength for 1.0 in. (25.4 mm) diameter round stock, and 196 ksi (1351 MPa) yield strength and 206 ksi (1420 MPa) ultimate strength for 1.5 in. (38.1 mm) diameter round stock. Figure 3-5 provides photographs of a representative projectile.

Because there was a gap between the inside diameter of the gun barrel and the projectile diameter, a sabot was used to seal the gun barrel and ensure the projectile flight remained level. Polypropylene was chosen for the sabot material and designed and fabricated to fit different types of projectiles in the test matrix (Table 3-5). The interior of the sabot was drilled to hold a projectile. The exterior was machined to reduce weight and ensure it would crush upon impact. Compressive strength of the sabot material was 4.8 ksi (33 MPa) and modulus of elasticity was 152 ksi (1.05 GPa). Figure 3-6 shows an assembly of the sabot and the projectile. Variety of the projectiles and corresponding sabots are presented with their geometric dimensions and material properties in Table 3-4. Figure 3-7 describes dimensions which each geometric parameter indicates in the assembly of the sabot and the projectile.

### 3.3 Test Matrix

The test matrix philosophy was designed to include test cases ranging from wall specimens that were expected to be perforated by projectiles, to wall specimens that were expected to stop projectiles for each SC wall specimen design configuration. Table 3-5 describes the details of the test matrix. Test case identifiers consist of six terms to indicate specific features of each test. The first three terms relate to the SC wall specimen features as described previously. The next three terms relate to projectile features and indicate nominal diameter ( $D_p$ : 1.0 in. and 1.5 in.), weight ( $W_p$ : 1.3 lbs, 2.0 lbs and 3.5 lbs), and impact velocity ( $V_o$ : 380 ft/s - 750 ft/s), respectively. The three-step design method (Bruhl et al. 2015), mentioned in the commentary of the AISC N690s1-15, Appendix N9, was adopted to calculate the expected projectile velocity which perforates a given wall design. This calculated perforation velocity is considered as the design velocity of the SC walls. Projectile impact velocities were then selected from above and below the design velocity. For test cases in which perforation was expected to occur the impact velocity was chosen to be approximately 10% greater than the design velocity. On the other hand, the design velocity was decreased by approximately 10% for test cases in which the projectile was expected to be stopped by the specimen. As seen in Table 3-5, at least one pair of test cases were planned expecting perforation or no-perforation (or stop) test results for the same specimen design configuration.

All the test cases were categorized as group 1, group 2 and group 3 according to their characteristic features. Test cases in group 1 and group 3 had the same flexural reinforcement ratio of 3.7%, but test cases in group 2 had flexural reinforcement ratio of 5.2%. Test cases in group 1 and group 2 had the same steel faceplate's nominal yield strength of 50 ksi, however, test cases in group 3 had steel faceplate's nominal yield strength of 65 ksi. Figure 3-8 through Figure 3-10 depicts how all the test cases in the matrix were positioned on the perforation resistance curves of

the SC wall specimens obtained using the three-step design method. Test cases on the left side of the curves were expected to stop the projectile. Test cases on the right side of the curves were expected to perforate the SC wall specimen.

### *3.4 Test Setup*

The test apparatus consisted of several parts as depicted in Figure 3-11 (a): gas gun assembly, gun barrel, front chamber, main support structure, rear chamber, and catcher chamber. For each test, the projectile, with a sabot, was loaded at the front of the gun barrel and launched by pressurized nitrogen gas from the gas gun assembly. Projectiles were inserted into a specially-fabricated sabot to maintain a seal between the gun barrel and the sabot, and to help ensure level flight of the projectile when exiting the gun barrel. The SC wall specimen was affixed by bolts to the frames in the main support structure inside the front chamber as shown in Figure 3-11 (b). Impact of a projectile into the SC wall specimen occurred within the front chamber which was designed as a protective shield to contain any shrapnel caused by the impact. When a projectile perforated the specimen, debris generated from the concrete core and steel faceplates proceeded backward from the specimen and was collected in the rear chamber. The catcher chamber was designed to collect anything passing through the rear chamber including projectile and pieces from the test specimen.

The gas gun assembly consisted of a pressurized tank and a pneumatic solenoid spool valve. The valve was designed to be remotely released from a protected location. Nitrogen gas was used as a propellant. The barrel was 20.8 ft (6.35 m) long and the inside diameter was 2.5 in. (63.5 mm). The gas gun assembly, including the barrel, was built by Hwun Park, a former Ph.D. student in the School of Aeronautics and Astronautics of Purdue University (Park 2011). The gun assembly was

made available for use for this research project in cooperation with Professor Weinong Chen of Purdue University.

The main support structure included structural steel vertical members, bottom fixtures, diagonal members and specimen holders designed to hold and support the specimen against the impact load. This structure was anchored to the floor using Hilti HSL-3-G-M20/30 anchors and the front and rear chambers were then bolted to the main support structure.

The front chamber, assembled from 0.5 in. (12.7 mm) thick steel plate, protects against an errant projectile and/or debris generated during the test. This chamber included space to allow a camera to record the projectile's flight before impact. The high-speed video recording from the camera was used to determine impact velocity. The front chamber was bolted to the support structure and anchored to the floor. A hinged door on the side of the chamber provided access to attach specimens to the main support structure. A 9 in. (228.6 mm) square opening, covered with a polycarbonate window, was included on the hinged door to provide a view portal for the high-speed video camera.

The rear chamber, assembled from 0.5 in. (12.7 mm) thick steel plate and bolted to the support structure, protects against projectiles which perforate a specimen and resultant debris. The catcher chamber collects the projectile and all debris that travels through the rear chamber. The catcher chamber was comprised of a structural steel HSS  $14 \times 14 \times 1/2$  with a 3 in. (76.2 mm) thick steel back plate.

The catcher chamber was set on casters for efficient clean-up at the end of each test. Figure 3-12 depicts test setup installed at the Robert L. and Terry L. Bowen laboratory, in Lyles School of Civil Engineering, Purdue University.

### 3.5 Instrumentation

A high-speed camera was used to capture the instance of the projectile impact on the SC wall and to measure the actual projectile impact velocity. A Photron Fastcam APX PX high-speed camera recorded the impact using 14,000 frames per second with frame rate and  $640 \times 304$  pixels resolution. The high-speed images were recorded through a square opening (view portal) on the front chamber. This view portal was covered with a 12 in. (304.8 mm) square, 2 in. (50.8 mm) thick transparent polycarbonate plate typically used for bullet proof applications. A checker board with a scale was positioned in front of the SC wall specimen inside the front chamber to enable precise measurement of the projectile velocity by checking the distance which the projectile proceeded through each recorded frame of high-speed video. Figure 3-13 shows a captured image of the inside of the front chamber through the view portal by a high-speed camera.

Damage to the front and rear of the specimens was quantitatively and qualitatively recorded and analyzed upon completion of each test. Qualitative measures included the nature of the damage (e.g. bulging or tearing of rear faceplate). Quantitative measures included the projectile penetration depth and the rear steel faceplate bulging depth. Penetration depth of a projectile was measured by the difference between the total length of a projectile subtracted by the exposed length of a projectile out of the penetrated SC wall specimen after the test. A contour gage was used to measure the bulging depth of all SC wall specimens which stopped the projectile. It contains a series of aligned teeth and when it is applied, each of these teeth is pushed back in the body of gage individually according to the target's shape so that the gage reads the entire profile of it. Bulging depth was determined as the maximum height value of the measured profile of the bulged rear steel faceplate. This manual measurement was made at the completion of each test. These tests did not measure a displacement time-history because of the risk of damage to displacement gages behind the specimens. Figure 3-14 illustrates how the bulging depth of the rear steel faceplate was

measured after each test. The resultant values were finalized comparing with the values examined from the cross-section cuts of the post-test specimens and summarized in CHAPTER 4.

Strain gage rosettes are placed on the rear steel faceplate of the SC wall specimens as shown in Figure 3-15. Strains were recorded using a National Instrument PXI-1052 chassis with PXI-6221 M Series Multifunctional DAQ system at a sampling rate of 40 kHz.

Table 3-1 Design details of the SC wall specimens

<i>Specimen identifier</i>	$T_{sc}$ (in)	$t_p$ (in)	$\rho$ (%)	$s/t_p$	$S/T_{sc}$	$\rho_t$ (%)	$f'_c$ * (ksi)	$s$ (in)	$d_s$ (in)	$S$ (in)	$d_t$ (in)	<i>Grade / Gage</i> **
3.7-0.37-50	4.00	0.0747	3.7%	26.8	0.5	0.37%	5.00	2.00	0.25	2.00	0.1380	50 / 14
3.7-0.37-65	4.00	0.0747	3.7%	26.8	0.5	0.37%	5.00	2.00	0.25	2.00	0.1380	65 / 14
3.7-0.53-50	4.00	0.0747	3.7%	26.8	0.5	0.53%	5.00	2.00	0.25	2.00	0.1640	50 / 14
5.2-0.48-50	4.00	0.1046	5.2%	19.1	1.0	0.48%	5.00	2.00	0.25	4.00	0.3125	50 / 12
3.7-1.23-50	4.00	0.0747	3.7%	26.8	0.5	1.23%	5.00	2.00	0.25	2.00	0.2500	50 / 14

\* Nominal strength of concrete infill

\*\* Grade and gage of steel faceplates

Table 3-2 Summary of material properties for steel faceplates and stud anchors

(Provided by suppliers)

<i>Materials</i>	$f_y$ ( <i>ksi</i> )	$f_u$ ( <i>ksi</i> )	$\epsilon_f$ (%)
A1011 steel sheet, gage 14, grade 50	55.6	67.9	29.6
A1011 steel sheet, gage 14, grade 65	72.7	79.8	25.4
A1011 steel sheet, gage 12, grade 50	58.1	66.5	31.5
Steel-headed shear stud anchors	61.6	76.1	20.0

Table 3-3 Best fitted variables for the power law material model (Bruhl 2015)

<i>Materials</i>	$E$ ( <i>ksi</i> )	$f_y$ ( <i>ksi</i> )	$f_u$ ( <i>ksi</i> )	$\epsilon_{sh}$ ( <i>in/in</i> )	$\epsilon_u$ ( <i>in/in</i> )	$n$
A1011 steel sheet, gage 14, grade 50	26000	57.9	64.8	0.0267	0.169	3.6
A1011 steel sheet, gage 14, grade 65	27000	68.0	84.4	0.0108	0.159	3.2
A1011 steel sheet, gage 12, grade 50	29000	57.7	68.4	0.0139	0.183	3.6
Tie bars	21000	59.5	66.0	0.0028	0.091	7.0

Table 3-4 Types of projectiles and sabots with their dimensions and material properties

<i>No.</i>	<i>Identifier</i>	<i>Projectile</i>					<i>Sabot</i>			
		$D_p$ (in)	$W_p$ (lbs)	$l$ (in)	$f_y$ (ksi)	$f_u$ (ksi)	$D_s$ (in)	$t$ (in)	$L$ (in)	$f_c$ (ksi)
1	1.0-1.3	1.0	1.3	6.00	192	205	2.498	1.50	6.00	4.8
2	1.0-2.0	1.0	2.0	9.00	192	205	2.498	1.50	8.00	4.8
3	1.5-1.3	1.5	1.3	2.625	196	206	2.498	3.00	5.00	4.8
4	1.5-2.0	1.5	2.0	4.00	196	206	2.498	2.00	5.00	4.8
5	2.5-3.5	1.5	3.5	7.00	196	206	2.498	1.50	6.75	4.8

Table 3-5 Missile impact test matrix for small-scale SC walls

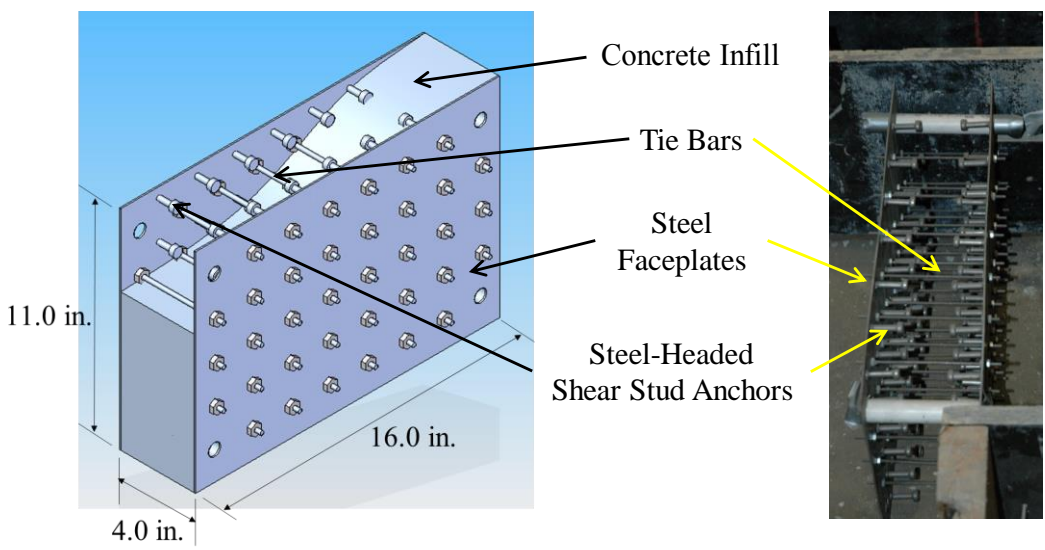
<i>Test group / No.</i>	<i>Test case identifier</i>	<i>SC wall</i>					<i>Projectile</i>			<i>Expected result *</i>	
		$\rho$ (%)	$S/T_{sc}$	$\rho_t$ (%)	$f'_c$ † (ksi)	$f_y^{pl}$ ‡ (ksi)	$D_p$ (in)	$W_p$ (lb)	$V_o$ (ft/s)		
<i>Gr. 1</i>	1	3.7-0.37-50-1.0-1.3-554	3.7	0.5	0.37	5	50	1.0	1.3	554	Stop
	2	3.7-0.37-50-1.0-1.3-677	3.7	0.5	0.37	5	50	1.0	1.3	677	Perf.
	3	3.7-0.37-50-1.0-2.0-430	3.7	0.5	0.37	5	50	1.0	2.0	430	Stop
	4	3.7-0.37-50-1.0-2.0-525	3.7	0.5	0.37	5	50	1.0	2.0	525	Perf.
	5	3.7-0.53-50-1.5-1.3-660	3.7	0.5	0.53	5	50	1.5	1.3	660	Stop
	6	3.7-0.53-50-1.5-1.3-750	3.7	0.5	0.53	5	50	1.5	1.3	750	Perf.
	7	3.7-0.53-50-1.5-2.0-513	3.7	0.5	0.53	5	50	1.5	2.0	513	Stop
	8	3.7-0.53-50-1.5-2.0-626	3.7	0.5	0.53	5	50	1.5	2.0	626	Perf.
	9	3.7-1.23-50-1.5-3.5-380	3.7	0.5	1.23	5	50	1.5	3.5	380	Stop
	10	3.7-1.23-50-1.5-3.5-465	3.7	0.5	1.23	5	50	1.5	3.5	465	Perf.
<i>Gr. 2</i>	1	5.2-0.48-50-1.0-2.0-445	5.2	1.0	0.48	5	50	1.0	2.0	445	Stop
	2	5.2-0.48-50-1.0-2.0-544	5.2	1.0	0.48	5	50	1.0	2.0	544	Perf.
	3	5.2-0.48-50-1.5-3.5-408	5.2	1.0	0.48	5	50	1.5	3.5	408	Stop
	4	5.2-0.48-50-1.5-3.5-498	5.2	1.0	0.48	5	50	1.5	3.5	498	Perf.
<i>Gr. 3</i>	1	3.7-0.37-65-1.0-2.0-443	3.7	0.5	0.37	5	65	1.0	2.0	443	Stop
	2	3.7-0.37-65-1.0-2.0-541	3.7	0.5	0.37	5	65	1.0	2.0	541	Perf.

†  $f'_c$  : Nominal compressive strength of concrete

‡  $f_y^{pl}$  : Nominal yield strength of steel faceplate

\* Stop: The specimen stopped the projectile

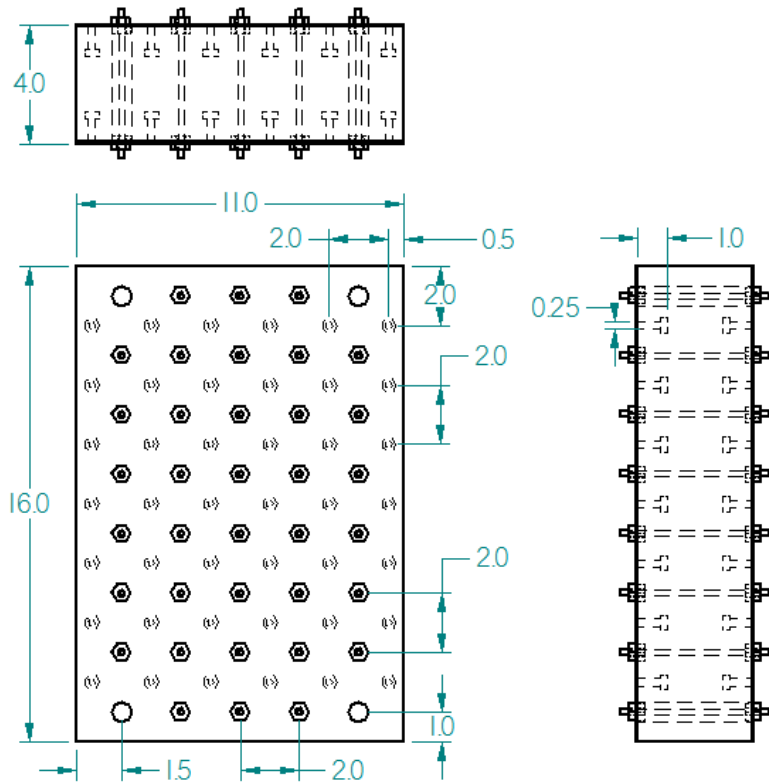
Perf.: The specimen was perforated by the projectile



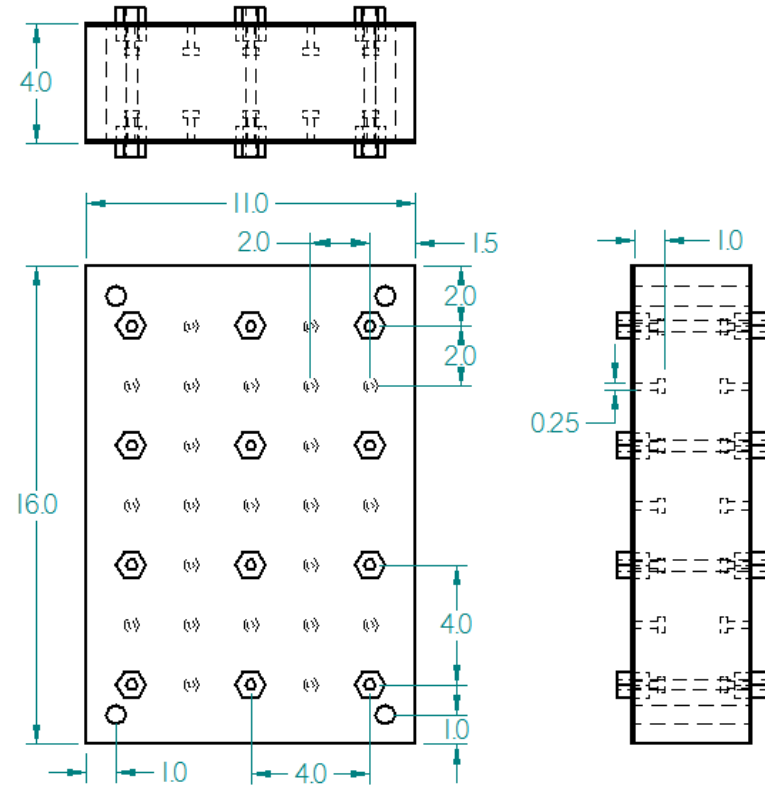
(a) 3D rendering of SC wall specimen

(b) Specimen before concrete cast

Figure 3-1 Three-dimensional rendering and module of SC wall specimen

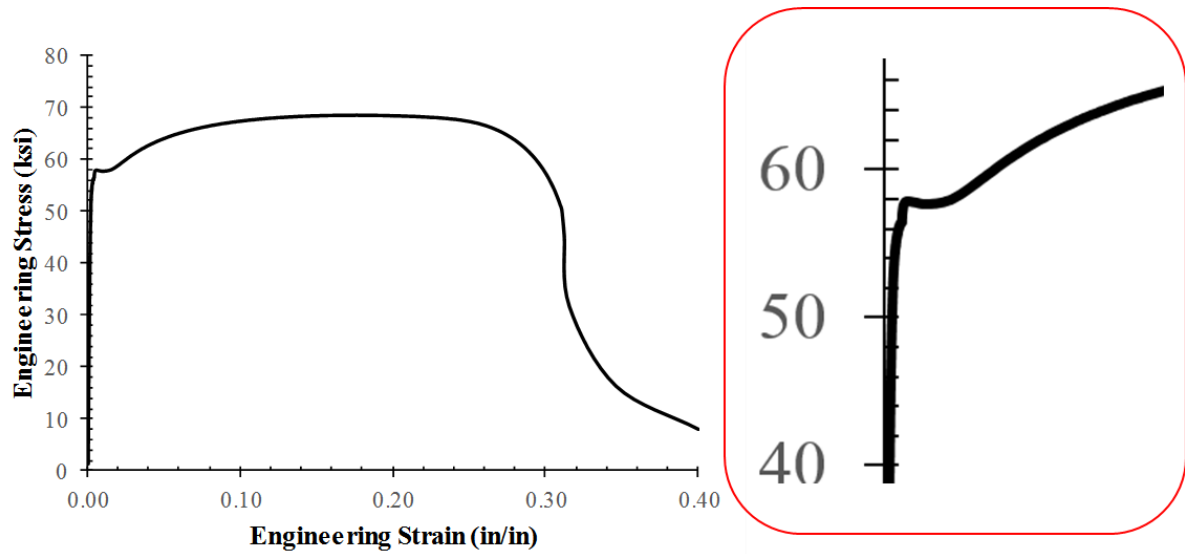


(a) Specimen in group 1 and group 3

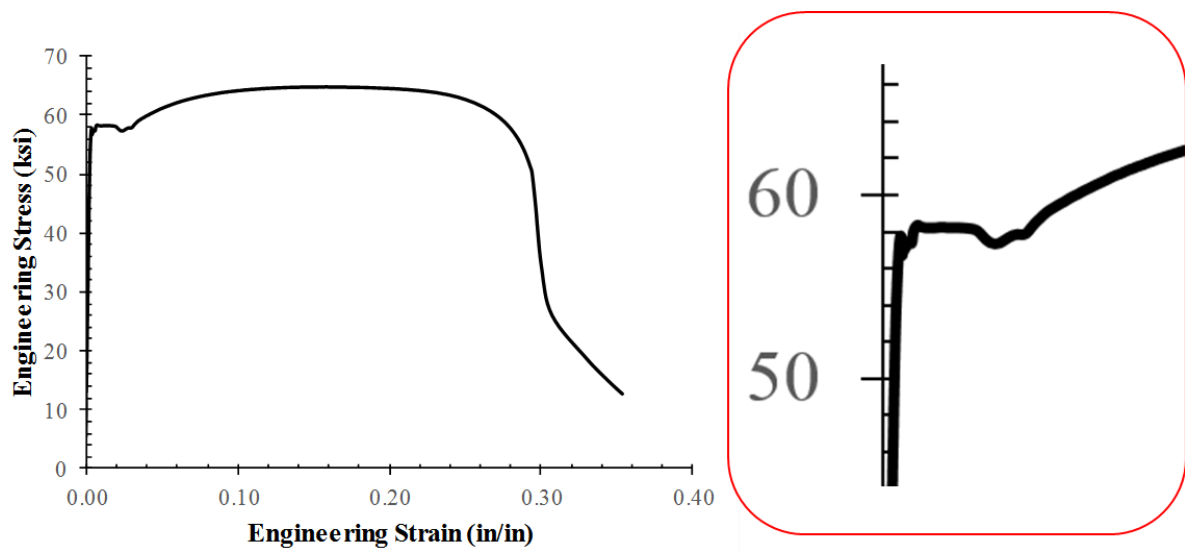


(b) Specimen in group 2

Figure 3-2 Representative design drawings of SC wall specimens (all dimensions are in inches)



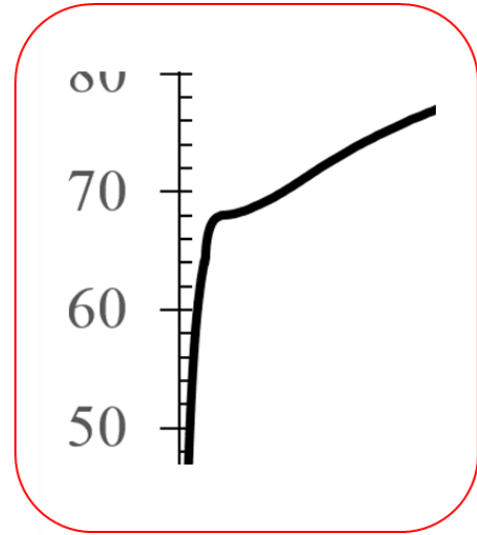
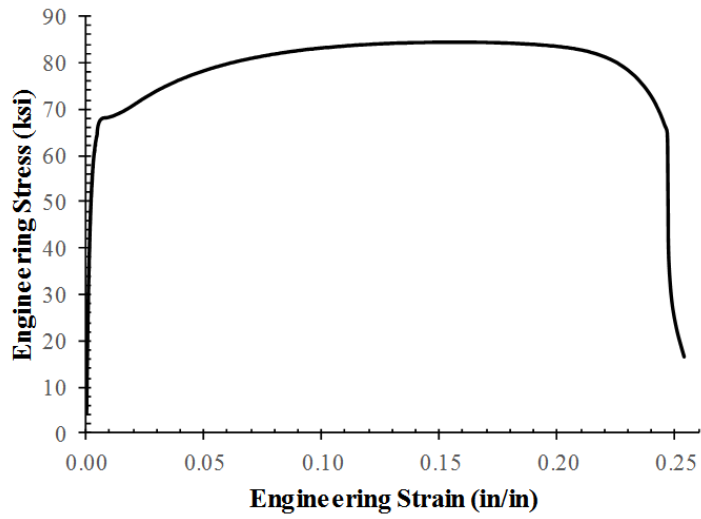
(a) A1011 steel sheet, gage 12, grade 50



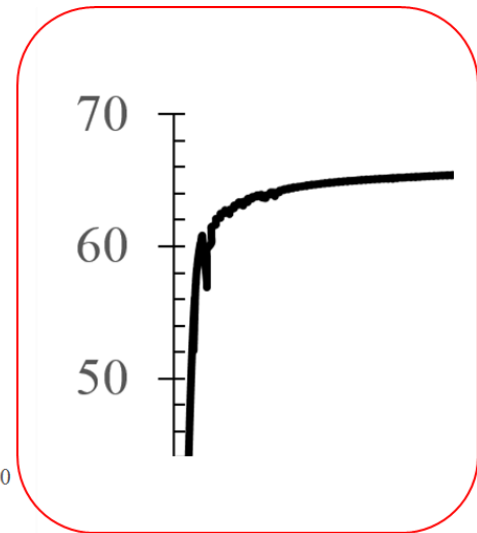
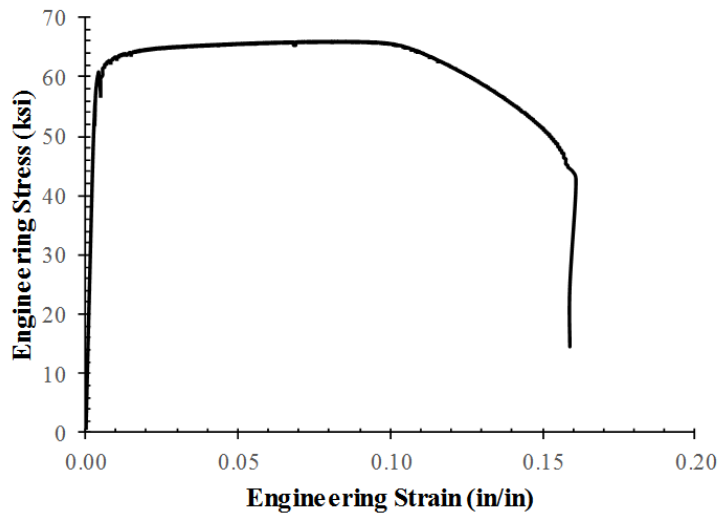
(b) A1011 steel sheet, gage 14, grade 50

Figure 3-3 Representative tensile stress-strain curves (Bruhl 2015)

Figure 3-3 Continued



(c) A1011 steel sheet, gage 14, grade 65



(d) Tie bar(s)



(a) Specimens during concrete casting



(b) Specimens after concrete casting

Figure 3-4 Photographs of concrete cast



Figure 3-5 Photographs of the 1.0 in. diameter, 1.3 lbs projectile

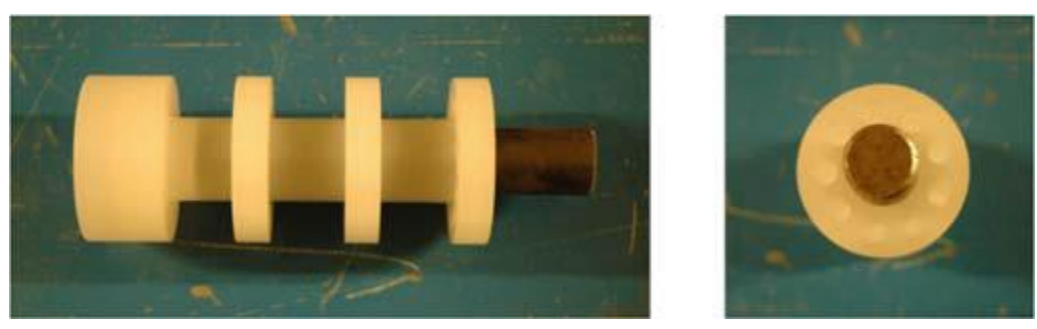


Figure 3-6 Photographs of the projectile and sabot assembly for 1.0 in. diameter, 1.3 lbs projectile

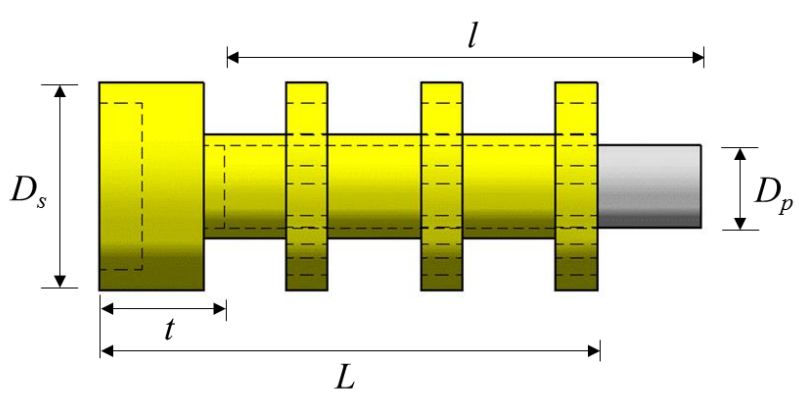
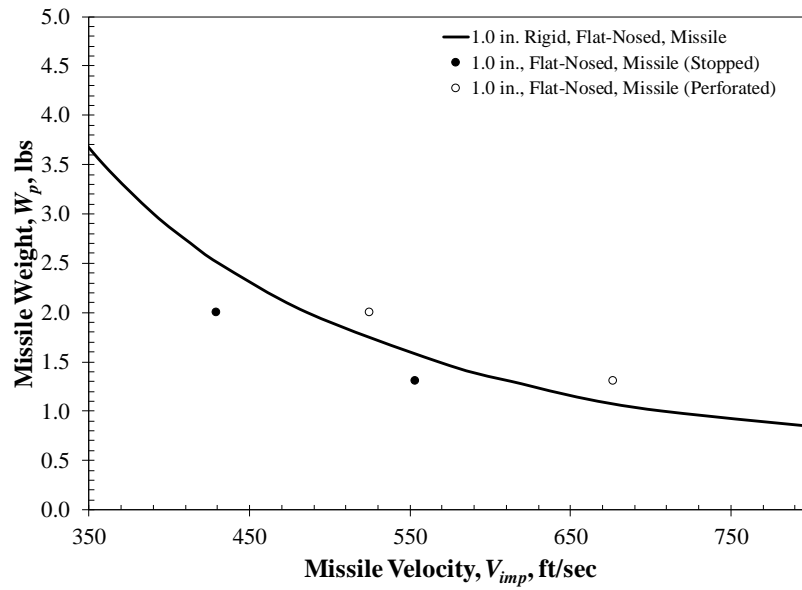
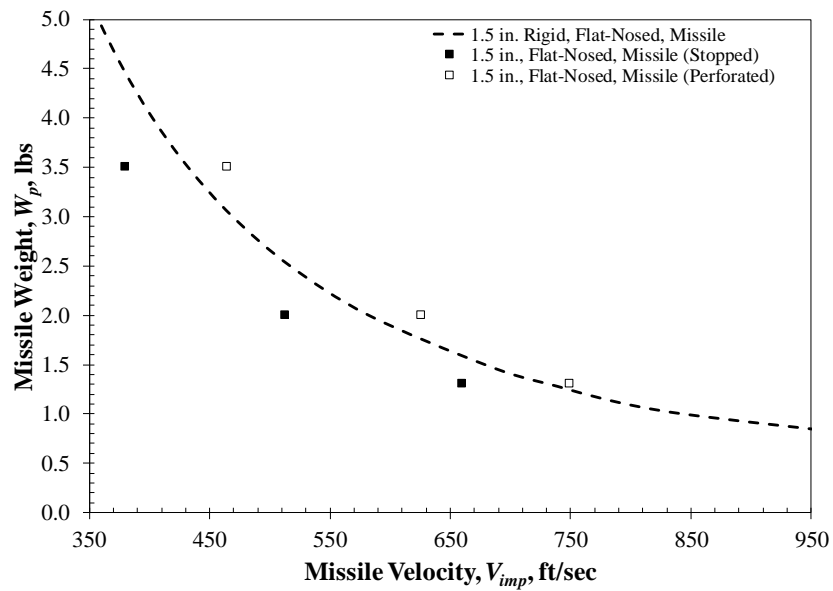


Figure 3-7 Schematic design of a projectile and sabot assembly

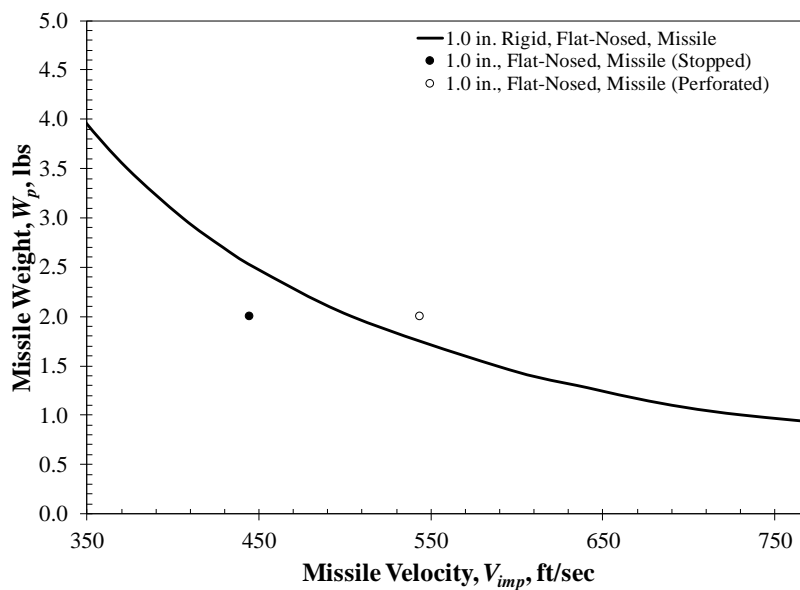


(a) 1.0 in. diameter projectile applied

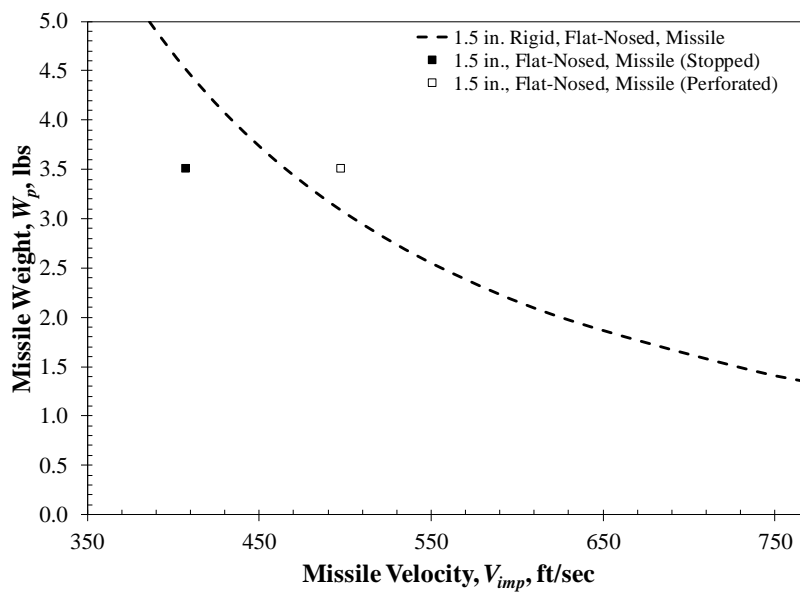


(b) 1.5 in. diameter projectiles applied

Figure 3-8 Test cases marked on perforation resistance curves in group 1



(a) 1.0 in. diameter projectile applied



(b) 1.5 in. diameter projectiles applied

Figure 3-9 Test cases marked on perforation resistance curves in group 2

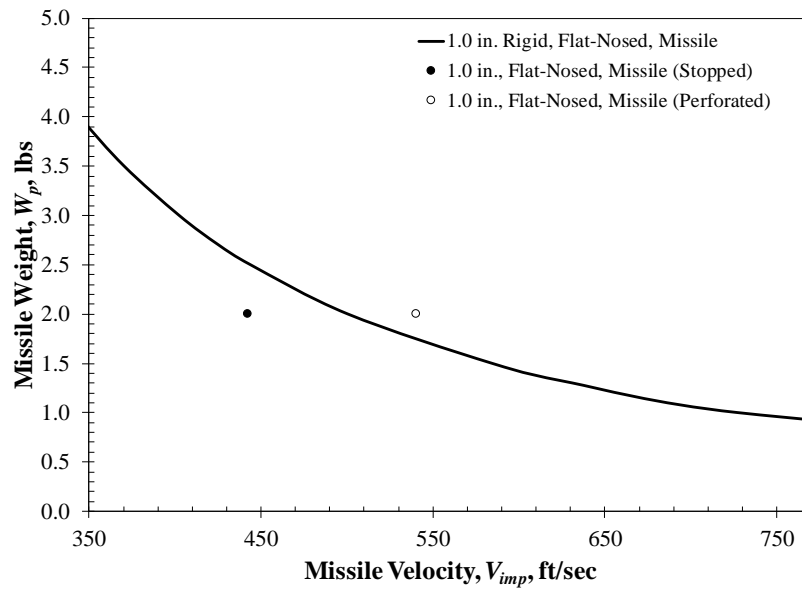
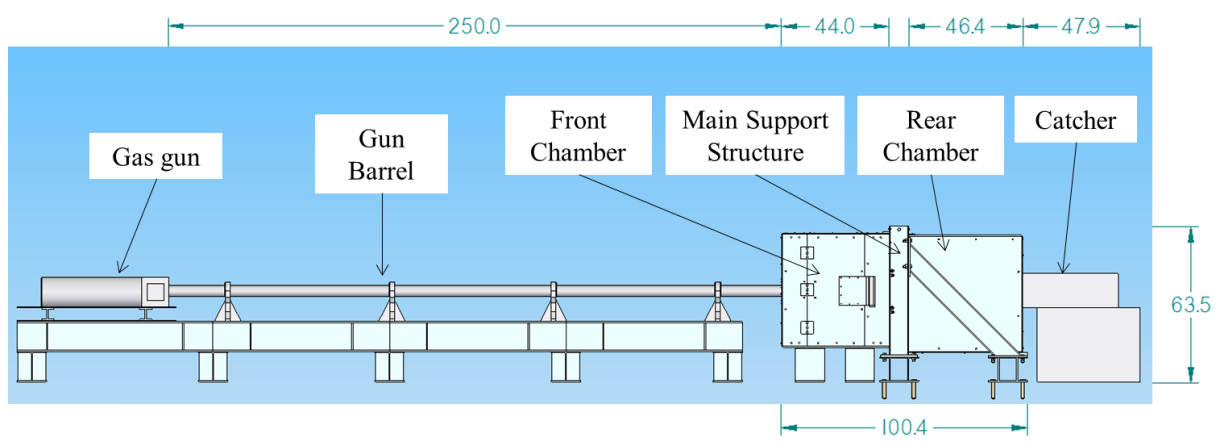
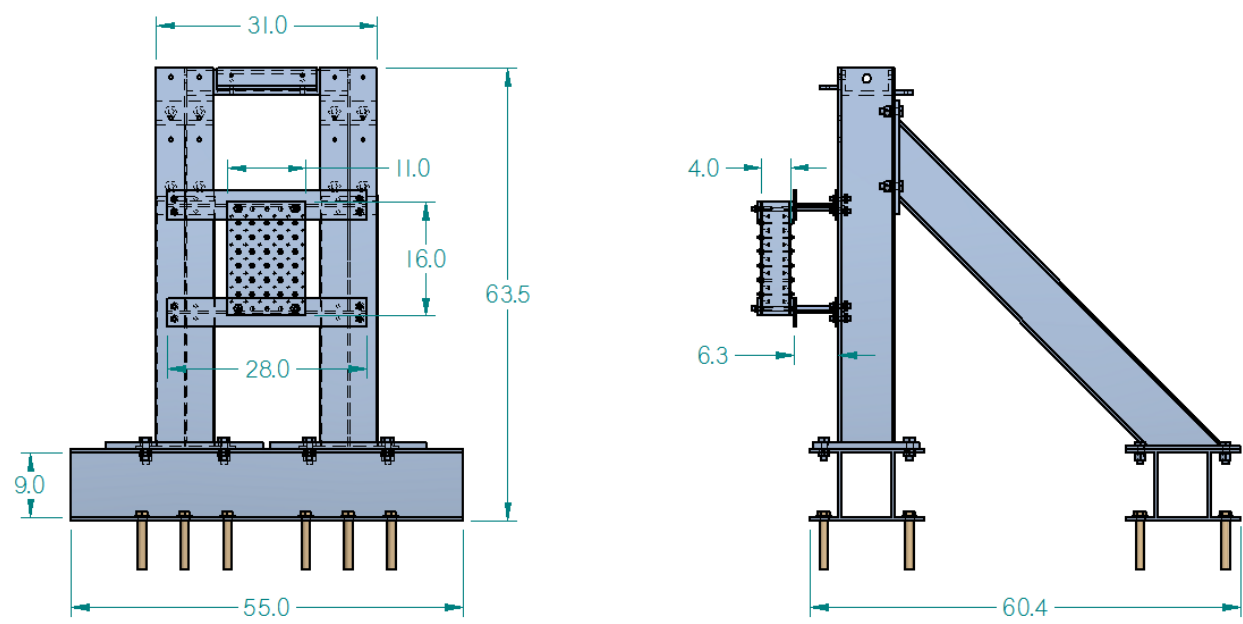


Figure 3-10 Test cases marked on perforation resistance curve in group 3



(a) Schematic view of the test setup



(b) Test specimen attached to the frames in the main support structure

Figure 3-11 Conceptual design of experimental test setup (all dimensions are in inches)

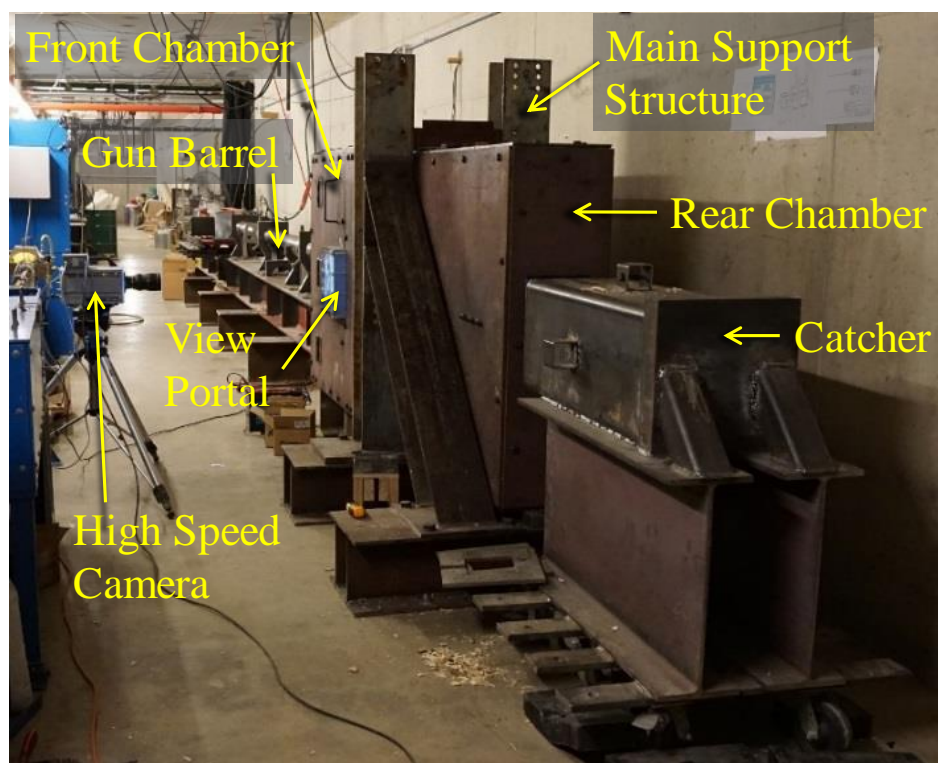
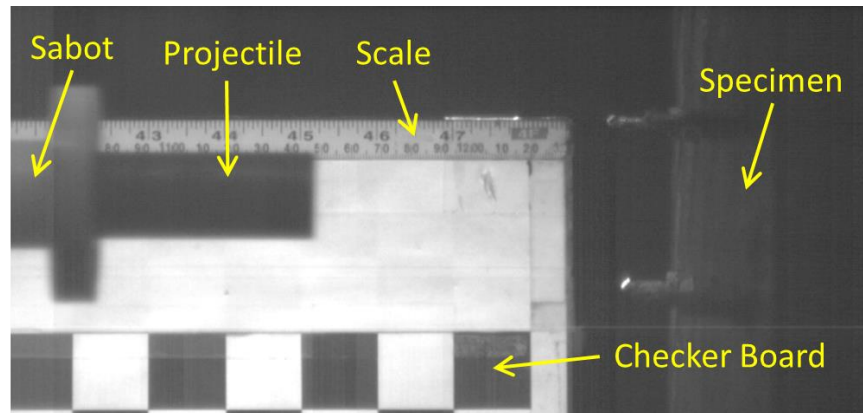
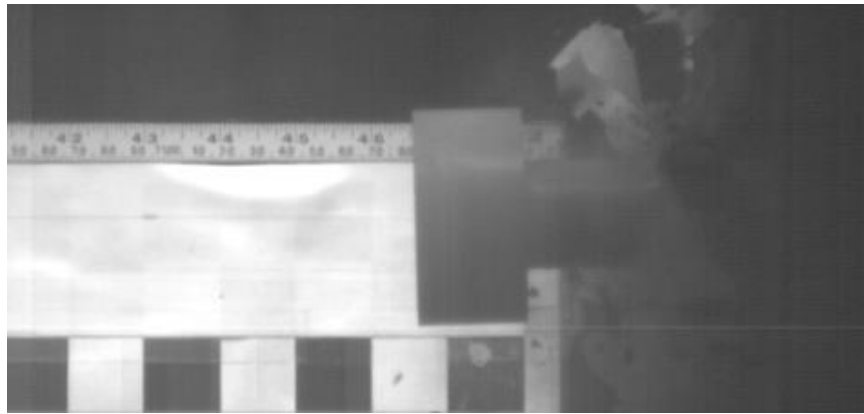


Figure 3-12 Photograph of the installed test setup



(a) Before projectile impact



(b) After projectile impact

Figure 3-13 Captured images of the inside of the front chamber by a high-speed camera (Test case number 7 in group 1)



Figure 3-14 Bulging depth measurement using a contour gage after test

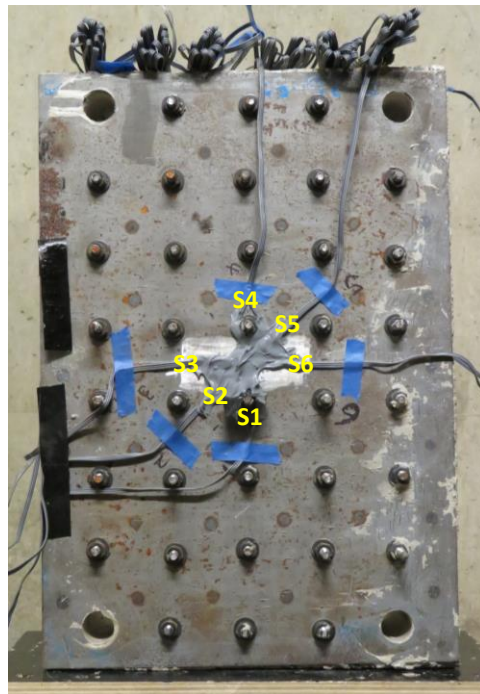


Figure 3-15 Representative layout of strain gage rosettes

## CHAPTER 4. EXPERIMENTAL INVESTIGATIONS

### 4.1 Introduction

A total of sixteen tests were conducted and the results were analyzed to investigate local failure behavior of SC walls subjected to missile impact. Each post-test SC wall specimen was examined carefully and the degree of damage was measured and summarized.

External damage behavior of SC wall specimens was investigated and damage mode of each post-test specimen was defined accordingly. Final (or generic) test result, which meant if a projectile was stopped by an SC wall specimen or an SC wall specimen was perforated by a projectile, was also compared with perforation resistance curve obtained from the three-step design method. It was used to evaluate the accuracy of the three-step design method.

Internal damage behavior of SC wall specimens was investigated. Local failure mechanism was proposed based on the observation on the cross-section cut of the post-test specimens. Penetration depth of a projectile into the specimen was measured. It was used to verify the performance of the modified NDRC equation which was applied in the three-step design method.

### 4.2 Test Results of Specimens

#### 4.2.1 Group 1: Test case number 1: 3.7-0.37-50-1.0-1.3-554

The global dimension of the specimen is 16 in. (406.4 mm)  $\times$  11 in. (279.4 mm)  $\times$  4 in. (101.6 mm) with flexural reinforcement ratio of 3.7%, shear reinforcement ratio of 0.37% and steel faceplate strength of grade 50. 0.25 in. (6.35 mm) diameter, 1.125 in. (28.58 mm) long, shear studs were spaced at 2 in. (50.8 mm) on each steel faceplate. Threaded rods with 0.138 in. (3.51 mm) diameter were spaced at 2 in. (50.8 mm). Measured concrete compressive strength on 28 days was 5.31 ksi (37 MPa). Further details on the specimen design were shown in Table 3-1.

Damage to the front and rear of the specimens was quantitatively and qualitatively described upon the completion of each test. Qualitative measures include the nature of the damage (e.g. rear faceplate is bulging or specimen is perforated). Quantitative measures included penetration depth of the projectile and bulging depth of the rear faceplate. A contour gage was used to measure the bulging depth of all specimens which stopped the projectile. This manual measurement was made after test completion. These tests did not measure a displacement time-history because of the risk of damage to displacement gages behind the specimens.

The test result showed that the SC wall specimen stopped the missile as expected. A projectile with 1.0 in. (25.4 mm) diameter and 1.3 lbs (0.6 kg) weight was used. Its velocity was measured as 593 ft/s (181 m/s). All surfaces of the specimen were examined to investigate for damage caused by the missile impact. Figure 4-1 shows the corresponding photographs of the post-test SC wall specimen. It was observed that the missile punched through the front steel faceplate and penetrated the specimen. The penetration depth was measured from a cross-section cut of the SC wall specimen and resulted in a 2.06 in. (52.4 mm) measurement. The rear steel faceplate was bulging with the maximum bulging depth measured as 0.25 in. (6.4 mm). There was little damage on the side surfaces of the specimen: no significant cracks, no spalling and only a little bit of delamination of the rear steel faceplate from the concrete core caused by the failure of the shear stud at that location. It was confirmed that a concrete frustum was formed in the concrete core as shown in Figure 4-17.

#### 4.2.2 Group 1: Test case number 2: 3.7-0.37-50-1.0-1.3-677

The global dimension of the specimen is 16 in. (406.4 mm)  $\times$  11 in. (279.4 mm)  $\times$  4 in. (101.6 mm) with flexural reinforcement ratio of 3.7%, shear reinforcement ratio of 0.37% and steel faceplate strength of grade 50. 0.25 in. (6.35 mm) diameter, 1.125 in. (28.58 mm) long, shear studs

were spaced at 2 in. (50.8 mm) on each steel faceplate. Threaded rods with 0.138 in. (3.51 mm) diameter were spaced at 2 in. (50.8 mm). Measured concrete compressive strength on 28 days was 5.31 ksi (37 MPa). Further details on the specimen design were shown in Table 3-1.

The test result showed that the SC wall specimen stopped the missile, which varied from the predicted result from the three-step design method. A projectile with 1.0 in. (25.4 mm) diameter and 1.3 lbs (0.6 kg) was used. Its velocity was measured as 674 ft/s (205 m/s). All surfaces of the specimen were examined to investigate for damage caused by the missile impact. Figure 4-2 shows corresponding photographs of the post-test SC wall specimen. It was observed that the missile punched through the front steel faceplate and penetrated the specimen. The penetration depth was measured from a cross-section cut of the SC wall specimen and resulted in a 3.06 in. (77.8 mm) measurement. The rear steel faceplate was bulging with the maximum bulging depth measured as 0.63 in. (15.9 mm) There was little damage on the side surfaces of the specimen: no significant cracks, no spalling and no delamination of the steel faceplate from the concrete core. A few tie bar ends around the center of the rear steel faceplate were broken and their heads were popped off. It was confirmed that a concrete frustum was formed in the concrete core as shown in Figure 4-18.

#### 4.2.3 Group 1: Test case number 3: 3.7-0.37-50-1.0-2.0-430

The global dimension of the specimen is 16 in. (406.4 mm)  $\times$  11 in. (279.4 mm)  $\times$  4 in. (101.6 mm) with flexural reinforcement ratio of 3.7%, shear reinforcement ratio of 0.37% and steel faceplate strength of grade 50. 0.25 in. (6.35 mm) diameter, 1.125 in. (28.58 mm) long, shear studs were spaced at 2 in. (50.8 mm) on each steel faceplate. Threaded rods with 0.138 in. (3.51 mm) diameter were spaced at 2 in. (50.8 mm). Measured concrete compressive strength on the day-of-test was 6.52 ksi (45 MPa). Further details on the specimen design were shown in Table 3-1.

The test result showed that the SC wall specimen stopped the missile as expected. A projectile with 1.0 in. (25.4 mm) diameter and 2.0 lbs (0.9 kg) weight was used. Its velocity was measured as 424 ft/s (129 m/s). All surfaces of the specimen were examined to investigate for damage caused by the missile impact. Figure 4-3 shows corresponding photographs of the post-test SC wall specimen. It was observed that the missile punched through the front steel faceplate and penetrated the specimen. The penetration depth was measured from a cross-section cut of the SC wall specimen and resulted in a 1.56 in. (39.7 mm) measurement. The rear steel faceplate was bulging with the maximum bulging depth measured as 0.25 in. (6.4 mm). There was a significant crack on the right side surface of the specimen which reflected the shear stud placement on the rear steel faceplate, however, there was no spalling and no delamination of the steel faceplate from the concrete core. A few tie bar ends around the center of the rear steel faceplate were broken and their heads were popped off. It was confirmed that a concrete frustum was formed in the concrete core as shown in Figure 4-19. A representative strain data obtained was presented in Figure 4-33.

#### 4.2.4 Group 1: Test case number 4: 3.7-0.37-50-1.0-2.0-525

The global dimension of the specimen is 16 in. (406.4 mm)  $\times$  11 in. (279.4 mm)  $\times$  4 in. (101.6 mm) with flexural reinforcement ratio of 3.7%, shear reinforcement ratio of 0.37% and steel faceplate strength of grade 50. 0.25 in. (6.35 mm) diameter, 1.125 in. (28.58 mm) long, shear studs were spaced at 2 in. (50.8 mm) on each steel faceplate. Threaded rods with 0.138 in. (3.51 mm) diameter were spaced at 2 in. (50.8 mm). Measured concrete compressive strength on the day-of-test was 6.52 ksi (45 MPa). Further details on the specimen design were shown in Table 3-1.

The test result showed that the SC wall specimen stopped the missile, which varied from the predicted result from the three-step design method. A projectile with 1.0 in. (25.4 mm) diameter and 2.0 lbs (0.9 kg) weight was used. Its velocity was measured as 513 ft/s (156 m/s). All surfaces

of the specimen were examined to investigate for damage caused by the missile impact. Figure 4-4 shows corresponding photographs of the post-test SC wall specimen. It was observed that the missile punched through the front steel faceplate and penetrated the specimen. The penetration depth was measured from a cross-section cut of the SC wall specimen and resulted in a 3.16 in. (80.2 mm) measurement. The rear steel faceplate was bulging with the maximum bulging depth measured as 0.58 in. (14.7). There were not significant cracks or spalling on the side surfaces of the specimen. However, there was delamination of the rear steel faceplate from the concrete core caused by the failure of the shear studs at corresponding location. It was confirmed that a concrete frustum was formed in the concrete core as shown in Figure 4-20. A representative strain data obtained was presented in Figure 4-34.

#### 4.2.5 Group 1: Test case number 5: 3.7-0.53-50-1.5-1.3-660

The global dimension of the specimen is 16 in. (406.4 mm)  $\times$  11 in. (279.4 mm)  $\times$  4 in. (101.6 mm) with flexural reinforcement ratio of 3.7%, shear reinforcement ratio of 0.53% and steel faceplate strength of grade 50. 0.25 in. (6.35 mm) diameter, 1.125 in. (28.58 mm) long, shear studs were spaced at 2 in. (50.8 mm) on each steel faceplate. Threaded rods with 0.164 in. (4.17 mm) diameter were spaced at 2 in. (50.8 mm). Measured concrete compressive strength on the day-of-test was 6.52 ksi (45 MPa). Further details on the specimen design were shown in Table 3-1.

The test result showed that the SC wall specimen stopped the missile as expected. A projectile with 1.5 in. (38.1 mm) diameter and 1.3 lbs (0.6 kg) weight was used. Its velocity was measured as 667 ft/s (203 m/s). All surfaces of the specimen were examined to investigate for damage caused by the missile impact. Figure 4-5 shows corresponding photographs of the post-test SC wall specimen. It was observed that the missile punched through the front steel faceplate and penetrated the specimen. The penetration depth was measured from a cross-section cut of the

SC wall specimen and resulted in a 1.38 in. (34.9 mm) measurement. The rear steel faceplate was bulging and the maximum bulging depth was measured as 0.56 in. (14.3 mm). There were cracks and a little bit of spalling or delamination of the rear steel faceplate from the concrete core on the side surfaces. It was confirmed that a concrete frustum was formed in the concrete core as shown in Figure 4-21.

#### 4.2.6 Group 1: Test case number 6: 3.7-0.53-50-1.5-1.3-750

The global dimension of the specimen is 16 in. (406.4 mm)  $\times$  11 in. (279.4 mm)  $\times$  4 in. (101.6 mm) with flexural reinforcement ratio of 3.7%, shear reinforcement ratio of 0.53% and steel faceplate strength of grade 50. 0.25 in. (6.35 mm) diameter, 1.125 in. (28.58 mm) long, shear studs were spaced at 2 in. (50.8 mm) on each steel faceplate. Threaded rods with 0.164 in. (4.17 mm) diameter were spaced at 2 in. (50.8 mm). Measured concrete compressive strength on the day-of-test was 6.52 ksi (45 MPa). Further details on the specimen design were shown in Table 3-1.

The test result showed that the SC wall specimen stopped the missile, which varied from the predicted result from the three-step design method. A projectile with 1.5 in. (38.1 mm) diameter and 1.3 lbs (0.6 kg) weight was used. Its velocity was measured as 760 ft/s (232 m/s). All surfaces of the specimen were examined to investigate for damage caused by the missile impact. Figure 4-6 shows corresponding photographs of the post-test SC wall specimen. It was observed that the missile punched through the front steel faceplate and penetrated the specimen. The penetration depth was measured indirectly by differentiating the protruding length of the projectile from the whole length of the projectile and resulted in a 2.00 in. (50.8 mm) measurement. The rear steel faceplate was bulging with the maximum bulging depth measured as 0.72 in. (18.3 mm). There was severe damage on the left side surface of the specimen. Significant spalling caused by concrete breakout around the shear studs near the edge, and broken or deformed shear studs at the edge side

were observed. There were considerable cracks and a little bit of spalling on the right side surface. A few tie bar ends on the rear steel faceplate were broken and their heads were popped off. It was confirmed that a concrete frustum was formed in the concrete core as shown in Figure 4-22.

#### 4.2.7 Group 1: Test case number 7: 3.7-0.53-50-1.0-2.0-513

The global dimension of the specimen is 16 in. (406.4 mm)  $\times$  11 in. (279.4 mm)  $\times$  4 in. (101.6 mm) with flexural reinforcement ratio of 3.7%, shear reinforcement ratio of 0.53% and steel faceplate strength of grade 50. 0.25 in. (6.35 mm) diameter, 1.125 in. (28.58 mm) long, shear studs were spaced at 2 in. (50.8 mm) on each steel faceplate. Threaded rods with 0.164 in. (4.17 mm) diameter were spaced at 2 in. (50.8 mm). Measured concrete compressive strength on the day-of-test was 6.20 ksi (43 MPa). Further details on the specimen design were shown in Table 3-1.

This test case was revised from the test matrix to quantify the actual perforation velocity. The projectile diameter was reduced from 1.5 in. (38.1 mm) to 1.0 in. (25.4 mm) and impact velocity was increased to 33.6% greater than the design velocity in an attempt to ensure perforation occurred.

The test result showed that the SC wall specimen was perforated by the missile. A projectile with 1.0 in. (25.4 mm) diameter and 2.0 lbs (0.9 kg) weight was used. Its velocity was measured as 640 ft/s (195 m/s). All surfaces of the specimen were examined to investigate for damage caused by the missile impact. Figure 4-7 shows corresponding photographs of the post-test SC wall specimen. It was observed that the missile punched through the front steel faceplate and went through the specimen. There was little damage on side surfaces of the specimen: no significant cracks, no spalling and no delamination of the steel faceplate from the concrete core. The perforation occurred in the exact center of the rear steel faceplate with resultant tearing in four

directions resembling a cross shape. It was confirmed that a concrete frustum was formed in the concrete core as shown in Figure 4-23.

#### 4.2.8 Group 1: Test case number 8: 3.7-0.53-50-1.0-2.0-626

The global dimension of the specimen is 16 in. (406.4 mm) × 11 in. (279.4 mm) × 4 in. (101.6 mm) with flexural reinforcement ratio of 3.7%, shear reinforcement ratio of 0.53% and steel faceplate strength of grade 50. 0.25 in. (6.35 mm) diameter, 1.125 in. (28.58 mm) long, shear studs were spaced at 2 in. (50.8 mm) on each steel faceplate. Threaded rods with 0.164 in. (4.17 mm) diameter were spaced at 2 in. (50.8 mm). Measured concrete compressive strength on the day-of-test was 6.28 ksi (43 MPa). Further details on the specimen design were shown in Table 3-1.

This test case was revised from the test matrix to quantify the actual perforation velocity. The projectile diameter was reduced from 1.5 in. (38.1 mm) to 1.0 in. (25.4 mm) and impact velocity was increased to 48.2% greater than the design velocity in an attempt to ensure perforation occurred.

The test result showed that the SC wall specimen was perforated by the missile. A projectile with 1.0 in. (25.4 mm) diameter and 2.0 lbs (0.9 kg) weight was used. Its velocity was measured as 710 ft/s (216 m/s). All surfaces of the specimen were examined to investigate for damage caused by the missile impact. Figure 4-8 shows the corresponding photographs of the post-test SC wall specimen. It was observed that the missile punched through the front steel faceplate and went through the specimen. There was not much damage on the side surfaces of the specimen: no significant cracks, no spalling and no delamination of the steel faceplate from the concrete core. The perforation occurred in the exact center of the rear steel faceplate with resultant tearing in three directions forming a triangle shape. It was confirmed that a concrete frustum was formed in the concrete core as shown in Figure 4-24.

#### 4.2.9 Group 1: Test case number 9: 3.7-1.23-50-1.5-3.5-380

The global dimension of the specimen is 16 in. (406.4 mm) × 11 in. (279.4 mm) × 4 in. (101.6 mm) with flexural reinforcement ratio of 3.7%, shear reinforcement ratio of 1.23% and steel faceplate strength of grade 50. 0.25 in. (6.35 mm) diameter, 1.125 in. (28.58 mm) long, shear studs were spaced at 2 in. (50.8 mm) on each steel faceplate. Threaded rods with 0.25 in. (6.35 mm) diameter were spaced at 2 in. (50.8 mm). Measured concrete compressive strength on the day-of-test was 6.28 ksi (43 MPa). Further details on the specimen design were shown in Table 3-1.

This test case was revised from the test matrix to quantify the actual perforation velocity. The impact velocity was increased to 30.3% greater than the design velocity in an attempt to ensure perforation occurred.

The test result showed that the SC wall specimen stopped the missile, which varied from the predicted result from the three-step design method. A projectile with 1.5 in. (38.1 mm) diameter and 3.5 lbs (1.6 kg) weight was used. Its velocity was measured as 550 ft/s (168 m/s). All surfaces of the specimen were examined to investigate for damage caused by the missile impact. Figure 4-9 shows the corresponding photographs of the post-test SC wall specimen. It was observed that the missile punched through the front steel faceplate and penetrated the specimen. The penetration depth was measured indirectly by differentiating the protruding length of the projectile from the whole length of the projectile and resulted in a 4.00 in. (101.6 mm) measurement. The rear steel faceplate was bulging as well as split. The maximum bulging depth was measured as 1.63 in. (41.3 mm). There was spalling and significant cracks on the left side surface. There was delamination, cracks and spalling on the right side surface. Rupture of the rear steel faceplate started from a tie bar hole and propagated horizontally to the next punched hole for the tie bar. The rupture propagated one full spacing to the left and one half spacing to the right with some vertical rupture downward. Some of the ends of the tie bars, around the center of the rear steel faceplate, were

found to be broken and popped off the specimen. It was confirmed that a concrete frustum was formed in the concrete core as shown in Figure 4-25. A representative strain data obtained was presented in Figure 4-35.

#### 4.2.10 Group 1: Test case number 10: 3.7-1.23-50-1.5-3.5-465

The global dimension of the specimen is 16 in. (406.4 mm)  $\times$  11 in. (279.4 mm)  $\times$  4 in. (101.6 mm) with flexural reinforcement ratio of 3.7%, shear reinforcement ratio of 1.23% and steel faceplate strength of grade 50. 0.25 in. (6.35 mm) diameter, 1.125 in. (28.58 mm) long, shear studs were spaced at 2 in. (50.8 mm) on each steel faceplate. Threaded rods with 0.25 in. (6.35 mm) diameter were spaced at 2 in. (50.8 mm). Measured concrete compressive strength on the day-of-test was 6.08 ksi (42 MPa). Further details on the specimen design were shown in Table 3-1.

This test case was revised from the test matrix to quantify the actual perforation velocity. The impact velocity was increased to 15.9% greater than the design velocity in an attempt to ensure perforation occurred.

The test result showed that the SC wall specimen stopped the missile, which varied from the predicted result from the three-step design method. A projectile with 1.5 in. (38.1 mm) diameter and 3.5 lbs (1.6 kg) weight was used. Its velocity was measured as 489 ft/s (149 m/s). All surfaces of the specimen were examined to investigate for damage caused by the missile impact. Figure 4-10 shows corresponding photographs of the post-test SC wall specimen. It was observed that the missile punched through the front steel faceplate and penetrated the specimen. The penetration depth was measured indirectly by differentiating the protruding length of the projectile from the whole length of the projectile and resulted in a 1.91 in. (48.4 mm) measurement. The rear steel faceplate was bulging with the maximum bulging depth measured as 0.59 in. (15.1 mm). There were some cracks and a bit of spalling on the left side surface. There were also some cracks on the

other side surfaces which were not severe. There was no delamination of the steel faceplate from the concrete core. It was confirmed that a concrete frustum was formed in the concrete core as shown in Figure 4-26. A representative strain data obtained was presented in Figure 4-36.

#### 4.2.11 Group 2: Test case number 1: 5.2-0.48-50-1.0-2.0-445

The global dimension of the specimen is 16 in. (406.4 mm)  $\times$  11 in. (279.4 mm)  $\times$  4 in. (101.6 mm) with flexural reinforcement ratio of 5.2%, shear reinforcement ratio of 0.48% and steel faceplate strength of grade 50. 0.25 in. (6.35 mm) diameter, 1.125 in. (28.58 mm) long, shear studs were spaced at 2 in. (50.8 mm) on each steel faceplate. Threaded rods with 0.3125 in. (7.94 mm) diameter were spaced at 2 in. (50.8 mm). Measured concrete compressive strength on the day-of-test was 6.53 ksi (45 MPa). Further details on the specimen design were shown in Table 3-1.

The test result showed that the SC wall specimen stopped the missile as expected. A projectile with 1.0 in. (25.4 mm) diameter and 2.0 lbs (0.9 kg) weight was used. Its velocity was measured as 467 ft/s (142 m/s). All surfaces of the specimen were examined to investigate for damage caused by the missile impact. Figure 4-11 shows corresponding photographs of the post-test SC wall specimen. It was observed that the missile punched through the front steel faceplate and penetrated the specimen. The penetration depth was measured indirectly by differentiating the protruding length of the projectile from the whole length of the projectile and resulted in a 2.09 in. (53.2 mm) measurement. The rear steel faceplate was bulging with the maximum bulging depth measured as 0.28 in. (7.1 mm). There were a few horizontal cracks on the left and right side surfaces of the specimen. There was no spalling and no delamination of the steel faceplate from the concrete core. It was confirmed that a concrete frustum was formed in the concrete core as shown in Figure 4-27. A representative strain data obtained was presented in Figure 4-37.

#### 4.2.12 Group 2: Test case number 2: 5.2-0.48-50-1.0-2.0-544

The global dimension of the specimen is 16 in. (406.4 mm)  $\times$  11 in. (279.4 mm)  $\times$  4 in. (101.6 mm) with flexural reinforcement ratio of 5.2%, shear reinforcement ratio of 0.48% and steel faceplate strength of grade 50. 0.25 in. (6.35 mm) diameter, 1.125 in. (28.58 mm) long, shear studs were spaced at 2 in. (50.8 mm) on each steel faceplate. Threaded rods with 0.3125 in. (7.94 mm) diameter were spaced at 2 in. (50.8 mm). Measured concrete compressive strength on the day-of-test was 6.53 ksi (45 MPa). Further details on the specimen design were shown in Table 3-1.

The test result showed that the SC wall specimen stopped the missile, which varied from the predicted result from the three-step design method. A projectile with 1.0 in. (25.4 mm) diameter and 2.0 lbs (0.9 kg) weight was used. Its velocity was measured as 549 ft/s (167 m/s). All surfaces of the specimen were examined to investigate for damage caused by the missile impact. Figure 4-12 shows corresponding photographs of the post-test SC wall specimen. It was observed that the missile punched through the front steel faceplate and penetrated the specimen. The penetration depth was measured indirectly by differentiating the protruding length of the projectile from the whole length of the projectile and resulted in a 3.31 in. (84.1 mm) measurement. The rear steel faceplate was bulging with the maximum bulging depth measured as 0.75 in. (19.1 mm). There were a few horizontal cracks on the left and right side surfaces of the specimen. Other than that, there was little damage on the side surfaces: no spalling and no delamination of the steel faceplate from the concrete core. It was confirmed that a concrete frustum was formed in the concrete core as shown in Figure 4-28. A representative strain data obtained was presented in Figure 4-38.

#### 4.2.13 Group 2: Test case number 3: 5.2-0.48-50-1.5-3.5-408

The global dimension of the specimen is 16 in. (406.4 mm)  $\times$  11 in. (279.4 mm)  $\times$  4 in. (101.6 mm) with flexural reinforcement ratio of 5.2%, shear reinforcement ratio of 0.48% and steel

faceplate strength of grade 50. 0.25 in. (6.35 mm) diameter, 1.125 in. (28.58 mm) long, shear studs were spaced at 2 in. (50.8 mm) on each steel faceplate. Threaded rods with 0.3125 in. (7.94 mm) diameter were spaced at 2 in. (50.8 mm). Measured concrete compressive strength on 28 days was 5.31 ksi (37 MPa). Further details on the specimen design were shown in Table 3-1.

The test result showed that the SC wall specimen stopped the missile as expected. A projectile with 1.5 in. (38.1 mm) diameter and 3.5 lbs (1.6 kg) weight was used. Its velocity was measured as 410 ft/s (125 m/s). All surfaces of the specimen were examined to investigate for damage caused by the missile impact. Figure 4-13 shows corresponding photographs of the post-test SC wall specimen. It was observed that the missile punched through the front steel faceplate and penetrated the specimen. The penetration depth was measured indirectly by differentiating the protruding length of the projectile from the whole length of the projectile and resulted in a 1.34 in. (34.1 mm) measurement. The rear steel faceplate was bulging with the maximum bulging depth measured as 0.38 in. (9.5 mm). There were a few horizontal cracks on the left and right side surfaces of the specimen. A small amount of concrete infill was dislodged on the right side surface but there was no spalling. It was confirmed that a concrete frustum was formed in the concrete core as shown in Figure 4-29.

#### 4.2.14 Group 2: Test case number 4: 5.2-0.48-50-1.5-3.5-498

The global dimension of the specimen is 16 in. (406.4 mm)  $\times$  11 in. (279.4 mm)  $\times$  4 in. (101.6 mm) with flexural reinforcement ratio of 5.2%, shear reinforcement ratio of 0.48% and steel faceplate strength of grade 50. 0.25 in. (6.35 mm) diameter, 1.125 in. (28.58 mm) long, shear studs were spaced at 2 in. (50.8 mm) on each steel faceplate. Threaded rods with 0.3125 in. (7.94 mm) diameter were spaced at 2 in. (50.8 mm). Measured concrete compressive strength on 28 days was 5.31 ksi (37 MPa). Further details on the specimen design were shown in Table 3-1.

The test result showed that the SC wall specimen stopped the missile, which varied from the predicted result from the three-step design method. A projectile with 1.5 in. diameter and 3.5 lbs weight was used. Its velocity was measured as 484 ft/s (148 m/s). All surfaces of the specimen were examined to investigate for damage caused by the missile impact. Figure 4-14 shows corresponding photographs of the post-test SC wall specimen. It was observed that the missile punched through the front steel faceplate and penetrated the specimen. The penetration depth was measured indirectly by differentiating the protruding length of the projectile from the whole length of the projectile and resulted in a 2.41 in. (61.1 mm) measurement. The rear steel faceplate was bulging with the maximum bulging depth measured as a 0.69 in. (17.5 mm) measurement. There were a few horizontal cracks on the left side surface of the specimen. There was huge spalling on the right side surface as shown in Figure 4-14 (f). It was confirmed that a concrete frustum was formed in the concrete core as shown in Figure 4-30. A representative strain data obtained was presented in Figure 4-39.

#### 4.2.15 Group 3: Test case number 1: 3.7-0.37-65-1.0-2.0-443

The global dimension of the specimen is 16 in. (406.4 mm)  $\times$  11 in. (279.4 mm)  $\times$  4 in. (101.6 mm) with flexural reinforcement ratio of 3.7%, shear reinforcement ratio of 0.37% and steel faceplate strength of grade 65. 0.25 in. (6.35 mm) diameter, 1.125 in. (28.58 mm) long, shear studs were spaced at 2 in. (50.8 mm) on each steel faceplate. Threaded rods with 0.138 in. (3.51 mm) diameter were spaced at 2 in. (50.8 mm). Measured concrete compressive strength on the day-of-test was 5.89 ksi (41 MPa). Further details on the specimen design were shown in Table 3-1.

This test case was revised from the test matrix to quantify the actual perforation velocity. The impact velocity was increased to 9.6% greater than the design velocity in an attempt to ensure perforation occurred.

The test result showed that the SC wall specimen stopped the missile, which varied from the predicted result from the three-step design method. A projectile with 1.0 in. (25.4 mm) diameter and 2.0 lbs (0.9 kg) weight was used. Its velocity was measured as 539 ft/s (164 m/s). All surfaces of the specimen were examined to investigate for damage caused by the missile impact. Figure 4-15 shows corresponding photographs of the post-test SC wall specimen. It was observed that the missile punched through the front steel faceplate and penetrated the specimen. The penetration depth was measured indirectly by differentiating the protruding length of the projectile from the whole length of the projectile and resulted in a 3.16 in. (80.2 mm) measurement. The rear steel faceplate was bulging with the maximum bulging depth measured as 0.69 in. (17.5 mm). There was a significant crack on the right surface of the specimen caused by concrete breakout in which the shear studs near the edge were embedded, and there was delamination of the rear steel faceplate from the concrete core. However, there was no spalling. There were a few cracks on the left side surface but not as severe as those on the right side surface. A few tie bar ends of the rear steel faceplate were broken and their heads were popped off. It was confirmed that a concrete frustum was formed in the concrete core as shown in Figure 4-31.

#### 4.2.16 Group 3: Test case number 2: 3.7-0.37-65-1.0-2.0-541

The global dimension of the specimen is 16 in. (406.4 mm)  $\times$  11 in. (279.4 mm)  $\times$  4 in. (101.6 mm) with flexural reinforcement ratio of 3.7%, shear reinforcement ratio of 0.37% and steel faceplate strength of grade 65. 0.25 in. (6.35 mm) diameter, 1.125 in. (28.58 mm) long, shear studs were spaced at 2 in. (50.8 mm) on each steel faceplate. Threaded rods with 0.138 in. (3.51 mm) diameter were spaced at 2 in. (50.8 mm). Measured concrete compressive strength on the day-of-test was 5.98 ksi (41 MPa). Further details on the specimen design were shown in Table 3-1.

This test case was revised from the test matrix to quantify the actual perforation velocity. The impact velocity was increased to 28.9% greater than the design velocity in an attempt to ensure perforation occurred.

The test result showed that the SC wall specimen was perforated by the missile. A projectile with 1.0 in. (25.4 mm) diameter and 2.0 lbs (0.9 kg) weight was used. Its velocity was measured as 634 ft/s (193 m/s). All surfaces of the specimen were examined to investigate for damage caused by the missile impact. Figure 4-16 shows corresponding photographs of the post-test SC wall specimen. It was observed that the missile punched through the front steel faceplate and went through the specimen. There were a few cracks on the left side surface of the specimen. There was significant spalling on the right side surface and a few shear studs were observed to have failed at their weld points. Some tie bar ends of the rear steel faceplate were broken and their heads were popped off. It was confirmed that a concrete frustum was formed in the concrete core as shown in Figure 4-32.

### 4.3 Summary of Tests Results

A total of sixteen tests were conducted to investigate local damage behavior of SC wall specimens against projectile impact. Test results are summarized in Table 4-1. Generic results of the tests were reported qualitatively as “Stop” or “Perforation (Perf.)” determined by if the specimen stopped the projectile or was perforated by the projectile. A specific damage mode was identified for each of test cases. All the test specimens were classified as one of the three damage modes: (i) bulging, (ii) splitting, or (iii) perforating. The extent of damage such as penetration depth of the projectile into the specimen,  $x_{c\_test}$ , and bulging depth of the rear steel faceplate,  $x_b$ , was measured quantitatively and summarized in Table 4-1. In each test case projectile velocity,  $V_{imp}$ , was measured using a high-speed camera with resulting values described in the table.

Concrete compressive strength was measured on the day of test and summarized in the table, except group 1 number 1 and 2 and group 2 number 3 and 4 test cases. For those cases,  $f'_c$  on 28-day was measured and presented instead in the table.

Of these test cases, three specimens were completely perforated while the remaining specimens stopped the projectile with various magnitudes of penetration depth. In all test cases in which the projectile impact velocity was less than the design velocity, the projectile was stopped by the SC wall specimen as expected and measurable bulging deformation occurred on the rear steel faceplate. Figure 4-2 depicts a representative test case in which the bulging deformation occurred. Test cases where the impact velocity was greater than the design velocity did not always show perforation of the specimens.

For group 1 test cases, specimens stopped the projectiles which had 1.0 in. (25.4 mm) diameter and 1.3 lbs (0.6 kg) weight with an increased velocity up to 10% greater than the design velocity. For the 1.0 in. (25.4 mm) diameter projectiles with 2.0 lbs (0.9 kg) weight, the specimens were perforated when the velocities were increased up to at least 32% greater than the design velocity. The 1.5 in. (38.1 mm) diameter, 3.5 lbs (1.6 kg) projectile was still stopped by the specimen when its velocity was increased up to 27% from the design velocity. For this test case, the rear faceplate was ruptured indicating the splitting damage mode which immediately precedes perforation. Figure 4-9 illustrates a representative test case where the splitting damage mode happened. For the projectile with the same diameter and 1.3 lbs (0.6 kg) weight, the test results showed the specimen stopped the projectile with an impact velocity of 4% greater than the design velocity.

Tests 7 to 10 of group 1 were revised from the original test matrix to quantify the actual perforation velocity. For tests 7 and 8, the projectile diameter was reduced from 1.5 in. (38.1 mm)

to 1.0 in. (25.4 mm) and impact velocity was increased to 32% and 46%, respectively in an attempt to ensure perforation occurred. Test 8 was conducted first to confirm that perforation would occur at the higher impact velocity. Verifying perforation occurred, test 7 was conducted to further narrow the range of velocity which results in perforation. Figure 4-7 shows a representative test case of perforating damage mode. Because test 7 resulted in perforating damage mode, the actual perforation velocity for the 1.0 in. (25.4 mm) diameter, 2.0 lbs (0.9 kg) weight, projectile can be considered to lie in the range between 6% and 32% greater than the design velocity for this specific wall configuration. For test 9 and 10 of group 1, only projectile velocities were changed in an attempt to ensure perforation. Test 10 was conducted first at an increased velocity of 13% but resulted in bulging deformation on the rear steel faceplate without perforation. Next, test 9 was performed with an increased velocity of 27% which ruptured the rear steel faceplate but the projectile was stopped by the specimen.

In group 2, two test cases in which the impact velocities were less than the design velocities produced test results of “stop” as expected, showing the same tendency as the group 1 tests. The remaining two test cases, test 2 and 4, were on the right side of the perforation resistance curves with the projectile velocities 9% and 4% greater than the design velocities, respectively, expecting perforation of the specimens. As a result, the projectiles were stopped in both cases. These results did not conform to the expected results.

Considering observations of test results in group 1 and 2, test cases in group 3 were also revised to change their projectile velocities. Test number 2 increased the impact velocity up to 27% greater than the design velocity in an attempt to make sure perforation occurred on the specimen. After verifying that this caused the perforation, test number 1’s impact velocity was revised expecting the projectile to be stopped by the specimen, in order to define velocity range of

the projectile in which perforation velocity would be positioned. The velocity was increased by 8% greater than the design velocity, and the projectile was stopped by the specimen.

#### *4.4 Behavior of SC Walls Subjected to Missile Impact*

##### *4.4.1 Damage to exterior surfaces of SC wall specimens*

After each test, all the exterior surfaces of the SC wall specimen were examined carefully to evaluate the degree (or level) of damage caused by the impactive loading of the projectile. The examination revealed that three different types of damage mode occurred in the SC wall specimens: bulging, splitting and perforating. Each damage mode could be distinguished clearly observing front and rear surfaces of the post-test specimen. Illustration of those surfaces was presented in Figure 4-1 through Figure 4-16 indicating specific damage mode, with additional photographs of the other surfaces of the post-test specimen to check the level of damage on them as well.

As indicated in Table 4-1, tests 7 and 8 from group 1 and test 2 from group 3 resulted in perforation. For test 9 from group 1 and test 2 from group 2, the rear steel faceplate split. All other test cases resulted in bulging damage mode, presenting bulging deformation in the rear faceplate of the specimen. Figure 4-2 illustrates a representative test case in which bulging damage mode occurred. The projectile punched through the front steel faceplate as shown in Figure 4-2 (a) and was stopped by the specimen with penetrating the concrete core. There was little damage on the side surfaces of the specimen (Figure 4-2 (c) through (f)): no significant cracks, no spalling and no delamination of the steel faceplates from the concrete core. Bulging deformation happened on the rear steel faceplate as shown in Figure 4-2 (b). Four tie bar ends around the center of the rear steel faceplate were broken and their heads were popped off.

Figure 4-9 shows a representative test case where splitting damage mode occurred. The projectile punched through the front steel faceplate as shown in Figure 4-9 (a) and was stopped by the specimen with penetrating the concrete core. There was spalling and significant cracks on the left side surface (Figure 4-9 (c)). There was delamination, cracks and spalling on the right side surface (Figure 4-9 (f)). Little damage was found on the top and bottom surfaces (Figure 4-9 (d) and (e)): no significant cracks, no spalling and no delamination of the steel faceplates from the concrete core. The rear steel faceplate was bulging as well as splitting open as illustrated in Figure 4-9 (b). Rupture of the rear steel faceplate started from a tie bar hole in the center and propagated horizontally to the next punched hole for the tie bar. The rupture propagated one full spacing to the left and one half spacing to the right with some vertical rupture downward. The ends of seven tie bars, around the center of the rear steel faceplate, were found to be broken and popped off the specimen.

Figure 4-7 illustrates a representative test case in which perforating damage mode occurred. The projectile passed through the specimen and a resultant hole was made in the center of the front steel faceplate measuring the same diameter as the projectile as shown in Figure 4-7 (a). There was little damage on side surfaces of the specimen (Figure 4-7 (c) through (f)): no significant cracks, no spalling and no delamination of the steel faceplate from the concrete core. Perforation occurred in the exact center of the rear steel faceplate with resultant tearing in four directions, forming a cross shape (Figure 4-7 (b)). Two tie bar ends located around the center of the rear steel faceplate were broken and their heads were popped off.

#### 4.4.2 Damage in the cross-section of SC wall specimens

Internal damage was also investigated to further evaluate the local damage behavior and failure mechanism of SC walls. Each post-test specimen was cut in half and the cross-section was

examined as illustrated in Figure 4-17 through Figure 4-32. Figure 4-40 shows how the internal damage had been progressing in a series of specimens: post-test specimens of number 3, 4 and 7 test cases in group 1. All the specimens had an identical flexural reinforcement ratio (3.7%) and steel faceplate strength (50 ksi, nominal) with a slightly different shear reinforcement ratio (0.37% and 0.53%). The same type of projectiles (1.0 in. (25.4 mm) diameter with 2.0 lbs (0.9 kg) weight) were applied, however, kinetic energy varied gradually by increasing impact velocities up to 424 ft/s (129 m/s), 513 ft/s (156 m/s), and 640 ft/s (195 m/s), respectively.

Figure 4-40 (a) shows the internal damage of post-test specimen number 3 in group 1. The projectile punched through the front steel faceplate first, then crushed the concrete core to 1.56 in. (39.7 mm) depth, and was stopped. At the tip of the stopped projectile, it was observed that concrete frustum was formed with  $61^\circ$  angle from the end of the concrete crush region. Cracks dividing the concrete frustum from the concrete core were initiated at the end of the concrete crush and propagated to the bottom of the concrete core. The maximum diameter of the frustum was measured as 9.25 in. (235.0 mm). Figure 4-40 (b) illustrates the internal damage of post-test specimen number s4 in group 1. The projectile punched through the front steel faceplate first, then crushed the concrete core to 3.16 in. (80.2 mm), and stopped. In the middle of the crush in the concrete, it was observed that multiple concrete frustums were formed and the cracks separating the frustums from the concrete core propagated until they reached the rear steel faceplate with the angle of  $56^\circ$  from the crack initiated point. The upper half of, the first generated, outer most frustum was crushed by the projectile and lower half remained uncrushed. The right half of the frustum was dislodged from the concrete core and pushed against the rear steel faceplate resulting in bulging deformation of the rear steel faceplate. The left half of the frustum did not seem to be fully dislodged from the concrete core. Figure 4-40 (c) presents the internal damage of post-test

specimen number 7 in group 1. The projectile perforated the specimen and passed through the entire thickness of the SC wall specimen. A punched through hole with an identical dimension of diameter as the projectile was made in the front steel faceplate. The crushed region in the concrete core left a cylindrically shaped void measuring 1.44 in. (36.5 mm) in depth and 1.0 in. (25.4 mm) in width which is the same dimension as the projectile's diameter. Concrete frustum was formed from the end of the cylindrically shaped void: some pieces in the frustum were lost in the process of cutting and opening the specimen. The frustum was dislodged from the concrete core and pressed against the rear steel faceplate, while the central area of the frustum was crushed by the projectile through its remaining depth. The projectile and the crushed concrete frustum kept pushing the rear steel faceplate, rupturing it, and eventually passed through it.

Details of the measured points to specify the degree of internal damage of the post-test SC wall specimen are illustrated in Figure 4-41. They include several geometric parameters, namely, depth of the cylindrically shaped void ( $t_d$ ), penetration depth measured at the tip of the projectile ( $t_n$ ), diameter of the cylindrically shaped void ( $d_1$ ), diameter of the concrete frustum on rear side ( $d_2$ ), and inclination angle of the dislodged surface of the concrete frustum ( $\theta$ ). All the measured dimensions are summarized in Table 4-2.

## 4.5 Discussions

### 4.5.1 Evaluation of the validity and accuracy of the three-step design method

In this research, a test program was established to investigate local failure behavior of SC walls. The three-step design method (American Institute of Steel Construction 2015; Bruhl et al. 2015a) was used as a basis to construct a test matrix for the program. Design velocities for each test case were calculated using the three-step design method, and then projectile velocities were determined accordingly depending on the desired test results. For test cases expecting wall

perforation, the projectile velocities were increased approximately 10% greater than the design velocities. On the other hand, for test cases expecting projectile stopping, the velocities were decreased by approximately 10% lesser than the design velocities. This philosophy and resulting test matrix enabled test results to evaluate the validity and to quantify the accuracy of the three-step design method.

The test results can be categorized based on the expected behavior and observed results as: (i) appropriate, (ii) conservative, or (iii) unconservative. Appropriate is when the observed behavior (projectile stopped or specimen perforated) is in accordance with expected behavior. Conservative is when the observed behavior (projectile stopped) is better than expected behavior (specimen perforated). Unconservative is when the observed behavior (specimen perforated) is worse than expected behavior (projectile stopped). All the test results were presented graphically in Figure 4-42 through Figure 4-44 with each test plotted on perforation resistance curves generated by the three-step design method. Test cases positioned on the left side of the perforation resistance curves stopped the projectile as expected. Test cases positioned on the right side of the curves did not necessarily show perforation of the specimens, but all did provide conservative results. The results from the test program were all either appropriate or conservative. There were no unconservative results. This provides confidence that the three-step design method can be used to design SC walls that will prevent perforation due to missile impact.

For the tests on specific SC wall cross-section designs with a 1.0 in. (25.4 mm) diameter, 2.0 lbs (0.9 kg) weight, projectile in group 1, the perforation velocity was experimentally determined to be in the range between 6% and 32% greater than the design velocity. In group 3 test cases, the perforation velocity was experimentally observed to be located in the range between 8% and 27% greater than the design velocity. Therefore, it was experimentally observed that the

design method contained conservatism of at least 6%: most likely greater than that considering the penetration depth for the test cases.

This conservatism may be attributed to the inherent conservative aspect of the design method coming from the statistical variability parameter ( $\beta$ ) meant to ensure a high probability of confidence of 95%. Generally, inherent conservatism in the design method is acceptable or even desirable for effective designs. However, it would be important to ensure efficient designs by minimizing the conservatism of the design method and to improve the accuracy of the design method with a better understanding of the failure mechanism of SC walls subjected to missile impact.

It should be noted that there is a conditional provision in the three-step design method which was neglected for obtaining the perforation resistance curves herein. This provision requires that a nose factor of 1.14, which corresponds to sharp nose shape, should be used regardless of the actual nose shape if the equation (5) in the paper (Bruhl et al. 2015a) is used with the projectile diameter of less than 5.9 in. (149.9 mm). This provision could apply to the test cases when 1.5 in. (38.1 mm) diameter projectile was used, however, this dropped the design velocities significantly compared with the current design velocities where the provision was not applied. Thus, the decision was made not to use the provision to evaluate the test results in this research because the three-step design method already contained enough conservatism. The provision would only add more conservatism.

#### 4.5.2 Comparison with modified NDRC equations

Modified NDRC equations (American Society of Civil Engineers 1980) have been used to set criteria for some limit states of traditional reinforced concrete (RC) structures against missile threat. These equations were incorporated into the three-step design method to determine

perforation velocity for the concrete core of SC structures. In this sense, it is meaningful to evaluate the effectiveness of the modified NDRC equations to estimate penetration depth for SC structures. This was accomplished by comparing penetration depth values from test results (shown in Table 4-1) with those calculated from the equations. The modified NDRC equations are shown below.

$$x = \sqrt{4 \cdot K \cdot N \cdot W \cdot d \cdot \left( \frac{v_o}{1000 \cdot d} \right)^{1.80}} , \quad \text{for } \frac{x}{d} \leq 2.0 \quad \text{Equation 4-1}$$

or

$$x = \left[ K \cdot N \cdot W \cdot \left( \frac{v_o}{1000 \cdot d} \right)^{1.80} \right] + d , \quad \text{for } \frac{x}{d} > 2.0 \quad \text{Equation 4-2}$$

Table 4-3 describes the results of the comparison between tested values and calculated values of the penetration depth into the concrete core of the SC wall specimens.

The measured value of penetration depth from the test results was described as  $x_{c\_test}$ , and the calculated value was expressed as  $x_{c\_calc}$ . Normalized penetration depth values by the concrete core thickness,  $T_c$ , for both measured and calculated, were also reported to provide an intuition on how much the projectile penetrated the concrete core of the wall. The ratio of the calculated penetration value to the measured penetration depth value,  $x_{c\_calc}/x_{c\_test}$ , was presented to show how effectively the equations estimated the actual penetration depth of the SC wall specimens. Out of the original sixteen test cases, three experienced perforation and were disregarded. In four out of the thirteen remaining tests, the calculated values overestimated the actual penetration depth at most 41% (group 2 number 3). The remaining nine tests showed that the calculated values underestimated the actual penetration depth at most 40% (group 1 number 9).

The measured and calculated penetration depth values, normalized by concrete thickness, are compared graphically in Figure 4-45. The ratio of calculated penetration depth,  $x_{c\_calc}$ , to concrete thickness,  $T_c$ , is on the vertical axis and the ratio of measured penetration depth,  $x_{c\_test}$ , to  $T_c$ , is on the horizontal axis. Figure 4-45 shows that when the projectile penetrated the SC walls with depth ranging from approximately one-third to two-thirds of the concrete thickness, the modified NDRC equations predicted it reasonably. However, if the penetration depth exceeded two-thirds of the concrete thickness, then the penetration depth calculated using the modified NDRC equations did not agree well with test results as shown in the figure.

Statistical analysis shows that for the test cases in which the penetration depth was within the range between one-third and two-thirds of the concrete thickness, the modified NDRC equations predicted the penetration depth in the concrete core of the SC wall specimens conservatively about 6% on average, as shown in Table 4-4.

This may be attributed to the differences in the damage between RC walls and SC walls as shown in Figure 4-46: scabbing in RC walls and bulging in SC walls (Kim et al. 2015). For the RC walls subjected to missile impact, the scabbing from the rear face could be severe and lead to early perforation when the penetration depth exceeds about two-thirds of the wall thickness. On the other hand, SC walls have a rear steel faceplate, which prevents scabbing from the rear surface of the wall. Therefore, the modified NDRC equations might not provide a reasonable estimation of penetration depth when it exceeds two-thirds of the concrete thickness of the SC wall.

#### *4.6 Proposed Local Failure Mechanism of SC Walls Subjected to Missile Impact*

Based on the observation of the internal damage of the SC wall specimens, described in the previous section, a more detailed failure mechanism of the SC walls is proposed below and depicted in Figure 4-47:

**Stage 1: Front steel faceplate damage**

A projectile impacts the front steel faceplate and punches through or damages it

**Stage 2: Drilling damage (Tunneling zone) in a concrete core**

The projectile crushes the concrete immediately in front of it creating a cylindrical hole (or tunneling zone). As the velocity of the projectile slows, the radial cracks form a frustum in the concrete core. The cracks forming the frustum in the concrete core begin to make a gap and push the rear steel faceplate. The rear steel faceplate might start to deform (or bulge).

**Stage 3: Concrete frustum formation in the concrete core and deformation of the rear steel faceplate**

The projectile dislodges the concrete frustum from the concrete core. The frustum pushes against the rear steel faceplate causing it to deform (or bulge) around the edge of the diameter of the frustum in the out of plane direction.

**Stage 4: Crushing in the concrete frustum repeating its formation**

The projectile proceeds in the concrete frustum and crushes the central area of the frustum leaving a cylindrical hole in it. Additional radial cracks create smaller frustums within the original one as it continues crushing the central area. Newly built frustums are dislodged and push the rear steel faceplate in consecutive order. The rear steel faceplate experiences bulging from outside to the center with increasing depth.

**Stage 5: Rear steel faceplate rupture**

The projectile, which has crushed the concrete core throughout the thickness and formed the last concrete frustum (or crushed the concrete frustum into particles), contacts with the rear steel faceplate with concrete debris preceding ahead. The projectile with the concrete debris

presses and ruptures the center of the rear steel faceplate and, if it has enough residual velocity, it passes through the SC wall.

Figure 4-47 illustrates each stage of the local failure mechanism of SC walls subjected to missile impact. For instance, Figure 4-40 (a) specimen from group 1, number 3 test case corresponded to stage 3 in the failure mechanism shown in Figure 4-47. It was observed that the projectile crushed the concrete core making a cylindrical hole and built a concrete frustum at the tip of the projectile. A small amount of bulging deformation occurred in the rear steel faceplate. Figure 4-40 (b) specimen from group 1, number 4 test case corresponds with stage 4 in the failure mechanism shown in Figure 4-47. Along with a cylindrically shaped hole made by the projectile which crashed the concrete, multiple concrete frustums were observed within the first formed frustum. There was also severe bulging deformation in the rear steel faceplate. Figure 4-40 (c) specimen from group 1, number 7 test case represents an illustration of stage 5 in the failure mechanism shown in Figure 4-47. The whole depth of the concrete core was crushed by the projectile and debris generated from the concrete frustums was forced out as the projectile passed through. The rear steel faceplate was observed to have experienced both bulging deformation and rupture.

When it comes to perforation failure of traditional RC walls, a projectile and its generated concrete frustum become a new missile and pass through the wall (Kar 1979). However, in SC walls the rear steel faceplate prevents the concrete frustum from flying out from the wall. That is, the concrete frustum is penetrated further by the projectile and new concrete frustums are generated repeatedly until the projectile penetrates the entire thickness of the concrete core. The projectile keeps on dissipating its kinetic energy while generating new concrete frustums. This is clearly different from the failure mechanism proposed in the three-step design method (Bruhl et al. 2015a).

#### 4.7 Conclusions

Experimental tests to investigate local failure behavior of SC walls subjected to missile impact were performed and a valuable set of test data was obtained. The test specimens were designed in small-scale due to its merits such as affordability in fabrication, convenience in preparation for indoor laboratory scale test, and ease of handling before and after test for investigation. The reduced scale test approach has been confirmed to be a valid test procedure and test data obtained at any scale can be used available to carry out impact studies of reinforced concrete structures (Walter and Wolde-Tinsae 1984). In this paper, the experimental methodology including test setup, specimen design, instrumentation, projectile and sabot design was proven to be appropriate to conduct missile impact studies on SC walls. In a few test cases though, where 1.5 in. (38.1 mm) diameter projectiles were used, concrete spalling on side faces occurred and the rear steel faceplate was delaminated. This might have caused insufficient constraints on the specimen, specifically to the concrete core and the rear steel faceplate, so that the SC wall specimen could not have provided appropriate stiffness in response to missile impact situation. Therefore, it would be recommended to use projectiles whose diameter is less than 1.5 in. (38.1 mm) for current specimen design.

The three-step design method (Bruhl et al. 2015) was evaluated using the test results and its accuracy was quantified. It was found that the method has a significant level of conservatism. The conservatism becomes greater as the diameter of a projectile is increased or lighter weight of a projectile is applied. This conservatism is likely attributed to the use of the statistical variability parameter ( $\beta$ ) in the design method and the incomplete assumed failure mechanism used in its development. In the design method, there is a conditional provision to use a nose factor of 1.14 regardless of the actual missile nose shape. This tends to add even more conservatism and should

probably not be applied, because the design method already has enough conservatism without the provision.

The modified NDRC equations, which were incorporated into the three-step design method, were evaluated to verify their effectiveness for estimating penetration depth in SC walls. Based on the observations, when a projectile penetrated a concrete core in the range of approximately one-third to two-thirds of the concrete thickness, the calculated values of penetration depth by the equations showed good agreement with the test results. However, when a projectile penetrated a concrete core more than two-thirds of its thickness, the calculated values were lesser than the test results, which means the calculation provided unconservative results. This is most likely due to the difference in damage mode between RC and SC walls.

Throughout the experimental program, three damage modes were observed: (i) bulging, (ii) splitting, and (iii) perforating. It was confirmed that the local failure mechanism could be explained in five stages: (i) front steel faceplate damage, (ii) drilling damage (tunneling zone) in a concrete core, (iii) concrete frustum formation in the concrete core and deformation of the rear steel faceplate, (iv) crushing in the concrete frustum repeating its formation, and (v) rear steel faceplate rupture. Stage four and five were SC wall specific characteristics caused by an attached rear steel faceplate, compared with the conventional RC walls.

Table 4-1 Summary of the test results

<i>Test group &amp; No.</i>	<i>Test case identifier</i>	$V_{imp}$ (ft/s)	$V_{des}$ (ft/s)	$V_{imp}/V_{des}$	<i>Expected result</i> *	<i>Test result</i> *	<i>Damage mode</i> **	$x_{c\_test}$ (in)	$x_b$ (in)	<i>Conc. Comp. Str.</i> (ksi)	
	1	3.7-0.37-50-1.0-1.3-554	593	613	0.97	Stop	Stop	B	2.06	0.25	5.31 <sup>†</sup> ...
	2	3.7-0.37-50-1.0-1.3-677	674	613	1.10	Perf.	Stop	B	3.06	0.63	5.31 <sup>†</sup> ...
	3	3.7-0.37-50-1.0-2.0-430	424	485	0.87	Stop	Stop	B	1.56	0.25	6.52
	4	3.7-0.37-50-1.0-2.0-525	513	485	1.06	Perf.	Stop	B	3.16	0.58	6.52
<i>Gr. 1</i>	5	3.7-0.53-50-1.5-1.3-660	667	732	0.91	Stop	Stop	B	1.38	0.56	6.52
	6	3.7-0.53-50-1.5-1.3-750	760	732	1.04	Perf.	Stop	B	2.00	0.72	6.52
	7	3.7-0.53-50-1.0-2.0-513	640	485	1.32	Perf.	Perf.	P	-	-	6.20
	8	3.7-0.53-50-1.0-2.0-626	710	485	1.46	Perf.	Perf.	P	-	-	6.28
	9	3.7-1.23-50-1.5-3.5-380	550	432	1.27	Perf.	Stop	S	4.00	1.63	6.28
	10	3.7-1.23-50-1.5-3.5-465	489	432	1.13	Perf.	Stop	B	1.91	0.59	6.08
	1	5.2-0.48-50-1.0-2.0-445	467	504	0.93	Stop	Stop	B	2.09	0.28	6.53
<i>Gr. 2</i>	2	5.2-0.48-50-1.0-2.0-544	549	504	1.09	Perf.	Stop	S	3.31	0.75	6.53
	3	5.2-0.48-50-1.5-3.5-408	410	465	0.88	Stop	Stop	B	1.34	0.38	5.31 <sup>†</sup> ...
	4	5.2-0.48-50-1.5-3.5-498	484	465	1.04	Perf.	Stop	B	2.41	0.69	5.31 <sup>†</sup> ...
<i>Gr. 3</i>	1	3.7-0.37-65-1.0-2.0-443	539	500	1.08	Perf.	Stop	B	3.16	0.69	5.89
	2	3.7-0.37-65-1.0-2.0-541	634	500	1.27	Perf.	Perf.	P	-	-	5.98

\* Stop: The specimen stopped the projectile  
Perf.: The specimen was perforated by the projectile

\*\* B: Bulging, S: Splitting, P: Perforating  
† Concrete compressive strength on 28-days.

Table 4-2 Summary of dimensions of internal damage in the cross-section of the SC wall specimens

<i>Test group &amp; No.</i>	<i>Test case identifier</i>	<i>t<sub>d</sub></i> (in)	<i>t<sub>n</sub></i> (in)	<i>d<sub>1</sub></i> (in)	<i>d<sub>2</sub></i> (in)	<i>θ</i> (degree)
1	3.7-0.37-50-1.0-1.3-554	1.19	2.06	1.0	8.88	56
2	3.7-0.37-50-1.0-1.3-677	1.50	3.06	1.0	8.75	59
3	3.7-0.37-50-1.0-2.0-430	1.56	1.56	1.0	9.25	61
4	3.7-0.37-50-1.0-2.0-525	1.16	3.16	1.0	9.00	56
<i>Gr. 1</i>	5 3.7-0.53-50-1.5-1.3-660	1.38	1.38	1.5	9.75	59
	6 3.7-0.53-50-1.5-1.3-750	1.19	2.00	1.5	9.75	57
	7 3.7-0.53-50-1.0-2.0-513	1.44	-	1.0	9.00	59
	8 3.7-0.53-50-1.0-2.0-626	1.88	-	1.0	8.13	61
	9 3.7-1.23-50-1.5-3.5-380	1.38	4.00	1.5	6.75	47
	10 3.7-1.23-50-1.5-3.5-465	1.91	1.91	1.5	7.84	58
	1 5.2-0.48-50-1.0-2.0-445	2.09	2.09	1.0	7.75	63
<i>Gr. 2</i>	2 5.2-0.48-50-1.0-2.0-544	1.69	3.31	1.0	7.00	55
	3 5.2-0.48-50-1.5-3.5-408	1.34	1.34	1.5	9.00	57
	4 5.2-0.48-50-1.5-3.5-498	1.38	2.41	1.5	9.00	57
<i>Gr. 3</i>	1 3.7-0.37-65-1.0-2.0-443	1.44	3.16	1.0	8.75	58
	2 3.7-0.37-65-1.0-2.0-541	1.38	-	1.0	9.25	59

Table 4-3 Summary of the comparison of penetration depth between test results and estimation by the modified NDRC equations

<i>Test group &amp; No.</i>	<i>Test case identifier</i>	$V_{imp}$ (ft/s)	<i>Experimental test</i>		<i>Manual calculation</i>		<i>Ratio</i>	
			$x_{c\_test}$ (in)	$x_{c\_test}/T_c$	$x_{c\_calc}$ (in)	$x_{c\_calc}/T_c$	$x_{c\_calc}/x_{c\_test}$	
	1	3.7-0.37-50-1.0-1.3-554	593	2.06	0.54	1.90	0.49	0.92
	2	3.7-0.37-50-1.0-1.3-677	674	3.06	0.80	2.14	0.56	0.70
	3	3.7-0.37-50-1.0-2.0-430	424	1.56	0.41	1.66	0.43	1.06
	4	3.7-0.37-50-1.0-2.0-525	513	3.16	0.82	1.97	0.51	0.62
Gr. 1	5	3.7-0.53-50-1.5-1.3-660	667	1.38	0.36	1.71	0.44	1.24
	6	3.7-0.53-50-1.5-1.3-750	760	2.00	0.52	1.92	0.50	0.96
	7	3.7-0.53-50-1.0-2.0-513	640	-	-	-	-	-
	8	3.7-0.53-50-1.0-2.0-626	710	-	-	-	-	-
	9	3.7-1.23-50-1.5-3.5-380	550	4.00	1.04	2.38	0.62	0.60
	10	3.7-1.23-50-1.5-3.5-465	489	1.91	0.50	2.15	0.56	1.13
Gr. 2	1	5.2-0.48-50-1.0-2.0-445	467	2.09	0.55	1.81	0.48	0.86
	2	5.2-0.48-50-1.0-2.0-544	549	3.31	0.87	2.09	0.55	0.63
	3	5.2-0.48-50-1.5-3.5-408	410	1.34	0.35	1.90	0.50	1.41
	4	5.2-0.48-50-1.5-3.5-498	484	2.41	0.63	2.21	0.58	0.92
Gr. 3	1	3.7-0.37-65-1.0-2.0-443	539	3.16	0.82	2.10	0.55	0.67
	2	3.7-0.37-65-1.0-2.0-541	634	-	-	-	-	-

Table 4-4 Statistical analysis results of the comparison between measured and calculated values

$x_{c\_calc}/x_{c\_test}$	
$\mu$	1.06
$\sigma$	0.18
<i>COV</i>	0.17



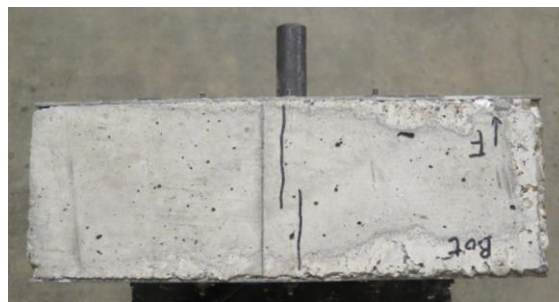
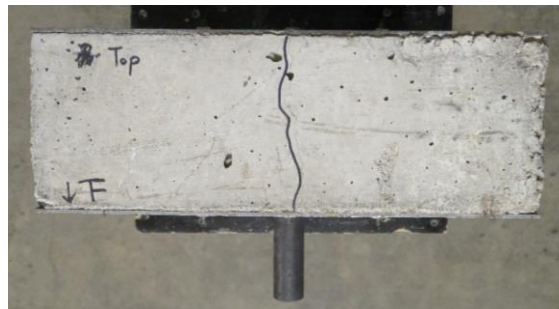
(a) Front



(b) Rear



(c) Left

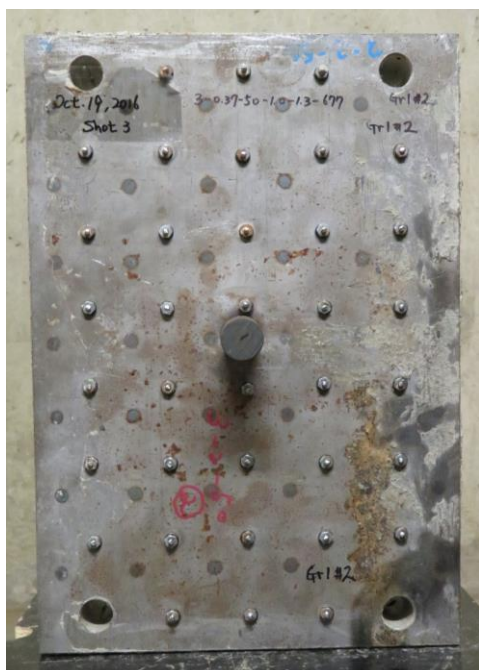


(d) Top / (e) Bottom



(f) Right

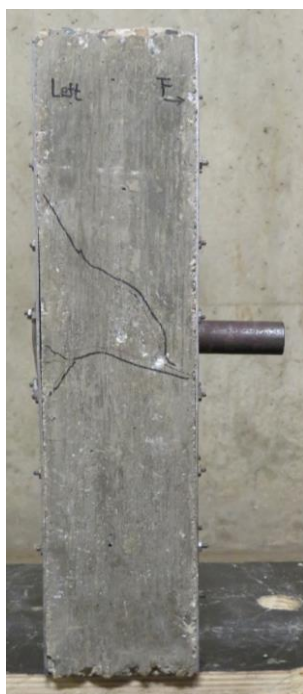
Figure 4-1 Photographs of damage in the post-test specimen: Gr.1 #1



(a) Front



(b) Rear



(c) Left



(d) Top / (e) Bottom

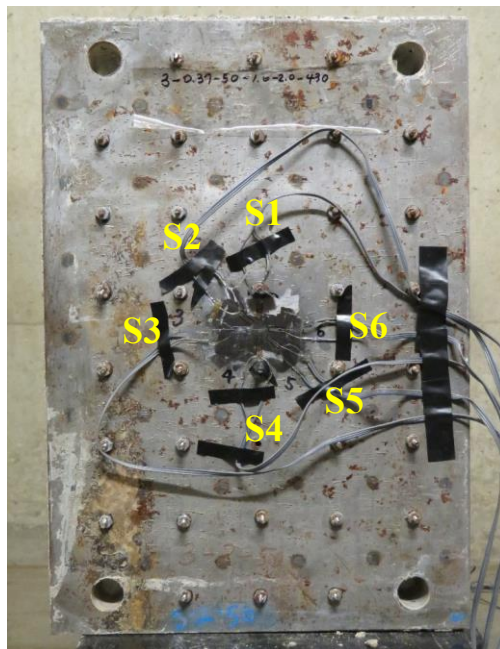


(f) Right

Figure 4-2 Photographs of damage in the post-test specimen: Gr.1 #2



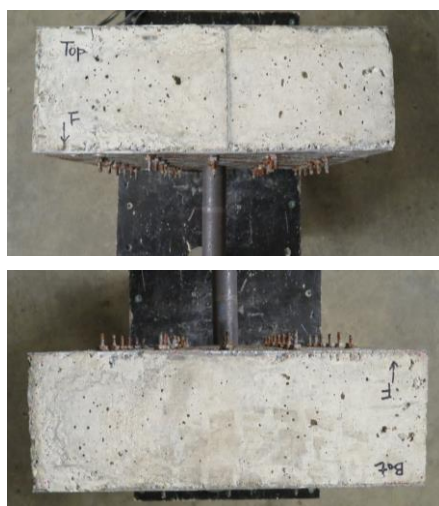
(a) Front



(b) Rear



(c) Left



(d) Top / (e) Bottom

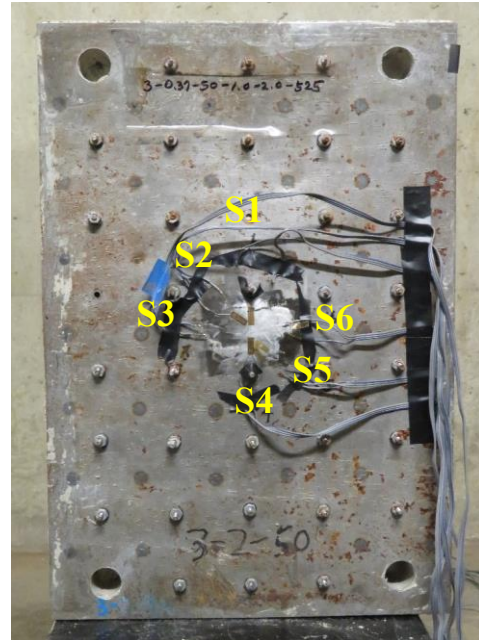


(f) Right

Figure 4-3 Photographs of damage in the post-test specimen: Gr.1 #3



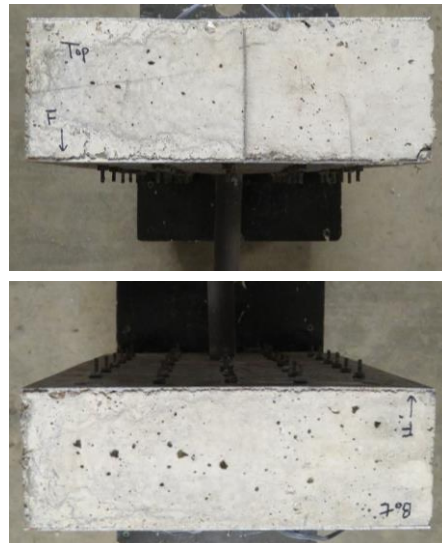
(a) Front



(b) Rear



(c) Left



(d) Top / (e) Bottom

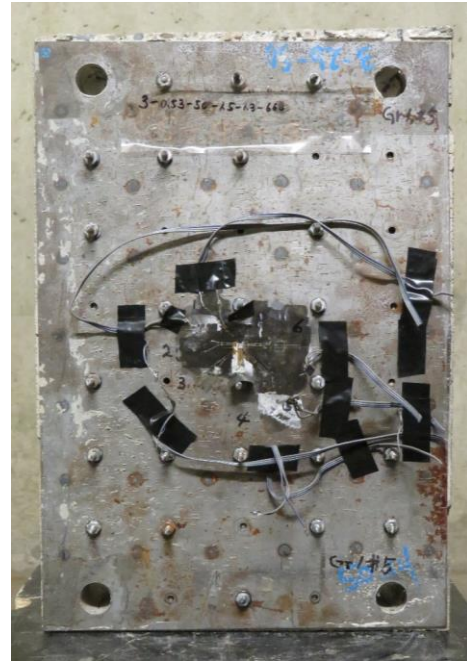


(f) Right

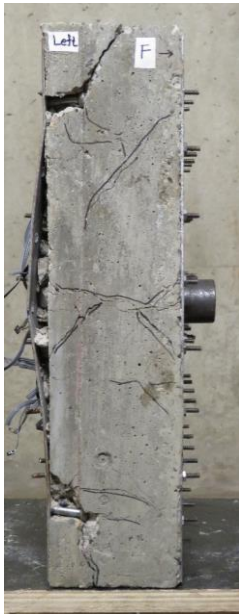
Figure 4-4 Photographs of damage in the post-test specimen: Gr.1 #4



(a) Front



(b) Rear



(c) Left



(d) Top / (e) Bottom



(f) Right

Figure 4-5 Photographs of damage in the post-test specimen: Gr.1 #5



(a) Front



(b) Rear



(c) Left



(d) Top / (e) Bottom



(f) Right

Figure 4-6 Photographs of damage in the post-test specimen: Gr.1 #6



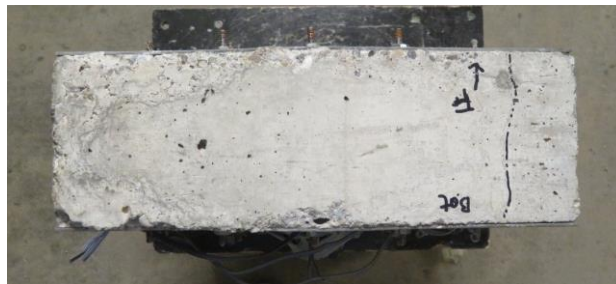
(a) Front



(b) Rear



(c) Left



(d) Top / (e) Bottom



(f) Right

Figure 4-7 Photographs of damage in the post-test specimen: Gr.1 #7



(a) Front



(b) Rear



(c) Left



(d) Top / (e) Bottom

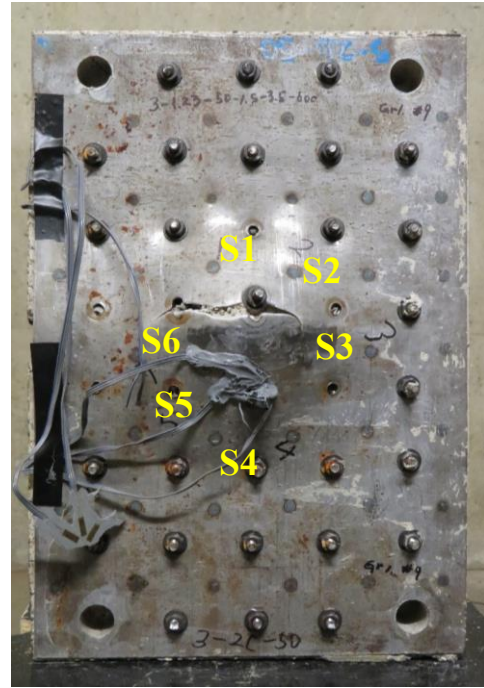


(f) Right

Figure 4-8 Photographs of damage in the post-test specimen: Gr.1 #8



(a) Front



(b) Rear



(c) Left



(d) Top / (e) Bottom

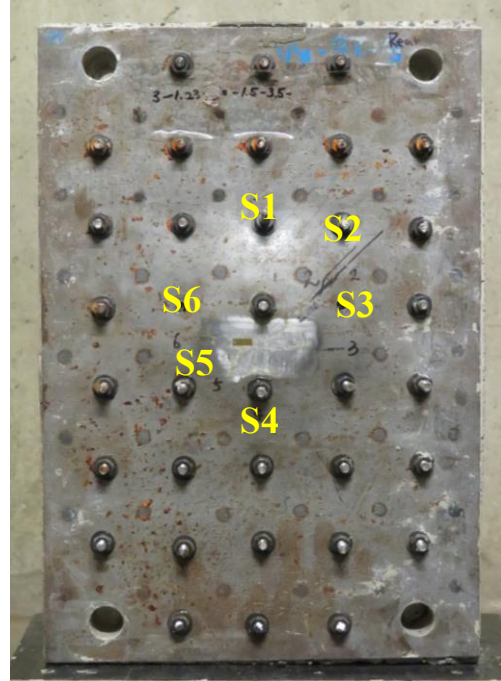


(f) Right

Figure 4-9 Photographs of damage in the post-test specimen: Gr.1 #9



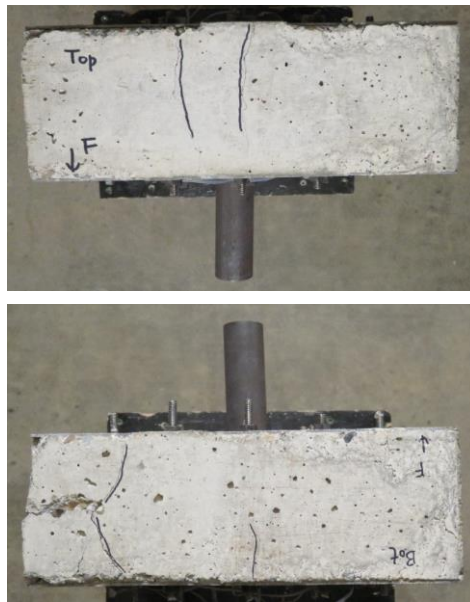
(a) Front



(b) Rear



(c) Left



(d) Top / (e) Bottom

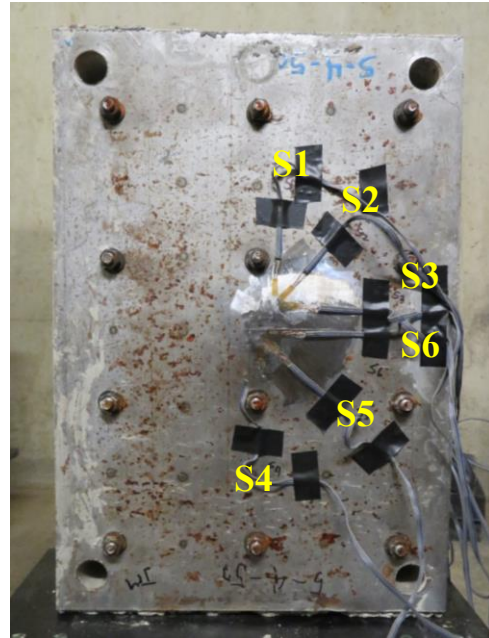


(f) Right

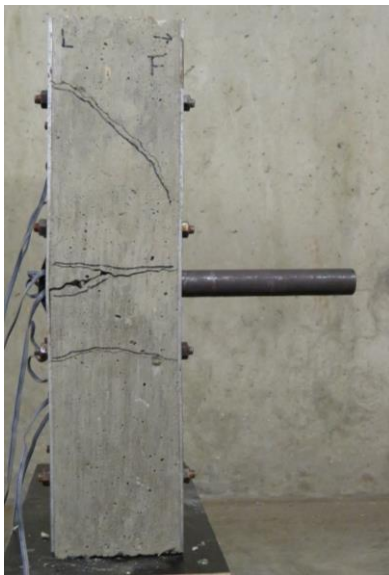
Figure 4-10 Photographs of damage in the post-test specimen: Gr.1 #10



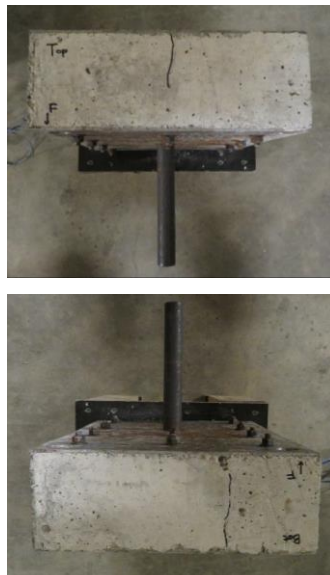
(a) Front



(b) Rear



(c) Left



(d) Top / (e) Bottom

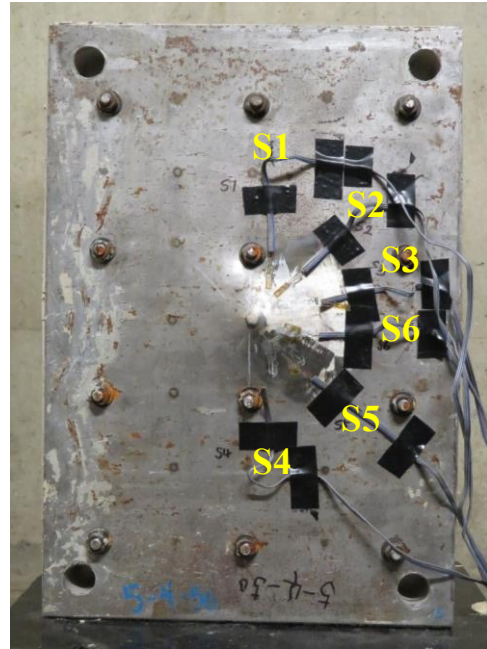


(f) Right

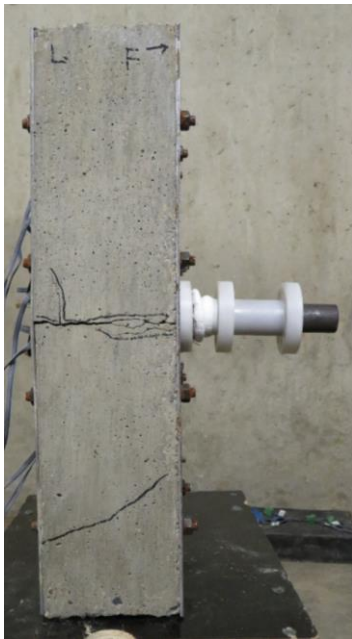
Figure 4-11 Photographs of damage in the post-test specimen: Gr.2 #1



(a) Front



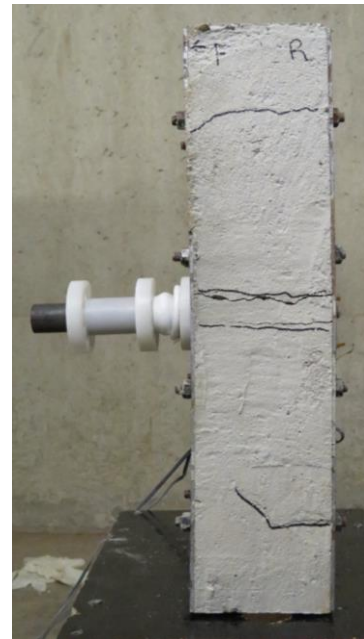
(b) Rear



(c) Left



(d) Top / (e) Bottom



(f) Right

Figure 4-12 Photographs of damage in the post-test specimen: Gr.2 #2



(a) Front



(b) Rear



(c) Left



(d) Top / (e) Bottom

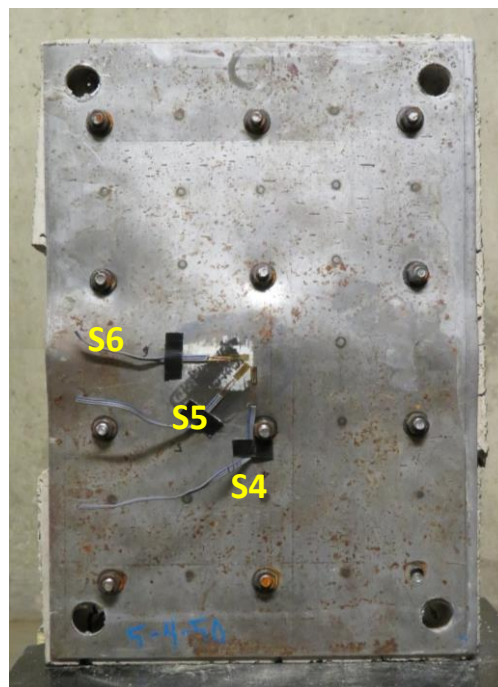


(f) Right

Figure 4-13 Photographs of damage in the post-test specimen: Gr.2 #3



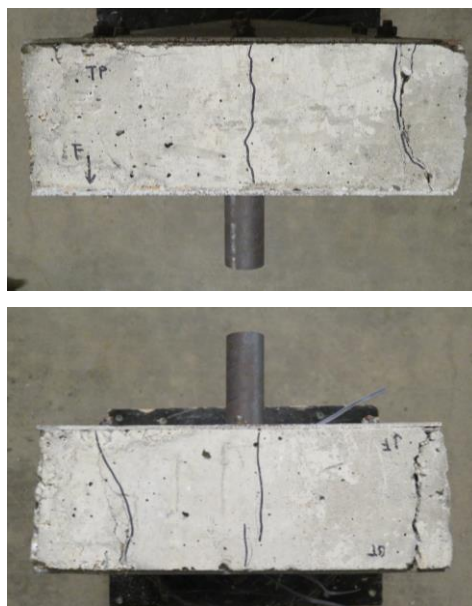
(a) Front



(b) Rear



(c) Left



(d) Top / (e) Bottom

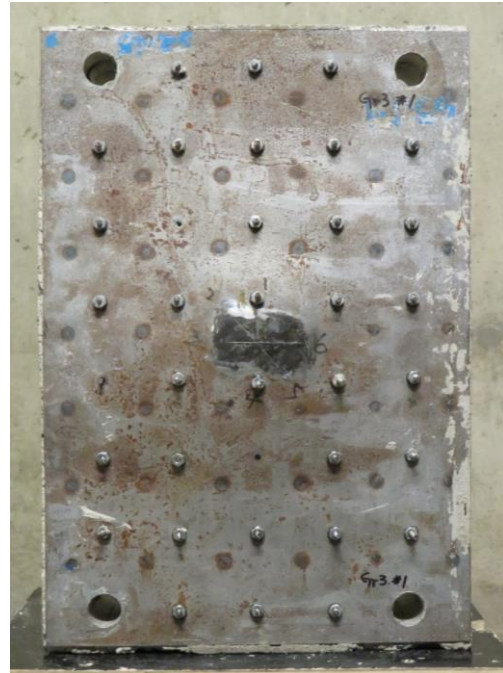


(f) Right

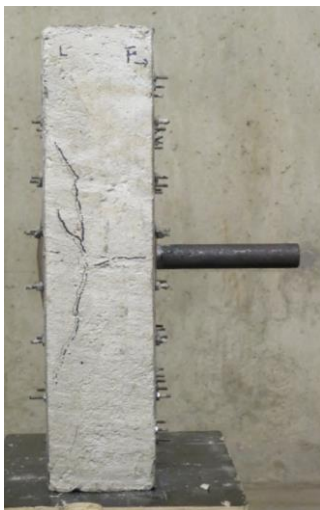
Figure 4-14 Photographs of damage in the post-test specimen: Gr.2 #4



(a) Front



(b) Rear



(c) Left



(d) Top / (e) Bottom



(f) Right

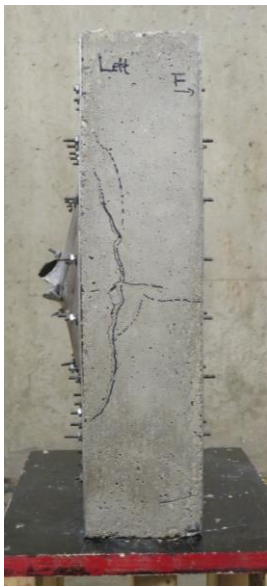
Figure 4-15 Photographs of damage in the post-test specimen: Gr.3 #1



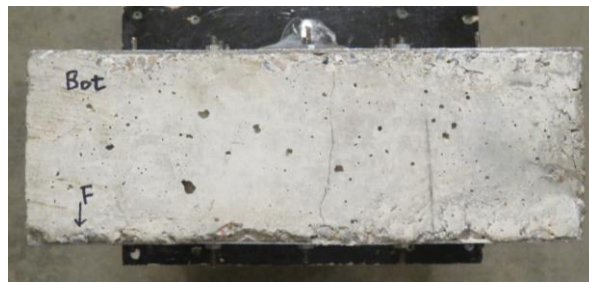
(a) Front



(b) Rear



(c) Left



(d) Top / (e) Bottom



(f) Right

Figure 4-16 Photographs of damage in the post-test specimen: Gr.3 #2



Figure 4-17 Photograph of damage in a cross-section cut from the post-test specimen: Gr.1 #1



Figure 4-18 Photograph of damage in a cross-section cut from the post-test specimen: Gr.1 #2



Figure 4-19 Photograph of damage in a cross-section cut from the post-test specimen: Gr.1 #3

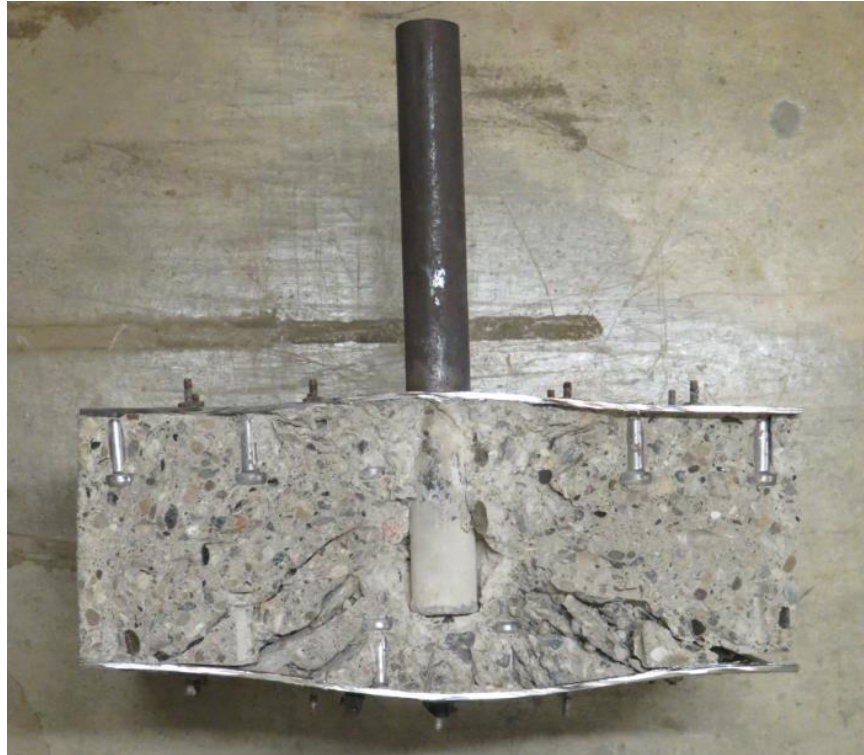


Figure 4-20 Photograph of damage in a cross-section cut from the post-test specimen: Gr.1 #4



Figure 4-21 Photograph of damage in a cross-section cut from the post-test specimen: Gr.1 #5



Figure 4-22 Photograph of damage in a cross-section cut from the post-test specimen: Gr.1 #6



Figure 4-23 Photograph of damage in a cross-section cut from the post-test specimen: Gr.1 #7



Figure 4-24 Photograph of damage in a cross-section cut from the post-test specimen: Gr.1 #8



Figure 4-25 Photograph of damage in a cross-section cut from the post-test specimen: Gr.1 #9



Figure 4-26 Photograph of damage in a cross-section cut from the post-test specimen: Gr.1 #10



Figure 4-27 Photograph of damage in a cross-section cut from the post-test specimen: Gr.2 #1



Figure 4-28 Photograph of damage in a cross-section cut from the post-test specimen: Gr.2 #2



Figure 4-29 Photograph of damage in a cross-section cut from the post-test specimen: Gr.2 #3



Figure 4-30 Photograph of damage in a cross-section cut from the post-test specimen: Gr.2 #4



Figure 4-31 Photograph of damage in a cross-section cut from the post-test specimen: Gr.3 #1



Figure 4-32 Photograph of damage in a cross-section cut from the post-test specimen: Gr.3 #2

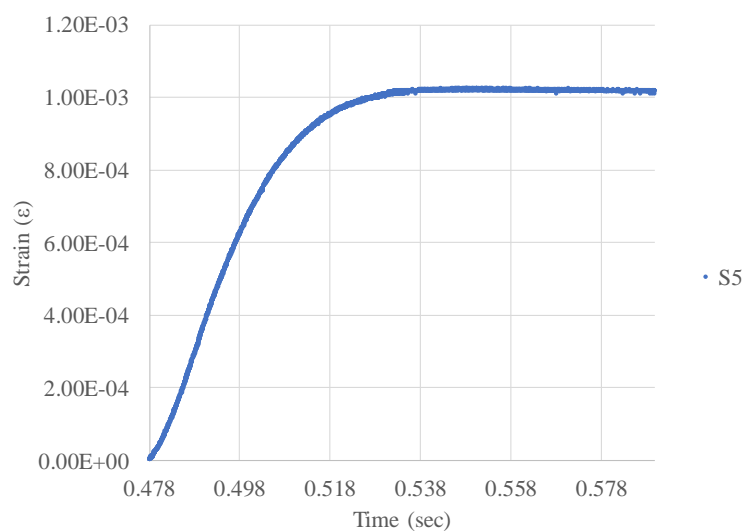


Figure 4-33 A representative strain data obtained from the post-test specimen: Gr.1 #3

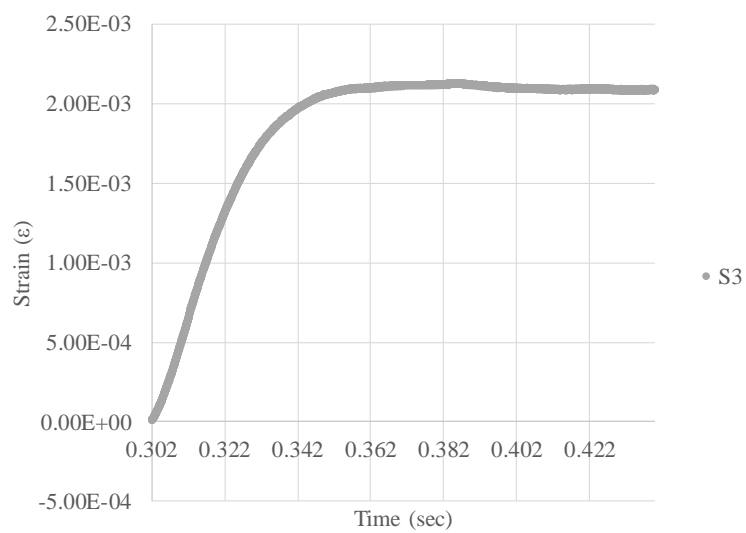


Figure 4-34 A representative strain data obtained from the post-test specimen: Gr.1 #4

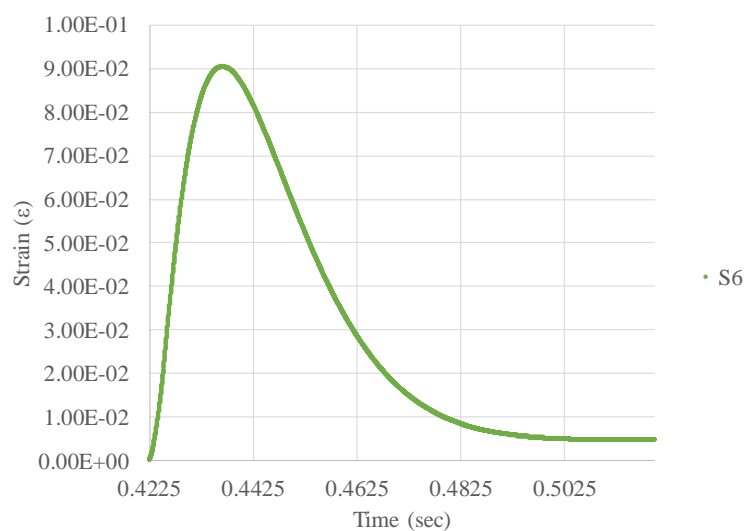


Figure 4-35 A representative strain data obtained from the post-test specimen: Gr.1 #9

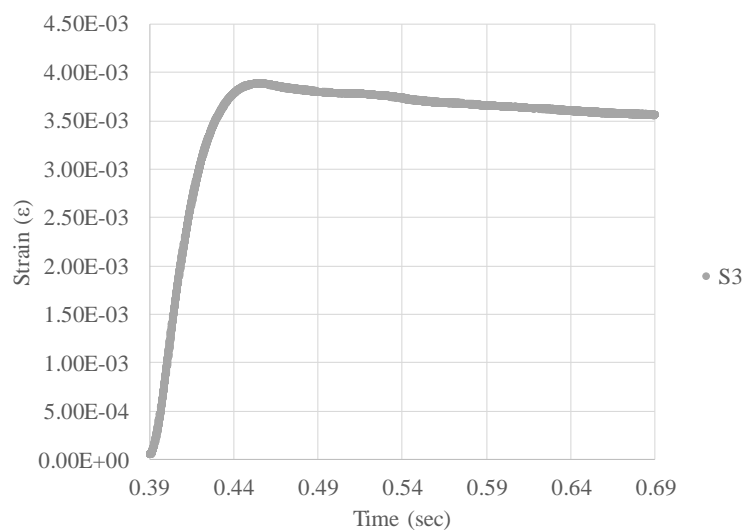


Figure 4-36 A representative strain data obtained from the post-test specimen: Gr.1 #10

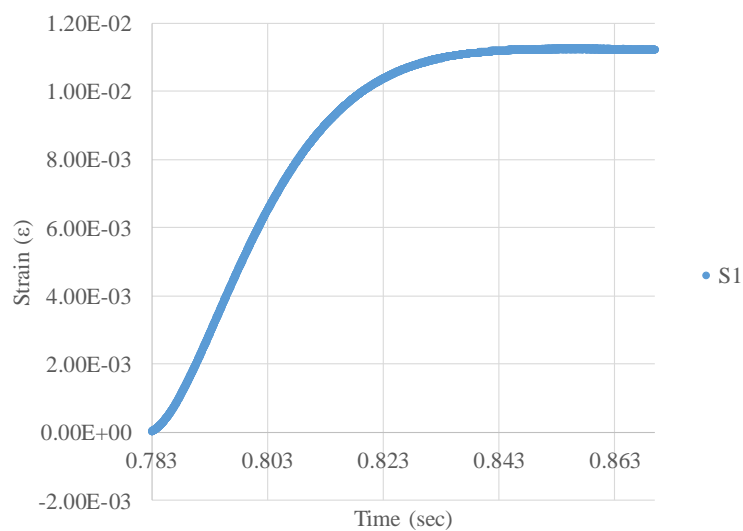


Figure 4-37 A representative strain data obtained from the post-test specimen: Gr.2 #1

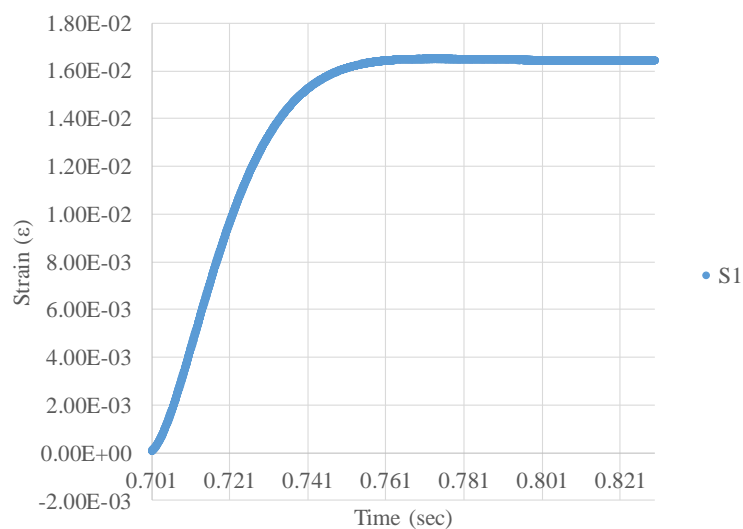


Figure 4-38 A representative strain data obtained from the post-test specimen: Gr.2 #2

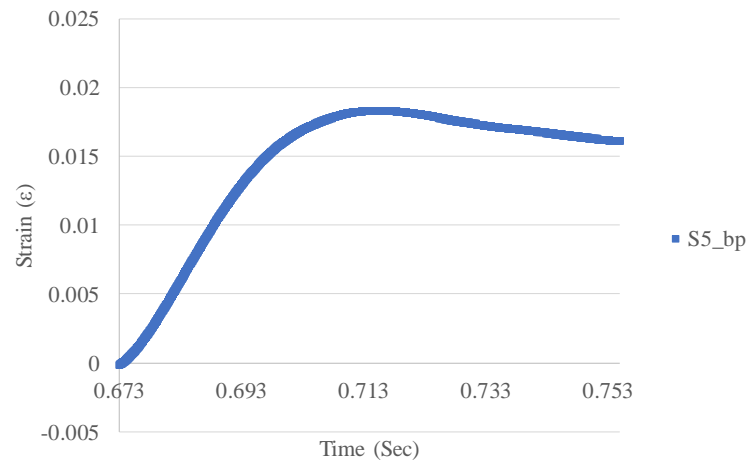


Figure 4-39 A representative strain data obtained from the post-test specimen: Gr.2 #4



(a) Group 1, No. 3



(b) Group 1, No. 4



(c) Group 1, No. 7

Figure 4-40 Photographs of internal damage progress in a series of post-test SC wall specimens

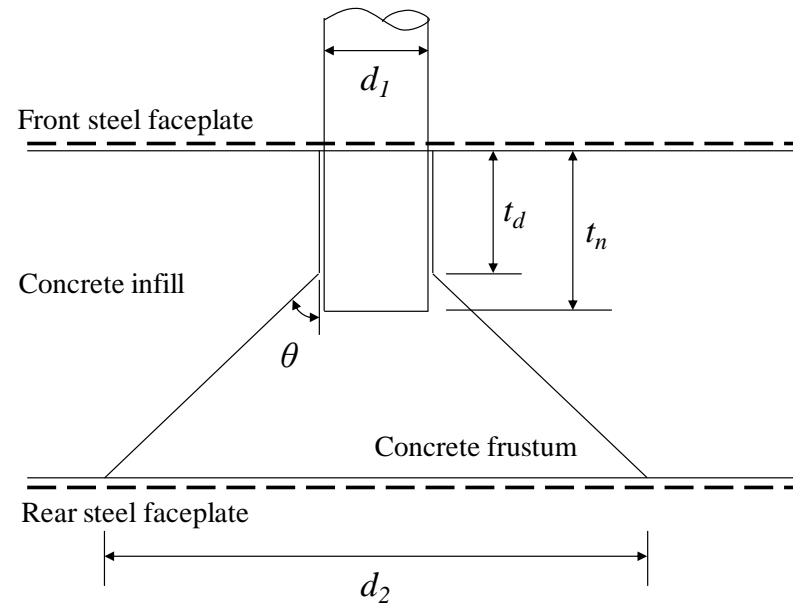
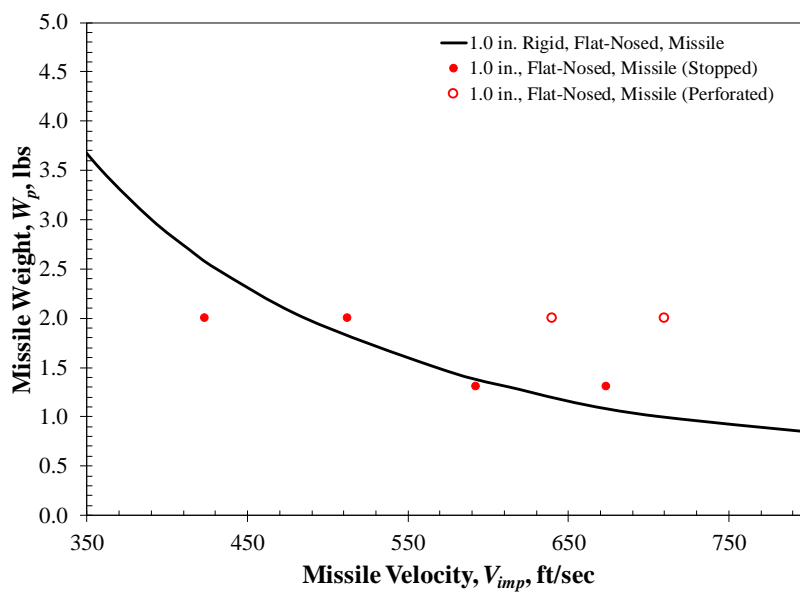
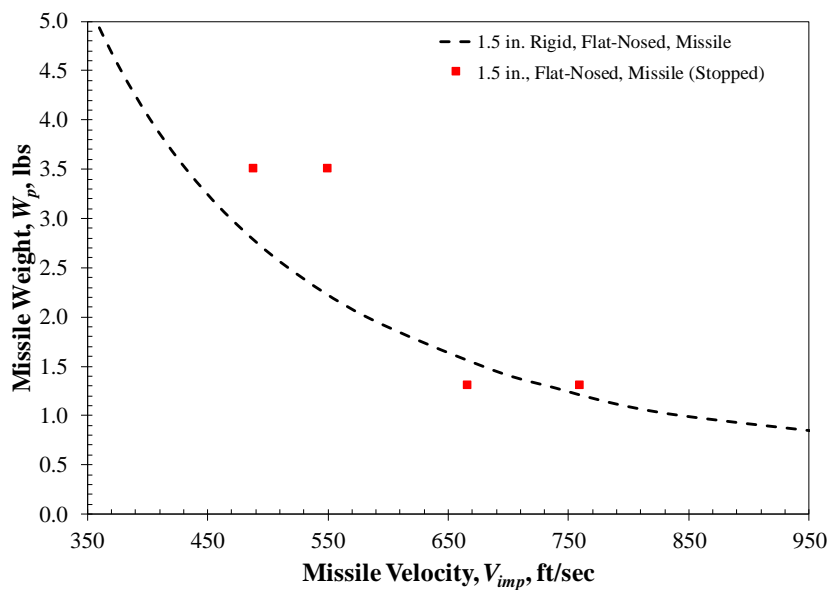


Figure 4-41 Schematic of internal damage details in the cross-section of post-test SC wall specimen

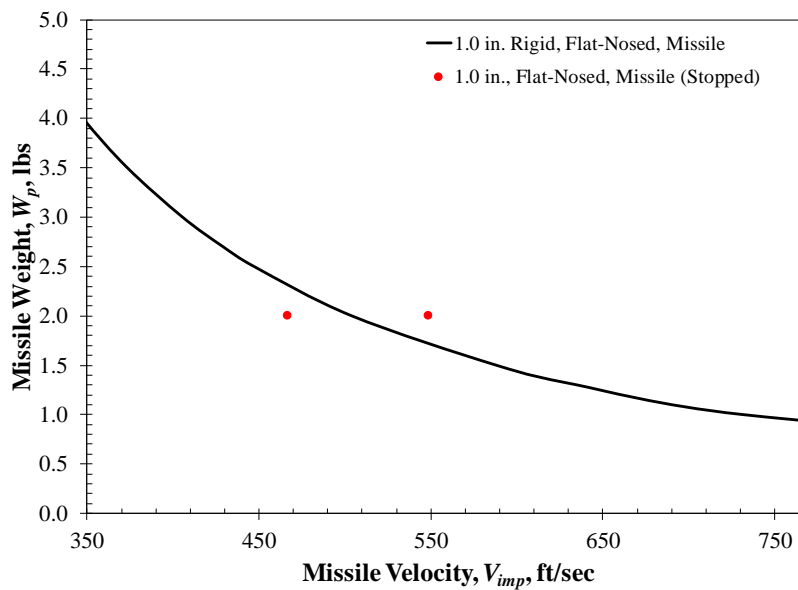


(a) 1.0 in. diameter projectile applied

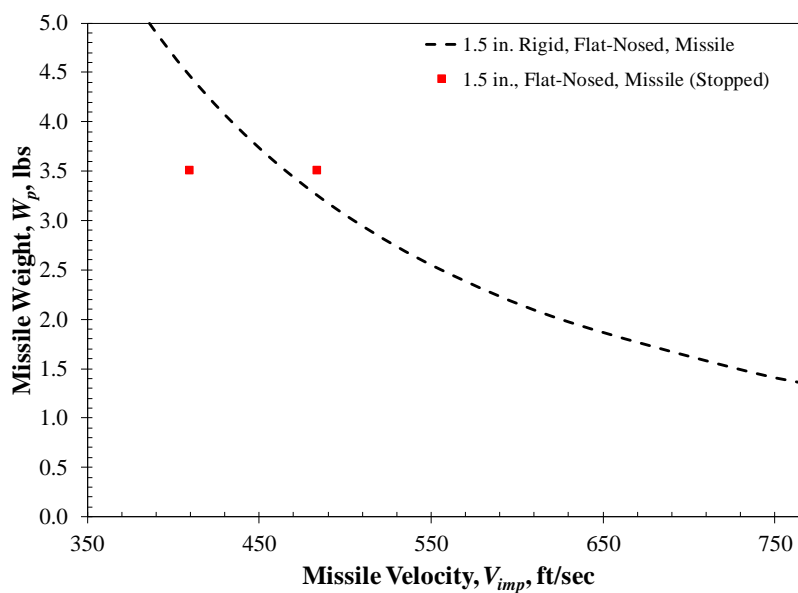


(b) 1.5 in. diameter projectile applied

Figure 4-42 Test results marked on the perforation resistance curves in group 1



(a) 1.0 in. diameter projectile applied



(b) 1.5 in. diameter projectile applied

Figure 4-43 Test results marked on the perforation resistance curves in group 2

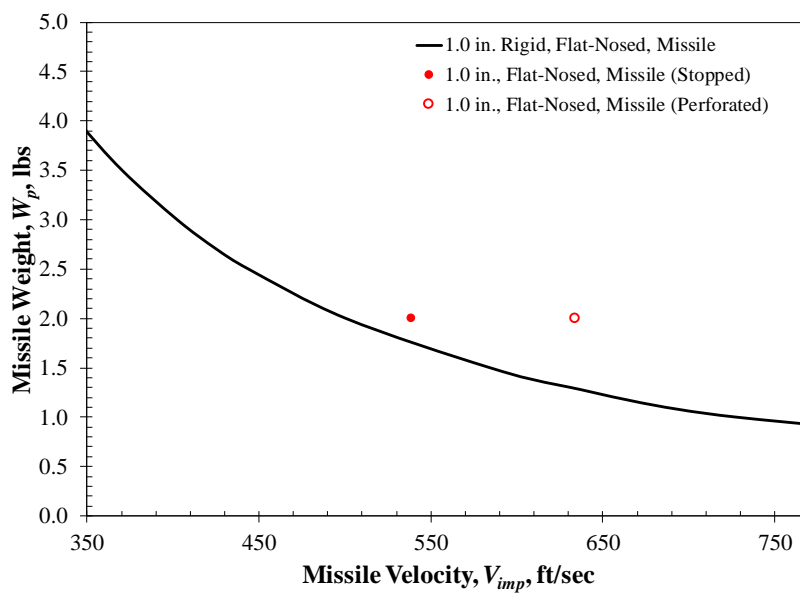


Figure 4-44 Test results marked on the perforation resistance curves in group 3

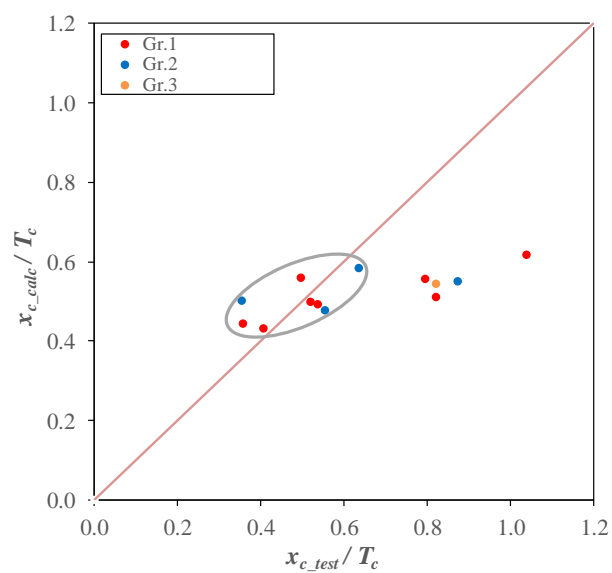
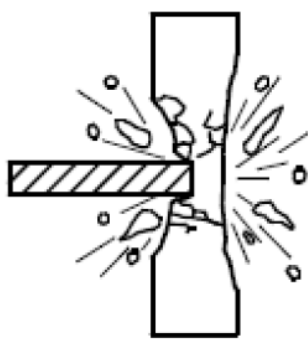
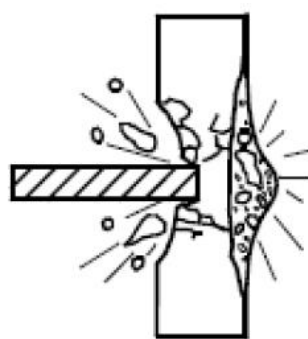


Figure 4-45 Graphical comparison of penetration depth between test result and calculation



(a) Scabbing in RC walls



(b) Bulging in SC walls

Figure 4-46 Comparison of damage mode between RC and SC walls subjected to missile impact (Hashimoto et al. 2005)

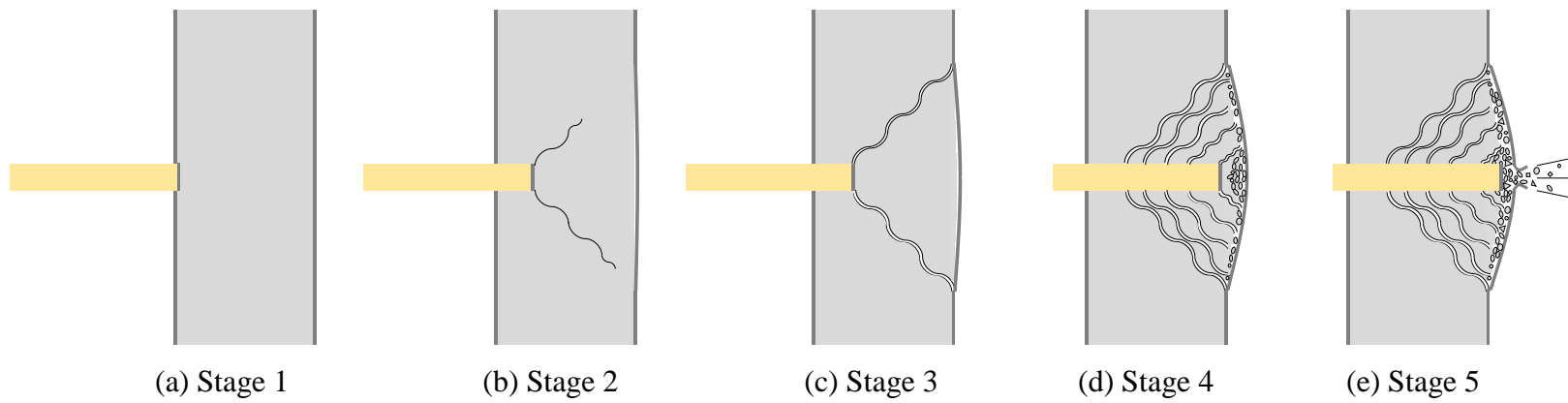


Figure 4-47 Stages in local failure mechanism of SC walls subjected to missile impact

## CHAPTER 5. NUMERICAL MODEL DEVELOPMENT AND BENCHMARKING

### 5.1 Introduction

To better understand the local damage behavior of SC walls subjected to missile impact, numerical models were developed and benchmarked to the experimental tests results presented in CHAPTER 4.

This chapter describes details on the numerical models including element type, element formulation, material model, and so on for each component of the SC wall specimen as well as contact or constraint options applied to build relationship among those interacting components for the impact process. This chapter also presents benchmarking analyses results of the numerical models to prove that they are appropriate to simulate the missile impact test on SC walls for this research project.

### 5.2 Development of Numerical Models

The small-scale missile impact test specimen consists of front and back steel faceplates, concrete infill, tie bars, and steel headed shear stud anchors. Finite element models were developed to investigate the failure behavior of SC walls more extensively when they are subjected to impact load. The models specify geometrical feature, incorporate material properties of each part of the specimens, and capture physical interaction among them. LS-DYNA, which is a commercial finite element analysis software, is used to develop three dimensional finite element model of the specimen. Finite element model details are described herein. Figure 5-1 shows the developed finite element model for this research project.

### 5.2.1 Steel Faceplate Modeling

The front and rear steel faceplates were modeled using fully integrated and selectively reduced solid elements which are intended for elements with poor aspect ratios (ELFORM: -1). This element formulation uses eight integration points and reduces shear locking phenomenon. Piecewise linear plasticity (MAT\_24) material model was adopted to represent material properties for the steel faceplates. Measured engineering stress-strain values presented in Figure 3-3 were converted to true stress-strain values to be used for material properties of the steel faceplates in finite element model. Failure strain of 0.15 was applied. Strain rate effect was considered in the finite element analysis using dynamic increase factor (DIF). UFC 3-340-02 (U.S. Department of Defense 2008) provides DIF values with regard to various strain rates for A514 plate as shown in Figure 5-2. Although A514 plate is not exactly the same material as A1011 steel sheet used in experimental test specimens, the chemical composition of A1011 steel sheet is similar to that of A514 plate. So, the DIF values were used assuming they are applicable to A1011 steel sheet. Material input parameters for the steel faceplates are summarized in Table 5-1.

### 5.2.2 Tie Bar and Steel-Headed Shear Stud Anchor Modeling

Tie bars and steel-headed shear stud anchors were implemented as beam elements with Hughes-Liu beam with cross section integration which uses 2 x 2 gauss quadrature rule for its integration (ELFORM: 1). The piecewise linear plasticity model (MAT\_24) was used for tie bars and stud anchors to account for the non-linear plastic behavior of the steel material. Measured tensile stress-strain data of the tie bar illustrated in Figure 3-3 was converted to true stress-strain data to be used for material properties of the tie bars in numerical model. For steel-headed shear stud anchors, tensile coupon test was not available and material properties provided by supplier or typical Grade 60 steel were used. Failure strain of 0.05 was applied for tie bars. No failure strain

was considered for steel-headed shear stud anchors. Material input parameters for the tie bars and steel-headed shear stud anchors were summarized in Table 5-2 and Table 5-3, respectively.

Because the steel-headed shear stud anchors were simplified as one dimensional beam elements in the finite element model, the load-slip displacement behavior (Ollgaard et al. 1971) caused by composite action which acts parallel to the steel faceplates is not inherently included. Therefore, a discrete beam element or connector element (ELFORM: 6) was added between the steel faceplates and the steel-headed shear stud anchors to account for load-slip behavior of the steel-headed shear stud anchors. Elastic spring discrete beam material model (MAT\_74) was used to implement the load-slip behavior. The maximum tensile displacement value,  $\Delta_{\max}$ , was calculated using Equation 5-1 (Shim et al. 2004).

$$\Delta_{\max} = (0.48 - 0.029f'_c)d_s \quad \text{Equation 5-1}$$

$d_s$  is a diameter of the steel-headed shear stud anchor. Load-slip behavior of the steel-headed shear stud anchors was applied to the model using both Equation 5-2 (Ollgaard et al. 1971) and Equation 5-3 (American Institute of Steel Construction 2011).

$$Q = Q_n(1 - e^{-18\Delta})^{2/5} \quad \text{Equation 5-2}$$

$$Q_n = 0.65A_s f_u \quad \text{Equation 5-3}$$

$A_s$  and  $f_u$  are cross-section area and ultimate strength of the steel-headed shear stud anchor, respectively. Material input parameters for the discrete beam element are summarized in Table 5-4.

### 5.2.3 Concrete Modeling

The concrete core was modeled using solid elements with element formulation of 1 (ELFORM: 1). This formulation is an eight-node constant stress solid element with a single integration point. Winfrith concrete with strain rate effect included (MAT\_84) was selected as a material model for the concrete core. Winfrith concrete model was developed for analysis of the response of reinforced concrete structures to severe dynamic loadings such as blast and impact (Broadhouse 1995; Broadhouse and Neilson 1987), and validated against a wide variety of experimental tests. It is a smeared crack (or pseudo crack) and smeared rebar model, but the rebars can be modeled separately and incorporated in the model. Eight-node solid elements with a single integration point (ELFORM=1) on double precision executable should be used to implement the Winfrith concrete model.

Measured concrete compressive strength presented in Table 4-1 was used to calculate input parameters for the Winfrith concrete model. Uniaxial compressive strength was calculated as multiplying the measured compressive strength by a factor of 1.25 because the Winfrith concrete model requires concrete cube strength (Schwer 2011). Generally, tensile strength of SC structures is approximately half of that of RC structures because of a higher degree of shrinkage cracking during curing process (URS Energy and Construction Inc. 2011). For the numerical model herein,  $3\sqrt{f'_c}$  was used based on the behavior from the static tests of SC walls described in prior research (Bruhl 2015).

The Winfrith concrete model can accommodate the strain rate effects when the RATE card is turned on. (RATE: 0) For this case the fracture energy contributed to open the crack should be calculated and entered in the parameter of FE. An equation to obtain fracture energy,  $G_f$ , with a function of aggregate size,  $a_{max}$ , was suggested (Wittmann 2002) and it is shown in Equation 5-4.

$$G_f = 1.297(a_{\max})^{0.32} \quad \text{Equation 5-4}$$

For the strain softening behavior of the concrete, the bilinear curve of average strain softening response (Broadhouse and Attwood 1993) in Figure 5-3 was implemented in the Winfrith concrete model.

When the fracture energy is specified first, then the two crack widths,  $w_i$ , can be calculated using the Equation 5-5, where  $c_i$  is 0.71 or 5.14. Failure strain,  $\varepsilon_f^{elem}$ , when the crack-normal stress goes to zero, can be calculated using Equation 5-6, where  $L^{elem}$  is the cube root of the element volume (Schwer, 2011).

$$w_i = c_i \frac{G_f}{f'_t} \quad \text{Equation 5-5}$$

$$\varepsilon_f^{elem} = \frac{w}{L^{elem}} \quad \text{Equation 5-6}$$

MAT\_ADD\_EROSION is applied to implement the concrete element failure in this concrete model. This material option enables the elements that satisfy failure (or erosion) criteria to be deleted from the calculation. Multiple failure criteria can be defined and they are applied independently. Once a sufficient number of failure criteria (NCS) is satisfied, corresponding elements are to be eroded. Material input parameters for the concrete core are summarized in Table 5-5 and Table 5-6.

#### 5.2.4 Projectile Modeling

The projectile was modeled using solid elements (ELFORM: 1) with piecewise linear plasticity model (MAT\_24). As an eight-node solid element, element formation of 1 element has a single integration point and needs hour glass stabilization. Material properties of the projectiles were obtained from coupon tests and the averaged values were 194 ksi of yield strength and 206 ksi of ultimate strength. Material input parameters for the projectile are summarized in Table 5-7.

#### 5.2.5 Spacer Plates Modeling

Spacer plates were inserted on the top and bottom surfaces of the SC walls when they were fixed to the main support structure of the test setup. In the finite element model the spacer plates were modeled using three dimensional solid elements which correspond to element formation of 1 (ELFORM: 1). At the same time, rigid material model (MAT\_20) was used in order to reduce an unnecessary analysis time because their structural behavior is out of interests. They provide boundary conditions to the SC walls, which are implemented by constraint option in the MAT\_20 cards. Material input parameters for the discrete beam element are summarized in Table 5-8.

#### 5.2.6 Other Modeling Details

AUTOMATIC\_SURFACE\_TO\_SURFACE command with SOFT=0 was used to implement contact between front/rear steel faceplates and spacer plates, which is a penalty-based contact approach. This contact approach calculates the contact spring stiffness using the size of the contact segments and its material properties. Because the material properties play an important role in the contact algorithm, the material stiffness parameters of the contacting surfaces should be approximately the same order of magnitude. That is, for contact between dissimilar materials, this contact algorithm is not recommended unless there is a previous experience that proves its effectiveness on the application. Otherwise, the contact is likely to be broken down.

The same command (AUTOMATIC\_SURFACE\_TO\_SURFACE) with SOFT=1 was used for contact between steel faceplates and concrete core where soft constraint-based contact approach was referred. This contact approach calculates the contact spring stiffness using the nodal masses associated with the contact and the time step size. Material properties are not taken into account for the stiffness calculation so that this approach is effective to be used for contact between dissimilar materials. In general, there is no big difference in the contact stiffness between SOFT=0 option and SOFT=1 option when it comes to contact between metal to metal. However, for contact between soft dense material and metal, the contact stiffness which is one or two orders of magnitude greater is obtained with SOFT=1 option. Thus, this approach is recommended for the contact between dissimilar materials.

ERODE\_SURFACE\_TO\_SURFACE command with SOFT=1 and EROSOP=1 was chosen for contact among the projectile, front/rear steel plates, and concrete core where element failure occurs and new contact faces are generated. It is always recommended that eroding contact should be applied to solid elements which are associated with contact definition combined with element deletion caused by failure criteria of materials. This contact type includes an algorithm which updates the contact surfaces when the corresponding solid elements are deleted by meeting the failure criteria. (Hallquist 2006)

AUTOMATIC\_BEAM\_TO\_SURFACE command with SOFT=1 option was applied for contact between the projectile and tie bars and shear studs so that beam to solid contact works properly when the projectile penetrates SC walls.

Steel headed shear stud anchors and tie bars are embedded in the concrete core of SC walls. Perfect bond among them was assumed. It is implemented by using command of CONSTRAINED\_LAGRANGE\_IN\_SOLID.

Belytschko-Bindeman hourglass type (TYPE 6) with hourglass coefficient setting to 0.1 (default) was used to control hourglass effects. This type assumes strain co-rotational stiffness form for 2D and 3D solid elements only. It is available for explicit and implicit solution methods.

### 5.3 *Benchmarking of the Numerical Models*

#### 5.3.1 Representative Analysis Results of Test Case Number 2 in Group 1

Observation of the rear steel faceplate deformation or rupture pattern of SC wall specimen may provide a way to see if the numerical modeling approach is on the right track. That is because three different damage modes, which were bulging, splitting and perforating, left their characteristic damage feature on the rear steel faceplate as shown in the experimental investigation, respectively.

Test case number 2 in group 1 was chosen as a representative test case in which bulging damage mode occurred. The rear steel faceplate of the post-test specimen is illustrated in Figure 5-4 (a). The projectile impacted the exact center of the specimen and the rear steel faceplate swelled up to 0.63 in. Figure 5-4 (b) shows the numerical analysis result which compared well with the test result. Convexly shaped, swelled rear steel faceplate in the test result was captured similarly in the numerical analysis result. Bulging depth of the rear steel faceplate was measured at 0.41 in. from the analysis result, which is less than the test result by 34%.

Figure 5-5 (a) illustrates the cross-section cut of the post-test SC wall specimen. It shows the tunneling region where the projectile drilled into the concrete core and the concrete frustum generated at the end of the tunneling region. The penetration depth of the projectile measured at 3.06 in. from the test result. Figure 5-5 (b) shows the cross-section cut of the corresponding numerical model. It indicates a similar internal damage pattern as depicted in the test result. The numerical analysis result presents the tunneling region made by the projectile crushing the concrete

core, followed by the concrete frustum whose boundary was illustrated explicitly by eroded elements. The penetration depth was measured at 2.85 in. and compared reasonably with the test result which was less than by 7%.

Projectile velocity – time history data is plotted in Figure 5-6. This provides clues on the residual velocity of the projectile and the amount of dissipated kinetic energy through the impact.

### 5.3.2 Representative Analysis Results of Test Case Number 9 in Group 1

Splitting damage mode, which occurred at test number 9 in group 1, showed that rupture on the rear steel faceplate started from a tie bar hole and propagated horizontally to the next punched hole for the tie bar. The rupture propagated one full spacing to the left and one half spacing to the right with some vertical rupture downward. Some of the ends of the tie bars, around the center of the rear steel faceplate, were found to be broken and popped off the specimen as can be seen in Figure 5-7 (a). Numerical analysis of this test case resulted in perforation damage mode. However, it is close to the splitting damage mode which is immediately before the perforation. And the shape of the ruptured steel faceplate agreed reasonably with the experimental test results as illustrated in Figure 5-7 (b).

Figure 5-8 (a) illustrates the cross-section cut of the post-test SC wall specimen. It shows the tunneling region where the projectile drilled into the concrete core and the concrete frustum generated at the end of the tunneling region. The penetration depth of the projectile measured at 4.00 in. from the test result. Figure 5-8 (b) shows the cross-section cut of the corresponding numerical model. It indicates a similar internal damage pattern as depicted in the test result. The numerical analysis result presents the tunneling region made by the projectile crushing the concrete core, followed by the concrete frustum whose boundary is illustrated explicitly by eroded elements.

Thus, failure mechanism of the SC wall was verified reasonably including the formation of the concrete frustum.

Figure 5-9 presents missile velocity – time history of the test case. This provides clues on the residual velocity of the projectile and the amount of dissipated kinetic energy through the impact.

### 5.3.3 Representative Analysis Results of Test Case Number 7 in Group 1

Test cases number 7 and 8 in group 1 produced perforation damage mode and the result of the former case was photographed as a representative perforation case in Figure 5-10 (a). The perforation occurred in the exact center of the rear steel faceplate with resultant tearing in four directions forming a cross shape. Figure 5-10 (b) shows the numerical analysis result which compared well with the test result. Examination of the numerical simulation revealed that splitting occurred, generating a cross shape of rupture, first in the center of the rear steel faceplate, and then the rupture proceeded horizontally and vertically. As the projectile was moving forward, the cross shape of rupture increased bigger and opened enough for the projectile to pass through. A couple of tie bar ends around the center of the rear steel faceplate were broken and their heads were popped off in the test result. This tendency was represented well in the numerical analysis results, also.

Figure 5-11 (a) illustrates the cross-section cut of the post-test SC wall specimen. It shows the tunneling region where the projectile drilled into the concrete core and the concrete frustum generated at the end of the tunneling region. Figure 5-11 (b) shows the cross-section cut of the corresponding numerical model. It indicates a similar internal damage pattern as depicted in the test result. The numerical analysis result presents the tunneling region made by the projectile crushing the concrete core, followed by the concrete frustum whose boundary was illustrated

explicitly by eroded elements. Thus, failure mechanism of the SC wall was verified reasonably including the formation of the concrete frustum.

Figure 5-12 presents missile velocity – time history of the test case. This provides clues on the residual velocity of the projectile and the amount of dissipated kinetic energy through the impact.

#### 5.3.4 Summary of Benchmarking Analyses

The finite element models were benchmarked using results from the experimental investigation. Table 5-9 shows the comparison of the results between experimental tests and numerical analyses. Velocity of projectile used in the numerical analysis is specified as  $V_{imp}$ . Generic result of the numerical analysis which simulates the experimental test is presented as ‘Stop (Stopped)’ or ‘Perf. (Perforated)’. Damage mode from each numerical model was categorized as bulging (B), splitting (S), or perforating (P), which is the same as damage mode from the experimental tests. Penetration depth of the projectile and bulging depth of the rear steel faceplate on the specimen measured after each test were compared with the numerical analyses results as a ratio of  $X_{c\_FEM}/X_{c\_test}$  and  $X_{bg\_FEM}/X_{bg\_test}$ , respectively. This ratio helps to evaluate the accuracy of estimations that the numerical models provide. Results of the benchmarking analyses are summarized in Table 5-9. They are also marked on the perforation resistance curves and compared with the experimental tests results graphically in Figure 5-13 through Figure 5-17.

In all but two test cases (number 9 and 10) in group 1, the numerical models gave the same damage modes as the experimental test results. The estimation of penetration depth and bulging depth showed good agreement with the test results. Based on the statistical evaluation of Table 5-10, the penetration depth was estimated with an average of 2% error and standard deviation of

22%. For bulging depth, the estimation from the numerical models was made with an average of 14% error and standard deviation of 19%, when compared to the experimental test results.

On the other hand, results of the numerical models in group 2 varied more than the experimental test results for group 1. Models number 1, number 3 and number 4 showed a good agreement in the damage mode with the test results, but model number 2 provided perforating damage mode which varies from the test result which showed bulging damage mode. Estimated penetration depth was 23% greater than the experimental results and estimated bulging depth was 71% higher than the experimental results as described in Table 5-11. Therefore, the numerical models provided significantly conservative results for group 2 test cases.

All two cases in group 3 showed a good agreement of the analysis results with the experimental test results. Penetration depth was estimated with an average of 2% error. Bulging depth was anticipated with an average of 34% error.

For the entire test cases of the benchmarking, statistical evaluation result shows that penetration depth was evaluated with an average of 6% error and standard deviation of 22%. Bulging depth was evaluated with an average of 9% error and standard deviation of 51%. Table 5-12 presented the statistical evaluation results of the entire finite element models' performance.

#### *5.4 Discussion*

In previous sections, numerical models were developed and benchmarked to the experimental tests results by comparing penetration depth, bulging depth and damage mode of each test case. Numerical analyses results showed reasonable agreement with the tests results for group 1 and group 3 test cases: with an averaged error of 2% for the penetration depth and 14% for the bulging depth for group 1 and with an averaged error of 2% for the penetration depth and 34% for the bulging depth for group 3. However, for group 2 test cases, the numerical analyses

results presented rather conservative results with an averaged error of 23% for penetration depth and more than three times for the bulging depth.

This non-conformance in group 2 test cases may be attributed to the joining method of tie bars and steel faceplates. There is a difference in the joining method of tie bars and steel faceplates in between the experimental test specimen and the numerical model. The tie bars in the experimental test specimen are threaded rod which is secured with hex nuts on both sides of the steel faceplate. However, in the numerical model the tie bars are joined to the steel faceplates directly, which means one node at one end of the tie bar is shared with the steel faceplate. When the shear reinforcement of the specimen was relatively small this difference in numerical modeling did not affect the results. But when the shear reinforcement ratio is increased, this means the tie bar diameter and hex nuts size became bigger, this numerical modeling approach may affect the behavior of the rear steel faceplate subjected to missile impact. Because, in reality, the interaction of the rear steel faceplate with thick hex nuts and tie bars may interrupt deformation of the rear steel faceplate and cause lesser penetration depth and bulging depth in the tests results than in the numerical analyses results.

In the experimental test case number 9 of group 1, there is a possibility that kinematic energy of the projectile would not have fully transferred to the SC wall specimen. The projectile stroke the hex nut and broke it which was fastened to the tie bar. It is assumed that a considerable amount of projectile's kinetic energy would have been dissipated in the process. Thus, the penetration depth of the projectile was less than the value expected to be reached. That is likely the reason why the numerical analysis overestimated the penetration depth considerably compared to the experimental test result.

The rear steel faceplate failure pattern was observed and compared with the analyses results to make sure the numerical modeling approach is correct. Perforating damage mode in group 1 number 7 (Figure 5-10) test case showed a cross shaped rupture of the rear steel faceplate. The numerical analysis of this test case provided the same rupture pattern as the test result, with the rupture starting at the center of the rear steel faceplate and propagating horizontally and vertically. Group 1 number 9 test specimen (Figure 5-7) showed splitting of the rear steel faceplate in the test result. Although the numerical model for this test case resulted in perforating damage mode, the rupture pattern of the rear steel faceplate illustrated similar trend as the test result: rupture started at the hole for the tie bar and propagated horizontally. Therefore, the observation of the rear steel faceplate rupture pattern showed that the analyses results agreed favorably with the tests results and proved that this numerical modeling approach was appropriate for the experimental tests.

### 5.5 *Conclusions*

Numerical models were developed using three dimensional finite element method in LS-DYNA software. In the model, steel faceplates and projectile were modeled with solid elements combined with piecewise linear plasticity material model. Concrete core was modeled using solid elements combined with Winfrith concrete model. Tie bars and steel-headed shear stud anchors were modeled with beam elements combined with piecewise linear plasticity material model. Zero length discrete beam elements were used to implement load-slip behavior of the shear studs caused by the composite action between concrete core and steel faceplate. Spacer plates were modeled with solid elements combined with rigid material model. Various contact and constraint algorithms were applied to implement relationship among each component of SC wall specimen and projectile.

Benchmarking analyses of the numerical model to the experimental test results were performed. Each numerical analysis result was investigated comparing penetration depth, bulging

depth and damage mode. Penetration depth was estimated reasonably with an averaged error of 6%. Bulging depth was estimated reasonably with an averaged error of 9%. Damage mode was predicted favorably except three out of sixteen test cases. Also, the rear steel faceplate rupture pattern of the numerical model was investigated and compared to the experimental test result. For each damage mode of bulging, splitting and perforating, numerical analysis provided a reasonable agreement on deformation or rupture pattern of the rear steel faceplate. Internal failure mechanism presented in the numerical models verified that front steel faceplate rupture, tunneling zone formation, concrete frustum formation, concrete crushing in the frustum, and rear steel faceplate rupture occurred successively, which conformed to the experimental test results.

Therefore, the numerical modeling approach herein can be determined to be acceptable to carry on the missile impact test simulation on the SC wall specimens for this research project.

Table 5-1 Material input parameters for steel faceplates (MAT\_24)

<i>Parameter</i>	<i>Value</i>
Mass density (RO, $lb \cdot sec^2 / in$ )	$7.330 \times 10^{-4}$
Young's modulus (E, $psi$ )	See Table 3-3
Poisson's ratio (PR)	0.3
Yield stress (SIGY, $psi$ )	See Table 3-3
Plastic strain at failure (FAIL)	0.15
Load curve for true stress - plastic strain (LCSS)	See Table 3-3
Load curve for strain rate effect (LCSR)	See Figure 5-2

Table 5-2 Material input parameters for tie bars (MAT\_24)

<i>Parameter</i>	<i>Value</i>
Mass density (RO, $lb \cdot sec^2 / in$ )	$7.330 \times 10^{-4}$
Young's modulus (E, $psi$ )	See Table 3-3
Poisson's ratio (PR)	0.3
Yield stress (SIGY, $psi$ )	See Table 3-3
Plastic strain at failure (FAIL)	0.05
Load curve for true stress - plastic strain (LCSS)	See Table 3-3

Table 5-3 Material input parameters for steel-headed shear stud anchors (MAT\_24)

<i>Parameter</i>	<i>Value</i>
Mass density (RO, $lbf \cdot sec^2 / in$ )	$7.330 \times 10^{-4}$
Young's modulus (E, $psi$ )	$29 \times 10^6$
Poisson's ratio (PR)	0.3
Yield stress (SIGY, $psi$ )	See Table 3-2
Plastic strain at failure (FAIL)	-
Load curve for true stress - plastic strain (LCSS)	By reference to typical Grade 60 steel

Table 5-4 Material input parameters for connector elements (MAT\_74)

<i>Parameter</i>	<i>Value</i>
Mass density (RO, $lbf \cdot sec^2 / in$ )	$7.330 \times 10^{-4}$
Tensile displacement at failure (TDF)	See Equation 5-1
Load curve for nonlinear behavior (FLCID)	See Equation 5-2 and 5-3

Table 5-5 Material input parameters for concrete core (MAT\_24)

<i>Parameter</i>	<i>Value</i>
Mass density (RO, $lb \cdot sec^2 / in$ )	$2.172 \times 10^{-4}$
Elastic modulus (TM, $psi$ )	$57000\sqrt{f'_c}$
Poisson's ratio (PR)	0.15
Uniaxial compressive strength (UCS, $psi$ )	$1.25f'_c$
Uniaxial tensile strength (UTS, $psi$ )	$3\sqrt{f'_c}$
Fracture energy (FE, $lb \cdot in / in^2$ )	See Equation 5-4
Aggregate size (ASIZE, $in$ )	$0.5(a_{max})$
Strain rate effect (RATE)	0
Unit conversion factor (CONM)	-1

Table 5-6 Material input parameters for erosion of concrete core (MAT\_ADD\_EROSION)

<i>Parameter</i>	<i>Value</i>
Number of failure conditions (NCS)	1
Maximum principal strain at failure (MXEPS)	See Equation 5-5 and 5-6

Table 5-7 Material input parameters for projectile (MAT\_24)

<i>Parameter</i>	<i>Value</i>
Mass density (RO, $lbf \cdot sec^2/in$ )	$7.330 \times 10^{-4}$
Young's modulus (E, $psi$ )	$29 \times 10^6$
Poisson's ratio (PR)	0.3
Yield stress (SIGY, $psi$ )	$194 \times 10^3$
Plastic strain to failure (FAIL)	-
Load curve for true stress - plastic strain (LCSS)	Accordingly

Table 5-8 Material input parameters for spacer plates (MAT\_20)

<i>Parameter</i>	<i>Value</i>
Mass density (RO, $lbf \cdot sec^2/in$ )	$7.330 \times 10^{-4}$
Young's modulus (E, $psi$ )	$29 \times 10^6$
Poisson's ratio (PR)	0.3
Center of mass constraint (CMO)	1
Translational constraints (CON1)	7
Rotational constraints (CON2)	7

Table 5-9 Comparison of results between experimental test and numerical analysis

Test Gr.	Test No.	Test Case Identifier	Experimental Results						Numerical Analyses Results					
			$V_{imp}$ (ft/s)	$V_{imp}/V_{des}$	Test Result*	Damage Mode**	Pene. Depth $x_{c\_test}$ (in)	Bulging Depth $x_{bg\_test}$ (in)	FEA Result*	Damage Mode**	Penetration Depth		Bulging Depth	
										$x_{c\_FEM}$ (in)	$x_{c\_FEM}/x_{c\_test}$	$x_{bg\_FEM}$ (in)	$x_{bg\_FEM}/x_{bg\_test}$	
	1	3-0.37-50-1.0-1.3-554	593	0.964	Stop	B	2.06	0.25	Stop	B	2.25	1.09	0.31	1.25
	2	3-0.37-50-1.0-1.3-677	674	1.096	Stop	B	3.06	0.63	Stop	B	1.77	0.58	0.41	0.66
	3	3-0.37-50-1.0-2.0-430	424	0.885	Stop	B	1.56	0.25	Stop	B	1.99	1.27	0.21	0.85
	4	3-0.37-50-1.0-2.0-525	513	1.071	Stop	B	3.16	0.58	Stop	B	3.18	1.01	0.44	0.76
Gr. 1	5	3-0.53-50-1.5-1.3-660	667	0.915	Stop	B	1.38	0.56	Stop	B	1.19	0.87	0.49	0.87
	6	3-0.53-50-1.5-1.3-750	760	1.043	Stop	B	2.00	0.72	Stop	B	2.08	1.04	0.53	0.74
	7	3-0.53-50-1.0-2.0-513	640	1.336	Perf.	P	-	-	Perf.	P	-	-	-	-
	8	3-0.53-50-1.0-2.0-626	710	1.482	Perf.	P	-	-	Perf.	P	-	-	-	-
	9	3-1.23-50-1.5-3.5-380	550	1.303	Stop	S	4.00	1.63	Perf.	P	-	-	-	-
	10	3-1.23-50-1.5-3.5-465	489	1.159	Stop	B	1.91	0.59	Perf.	P	-	-	-	-
	1	5-0.48-50-1.0-2.0-445	467	0.943	Stop	B	2.09	0.28	Stop	B	2.17	1.04	0.41	1.45
Gr. 2	2	5-0.48-50-1.0-2.0-544	549	1.109	Stop	S	3.31	0.75	Perf.	P	-	-	-	-
	3	5-0.48-50-1.5-3.5-408	410	0.905	Stop	B	1.34	0.38	Stop	B	1.64	1.22	0.90	2.40
	4	5-0.48-50-1.5-3.5-498	484	1.068	Stop	B	2.41	0.69	Stop	B	3.43	1.43	0.88	1.28
Gr. 3	1	3-0.37-65-1.0-2.0-443	539	1.096	Stop	B	3.16	0.69	Stop	B	3.23	1.02	0.45	0.66
	2	3-0.37-65-1.0-2.0-541	634	1.289	Perf.	P	-	-	Perf.	P	-	-	-	-

\* Stop: The specimen stopped the projectile  
 Perf.: The specimen was perforated by the projectile  
 \*\* B: Bulging, S: Splitting, P: Perforating

Table 5-10 Statistical evaluation of FE models' performance: test cases in group 1

	<b>Penetration</b>	<b>Bulging</b>
	$x_{c\_FEM}/x_{c\_test}$	$x_{bg\_FEM}/x_{bg\_test}$
$\mu$	0.98	0.86
$\sigma$	0.22	0.19
<i>COV</i>	0.22	0.22

Table 5-11 Statistical evaluation of FE models' performance: test cases in group 2

	<b>Penetration</b>	<b>Bulging</b>
	$x_{c\_FEM}/x_{c\_test}$	$x_{bg\_FEM}/x_{bg\_test}$
$\mu$	1.23	1.71
$\sigma$	0.16	0.49
<i>COV</i>	0.13	0.29

Table 5-12 Statistical evaluation of FE models' performance: entire test cases

	<b>Penetration</b>	<b>Bulging</b>
	$x_{c\_FEM}/x_{c\_test}$	$x_{bg\_FEM}/x_{bg\_test}$
$\mu$	1.06	1.09
$\sigma$	0.22	0.51
<i>COV</i>	0.21	0.47

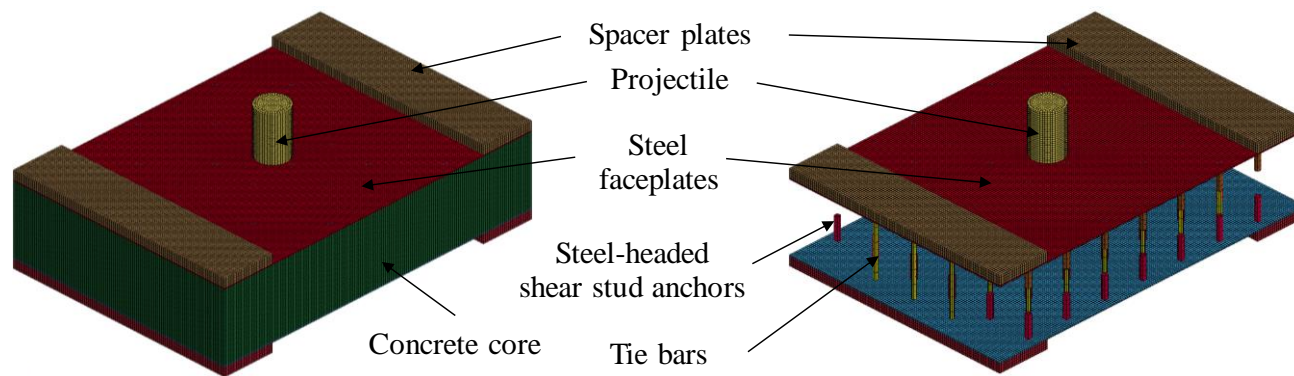


Figure 5-1 Finite element model developed in LS-DYNA

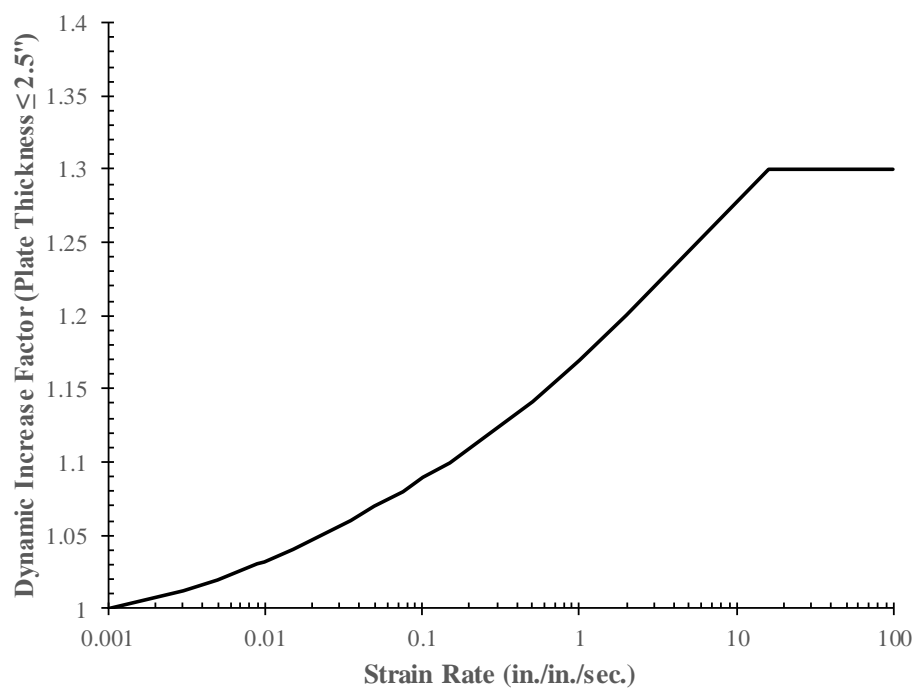


Figure 5-2 Dynamic increase factor for the steel faceplates (U.S. Department of Defense 2008)

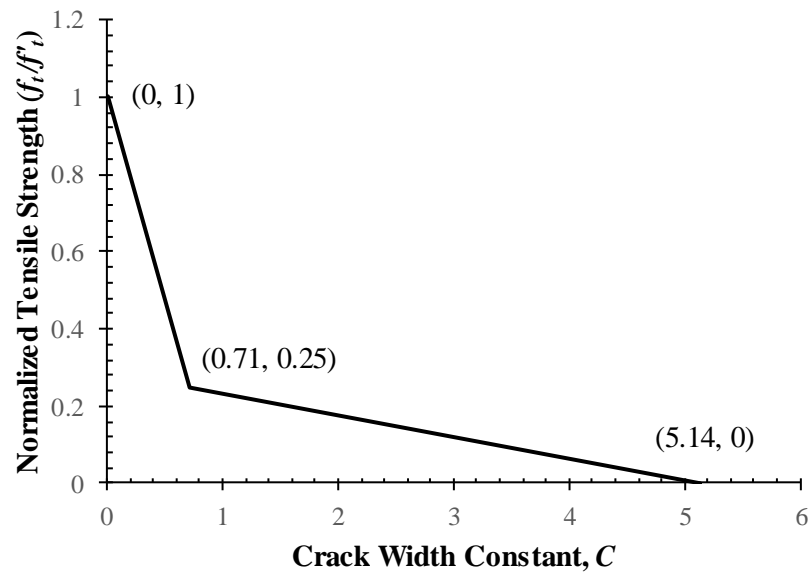


Figure 5-3 The average strain softening response (Broadhouse and Attwood 1993)

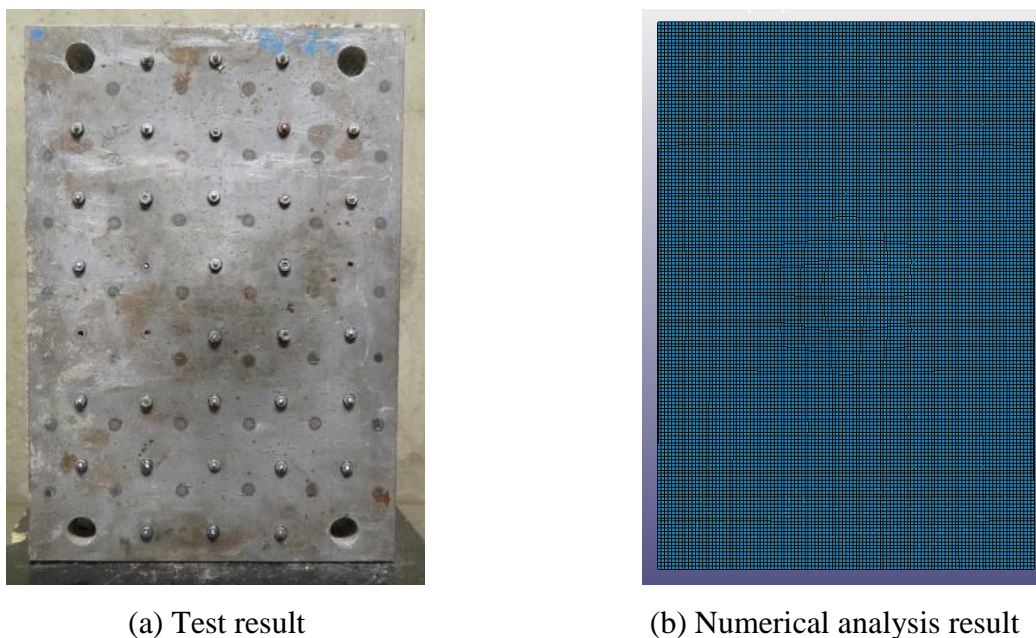


Figure 5-4 Bulging damage mode in experimental test and numerical analysis: Group 1, test number 2

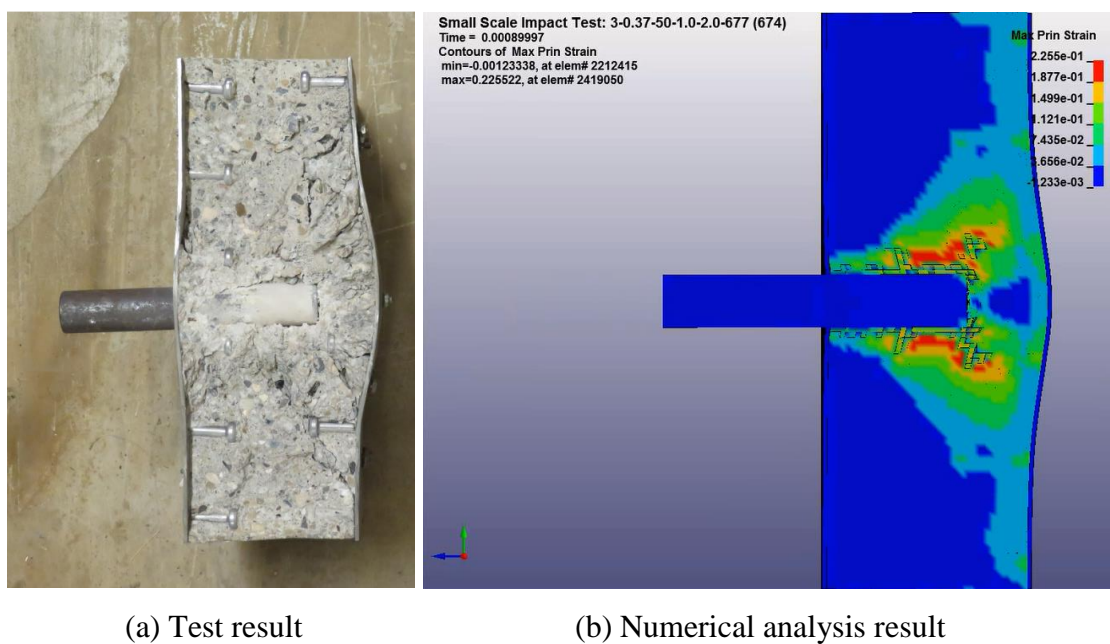


Figure 5-5 Comparison of internal damage behavior between test result and numerical analysis result: Group 1, test number 2

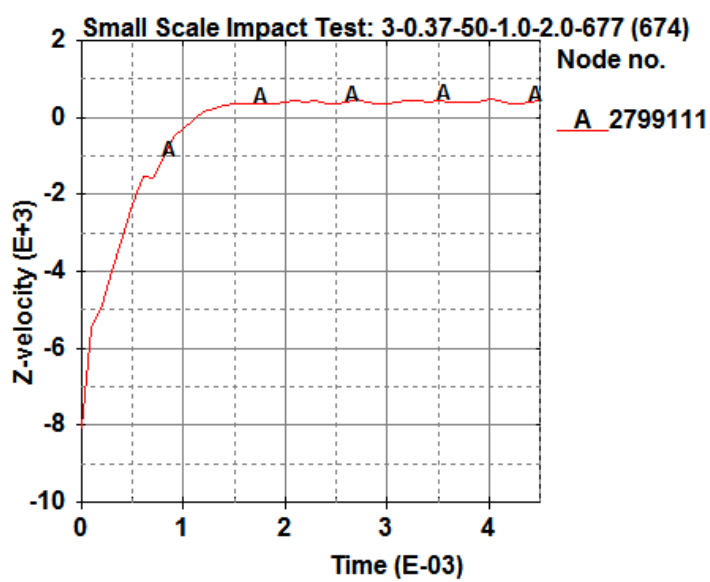
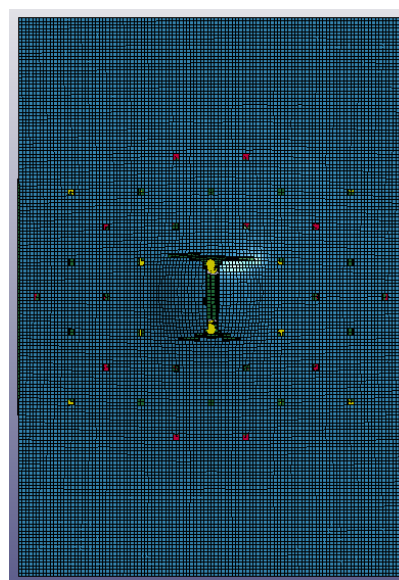


Figure 5-6 Projectile velocity – time history: Group 1, test number 2



(a) Test result

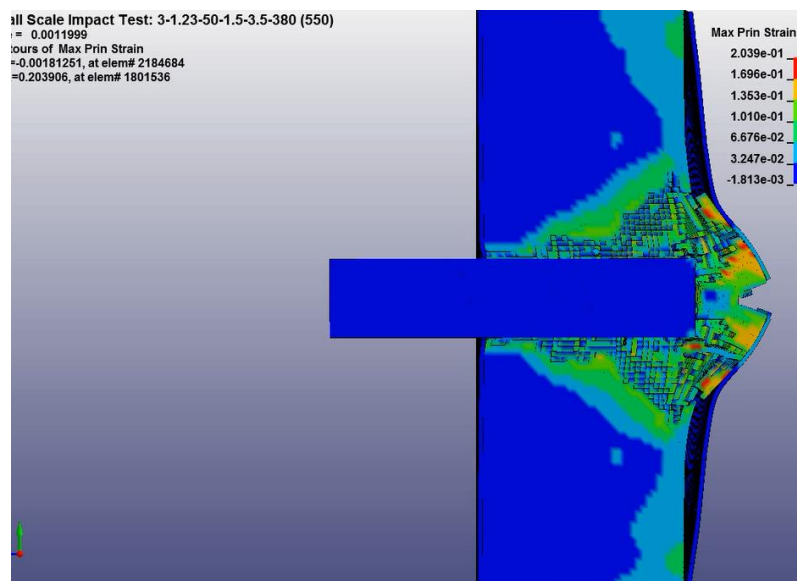


(b) Numerical analysis result

Figure 5-7 Splitting damage mode in experimental test and numerical analysis: Group 1, test number 9



(a) Test result



(b) Numerical analysis result

Figure 5-8 Comparison of internal damage behavior between test result and numerical analysis result: Group 1, test number 9

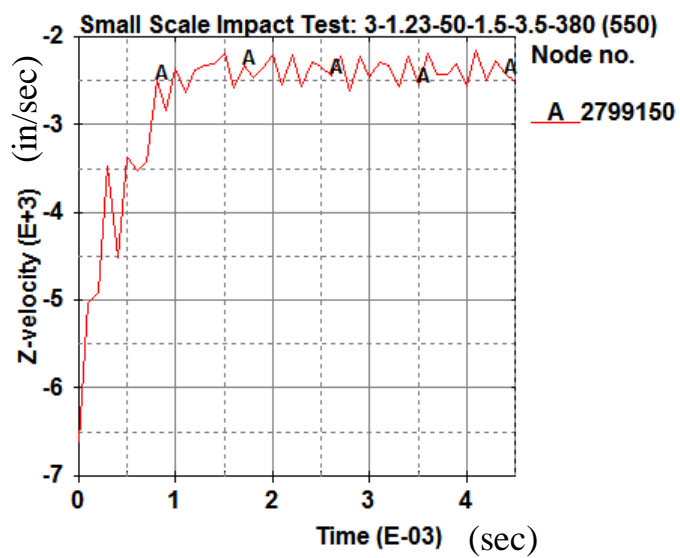
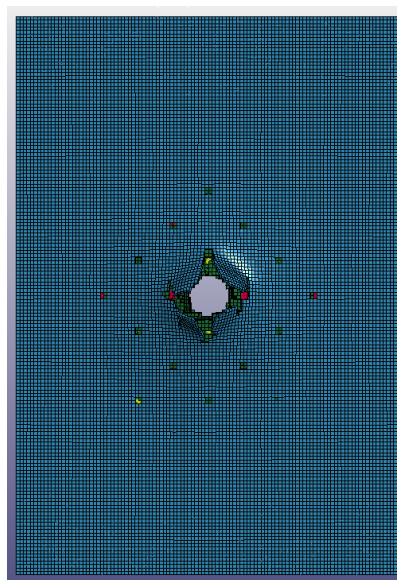


Figure 5-9 Projectile velocity – time history: Group 1, test number 9



(a) Test result

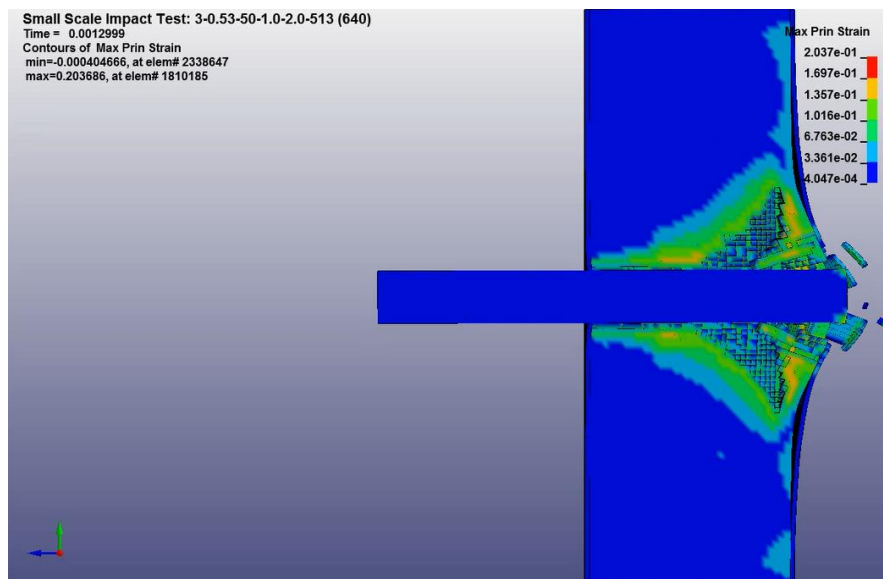


(b) Numerical analysis result

Figure 5-10 Perforation failure in experimental test and numerical analysis: Group 1, test number 7



(a) Test result



(b) Numerical analysis result

Figure 5-11 Comparison of internal damage behavior between test result and numerical analysis result: Group 1, test number 7

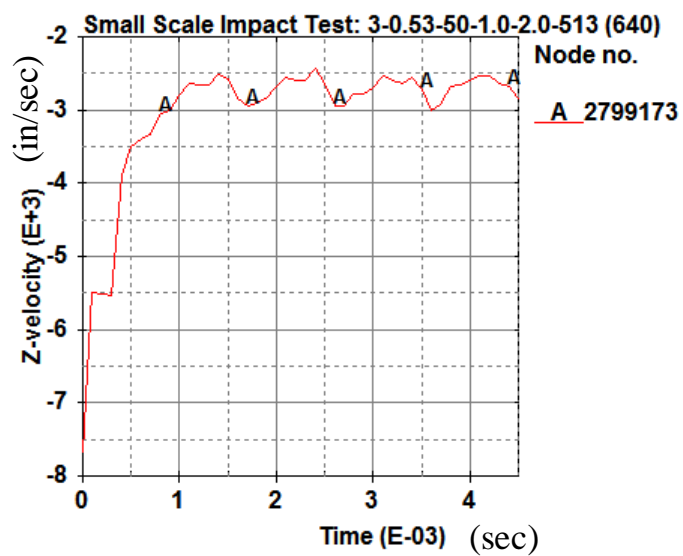
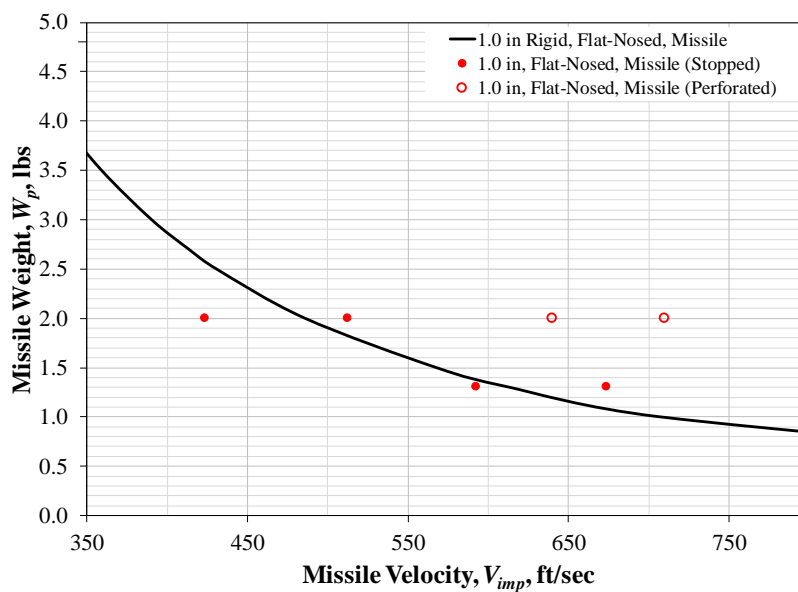
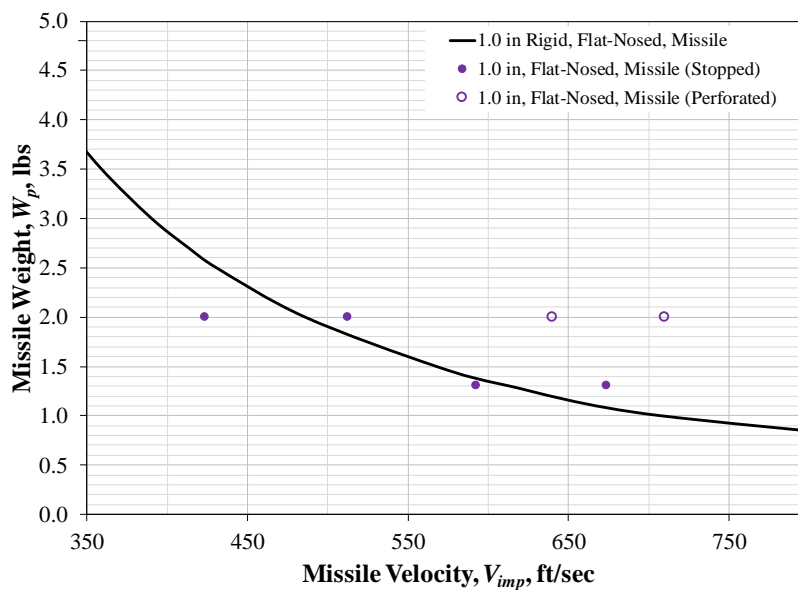


Figure 5-12 Projectile velocity – time history: Group 1, test number 7

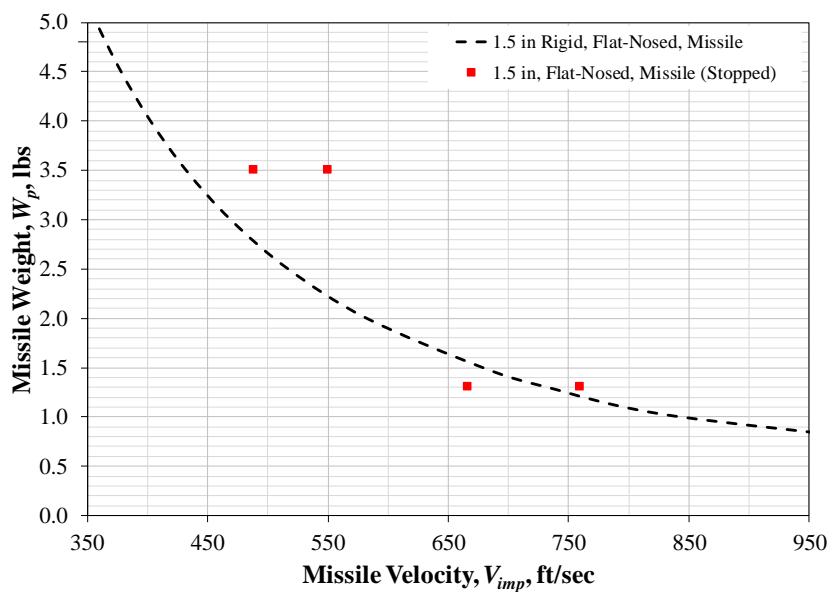


(a) Experimental tests results

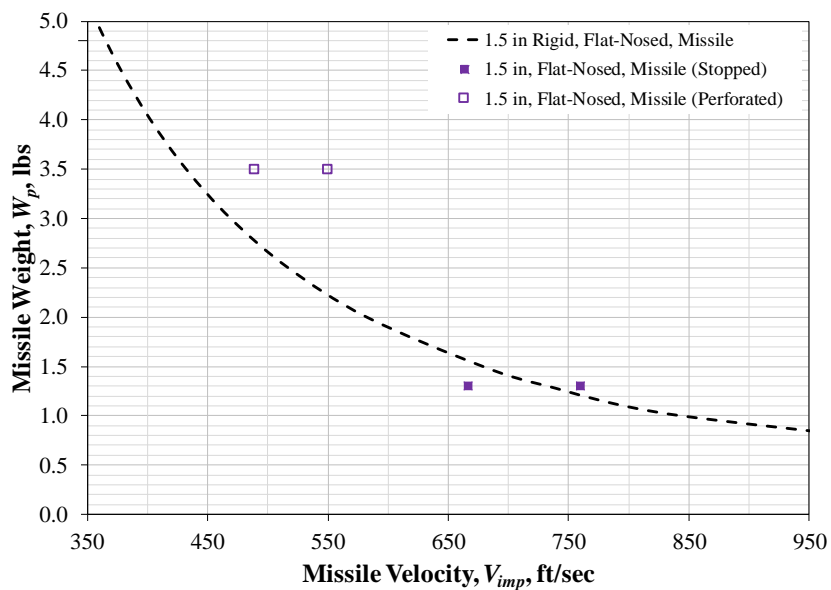


(b) Benchmarking analyses results

Figure 5-13 Comparison of experimental tests results and benchmarking analyses results when the 1.0 in. diameter projectiles were used in group 1

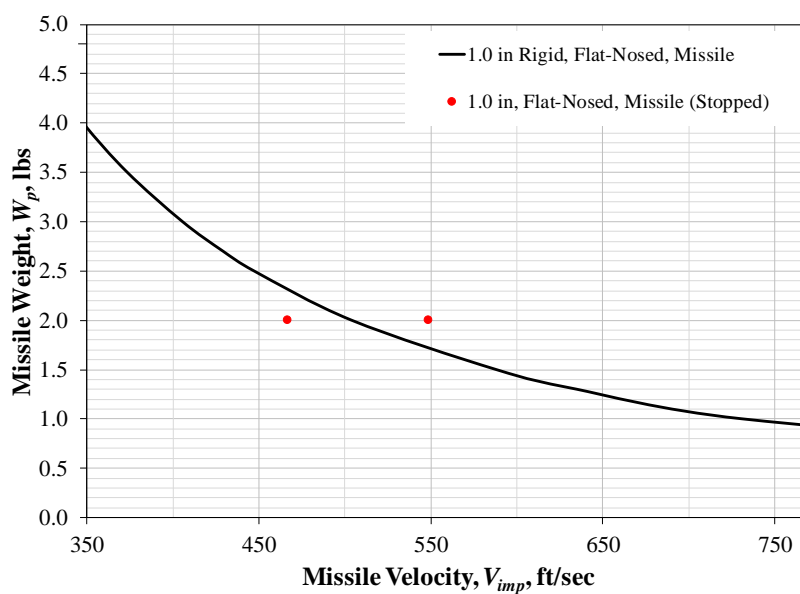


(a) Experimental tests results

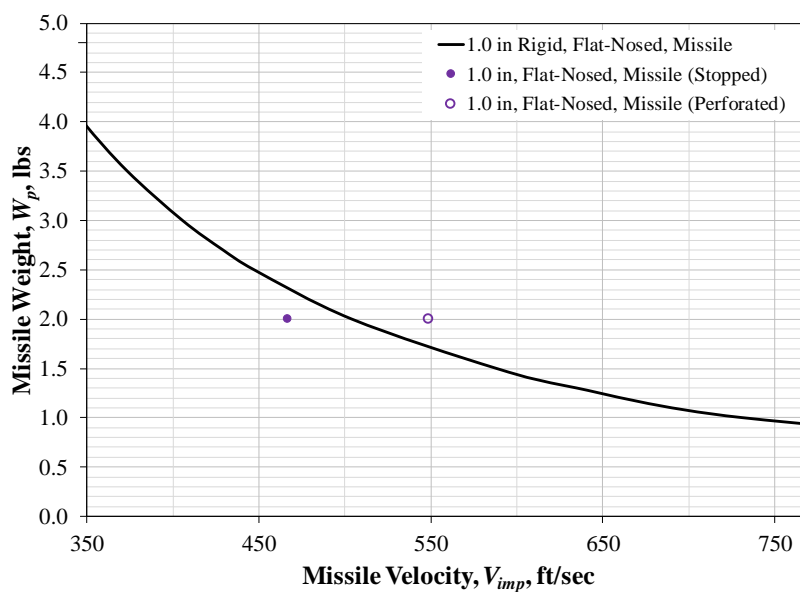


(b) Benchmarking analyses results

Figure 5-14 Comparison of experimental tests results and benchmarking analyses results when the 1.5 in. diameter projectiles were used in group 1

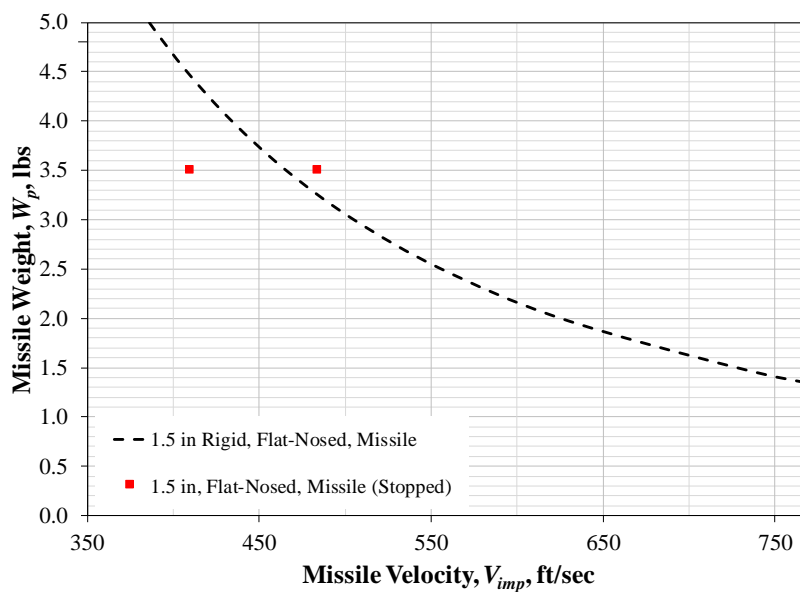


(a) Experimental tests results

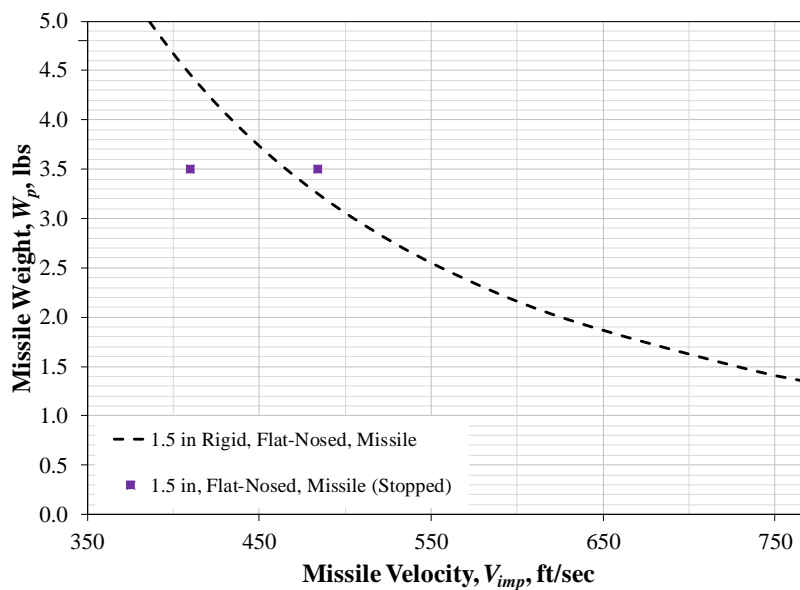


(b) Benchmarking analyses results

Figure 5-15 Comparison of experimental tests results and benchmarking analyses results when the 1.0 in. diameter projectiles were used in group 2

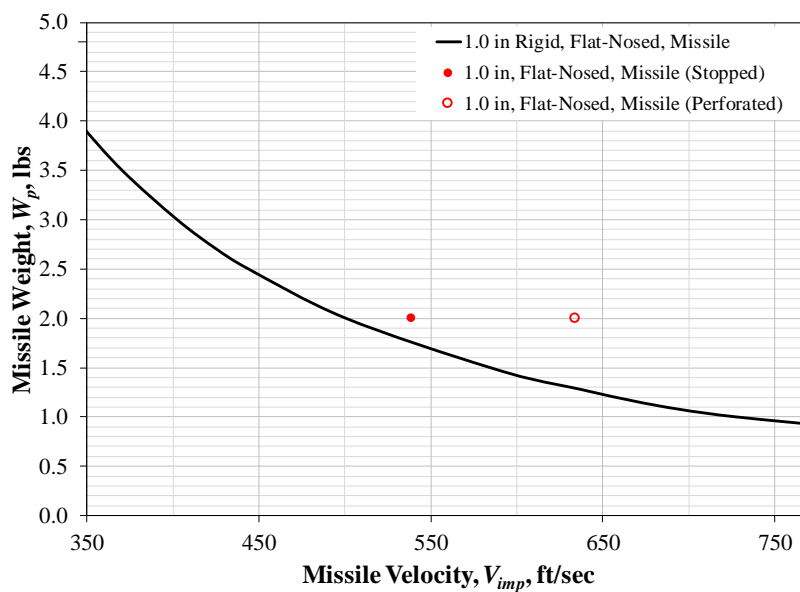


(a) Experimental tests results

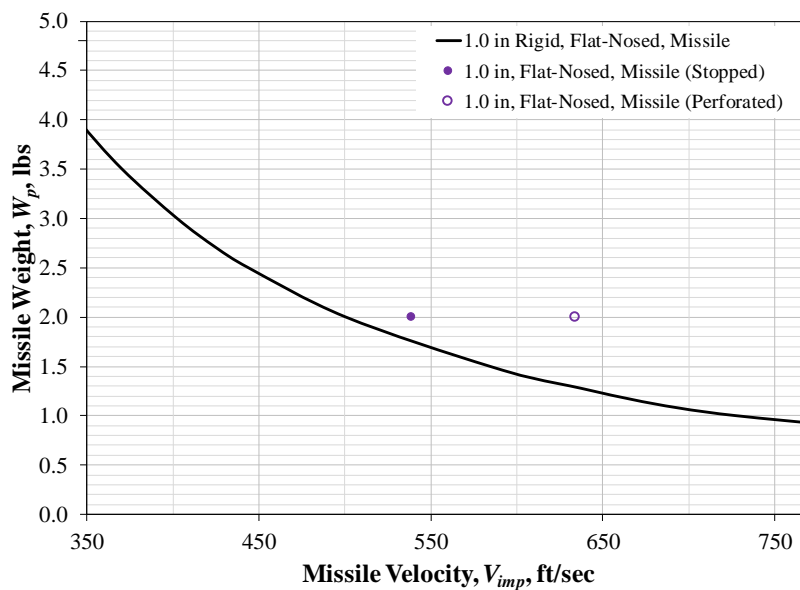


(b) Benchmarking analyses results

Figure 5-16 Comparison of experimental tests results and benchmarking analyses results when the 1.5 in. diameter projectiles were used in group 2



(a) Experimental tests results



(b) Benchmarking analyses results

Figure 5-17 Comparison of experimental tests results and benchmarking analyses results when the 1.0 in. diameter projectiles were used in group 3

## CHAPTER 6. NUMERICAL PARAMETRIC STUDIES

### 6.1 Introduction

In CHAPTER 4, the velocity ranges in which perforation damage mode occurred were obtained by experimental testing. However, these velocity ranges were limited to two test categories where 1.0 in. diameter projectiles with 2.0 lbs weight were used in the test group 1 and 3. More missile impact test data is needed to figure out the velocity ranges for the rest of the test categories and to further narrow the obtained velocity ranges in order to verify the accuracy of the design method of SC walls against missile impact. To accomplish this, the benchmarked numerical models in CHAPTER 5 were used to conduct a set of numerical parametric study simulations of the experimental missile impact tests with varied missile parameters. The numerical analyses results were combined with the previous benchmarking analyses results and used to specify the velocity ranges in which the perforation velocities were located.

Benchmarked numerical models were also used to evaluate the influence of design parameters on local damage behavior of SC walls. Another set of numerical parametric study simulations were conducted varying critical design parameters of SC walls. Then, their effect on the penetration depth of the projectile into the concrete core of the SC wall specimens was investigated.

### 6.2 Parametric Study to Specify Perforation Velocities

#### 6.2.1 Parametric study matrix

The SC wall specimen design for numerical simulations was the same as the experimental test specimen design. The global dimensions were 16 in.  $\times$  11 in.  $\times$  4 in. Flexural reinforcement ratio,  $\rho$ , varied from 3.7% to 5.2%. Shear reinforcement ratio,  $\rho_t$ , ranged from 0.37% to 1.23%.

Steel faceplate strength varied from Grade 50 to Grade 65. Also, the same diameters ( $D_p$ ) of projectile as the experimental tests, 1.0 in. and 1.5 in., were applied to the numerical simulations. Projectile weight ( $W_p$ ) ranged from 1.3 lbs to 3.5 lbs. A weight of 2.7 lbs was a new addition to the numerical simulations.

The numerical parametric study plan was developed according to the following strategies. First, a series of numerical analyses were planned in order to narrow the velocity ranges obtained from the current experimental tests data. Even though the velocity ranges were determined previously, the interval of the velocity ranges was relatively large so further experimental tests were necessary to reduce the interval between the data points. However, no more experimental tests could be conducted due to limited resources, i.e., research project budget, time and man power. Thus, numerical simulations were chosen as an alternative to generate further data points so that the velocity ranges, in which the perforation velocities were located, could be narrowed. Second, another series of numerical analyses were planned to provide additional data points which were out of the experimental test cases. Additional numerical simulations were conducted with new projectile parameters. These numerical simulation results will be applied to verify the accuracy of the modified design method proposed and developed in the next chapter.

A total of 40 numerical simulations were conducted as the numerical parametric study. The details of the parametric study analysis matrix are illustrated in Table 6-1. The parametric study includes three analysis groups separated by two design parameters: the flexural reinforcement ratio and the steel faceplate strength. The analysis group 1, consisted of 26 analysis cases, had the flexural reinforcement ratio of 3.7% and the steel faceplate strength of Grade 50. Analysis number 1 to 9, 15 to 18, and 25 to 26 in group 1 were prepared to narrow velocity ranges in which the perforation velocities would be located. Impact velocities of the projectile of these analysis cases

were adjusted to fit between the two data points where the projectile perforated the SC wall specimen or the projectile was stopped by the SC wall specimen. The other analysis cases were prepared to generate supplemental data points for verifying the modified design method to be proposed later. When 1.0 in. diameter projectiles were applied in these analysis cases, projectile weights of 2.7 lbs and 3.5 lbs, which were not considered in the experimental tests, were additionally considered. When 1.5 in. diameter projectiles were applied in these analysis cases, projectile weight of 2.0 lbs, which was not considered in the experimental tests, was additionally considered.

The analysis group 2, consisted of 9 analysis cases, had the flexural reinforcement ratio of 5.2 % and the same steel faceplate strength as group 1. Analysis number 1, 6 and 7 in group 2 were prepared to narrow the velocity range in which the perforation velocity would be located. Impact velocities of the projectiles of these analysis cases were adjusted to fit between the two data points where the projectile perforated the SC wall specimen or the projectile was stopped by the SC wall specimen. The other analysis cases were prepared to generate supplemental data points for verifying the modified design method to be proposed later. When 1.0 in. diameter projectiles were applied in these analysis cases, projectile weight of 2.7 lbs, which was not considered in the experimental tests, was additionally considered. When 1.5 in. diameter projectiles were applied in these analysis cases, projectile weight of 2.0 lbs, which was not considered in the experimental tests, was additionally considered for this purpose.

Analysis group 3, consisted of 5 analysis cases, had the same flexural reinforcement ratio as group 1 and the steel faceplate strength of Grade 65. Analysis number 1 to 3 in group 3 were prepared to narrow the velocity range in which the perforation velocity would be located. Impact velocities of the projectile of these analysis cases were adjusted to fit between the two data points

where the projectile perforated the SC wall specimen or the projectile was stopped by the SC wall specimen. The other analysis cases were prepared to generate supplemental data points for verifying the modified design method to be proposed later. When 1.0 in. diameter projectiles were applied in these analysis cases, projectile weight of 2.7 lbs, which was not considered in the experimental tests, was additionally considered.

### 6.2.2 Parametric study results

For each numerical analysis case, it was observed if the SC wall specimen was perforated or not. The result of this observation was presented as *FEA result* and described as ‘Stop (Stopped)’ or ‘Perf. (Perforated)’. Damage behavior of the SC wall specimen was examined and reported as *Damage mode*, which was classified as ‘B (Bulging)’, ‘S (Splitting)’, and ‘P (Perforating)’. Penetration depth of the projectile into the concrete core of the SC wall specimen was examined and summarized as  $x_{c\_FEM}$ . Bulging depth of the rear steel faceplate of the SC wall specimen was examined and recorded as  $x_{bg\_FEM}$ . Details of the results of the numerical parametric study analyses are summarized in Table 6-2.

When the projectiles of 1.0 in. diameter with 1.3 lbs weight were used in group 1 analysis cases, the perforation velocity was found to be located in the velocity range between 21.5% and 25.6% greater than the design velocity ( $V_{des}$ ). No velocity range of the perforation velocity had been obtained previously from the experimental tests results or the benchmarking analyses results, because the perforation damage mode did not occur in both the experimental tests and the benchmarking analyses. When the projectiles of 1.0 in. diameter with 2.0 lbs weight were used, the perforation velocity was found to be located in the velocity range between 11.3% and 15.1% greater than the design velocity, which was narrowed from the velocity range between 5.8% and 32.0% greater than the design velocity obtained from the experimental tests. When the projectile

of 1.0 in. diameter with 2.7 lbs weight was used, the perforation velocity was found to be located in the velocity range between 15.0% and 19.9% greater than the design velocity. When the projectiles of 1.0 in. diameter with 3.5 lbs weight were used, the perforation velocity was found to be located in the velocity range between 15.0% and 19.8% greater than the design velocity. No experimental tests were conducted to obtain velocity ranges of the perforation velocities for these two projectile weights (2.7 lbs and 3.5 lbs).

When the projectiles of 1.5 in. diameter with 1.3 lbs weight were used in group 1 analysis cases, the perforation velocity was found to be located in the velocity range between 24.6% and 29.8% greater than the design velocity. No velocity range of the perforation velocity was obtained previously from the experimental tests results or the benchmarking analyses results, because the perforation damage mode did not occur in both the experimental tests and the benchmarking analyses. When the projectiles of 1.5 in. diameter with 2.0 lbs weight were used, the perforation velocity was found to be located in the velocity range between 18.6% and 22.0% greater than the design velocity. No experimental tests were conducted to obtain velocity range of the perforation velocity for this projectile weight. When the projectiles of 1.5 in. diameter with 3.5 lbs weight were used, the perforation velocity was found to be located in the velocity range between 7.6% and 10.4% greater than the design velocity. No velocity range of the perforation velocity was obtained previously from the experimental tests results or the benchmarking analyses results.

When the projectiles of 1.0 in. diameter with 2.0 lbs weight were used in group 2 analysis cases, the perforation velocity was found to be located in the velocity range between 4.8% and 8.9% greater than the design velocity, which was narrowed from the velocity range between 7.3% lower than the design velocity and 8.9% greater than the design velocity obtained from the experimental tests results and the benchmarking analyses results. When the projectiles of 1.0 in.

diameter with 2.7 lbs weight were used, the perforation velocity was found to be located in the velocity range between 10.7% and 15.4% greater than the design velocity. No experimental tests were conducted to obtain velocity range of the perforation velocity for this projectile weight.

When the projectiles of 1.5 in. diameter with 2.0 lbs weight were used in group 2 analysis cases, the perforation velocity was found to be located in the velocity range between 10.4% and 13.6% greater than the design velocity. No experimental tests were conducted to obtain velocity range of the perforation velocity for this projectile weight. When the projectiles of 1.5 in. diameter with 3.5 lbs weight were used, the perforation velocity was found to be located in the velocity range between 8.8% and 13.5% greater than the design velocity. No velocity range of the perforation velocity was obtained previously from the experimental tests results or the benchmarking analyses results, because the perforation damage mode did not occur in both the experimental tests and the benchmarking analyses.

When the projectiles of 1.0 in. diameter with 2.0 lbs weight were used in group 3 analysis cases, the perforation velocity was found to be located in the velocity range between 11.6% and 13.6% greater than the design velocity, which was narrowed from the velocity range between 7.8% and 26.8% greater than the design velocity obtained from the experimental tests. When the projectiles of 1.0 in. diameter with 2.7 lbs weight were used, the perforation velocity was found to be located in the velocity range between 11.8% and 16.5% greater than the design velocity. No experimental tests were conducted to obtain velocity range of the perforation velocity for this projectile weight.

Summary of the velocity ranges for the perforation velocity obtained from the experimental tests and the numerical parametric study is presented in Table 6-3 and Table 6-4, respectively.

All the numerical analyses results of the parametric study, including the benchmarking analyses, are illustrated graphically in Figure 6-1 through Figure 6-3, in terms of impacting velocity versus the weight of the projectile. For each group, numerical analyses results were marked as solid or hollow circles or squares in three colors: purple, red, and blue. Data points, resultant from the benchmarking numerical analyses in CHAPTER 5, were marked in a purple color. Data points, resultant from the numerical parametric study analyses to narrow the velocity ranges in which the perforation velocities were located or to generate extended data of the experimental tests results, were marked in a green color. Data points, resultant from the numerical parametric study analyses in which additional projectile weights from the experimental tests data were applied to generate supplemental results for later use, were marked in a blue color. Analysis cases ending with the result of ‘Perf.’ were expressed as hollow circles for 1.0 in. diameter projectiles or as hollow squares for 1.5 in. diameter projectiles. Analysis cases ending with the result of ‘Stop’ were expressed as solid circles for 1.0 in. diameter projectiles or as solid squares for 1.5 in. diameter projectiles.

In summary, these results of the parametric study provided more specific information on the anticipated perforation velocities for each test group than the experimental test results did. These will eventually be used to evaluate and verify the performance of the modified design method of SC walls subjected to missile impact, which is proposed in CHAPTER 7. In addition, data points plotted in Figure 6-1 through Figure 6-3 confirm that the numerical simulations provided results that were in reasonable agreement with the current experimental tests data.

### 6.3 Parametric Study to Evaluate the Influence of Parameters

#### 6.3.1 Parametric study matrix

For this numerical parametric study, SC wall specimens of the same scale as the experimental test specimens were used in the numerical analyses. The global dimension of the SC wall specimens was 16 in.  $\times$  11 in.  $\times$  4 in. The flexural reinforcement ratio ( $\rho$ ), the shear reinforcement ratio ( $\rho_t$ ), and the steel faceplate strength were considered as parameters of interest. The parametric study had a total of 12 analysis cases which were separated into three analysis groups according to their parameters of interest. With the exception of analysis number 8, 9, and 10, these analysis cases were shared with the previous numerical parametric study or the benchmarking analysis cases (Table 6-2) which were conducted to discern specified perforation velocity ranges. The details of the numerical parametric study matrix are illustrated in Table 6-5.

Analysis group 1, consisted of 6 analysis cases, was designed to evaluate the influence of the shear reinforcement ratio on the analysis results; especially the penetration depth of the projectile into the concrete core of the SC wall specimen. In these cases, the design parameters of the SC wall specimens such as the flexural reinforcement ratio and the steel faceplate strength remained constant at 3.7% and Grade 50, respectively. The shear reinforcement ratio varied from 0.37% to 0.53%. The projectile parameters, the diameter ( $D_p$ ) and the weight ( $W_p$ ), remained constant at 1.0 in. and 2.0 lbs, respectively. The impact velocity ( $V_{imp}$ ) ranged from 528 ft/s to 558 ft/s. Three out of six analysis cases, which were analysis number 1, 5 and 6, were also used as control cases to evaluate the influence of the flexural reinforcement ratio and the steel faceplate strength.

Analysis group 2, consisted of 3 analysis cases, was designed to evaluate the influence of the flexural reinforcement ratio on the analysis results; especially the penetration depth of the projectile into the concrete core of the SC wall specimen. In these cases, the design parameters of

the SC wall specimens such as the flexural reinforcement ratio, the shear reinforcement ratio, and the steel faceplate strength remained constant at 5.2%, 0.48% and Grade 50, respectively. The projectile parameters, the diameter and the weight, remained constant at 1.0 in. and 2.0 lbs, respectively. The impact velocity ranged from 528 ft/s to 558 ft/s.

Analysis group 3, consisted of 3 analysis cases, was designed to evaluate the influence of the steel faceplate strength on the analysis results; especially the penetration depth of the projectile into the concrete core of the SC wall specimen. In these cases, the design parameters of the SC wall specimens such as the flexural reinforcement ratio, the shear reinforcement ratio, and the steel faceplate strength remained constant at 3.7%, 0.37% and Grade 65, respectively. The projectile parameters, the diameter and the weight, remained constant at 1.0 in. and 2.0 lbs, respectively. The impact velocity ranged from 528 ft/s to 558 ft/s.

### 6.3.2 Parametric study results

For each analysis case, perforation check, damage behavior of the SC wall specimen, and the penetration depth of the projectile was investigated. The perforation check of the SC wall specimen was itemized as *FEA Result* and reported as ‘Stop’ for cases when the projectile was stopped by the SC wall specimen and ‘Perf.’ for cases when the SC wall specimen was perforated by the projectile. The damage behavior of the SC wall specimen was itemized as *Damage Mode* and reported as ‘B’ for bulging damage mode, ‘S’ for splitting damage mode, and ‘P’ for perforating damage mode. The penetration depth of the projectile into the concrete core of the SC wall specimen was examined and reported as  $x_{c\_FEM}$ . Details of the numerical parametric study analyses results are summarized in Table 6-6.

In analysis group 1, analysis number 1, 2, and 3 were compared with analysis number 4, 5, and 6, respectively, to evaluate the influence of the shear reinforcement ratio on the analysis

results. All the analysis cases in group 1 had identical SC wall design parameters and projectile parameters, with the exception of the shear reinforcement ratio and the projectile impact velocity. They had the flexural reinforcement ratio of 3.7%, and the steel faceplate strength of Grade 50. The diameter and the weight of the projectiles were 1.0 in. and 2.0 lbs. Analysis number 1, 2, and 3 had the shear reinforcement ratio of 0.37%. Analysis number 4, 5, and 6 had a varied shear reinforcement ratio of 0.53%. In analysis number 1 and 4, the projectile impact velocities were the same at 528 ft/s. Both analysis cases provided similar aspects of results. The projectiles were stopped by the SC wall specimens. The rear steel faceplate of each SC wall specimen displayed bulging deformation. The penetration depth of the projectile in each analysis case was reported as 3.22 in. and 3.46 in.; a negligible difference of 6.9%. In analysis number 2 and 5, the projectile impact velocities were the same at 540 ft/s. As in the previous pair, both analysis cases provided similar aspects of results. The projectiles were stopped by the SC wall specimens. The rear steel faceplate of each SC wall specimen displayed splitting damage mode. The penetration depth of the projectile in each analysis case was reported as 3.94 in. and 3.99 in.; a negligible difference of 1.3%. In analysis number 3 and 6, the projectile impact velocities were the same at 558 ft/s. As in the previous pairs, both analysis cases provided similar aspects of results. The projectiles perforated the SC wall specimens.

In analysis group 2, analysis number 1, 2, and 3 were compared with analysis number 4, 5, and 6 of the analysis group 1, respectively, to evaluate the influence of the flexural reinforcement ratio on the analysis results. All the analysis cases in group 2 had identical SC wall design parameters and projectile parameters, with the exception of projectile impact velocity. They had the flexural reinforcement ratio of 5.2%, the shear reinforcement ratio of 0.48%, and the steel faceplate strength of Grade 50. The diameter and the weight of the projectiles were 1.0 in. and 2.0

lbs. Analysis number 4, 5, and 6 of the analysis group 1 had a varied flexural reinforcement ratio of 3.7%. The shear reinforcement ratio of analysis number 4, 5, and 6 in analysis group 1 was not exactly the same as that of analysis cases in analysis group 2. However, the difference was minimal and based on the observation of analysis group 1, it was assumed that the shear reinforcement ratio has a negligible influence on the analysis results. In analysis number 1 of group 2 and analysis number 4 of group 1, the projectile impact velocities were the same at 528 ft/s. The projectiles were stopped by the SC wall specimens in both analysis cases. The rear steel faceplate of each SC wall specimen displayed bulging deformation. The penetration depth of the projectile was reported as 3.40 in. and 3.46 in., respectively; a negligible difference of 1.8%. In analysis number 2 of group 2 and analysis number 5 of group 1, the projectile impact velocities were the same at 540 ft/s. The projectiles were stopped by the SC wall specimens in both analysis cases. The rear steel faceplate of each SC wall specimen displayed splitting damage mode. The penetration depth of the projectile in each analysis case was reported as 3.49 in. and 3.99 in.; a considerable difference of 14.3%. In analysis number 3 of group 2 and analysis number 6 of group 1, the projectile impact velocities were the same at 558 ft/s. The projectiles perforated the SC wall specimens in both analysis cases. The rear steel faceplate of each SC wall specimen displayed the perforating damage mode.

In analysis group 3, analysis number 1, 2, and 3 were compared with analysis number 1, 2, and 3 of the analysis group 1, respectively, to evaluate the influence of the steel faceplate strength on the analysis results. All the analysis cases in group 3 had identical SC wall design parameters and projectile parameters as one another, with the exception of the projectile impact velocity. They had the flexural reinforcement ratio of 3.7%, the shear reinforcement ratio of 0.37%, and the steel faceplate strength of Grade 65. The diameter and the weight of the projectiles were 1.0 in. and 2.0 lbs. Analysis number 1, 2, and 3 of analysis group 1 had a varied steel faceplate strength of Grade

50. In analysis number 1 of group 3 and analysis number 1 of group 1, the projectile impact velocities were the same at 528 ft/s. The projectiles were stopped by the SC wall specimens in both analysis cases. The rear steel faceplate of each SC wall specimen displayed bulging deformation. The penetration depth of the projectile in each analysis case was reported as 3.14 in. and 3.22 in., respectively; a negligible difference of 2.5%. In analysis number 2 of group 3 and analysis number 2 of group 1, the projectile impact velocities were 540 ft/s and 539ft/s, respectively, which were almost identical. The projectiles were stopped by the SC wall specimens in both analysis cases. The rear steel faceplate of each SC wall specimen displayed splitting damage mode. The penetration depth of the projectile in each analysis case was reported as 3.23 in. and 3.94 in.; a considerable difference of 22.0%. In analysis number 3 of group 3 and analysis number 3 of group 1, the projectile impact velocities were the same at 558 ft/s. The projectiles perforated the SC wall specimens in both analysis cases. The rear steel faceplate of each SC wall specimen displayed perforating damage mode.

Details of the numerical parametric study analyses results are summarized in Table 6-6 and illustrated graphically in Figure 6-4 through Figure 6-6. Figure 6-4 shows the influence of the shear reinforcement ratio on the penetration depth of the projectile into the concrete core. Even though the SC wall specimens with varied shear reinforcement ratio from 0.37% to 0.53% are compared, the penetration depth values do not have a considerable difference. As the projectile impact velocity increases from 528 ft/s to 540 ft/s, the penetration depth increases but it's increase rate is minimal; 0.060 in/ft/s for the SC wall specimens with the shear reinforcement ratio of 0.37%, and 0.044 in/ft/s for the SC wall specimens with the shear reinforcement ratio of 0.53%. Thus, it can be concluded the influence of the shear reinforcement ratio is not significant. Figure 6-5 shows the influence of the flexural reinforcement ratio on the penetration depth of the projectile

into the concrete core. For the SC wall specimens with the flexural reinforcement ratio of 3.7%, as the impact velocity of the projectile increases from 528 ft/s to 540 ft/s, the penetration depth increases at a rate of 0.044 in/ft/s. For the SC wall specimens with the flexural reinforcement ratio of 5.3%, as the impact velocity of the projectile increases from 528 ft/s to 540 ft/s, the penetration depth increases at a rate of 0.008 in/ft/s. The increase rate of the penetration depth of the SC wall specimens with the lower flexural reinforcement ratio is about five times greater than that of the SC wall specimens with the higher flexural reinforcement ratio. Thus, it can be concluded that the influence of the flexural reinforcement ratio is considerable. Figure 6-6 shows the influence of the steel faceplate strength on the penetration depth of the projectile into the concrete core. For SC wall specimens with Grade 50 steel faceplates, as the impact velocity of the projectile increases from 528 ft/s to 540 ft/s, the penetration depth increases at a rate of 0.060 in/ft/s. For SC wall specimens with Grade 65 steel faceplates, as the impact velocity of the projectile increases from 528 ft/s to 539 ft/s, the penetration depth increases at a rate of 0.008 in/ft/s. The increase rate of the penetration depth of the SC wall specimens with Grade 50 steel faceplates is about seven times greater than that of the SC wall specimens with Grade 65 steel faceplates. Thus, it can be concluded that the influence of the steel faceplate strength is considerable.

#### *6.4 Conclusions*

In this chapter, two different numerical parametric studies were conducted. In the first parametric study, a series of numerical analyses were performed to generate data points to specify the velocity ranges in which perforation velocities were located. The specified velocity ranges for three analysis groups were summarized in terms of the varied projectile parameters in Table 6-3 and Table 6-4. These data points will be used to evaluate and verify the accuracy of the modified design method which is proposed in CHAPTER 7.

In the second parametric study, another series of numerical analyses were investigated to evaluate the influence of design parameters of SC walls on their local damage behavior. It was found that flexural reinforcement ratio and steel faceplate strength are significant design parameters which influence the penetration depth of the projectile into the concrete core of the SC wall specimens. The shear reinforcement ratio was found to not be a critical design parameter in terms of the penetration depth.

Table 6-1 Numerical parametric study matrix (1<sup>st</sup>)

<i>Analysis Gr.</i>	<i>Analysis No.</i>	<i>Analysis Identifier</i>	$t_{sc}$ (in)	$L/t_{sc}$	$t_p$ (in)	$\rho$ (%)	$S/t_{sc}$	$\rho_t$ (%)	$f'_c$ (ksi)	$f_y^{pl}$ (ksi)	$D$ (in)	$W_p$ (lbs)	$V_{imp}$ (ft/s)
	1	3-0.37-50-1.0-1.3-745	4	2.75	0.0747	3.74	0.5	0.37	5	50	1.0	1.3	745
	2	3-0.37-50-1.0-1.3-770	4	2.75	0.0747	3.74	0.5	0.37	5	50	1.0	1.3	770
	3	3-0.37-50-1.0-1.3-800	4	2.75	0.0747	3.74	0.5	0.37	5	50	1.0	1.3	800
	4	3-0.37-50-1.0-2.0-528	4	2.75	0.0747	3.74	0.5	0.37	5	50	1.0	2.0	528
	5	3-0.37-50-1.0-2.0-540	4	2.75	0.0747	3.74	0.5	0.37	5	50	1.0	2.0	540
	6	3-0.37-50-1.0-2.0-558	4	2.75	0.0747	3.74	0.5	0.37	5	50	1.0	2.0	558
	7	3-0.53-50-1.5-1.3-875	4	2.75	0.0747	3.74	0.5	0.53	5	50	1.5	1.3	875
	8	3-0.53-50-1.5-1.3-912	4	2.75	0.0747	3.74	0.5	0.53	5	50	1.5	1.3	912
	9	3-0.53-50-1.5-1.3-950	4	2.75	0.0747	3.74	0.5	0.53	5	50	1.5	1.3	950
	10	3-0.53-50-1.5-2.0-667	4	2.75	0.0747	3.74	0.5	0.53	5	50	1.5	2.0	667
	11	3-0.53-50-1.5-2.0-690	4	2.75	0.0747	3.74	0.5	0.53	5	50	1.5	2.0	690
	12	3-0.53-50-1.5-2.0-710	4	2.75	0.0747	3.74	0.5	0.53	5	50	1.5	2.0	710
	13	3-0.53-50-1.5-2.0-728	4	2.75	0.0747	3.74	0.5	0.53	5	50	1.5	2.0	728
<i>Gr.1</i>	14	3-0.53-50-1.5-2.0-757	4	2.75	0.0747	3.74	0.5	0.53	5	50	1.5	2.0	757
	15	3-0.53-50-1.0-2.0-528	4	2.75	0.0747	3.74	0.5	0.53	5	50	1.0	2.0	528
	16	3-0.53-50-1.0-2.0-540	4	2.75	0.0747	3.74	0.5	0.53	5	50	1.0	2.0	540
	17	3-0.53-50-1.0-2.0-558	4	2.75	0.0747	3.74	0.5	0.53	5	50	1.0	2.0	558
	18	3-0.53-50-1.0-2.0-577	4	2.75	0.0747	3.74	0.5	0.53	5	50	1.0	2.0	577

Table 6-1 continued

	19	3-0.53-50-1.0-2.7-455	4	2.75	0.0747	3.74	0.5	0.53	5	50	1.0	2.7	455
	20	3-0.53-50-1.0-2.7-475	4	2.75	0.0747	3.74	0.5	0.53	5	50	1.0	2.7	475
	21	3-0.53-50-1.0-2.7-495	4	2.75	0.0747	3.74	0.5	0.53	5	50	1.0	2.7	495
	22	3-0.53-50-1.0-3.5-395	4	2.75	0.0747	3.74	0.5	0.53	5	50	1.0	3.5	395
	23	3-0.53-50-1.0-3.5-413	4	2.75	0.0747	3.74	0.5	0.53	5	50	1.0	3.5	413
	24	3-0.53-50-1.0-3.5-430	4	2.75	0.0747	3.74	0.5	0.53	5	50	1.0	3.5	430
	25	3-1.23-50-1.5-3.5-465	4	2.75	0.0747	3.74	0.5	1.23	5	50	1.5	3.5	465
	26	3-1.23-50-1.5-3.5-477	4	2.75	0.0747	3.74	0.5	1.23	5	50	1.5	3.5	477
	1	5-0.48-50-1.0-2.0-528	4	2.75	0.1046	5.23	1.0	0.48	5	50	1.0	2.0	528
	2	5-0.48-50-1.0-2.7-450	4	2.75	0.1046	5.23	1.0	0.48	5	50	1.0	2.7	450
	3	5-0.48-50-1.0-2.7-467	4	2.75	0.1046	5.23	1.0	0.48	5	50	1.0	2.7	467
	4	5-0.48-50-1.0-2.7-475	4	2.75	0.1046	5.23	1.0	0.48	5	50	1.0	2.7	475
<i>Gr.2</i>	5	5-0.48-50-1.0-2.7-495	4	2.75	0.1046	5.23	1.0	0.48	5	50	1.0	2.7	495
	6	5-0.48-50-1.5-3.5-506	4	2.75	0.1046	5.23	1.0	0.48	5	50	1.5	3.5	506
	7	5-0.48-50-1.5-3.5-528	4	2.75	0.1046	5.23	1.0	0.48	5	50	1.5	3.5	528
	8	5-0.48-50-1.5-2.0-690	4	2.75	0.1046	5.23	1.0	0.48	5	50	1.5	2.0	690
	9	5-0.48-50-1.5-2.0-710	4	2.75	0.1046	5.23	1.0	0.48	5	50	1.5	2.0	710
	1	3-0.37-65-1.0-2.0-558	4	2.75	0.0747	3.74	0.5	0.37	5	65	1.0	2.0	558
	2	3-0.37-65-1.0-2.0-568	4	2.75	0.0747	3.74	0.5	0.37	5	65	1.0	2.0	568
<i>Gr.3</i>	3	3-0.37-65-1.0-2.0-577	4	2.75	0.0747	3.74	0.5	0.37	5	65	1.0	2.0	577
	4	3-0.37-65-1.0-2.7-475	4	2.75	0.0747	3.74	0.5	0.37	5	65	1.0	2.7	475
	5	3-0.37-65-1.0-2.7-495	4	2.75	0.0747	3.74	0.5	0.37	5	65	1.0	2.7	495

Table 6-2 Summary of the numerical parametric study results (1<sup>st</sup>)

Anal ysis Gr.	Total No.	Test / Bench- mark No.	Param. Study No.	Test Case Identifier	Experimental Tests Results							Numerical Parametric Study Results					
					$V_{imp}$ (ft/s)	$V_{des}$ (ft/s)	$V_{imp}/V_{des}$	Test Result	Damage Mode	Pene. Depth $x_{c\_test, (in)}$	Bulging Depth $x_{bg\_test, (in)}$	FEA Result	Damage Mode	Penetration Depth		Bulging Depth	
														$x_{c\_FEM, (in)}$	$x_{c\_FEM}/x_{c\_test}$	$x_{bg\_FEM, (in)}$	$x_{bg\_FEM}/x_{bg\_test}$
Gr.1	1	1	-	3-0.37-50-1.0-1.3-554	593	613	0.967	Stop	B	2.06	0.25	Stop	B	2.25	1.09	0.31	1.25
	2	2	-	3-0.37-50-1.0-1.3-677	674	613	1.100	Stop	B	3.06	0.63	Stop	B	1.77	0.58	0.41	0.66
	3	-	1	3-0.37-50-1.0-1.3-745	745	613	1.215	-	-	-	-	Stop	B	3.59	-	0.81	-
	4	-	2	3-0.37-50-1.0-1.3-770	770	613	1.256	-	-	-	-	Perf.	P	-	-	-	-
	5	-	3	3-0.37-50-1.0-1.3-800	800	613	1.305	-	-	-	-	Perf.	P	-	-	-	-
	6	3	-	3-0.37-50-1.0-2.0-430	424	485	0.874	Stop	B	1.56	0.25	Stop	B	1.99	1.28	0.21	0.85
	7	4	-	3-0.37-50-1.0-2.0-525	513	485	1.058	Stop	B	3.16	0.58	Stop	B	3.18	1.01	0.44	0.76
	8	-	4	3-0.37-50-1.0-2.0-528	528	485	1.089	-	-	-	-	Stop	B	3.22	-	0.48	-
	9	-	5	3-0.37-50-1.0-2.0-540	540	485	1.113	-	-	-	-	Stop	S	3.94	-	(Elem. Del.)	-
	10	-	6	3-0.37-50-1.0-2.0-558	558	485	1.151	-	-	-	-	Perf.	P	-	-	-	-
	11	5	-	3-0.53-50-1.5-1.3-660	667	732	0.911	Stop	B	1.38	0.56	Stop	B	1.19	0.86	0.49	0.87
	12	6	-	3-0.53-50-1.5-1.3-750	760	732	1.038	Stop	B	2.00	0.72	Stop	B	2.08	1.04	0.53	0.74
	13	-	7	3-0.53-50-1.5-1.3-875	875	732	1.195	-	-	-	-	Stop	B	2.93	-	0.93	-
	14	-	8	3-0.53-50-1.5-1.3-912	912	732	1.246	-	-	-	-	Stop	S	3.75	-	1.65	-
	15	-	9	3-0.53-50-1.5-1.3-950	950	732	1.298	-	-	-	-	Perf.	P	-	-	-	-
	16	-	10	3-0.53-50-1.5-2.0-667	667	582	1.146	-	-	-	-	Stop	B	3.36	-	1.17	-
	17	-	11	3-0.53-50-1.5-2.0-690	690	582	1.186	-	-	-	-	Stop	B	3.82	-	1.31	-
	18	-	12	3-0.53-50-1.5-2.0-710	710	582	1.220	-	-	-	-	Perf.	P	-	-	-	-

Table 6-2 continued

Anal ysis Gr.	Total No.	Test / Bench- mark No.	Param. Study No.	Test Case Identifier	Experimental Tests Results							Numerical Parametric Study Results					
					$V_{imp}$	$V_{des}$	$V_{imp}$	Test	Damage	Pene. Depth	Bulging Depth	FEA	Damage	Penetration Depth		Bulging Depth	
					(ft/s)	(ft/s)	/ $V_{des}$	Result	Mode	$x_{c\_test, (in)}$	$x_{bg\_test, (in)}$	Result	Mode	$x_{c\_FEM, (in)}$	$x_{c\_FEM}/x_{c\_test}$	$x_{bg\_FEM, (in)}$	$x_{bg\_FEM}/x_{bg\_test}$
	19	-	13	3-0.53-50-1.5-2.0-728	728	582	1.251	-	-	-	-	Perf.	P	-	-	-	-
	20	-	14	3-0.53-50-1.5-2.0-757	757	582	1.301	-	-	-	-	Perf.	P	-	-	-	-
	21	-	15	3-0.53-50-1.0-2.0-528	528	485	1.089	-	-	-	-	Stop	B	3.46	-	0.46	-
	22	-	16	3-0.53-50-1.0-2.0-540	540	485	1.113	-	-	-	-	Stop	S	3.99	-	(Elem. Del.)	-
	23	-	17	3-0.53-50-1.0-2.0-558	558	485	1.151	-	-	-	-	Perf.	P	-	-	-	-
	24	-	18	3-0.53-50-1.0-2.0-577	577	485	1.190	-	-	-	-	Perf.	P	-	-	-	-
	25	7	-	3-0.53-50-1.0-2.0-513	640	485	1.320	Perf.	P	-	-	Perf.	P	-	-	-	-
	26	8	-	3-0.53-50-1.0-2.0-626	710	485	1.464	Perf.	P	-	-	Perf.	P	-	-	-	-
Gr.1	27	-	19	3-0.53-50-1.0-2.7-455	455	413	1.102	-	-	-	-	Stop	B	3.14	-	0.60	-
	28	-	20	3-0.53-50-1.0-2.7-475	475	413	1.150	-	-	-	-	Stop	B	3.51	-	0.69	-
	29	-	21	3-0.53-50-1.0-2.7-495	495	413	1.199	-	-	-	-	Perf.	P	-	-	-	-
	30	-	22	3-0.53-50-1.0-3.5-395	395	359	1.100	-	-	-	-	Stop	B	3.20	-	0.64	-
	31	-	23	3-0.53-50-1.0-3.5-413	413	359	1.150	-	-	-	-	Stop	S	3.64	-	(Elem. Del.)	-
	32	-	24	3-0.53-50-1.0-3.5-430	430	359	1.198	-	-	-	-	Perf.	P	-	-	-	-
	33	-	25	3-1.23-50-1.5-3.5-465	465	432	1.076	-	-	-	-	Stop	S	3.68	-	(Elem. Del.)	-
	34	-	26	3-1.23-50-1.5-3.5-477	477	432	1.104	-	-	-	-	Perf.	P	-	-	-	-
	35	9	-	3-1.23-50-1.5-3.5-380	550	432	1.273	Stop	S	4.00	1.63	Perf.	P	-	-	-	-
	36	10	-	3-1.23-50-1.5-3.5-465	489	432	1.132	Stop	B	1.91	0.59	Perf.	P	-	-	-	-

Table 6-2 continued

Anal ysis Gr.	Total No.	Test / Bench- mark No.	Param. Study No.	Test Case Identifier	Experimental Tests Results							Numerical Parametric Study Results						
					$V_{imp}$ (ft/s)	$V_{des}$ (ft/s)	$V_{imp}/V_{des}$	Test Result	Damage Mode	Pene. Depth $x_{c\_test}$ , (in)	Bulging Depth $x_{bg\_test}$ , (in)	FEA Result	Damage Mode	Penetration Depth		Bulging Depth		
											$x_{c\_FEM}$ , (in)	$x_{c\_FEM}/x_{c\_test}$	$x_{bg\_FEM}$ , (in)	$x_{bg\_FEM}/x_{bg\_test}$				
	37	1	-	5-0.48-50-1.0-2.0-445	467	504	0.927	Stop	B	2.09	0.28	Stop	B	2.17	1.04	0.41	1.45	
	38	-	27	5-0.48-50-1.0-2.0-528	528	504	1.048	-	-	-	-	Stop	S	3.40	-	(Elem. Del.)	-	
	39	2	-	5-0.48-50-1.0-2.0-544	549	504	1.089	Stop	S	3.31	0.75	Perf.	P	-	-	-	-	
	40	-	28	5-0.48-50-1.0-2.7-450	450	429	1.049	-	-	-	-	Stop	B	2.92	-	(Elem. Del.)	-	
	41	-	29	5-0.48-50-1.0-2.7-467	467	429	1.089	-	-	-	-	Stop	B	3.11	-	(Elem. Del.)	-	
	42	-	30	5-0.48-50-1.0-2.7-475	475	429	1.107	-	-	-	-	Stop	B	3.24	-	(Elem. Del.)	-	
Gr.2	43	-	31	5-0.48-50-1.0-2.7-495	495	429	1.154	-	-	-	-	Perf.	P	-	-	-	-	
	44	3	-	5-0.48-50-1.5-3.5-408	410	465	0.882	Stop	B	1.34	0.38	Stop	B	1.64	1.22	0.90	2.40	
	45	4	-	5-0.48-50-1.5-3.5-498	484	465	1.041	Stop	B	2.41	0.69	Stop	B	3.43	1.42	0.88	1.28	
	46	-	32	5-0.48-50-1.5-3.5-506	506	465	1.088	-	-	-	-	Stop	S	4.38	-	-	-	
	47	-	33	5-0.48-50-1.5-3.5-528	528	465	1.135	-	-	-	-	Perf.	P	-	-	-	-	
	48	-	34	5-0.48-50-1.5-2.0-690	690	625	1.104	-	-	-	-	Stop	S	4.07	-	(Elem. Del.)	-	
	49	-	35	5-0.48-50-1.5-2.0-710	710	625	1.136	-	-	-	-	Perf.	P	-	-	-	-	
	50	1	-	3-0.37-65-1.0-2.0-443	539	500	1.078	Stop	B	3.16	0.69	Stop	B	3.23	1.02	0.45	0.66	
	51	-	36	3-0.37-65-1.0-2.0-558	558	500	1.116	-	-	-	-	Stop	B	3.54	-	0.53	-	
	52	-	37	3-0.37-65-1.0-2.0-568	568	500	1.136	-	-	-	-	Perf.	P	-	-	-	-	
Gr. 3	53	-	38	3-0.37-65-1.0-2.0-577	577	500	1.154	-	-	-	-	Perf.	P	-	-	-	-	
	54	2	-	3-0.37-65-1.0-2.0-541	634	500	1.268	Perf.	P	-	-	Perf.	P	-	-	-	-	
	55	-	39	3-0.37-65-1.0-2.7-475	475	425	1.118	-	-	-	-	Stop	S	3.66	-	(Elem. Del.)	-	
	56	-	40	3-0.37-65-1.0-2.7-495	495	425	1.165	-	-	-	-	Perf.	P	-	-	-	-	

\*

Stop: The specimen stopped the projectile

Perf.: The specimen was perforated by the projectile

\*\*

B: Bulging, S: Splitting, P: Perforating

Table 6-3 Summary of the perforation velocity ranges in the three experimental test groups

	<i>Group 1</i>				<i>Group 2</i>				<i>Group 3</i>			
	<i>1.0 in. diameter Proj.</i>		<i>1.5 in. diameter Proj.</i>		<i>1.0 in. diameter Proj.</i>		<i>1.5 in. diameter Proj.</i>		<i>1.0 in. diameter Proj.</i>		<i>1.5 in. diameter Proj.</i>	
$W_p$ (lbs)	$V_{imp}$ (ft/sec)	$V_{imp}/V_{des}$										
1.3	-	-	-	-	-	-	-	-	-	-	-	-
2.0	513 - 640	1.058 - 1.320	-	-	-	-	-	-	539 - 634	1.078 - 1.268	-	-
2.7	-	-	-	-	-	-	-	-	-	-	-	-
3.5	-	-	-	-	-	-	-	-	-	-	-	-

Table 6-4 Summary of the perforation velocity ranges in the three numerical analysis groups

	<i>Group 1</i>				<i>Group 2</i>				<i>Group 3</i>			
	<i>1.0 in. diameter Proj.</i>		<i>1.5 in. diameter Proj.</i>		<i>1.0 in. diameter Proj.</i>		<i>1.5 in. diameter Proj.</i>		<i>1.0 in. diameter Proj.</i>		<i>1.5 in. diameter Proj.</i>	
$W_p$ (lbs)	$V_{imp}$ (ft/sec)	$V_{imp}/V_{des}$										
1.3	745 - 770	1.215 - 1.256	912 - 950	1.246 - 1.298	-	-	-	-	-	-	-	-
2.0	540 - 558	1.113 - 1.151	690 - 710	1.186 - 1.220	528 - 549	1.048 - 1.089	690 - 710	1.104 - 1.136	558 - 568	1.116 - 1.136	-	-
2.7	475 - 495	1.150 - 1.199	-	-	475 - 495	1.107 - 1.154	-	-	475 - 495	1.118 - 1.165	-	-
3.5	413 - 430	1.150 - 1.198	465 - 477	1.076 - 1.104	-	-	506 - 528	1.088 - 1.135	-	-	-	-

Table 6-5 Numerical parametric study matrix (2<sup>nd</sup>)

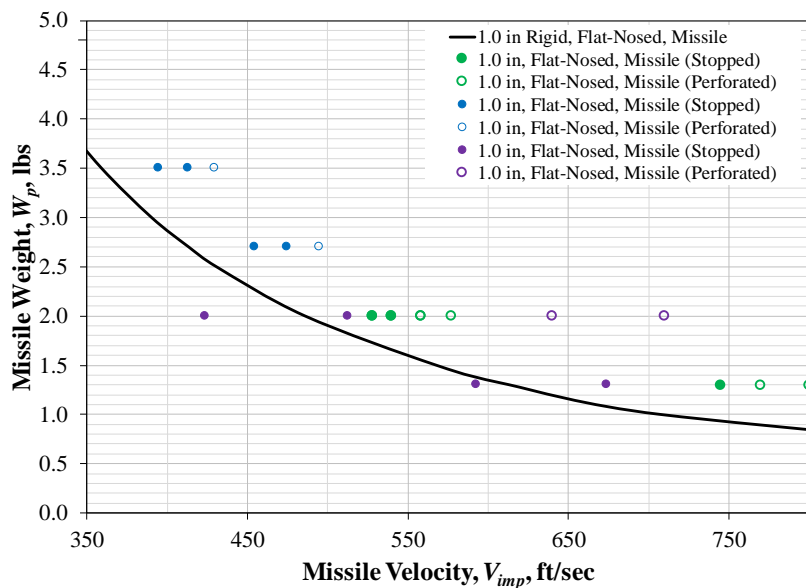
<i>Analysis group / number</i>	<i>Test case identifier</i>	$t_{sc}$ (in)	$L/t_{sc}$	$t_p$ (in)	$\rho$ (%)	$S/t_{sc}$	$\rho_t$ (%)	$f'_c$ (ksi)	$f_y^{pl}$ (ksi)	$D$ (in)	$W_p$ (lbs)	$V_{imp}$ (ft/s)	
<i>Gr.1</i>	1	3-0.37-50-1.0-2.0-528	4	2.75	0.0747	3.7	0.5	<b>0.37</b>	5	50	1.0	2.0	528
	2	3-0.37-50-1.0-2.0-540	4	2.75	0.0747	3.7	0.5	<b>0.37</b>	5	50	1.0	2.0	540
	3	3-0.37-50-1.0-2.0-558	4	2.75	0.0747	3.7	0.5	<b>0.37</b>	5	50	1.0	2.0	558
	4	3-0.53-50-1.0-2.0-528	4	2.75	0.0747	3.7	0.5	<b>0.53</b>	5	50	1.0	2.0	528
	5	3-0.53-50-1.0-2.0-540	4	2.75	0.0747	3.7	0.5	<b>0.53</b>	5	50	1.0	2.0	540
	6	3-0.53-50-1.0-2.0-558	4	2.75	0.0747	3.7	0.5	<b>0.53</b>	5	50	1.0	2.0	558
<i>Gr.2</i>	1	5-0.48-50-1.0-2.0-528	4	2.75	0.1046	<b>5.2</b>	1.0	0.48	5	50	1.0	2.0	528
	2	5-0.48-50-1.0-2.0-540	4	2.75	0.1046	<b>5.2</b>	1.0	0.48	5	50	1.0	2.0	540
	3	5-0.48-50-1.0-2.0-558	4	2.75	0.1046	<b>5.2</b>	1.0	0.48	5	50	1.0	2.0	558
<i>Gr.3</i>	1	3-0.37-65-1.0-2.0-528	4	2.75	0.0747	3.7	0.5	0.37	5	<b>65</b>	1.0	2.0	528
	2	3-0.37-65-1.0-2.0-443	4	2.75	0.0747	3.7	0.5	0.37	5	<b>65</b>	1.0	2.0	539
	3	3-0.37-65-1.0-2.0-558	4	2.75	0.0747	3.7	0.5	0.37	5	<b>65</b>	1.0	2.0	558

Table 6-6 Summary of the numerical parametric study results (2<sup>nd</sup>)

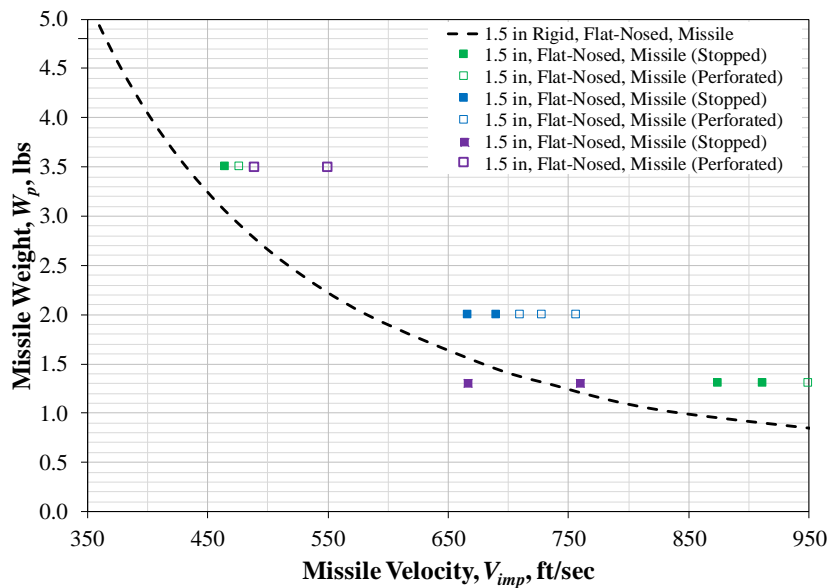
<i>Analysis group / number</i>	<i>Test case identifier</i>	<i>Param. studied</i>	$\rho$ (%)	$\rho_t$ (%)	$f_y^{pl}$ (ksi)	$V_{imp}$ (ft/s)	<i>FEA result</i> *	<i>Damage mode</i> **	$x_{c\_FEM}$ (in)	
<i>Gr.1</i>	1	3-0.37-50-1.0-2.0-528	$\rho_t, f_y$	3.7	0.37	50	528	Stop	B	3.22
	2	3-0.37-50-1.0-2.0-540	$\rho_t, f_y$	3.7	0.37	50	540	Stop	S	3.94
	3	3-0.37-50-1.0-2.0-558	$\rho_t, f_y$	3.7	0.37	50	558	Perf.	P	-
	4	3-0.53-50-1.0-2.0-528	$\rho_t, \rho$	3.7	0.53	50	528	Stop	B	3.46
	5	3-0.53-50-1.0-2.0-540	$\rho_t, \rho$	3.7	0.53	50	540	Stop	S	3.99
	6	3-0.53-50-1.0-2.0-558	$\rho_t, \rho$	3.7	0.53	50	558	Perf.	P	-
<i>Gr.2</i>	1	5-0.48-50-1.0-2.0-528	$\rho$	5.2	0.48	50	528	Stop	S	3.40
	2	5-0.48-50-1.0-2.0-540	$\rho$	5.2	0.48	50	540	Stop	S	3.49
	3	5-0.48-50-1.0-2.0-558	$\rho$	5.2	0.48	50	558	Perf.	P	-
<i>Gr.3</i>	1	3-0.37-65-1.0-2.0-528	$f_y$	3.7	0.37	65	528	Stop	B	3.14
	2	3-0.37-65-1.0-2.0-443	$f_y$	3.7	0.37	65	539	Stop	B	3.23
	3	3-0.37-65-1.0-2.0-558	$f_y$	3.7	0.37	65	558	Stop	B	3.54

\* Stop: The specimen stopped the projectile  
 Perf.: The specimen was perforated by

\*\* B: Bulging, S: Splitting, P: Perforating

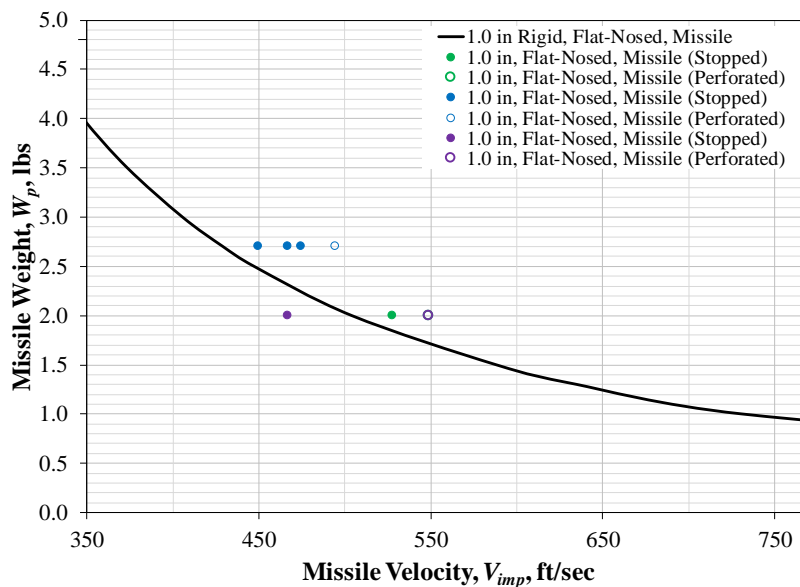


(a) 1.0 in. diameter projectile applied

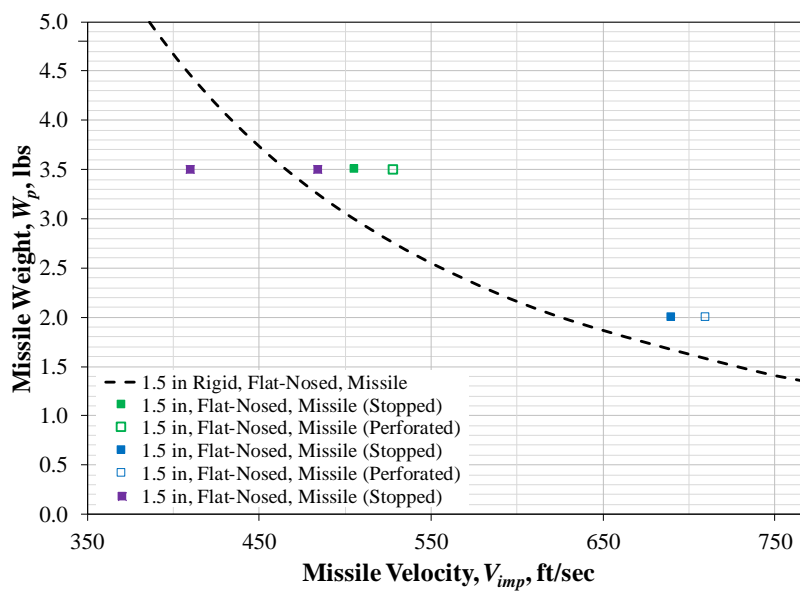


(b) 1.5 in. diameter projectile applied

Figure 6-1 Numerical parametric study results on the perforation resistance curve of analysis group 1 (Benchmarking analyses results are included)

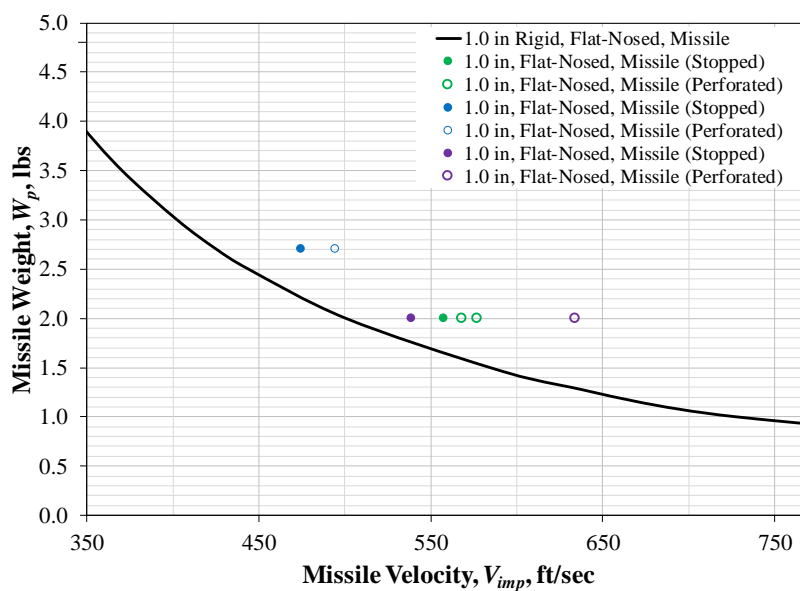


(a) 1.0 in. diameter projectile applied



(b) 1.5 in. diameter projectile applied

Figure 6-2 Numerical parametric study results on the perforation resistance curve of analysis group 2 (Benchmarking analyses results are included)



(a) 1.0 in. diameter projectile applied

Figure 6-3 Numerical parametric study results on the perforation resistance curve of analysis group 3 (Benchmarking analyses results are included)

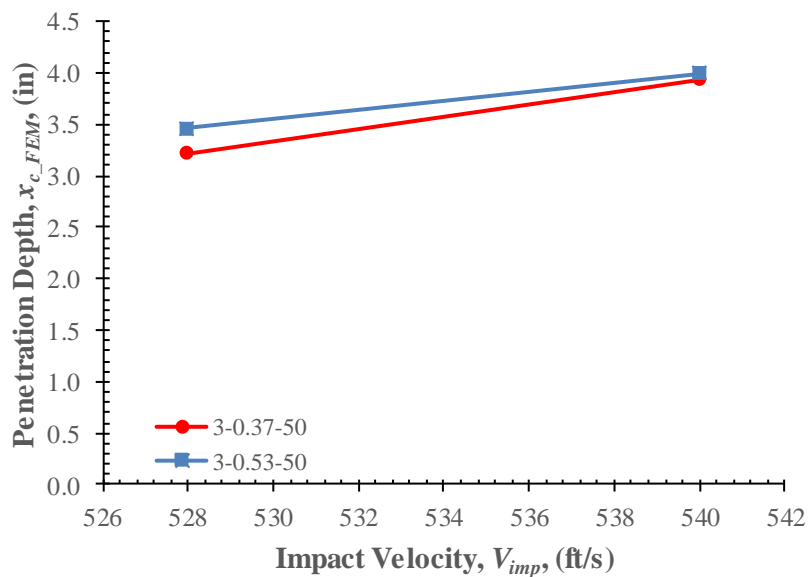


Figure 6-4 Influence of the shear reinforcement ratio ( $\rho_t$ ) of SC walls on the penetration depth

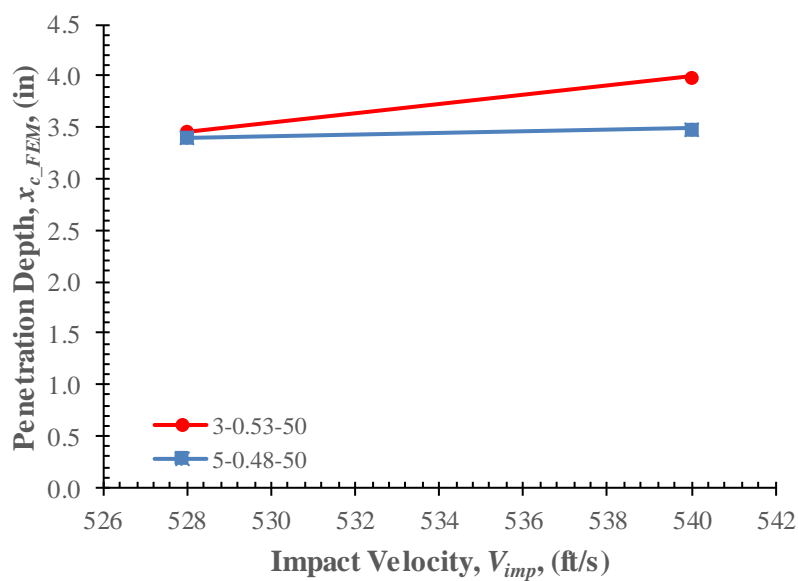


Figure 6-5 Influence of the flexural reinforcement ratio ( $\rho$ ) of SC walls on the penetration depth

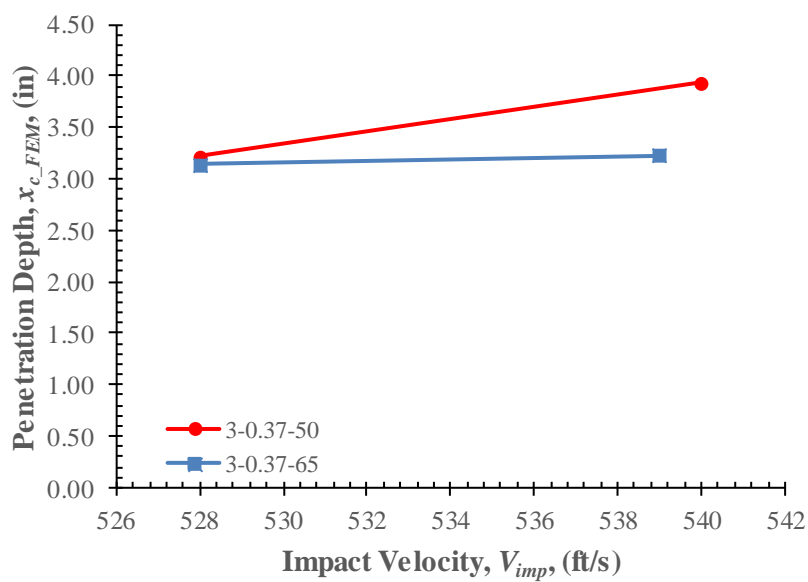


Figure 6-6 Influence of the steel faceplate strength of SC walls on the penetration depth

## CHAPTER 7. DEVELOPMENT OF MODIFIED DESIGN METHOD

### 7.1 Introduction

Previously, the three-step design method (Bruhl et al. 2015a) was proposed to prevent perforation failure of SC walls subjected to missile impact. The three-step design method appears in the commentary of the AISC N690s1-15 as one of the rational methods to prevent perforation failure of SC walls, however, there is still room for improvement in terms of accuracy and conservatism aspects in the application of this method.

The three-step design method uses the modified NDRC equations (American Society of Civil Engineers 1980) in its internal algorithm to calculate the perforation velocity of the concrete core thickness of SC walls. However, based on the experimental investigations in CHAPTER 4, the modified NDRC equations turned out to not provide an accurate penetration depth value of a projectile when it is applied to SC walls. Furthermore, the three-step design method presented considerable conservatism to estimate perforation velocity of a projectile for SC walls compared to current experimental data of small-scale missile impact tests.

In this chapter, a modification factor equation,  $K_{sc}$ , is introduced to increase accuracy in estimating the penetration depth of a projectile into the concrete core of SC walls. The modification factor equation is used with the modified NDRC equations and its effectiveness is verified. Then, the modified design method is proposed incorporating the modification factor equation and revised local failure mechanism which was obtained from the experimental investigations. Lastly, the modified design method is verified using the small-scale missile impact test data from this research project and the larger-scale missile impact test data obtained from South Korean's tests.

## 7.2 Evaluation on Effectiveness of Penetration Depth Calculation

### 7.2.1 Evaluation of modified NDRC equations

NEI 07-13 (ERIN Engineering & Research Inc. 2011) suggests design formulae to calculate the penetration depth of a missile in RC walls and to determine the required wall thickness to prevent critical damage such as scabbing and perforation for RC walls subjected to missile impact. The original three-step design method (Bruhl et al. 2015a) adopted the modified NDRC equations in NEI 07-13 to calculate perforation velocity of the concrete core of SC walls. These modified NDRC equations are typically used for calculating the penetration depth for RC walls. SC walls have been determined to provide more protection than RC walls due to their affixed steel faceplates, so that the modified NDRC equations might not necessarily provide accurate values of penetration depth for SC walls. Thus, it would be important to evaluate the performance of the modified NDRC equations in estimating penetration depth of SC walls in order to figure out how to improve the three-step design method.

Modified NDRC equations (American Society of Civil Engineers 1980; ERIN Engineering & Research Inc. 2011) are depicted below:

$$x = \sqrt{4 \cdot K \cdot N \cdot W \cdot d \cdot \left( \frac{V_{imp}}{1000 \cdot d} \right)^{1.80}}, \quad \text{for } \frac{x}{d} \leq 2.0 \quad \text{Equation 7-1}$$

$$x = \left[ K \cdot N \cdot W \cdot \left( \frac{V_{imp}}{1000 \cdot d} \right)^{1.80} \right] + d, \quad \text{for } \frac{x}{d} > 2.0 \quad \text{Equation 7-2}$$

where  $x$  is the penetration depth into concrete in inches,  $K$  is the concrete strength factor in psi,  $W$  is the weight of the projectile in lbs,  $N$  is the nose shape factor of the projectile,  $V_{imp}$  is the impacting velocity of the projectile, and  $d$  is the effective diameter of the projectile.

From the experimental investigation of the small-scale impact tests, measured values of penetration depth,  $x_{c\_test}$ , and calculated values of penetration depth,  $x_{c\_calc}$ , obtained using the modified NDRC equations (Equation 7-1 and Equation 7-2), are summarized in Table 7-1. For test cases which resulted in no perforation of SC walls, penetration depth between measured and calculated values are compared and illustrated graphically in Figure 7-1.

As seen in Figure 7-1, the modified NDRC equations are in agreement with measured penetration depth values between one third and two thirds of concrete thickness. However, above two thirds of concrete thickness, there was a non-negligible deviation between  $x_{c\_test}$  and  $x_{c\_calc}$ . Thus, the penetration depth calculating equations need to be modified for use in SC walls to improve the performance of the three-step design method.

### 7.2.2 Introduction to modification factor equation, $K_{SC}$

In this section, a modification factor equation,  $K_{SC}$ , is introduced to correct estimated values of penetration depth calculated using the modified NDRC equations.  $K_{SC}$  was derived from multiple regression analysis using combinations of parameters from SC wall section design and projectile. The penetration depth of SC walls was calculated using the equations below:

$$x_{c\_calc} = K_{SC} \cdot x_{c\_NDRC} \quad \text{Equation 7-3}$$

$$K_{SC} = -0.612 + 3.472 \cdot \left( \frac{x_{c\_NDRC}}{T_c} \right) \quad \text{Equation 7-4}$$

where estimated penetration depth value of SC walls is  $x_{c\_calc}$ , calculated penetration depth value from the modified NDRC equations is  $x_{c\_NDRC}$ , and concrete thickness is  $T_c$ .

The R-squared value of the derived  $K_{SC}$  equation was 0.332. Comparison was made between measured penetration depth value,  $x_{c\_test}$ , and calculated penetration depth value,  $x_{c\_calc}$ , to evaluate the performance of the modification factor equation ( $K_{SC}$ ) used with the modified NDRC equations in estimating the penetration depth in SC walls. The result is illustrated graphically in Figure 7-2 with  $x_{c\_test}$  and  $x_{c\_calc}$  values normalized by  $T_c$ , respectively.

As shown in Figure 7-2, the calculated values of penetration depth ( $x_{c\_calc}$ ) agree well with the measured values of penetration depth ( $x_{c\_test}$ ). Enhancement in estimating the penetration depth of SC walls by applying the modification factor equation ( $K_{SC}$ ) is verified by comparing Figure 7-1 and Figure 7-2.

It is also evaluated how accurately the penetration depth can be estimated. As a measure of accuracy, a degree of conservatism was adopted which is expressed as the penetration depth ratio of measured values from the experimental tests to calculated values by applying the modification factor equation ( $K_{SC}$ ),  $x_{c\_test}/x_{c\_calc}$ . A degree of conservatism between the modified NDRC equations and those with  $K_{SC}$  applied is compared in terms of the level of confidence and illustrated in Figure 7-3. In the figure, Equation 7-4 shows improved results when the required level of confidence is greater than 30.8%. Conservatism is found to be reduced significantly. For the remaining ranges of the level of confidence, there is no big difference in results between the modified NDRC equations and those with  $K_{SC}$  applied. Thus, it can be concluded that the accuracy in estimating the penetration depth is increased by applying  $K_{SC}$ .

### 7.2.3 Perforation resistance curve generated by applying modification factor equation, $K_{SC}$

Next, the effect of the modification factor ( $K_{SC}$ ) on the three-step method was evaluated. Perforation velocities were calculated using the three-step design method with  $K_{SC}$  applied. The results were then compared with test results as well as numerical parametric analyses results. Perforation resistance curves were generated by curve fitting of the perforation velocities and presented in Figure 7-4 to Figure 7-8.

According to the observation on these figures, the perforation resistance curves show very good agreement for both experimental test results and numerical parametric analyses results when the modification factor  $K_{SC}$  applied.

## 7.3 *Evaluation on Effectiveness of Steel Faceplate Thickness Calculation*

### 7.3.1 Analytical model to determine required steel faceplate thickness of SC walls

Borvik's analytical model (Børvik et al. 2009) was applied in the three-step design method to determine the required steel faceplate thickness of SC walls to prevent perforation against projectile impactive loading. Borvik's analytical model was developed based on the cylindrical cavity-expansion theory (CET), which was approved by observations from experimental tests (Forrestal et al. 1990; Piekutowski et al. 1996; Rosenberg and Forrestal 1988; Warren et al. 2001). This particular analytical model was used for preventing perforation of aluminum plates by conical-nosed rigid projectiles, but it can be applied to strain hardening ductile metals impacted by projectiles with various nose shape as well (Forrestal et al. 1990, 1991, 1995). Equations in the analytical model were rearranged to determine the required steel plate thickness,  $t_{p\_req}$ . Further details about the steel faceplate thickness calculation are described in section 7.4.4.

### 7.3.2 Effect of strain hardening coefficient and strain rate

Typically, the strain hardening exponent,  $n$ , for steel plates varies depending on the type of materials or the manufacturing process. The variation of  $n$  has a significant influence on  $\sigma_r$ , which affects  $t_{p\_req}$  directly. In the three-step design method,  $n = 0.2$  is used to calculate  $\sigma_r$  for structural steel plate which is greater than 0.25 in. (6 mm) thick or  $n = 0.1$  for steel plate which is less than 0.25 in. (6 mm) thick. Details of these equations are explained in section 7.4.4.

Meanwhile, the strength of materials is affected, in general, by high strain rate. NEI 07-13 (ERIN Engineering & Research Inc. 2011) suggests a dynamic increase factor (DIF), which can be applied to yield strength and ultimate strength of materials, as one of the ways to incorporate the strain rate effect. However, the strain rate effect was neglected in the CET analytical model. In Borvik et al.'s research (Børvik et al. 2009), numerical analyses were performed to evaluate the importance of the strain rate effect and the results were compared to the experimental tests results. It was found that the strain rate effect was not significant because the strain rate sensitivity was small. Therefore, it was decided that the strain rate effect should not be considered herein.

But, the modification of the penetration depth calculating equation, by itself, yielded significant improvement in the results of the three-step design method as shown in section 7.2. The modification reduced the inherent conservatism sufficiently to better anticipate perforation velocities. The resultant perforation resistance curve obtained agreed quite well with both the experimental tests results and the numerical parametric analyses results. Thus, it appears not to be necessary to make a modification to the steel faceplate thickness calculating equations.

## 7.4 Development of Modified Design Method

### 7.4.1 Experimental test database

In earlier sections, modification factor equation ( $K_{SC}$ ) for penetration depth calculation was suggested based on experimental investigations on the small-scale missile impact tests data. In order to develop more reliable design methodology or equations, which can be generally applicable beyond the small-scale SC walls, it is necessary to have extended test data with increased number of test cases of SC walls with different scales. Bruhl et al. (Bruhl et al. 2015a) compiled experimental tests data of RC and SC walls against projectile impact load conducted by other researchers over a period of three decades. This experimental database includes 130 test cases of SC walls, of which 91 out of 130 test cases stopped the projectiles. 58 test cases among these 91 test cases reported the penetration depth value of the projectile in SC walls. These 58 tests along with the 13 tests from the small-scale missile impact tests, which were conducted for this project, were used to develop a modified three-step design method and to evaluate its performance in estimating perforation velocities for SC walls. The experimental database is presented in APPENDIX.

### 7.4.2 Derivation of penetration depth equation for SC walls, $x_{c\_SC\_calc}$

Because current modified NDRC equations do not provide accurate enough estimation of the penetration depth value of SC walls, a new formula needs to be developed to calculate penetration depth value of a projectile, especially applicable to SC walls. Parameters influencing the penetration depth calculation were determined to be concrete strength factor,  $K$ , projectile weight,  $W$ , nose shape factor,  $N$ , impacting velocity,  $V_{imp}$ , projectile diameter,  $d$ , projectile deformability factor,  $\alpha_p$ . Multiple non-linear regression analyses were conducted to derive the formula statistically, with the two equations below being selected for penetration depth calculation.

$$x_{c\_SC\_calc1} = 5.115 \cdot \alpha_p \cdot K^{-0.377} \cdot W^{0.349} \cdot N^{1.493} \cdot d^{0.183} \cdot \left( \frac{V_{imp}}{1000 \cdot d} \right)^{0.367} \quad \text{Equation 7-5}$$

$$x_{c\_SC\_calc2} = \alpha_p \cdot \left[ 5.115 \cdot K^{-0.377} \cdot W^{0.349} \cdot N^{1.493} \cdot d^{0.183} \cdot \left( \frac{V_{imp}}{1000 \cdot d} \right)^{0.367} \right]$$

$$, \quad \text{for } \frac{x_{c\_SC\_calc2}}{\alpha_p d} \leq 2.0$$

$$x_{c\_SC\_calc2} = \alpha_p \cdot \left[ -3.495 \cdot K^{-1.069} \cdot W^{-0.706} \cdot N^{0.609} \cdot \left( \frac{V_{imp}}{1000 \cdot d} \right)^{-1.418} + 4.060 \cdot d^{0.597} \right] \quad \text{Equation 7-6}$$

$$, \quad \text{for } \frac{x_{c\_SC\_calc2}}{\alpha_p d} > 2.0$$

The R-squared values for Equation 7-5 and Equation 7-6 were 0.971 and 0.975, respectively. Performance of these two equations and the original modified NDRC equation were evaluated comparing the penetration depth between measured values and calculated values on the basis of the combined experimental tests database. The comparison is illustrated graphically in Figure 7-9.

Then, the degree of conservatism in penetration depth calculation equations was evaluated in terms of the level of confidence. Penetration depth ratios between measured value and calculated value,  $x_{c\_test}/x_{c\_calc}$ , from these two equations, as well as the modified NDRC equations, was calculated and compared. Figure 7-10 depicts the evaluation results of these two equations and the modified NDRC equations.

Based on the observations in Figure 7-10, Equation 7-5 shows improved results compared to the modified NDRC equations when the required level of confidence is less than 62.0%.

However, when the required level of confidence is greater than 62.0%, the modified NDRC equation presents better results. Equation 7-6 shows a similar or better trend providing improved results compared to the modified NDRC equations when the required level of confidence is less than 80.3%. However, when the required level of confidence is greater than 80.3%, the modified NDRC equation presents similar or better results.

In summary, from the observation of Figure 7-9 and Figure 7-10, the newly developed equations provided no significant improvement in calculating penetration depth of projectile for SC walls compared to the modified NDRC equations.

#### 7.4.3 Derivation of modification factor equation, $K_{sc}$

In previous section 7.2.3, it was proven that the modification factor equation,  $K_{SC}$ , is effective in providing improved results of penetration depth estimate values in SC walls when used alongside the modified NDRC equations. Following, the modification factor equation,  $K_{SC}$ , is developed further, based on extended experimental tests database, for its enhanced reliability. The extended experimental tests data includes both previously reported experimental tests database (Bruhl et al. 2015a) and currently conducted small-scale missile impact tests data.

Multiple regression analysis was used to derive the  $K_{SC}$  equation. Parameters determined to be significant were concrete strength factor,  $K$ , concrete core thickness,  $T_c$ , steel faceplate yield strength,  $f_y$ , concrete compressive strength,  $f'_c$ , projectile weight,  $W$ , projectile nose shape factor,  $N$ , projectile diameter,  $d$ , projectile deformability factor,  $\alpha_p$ , and penetration depth value calculated by the modified NDRC equations,  $x_{c\_NDRC}$ . As leading candidates, five  $K_{SC}$  equations were selected as follows:

$$K_{SC\_1} = 2.073 - 0.661 \cdot K + 0.688 \cdot \left( \frac{\alpha_p \cdot d}{T_c} \right) + 0.835 \cdot \left( \frac{x_{c\_NDRC}}{T_c} \right) \quad \text{Equation 7-7}$$

$$K_{SC\_2} = -47.667 + 5.307 \cdot K^{-0.588} + 9.261 \cdot 10^{-7} \cdot W^{1.563} + 0.221 \cdot N^{56.525} \\ + 2.230 \cdot \left( \frac{V_{imp}}{1000 \cdot d} \right)^{0.113} + 43.608 \cdot \left( \frac{\alpha_p \cdot d}{T_c} \right)^{0.006} + 0.766 \cdot \left( \frac{x_{c\_NDRC}}{T_c} \right)^{1.670} \quad \text{Equation 7-8}$$

$$K_{SC\_3} = -85.209 + 20.877 \cdot K^{-0.119} + 2.019 \cdot 10^{-5} \cdot W^{1.230} + 0.215 \cdot N^{26.058} \\ + 1.623 \cdot \left( \frac{V_{imp}}{1000 \cdot d} \right)^{0.208} + 19.085 \cdot \left( \frac{\alpha_p \cdot d}{T_c} \right)^{0.017} + 34.127 \cdot \left( \frac{x_{c\_NDRC}}{T_c} \right) \\ - 15.279 \cdot \left( \frac{x_{c\_NDRC}}{T_c} \right)^2 + 28.692 \cdot \left( \frac{x_{c\_NDRC}}{T_c} \right)^{-0.251} \quad \text{Equation 7-9}$$

$$K_{SC\_4} = -184.476 + 22.159 \cdot K^{-0.125} + 0.239 \cdot W^{-0.482} + 8.047 \cdot N^{0.092} \\ + 50.788 \cdot \left( \frac{\alpha_p \cdot d}{T_c} \right)^{0.004} + 37.256 \cdot \left( \frac{x_{c\_NDRC}}{T_c} \right) - 15.853 \cdot \left( \frac{x_{c\_NDRC}}{T_c} \right)^2 \\ + 85.939 \cdot \left( \frac{x_{c\_NDRC}}{T_c} \right)^{-0.106} \quad \text{Equation 7-10}$$

The R-squared values for these five equations were 0.457, 0.551, 0.656, and 0.630, respectively. Performance of these modification factor equations was evaluated comparing penetration depth between measured value and calculated value from the extended experimental tests database. The comparison is illustrated graphically in Figure 7-11.

Next, the degree of conservatism in penetration depth calculating equations was evaluated in terms of level of confidence. Degree of conservatism of the equation can be expressed as the ratio of measured penetration depth value to calculated penetration depth value,  $x_{c\_test}/x_{c\_calc}$ . Figure

7-12 shows the comparison of the achievable penetration depth ratio ( $x_{c\_test}/x_{c\_calc}$ ) corresponding to the required level of confidence.

Equation 7-7 shows improved results over the whole range of the required level of confidence, except for ranges from 56.3% to 69.0% and greater than or equal to 98.6%. Equation 7-8 shows improved results when the required level of confidence is less than or equal to 52.1%, ranging from 70.4% to 93.0%, and from 95.8% to 97.2%. Equation 7-9 shows improved results over the whole range of the required level of confidence, except for ranges less than or equal to 4.2%. Equation 7-10 shows improved results over the whole range of the required level of confidence.

#### 7.4.4 Proposed modified design method

According to the previous experimental investigations of the small-scale missile impact tests, the three-step design method (Bruhl et al. 2015a) was proven to have a significant conservatism. Following, a modified design method to prevent perforation failure of SC walls against missile impact is proposed which improves on the conservative aspect of the three-step design method. Details of the design procedure are described as follows:

##### **Step 1: Determine the concrete core thickness, $T_c$**

For an existing structure which is to be retrofitted or remodeled, concrete core thickness,  $T_c$ , is determined according to its design control documents or any specific restrictions related to the existing structure. For new construction,  $T_c$  is decided referring to codes or standards such as NEI 07-13 or DOE-STD-3014 (U.S. Department of Energy 2006). These codes or standards are for RC walls though, when considering SC walls, it has been determined that  $T_c$  can be reduced by 30% (Mizuno et al. 2005b)

**Step 2: Determine the residual velocity,  $V_r$ , of the projectile with the concrete frustum**

Based on observations of the experimental results from the small-scale missile impact tests, a failure mechanism is proposed as illustrated in Figure 7-13.

Unlike the failure mechanism described in the three-step design method (Bruhl et al. 2015), in the proposed failure mechanism, the concrete frustum starts forming in the midst of concrete core, by which time the projectile would have lost a significant amount of momentum after a tunneling region (or zone) was made. Multiple concrete frustums are then generated as the projectile proceeds forward. The last concrete frustum in the series of frustums is involved in this design calculation.

The concrete frustum weight is calculated as follows:

$$\begin{aligned} W_{cf} &= \frac{1}{3} \pi \rho_c (T_c - x_{c\_SC}) (r_2^2 + r_1 r_2 + r_1^2) \quad \text{for } x_{c\_SC} < T_c \\ W_{cf} &= 0 \quad \text{for } x_{c\_SC} \geq T_c \end{aligned} \quad \text{Equation 7-11}$$

where,

$$\begin{aligned} r_2 &= r_1 + (T_c - x_{c\_SC}) \cdot \tan \theta \quad \text{for } x_{c\_SC} < T_c \\ r_2 &= N / A \quad \text{for } x_{c\_SC} \geq T_c \end{aligned} \quad \text{Equation 7-12}$$

$$x_{c\_SC} = K_{SC} \cdot x_{c\_NDRC} \quad \text{Equation 7-13}$$

Modification factor equation,  $K_{SC}$ , was used to adjust the resultant value obtained from the modified NDRC equations applied to SC walls and to reduce the inherent conservatism.  $K_{SC}$  was

chosen from a few candidate equations after evaluating the performance of each equation as described in previous section 7.4.3. Following is the equation showing  $K_{SC}$ :

$$K_{SC} = 2.073 - 0.661 \cdot K + 0.688 \cdot \left( \frac{\alpha_p \cdot d}{T_c} \right) + 0.835 \cdot \left( \frac{x_{c\_NDRC}}{T_c} \right) \quad \text{Equation 7-14}$$

As illustrated in Figure 7-12 (a), this  $K_{SC}$  provides a level of confidence of about 50% (49.3%) which is appropriate for the best estimate approach aiming at the beyond design basis accident (BDBA).

Concrete wall perforation velocity,  $V_p$ , was formulated rearranging equations in NEI 07-13 as follows:

$$V_p = 1000 \cdot d \cdot \left( \frac{d}{1.44 \cdot K \cdot W \cdot N \cdot K_{SC}^2} \left( 2.2 \pm \sqrt{4.84 - 1.2 \left( \frac{T_c}{\alpha_p d} \right)} \right)^2 \right)^{5/9} \quad \text{Equation 7-15}$$

for  $\frac{T_c}{\alpha_p d} \leq 2.65$

$$V_p = 1000 \cdot d \cdot \left( \frac{d}{4K \cdot W \cdot N \cdot K_{SC}^2} \left( \frac{T_c}{1.29\alpha_p d} - 0.53 \right)^2 \right)^{5/9} \quad \text{Equation 7-16}$$

for  $2.65 < \frac{T_c}{\alpha_p d} < 3.27$

$$V_p = 1000 \cdot d \cdot \left( \frac{d}{K \cdot W \cdot N \cdot K_{SC}} \left( \frac{T_c}{1.29 \alpha_p d} - (0.53 + K_{SC}) \right) \right)^{5/9}$$

for  $\frac{T_c}{\alpha_p d} \geq 3.27$

Equation 7-17

$K_{SC}$  replaced the statistical variation coefficient,  $\beta$ , which was used in  $V_p$  equations in the three-step design method.

Residual velocity was calculated based on energy balance, which is described in NEI 07-13, as shown below:

$$V_r = \sqrt{\left( \frac{W}{W + W_{cf}} \right) \cdot (V_{imp}^2 - V_p^2)}$$

Equation 7-18

### Step 3: Calculate required steel faceplate thickness, $t_{p\_req}$

Borvik's cavity expansion theory (CET) was adopted in this step and the equation for calculating required steel faceplate thickness is presented as follows:

$$t_{p\_req} = 0.72 \sqrt{\frac{(12V_r)^2 m_t}{\frac{\pi}{2} d^2 \sigma_r}}$$

Equation 7-19

where,

$$m_t = \frac{W + W_{cf}}{386 \text{ in} / \text{s}^2}$$

Equation 7-20

The total mass of the projectile,  $m_t$ , consists of projectile weight,  $W$ , and concrete frustum weight,  $W_{cf}$ , divided by the acceleration of gravity.

For the von Mises yield criterion, true radial compressive stress,  $\sigma_r$ , is expressed as below:

$$\sigma_r = \frac{f_y}{\sqrt{3}} \left( 1 + \left( \frac{E}{\sqrt{3}f_y} \right)^n \int_0^b \frac{(-\ln(x))^n}{1-x} dx \right) \quad \text{Equation 7-21}$$

$$b = 1 - \frac{\sqrt{3}f_y}{E} \quad \text{Equation 7-22}$$

The three-step design method suggests two simplified equations to determine true radial compressive stress according to different strain hardening exponents or different steel faceplate thickness as follows:

$$\sigma_r = 5.1f_y + 101000 \quad \text{Equation 7-23}$$

$$\sigma_r = 3.9f_y + 64000 \quad \text{Equation 7-24}$$

Equation 7-23 was developed using an elastic modulus of 29,000 ksi and a strain hardening exponent ( $n$ ) of 0.2. It is applicable to steel faceplates which are thicker than or equal to 0.25 in. (6 mm). When a steel faceplates' thickness is less than 0.25 in. (6 mm), this equation will give unconservative results because the steel faceplates have smaller values of strain hardening coefficient between 0.08 to 0.1. Thus, Equation 7-24 was developed using a strain hardening exponent of 0.1, which is applicable to steel faceplates thinner than 0.25 in. (6 mm).

Calculation procedures of the proposed modified design method are presented in the flow chart in Figure 7-14. Major differences between the original three-step design method and the proposed modified design method are summarized in Table 7-2.

## 7.5 *Evaluation of the proposed modified design method*

### 7.5.1 Evaluation of the proposed modified design method - using the small-scale missile impact test data

Performance of the proposed modified design method was evaluated and its accuracy was verified in estimating perforation velocity of a projectile in SC walls. Perforation resistance curves were obtained using the modified design method and compared with the experimental test data and numerical parametric analyses data of the small-scale missile impact tests. The comparison is illustrated in Figure 7-15 to Figure 7-19.

In Figure 7-15 (a), when projectiles of 1.0 in. diameter are applied, the perforation resistance curve agrees well with the experimental test data. The estimated perforation velocity by the modified design method is exactly located in the perforation velocity range obtained from the experimental test data when projectile weight is 2.0 lbs. When projectile weight is 1.3 lbs, the estimated perforation velocity exceeds all the impact velocities which did not perforate the SC wall specimens. In Figure 7-15 (b), when projectiles of 1.0 in. diameter are applied, the perforation resistance curve shows a good agreement with the numerical parametric analyses data. For 3.5 lbs and 2.7 lbs projectiles, the perforation velocities estimated by the modified design method are exactly located in the perforation velocity range obtained from the numerical parametric analyses. For 1.3 lbs projectiles, the perforation velocity resulted from the numerical parametric analyses is located in the range from 1.6% to 5.0% greater than the perforation velocity estimated by the modified design method. For 2.0 lbs projectiles, the perforation velocity resulted from the

numerical parametric analyses is located in the range from 3.5% to 6.6% less than the perforation velocity estimated by the modified design method. This unconservative aspect, however, is acceptable considering the modified design method is based on the best estimation approach for the beyond design basis accident (BDBA). Thus, in both cases of experimental tests data and numerical parametric analyses data, the modified design method provided reasonable or acceptable estimates of perforation velocities which were increased by an average of 19.1% over the original three-step design method.

In Figure 7-16 (a), when projectiles of 1.5 in. diameter are applied, the perforation resistance curve agrees well with experimental test data when projectile weight is 1.3 lbs. When projectile weight is 3.5 lbs, the perforation resistance curve shows conservative aspect. Quantitative evaluation of the conservatism was not available because there was no test case in which SC wall specimen was perforated - when 3.5 lbs projectile was shot at 550 ft/s, the splitting damage mode occurred in the SC wall specimen which immediately precedes perforation. In Figure 7-16 (b), when projectiles of 1.5 in. diameter are applied, the perforation resistance curve shows a reasonable agreement with the numerical parametric analyses data. When projectile weights are 1.3 lbs and 2.0 lbs, estimated perforation velocities show a slightly conservative aspect. The perforation velocities obtained from the numerical parametric analyses are located in the range from 12.5% to 17.1%, and from 7.5% to 10.6% greater than the perforation velocity estimated by the modified design method, respectively, for 1.3 lbs and 2.0 lbs projectiles. When projectile weight is 3.5 lbs, the perforation velocity estimated by the modified design method is exactly located in the perforation velocity range obtained from the numerical parametric analyses. Thus, in both cases of experimental tests data and numerical parametric analyses data, the modified

design method provided reasonable or acceptable estimates of perforation velocities which were increased by an average of 10.4% over the original three-step design method.

In Figure 7-17 (a), when projectiles of 1.0 in. diameter are applied, the perforation resistance curve agrees well with the experimental tests data. Estimated perforation velocity exceeded all the test cases in which the projectiles were stopped by the SC walls - there was no test case in which SC wall was perforated. In Figure 7-17 (b), when projectiles of 1.0 in. diameter are applied, the perforation resistance curve shows reasonable agreement with the numerical parametric analyses data. The perforation velocity resulted from the numerical parametric analyses is located in the range from 6.2% to 9.7% less than the perforation velocity estimated by the modified design method when projectile weight is 2.0 lbs, and in the range from 0.4% to 4.4% less than the perforation velocity estimated by the modified design method when projectile weight is 2.7 lbs. This unconservative aspect, however, is acceptable considering the modified design method is based on the best estimation approach for the BDBA. In both cases, experimental tests data and numerical parametric analyses data, the modified design method provided reasonable or acceptable estimates of perforation velocities with the conservative aspect reduced by an average of 16.0%, compared to the original three-step design method.

In Figure 7-18 (a), when projectiles of 1.5 in. diameter are applied, the perforation resistance curve agrees well with the experimental tests data. Estimated perforation velocity exceeded all the test cases in which the projectiles were stopped by the SC walls - there was no test case in which SC wall was perforated. In Figure 7-18 (b), when projectiles of 1.5 in. diameter are applied, the perforation resistance curve shows a reasonable agreement with the numerical parametric analyses data. The perforation velocity resulted from the numerical parametric analyses is located in the range from 3.0% to 6.0% greater than the perforation velocity estimated by the

modified design method when projectile weight is 2.0 lbs, and in the range from 2.0% to 6.5% greater than the perforation velocity estimated by the modified design method when projectile weight is 3.5 lbs. In both cases, experimental tests data and numerical parametric analyses data, the modified design method provided reasonable or acceptable estimates of perforation velocities which were increased by an average of 7.0% over the original three-step design method.

In Figure 7-19 (a), when projectiles of 1.0 in. diameter are applied, the perforation resistance curve agrees well with the experimental test data. The estimated perforation velocity is exactly located in the perforation velocity range obtained from the experimental test data when projectile weight is 2.0 lbs. In Figure 7-19 (b), when projectiles of 1.0 in. diameter are applied, the perforation resistance curve shows a reasonable agreement with the numerical parametric analyses data. The perforation velocity resulted from the numerical parametric analyses is located in the range from 3.4% to 5.1% less than the perforation velocity estimated by the modified design method when projectile weight is 2.0 lbs, and in the range from 4.8% to 0.8% less than the perforation velocity estimated by the modified design method when projectile weight is 2.7 lbs. The unconservative aspect shown here, however, is acceptable considering the modified design method is based on the best estimation approach for the BDBA. In both cases, experimental tests data and numerical parametric analyses data, the modified design method provided reasonable or acceptable estimates of perforation velocities with the conservative aspect reduced by an average of 17.5%, compared to the original three-step design method.

Perforation velocity ranges obtained from both experimental tests and numerical analyses are summarized in Table 7-3 and Table 7-4;  $V_{des}$  is a design velocity calculated by the original three-step design method, and  $V_{m\_des}$  is a perforation velocity estimated by the modified design method.

## 7.5.2 Larger-scale missile impact tests

Following is a summary of the larger-scale missile impact tests conducted in South Korea, as a part of this research project. These larger-scale missile impact tests have also been summarized in conference papers and forthcoming journal papers.

### 7.5.2.1 Specimen design and material properties

Larger-scale SC wall specimens had identical global dimensions with the exception of a wall thickness. Width  $\times$  height dimensions were 2,000 mm (78.7 in.)  $\times$  2,000 mm (78.7 in.) for all test specimens and SC wall thickness varied from 240 mm (9.4 in.) to 480 mm (18.9 in.). Flexural reinforcement ratios ( $\rho$ ) varied from 3.7% to 5.0%. Tie bars were applied to only limited numbers of specimens providing a shear reinforcement ratio ( $\rho_t$ ) of 0.24% for two test cases in group 1. Steel faceplate's nominal yield strengths varied from 355 Mpa (51.4 ksi) to 460 Mpa (66.7 ksi). A concrete mixture with nominal specified strength of 35 Mpa (5072 psi) was used. The projectiles, made of solid steel, had a diameter of 150 mm with varied weight ranging from 40 Kg (88.2 lbf) to 80 Kg (176.4 lbf). The nose shape of the projectiles was rounded, but close to blunt due to low curvature of the projectiles' head.

Material properties of the steel faceplates were obtained from coupon tests. Their yield strengths were reported in Table 7-6. Concrete compressive strength was measured on the day of the test and reported in Table 7-6. Details of the SC wall specimen design and projectile parameters are summarized in Table 7-6.

### 7.5.2.2 Test matrix and test results

A total of ten test cases were excerpted for use in this research from thirteen larger-scale missile impact tests in Korea. One of the excluded test cases failed to get useful test data due to an early triggered projectile. The other two excluded tests were deemed not appropriate for use (for

evaluation purpose) due to inconsistency in the SC wall specimen design in the test group to which they belonged. Details of the test matrix and test results are described in Table 7-6.

The test matrix consisted of five test groups according to design features of the SC wall specimens. Each test group had two test cases. In group 1, the SC wall specimens had a wall thickness ( $T_{sc}$ ) of 320 mm (12.6 in.), flexural reinforcement ratio of 3.8%, and shear reinforcement ratio of 0.24%. Test case number 1 of group 1 fired a 60 Kg (132 lbf) projectile at a velocity of 165 m/s (541 ft/s). Test results showed that the SC wall specimen stopped the projectile with splitting damage mode occurring at the rear steel faceplate. Test case number 2 of group 1 fired the same weight projectile as test case number 1 of group 1 at a velocity of 180 m/s (591 ft/s). Test results demonstrated that the SC wall specimen was perforated by the projectile and perforation damage mode occurred at the rear steel faceplate. Thus, perforation velocity can be determined to be in the range between 21.3% and 32.4% greater than the design velocity,  $V_{des}$ , which was calculated by applying the three-step design method.

In group 2, SC wall specimens had a wall thickness of 480 mm (18.9 in.) and flexural reinforcement ratio of 3.8%. Test case number 1 of group 2 fired an 80 Kg (176 lbf) projectile at a velocity of 198 m/s (650 ft/s). Test results showed that the SC wall specimen stopped the projectile and bulging damage mode occurred at the rear steel faceplate. Test case number 2 of group 2 fired the same weight projectile as test case number 1 of group 2 at a velocity of 224 m/s (735 ft/s). Test results demonstrated that the SC wall specimen was perforated by the projectile and perforation damage mode occurred at the rear steel faceplate. Thus, perforation velocity can be determined to be in the range between 21.5% and 37.4% greater than the design velocity ( $V_{des}$ ).

In group 3, SC wall specimens had a wall thickness of 240 mm (9.4 in.) and flexural reinforcement ratio of 5.0%. Test case number 1 of group 3 fired a 40 Kg (88 lbf) projectile at a

velocity of 179 m/s (587 ft/s). Test results showed that the SC wall specimen stopped the projectile and bulging damage mode occurred at the rear steel faceplate. Test case number 2 of group 3 fired the same weight projectile as test case number 1 of group 3 at a velocity of 203 m/s (666 ft/s). Test result demonstrated that the SC wall specimen was perforated by the projectile and perforation damage mode occurred at the rear steel faceplate. Thus, perforation velocity can be determined to be in the range between 16.2% and 31.8% greater than the design velocity ( $V_{des}$ ).

In group 4, SC wall specimens had a wall thickness of 360 mm (14.2 in.) and flexural reinforcement ratio of 5.0%. Test case number 1 of group 4 fired a 60 Kg (132 lbf) projectile at a velocity of 180 m/s (591 ft/s). Test results showed that the SC wall specimen stopped the projectile and bulging damage mode occurred at the rear steel faceplate. Test case number 2 of group 4 fired the same weight projectile as test case number 1 of group 4 at a velocity of 198 m/s (650 ft/s). Test results demonstrated that the SC wall specimen also stopped the projectile and bulging damage mode occurred at the rear steel faceplate. Thus, a perforation velocity was not determined experimentally for this test group.

In group 5, SC wall specimens had the same cross-section design configuration as the specimens in group 4, with the exception of the steel faceplate strength. High strength steel (HAS 600) with a nominal yield strength of 460 MPa was used. SM 355 with a nominal yield strength of 355 MPa steel was used for the other test groups. Test case number 1 of group 5 fired an 80 Kg (176 lbf) projectile at a velocity of 130 m/s (427 ft/s). The test result showed that the SC wall specimen stopped the projectile and bulging damage mode occurred at the rear steel faceplate. Test case number 2 of group 5 fired the same weight projectile as test case number 1 of group 5 at a velocity of 168 m/s (551 ft/s). Test results demonstrated that the SC wall specimen was perforated by the projectile and perforation damage mode occurred at the rear steel faceplate. Thus,

perforation velocity can be determined to be in the range between -14.5% and 10.5% greater than the design velocity ( $V_{des}$ ).

### 7.5.3 Evaluation of the proposed modified design method - using the larger-scale missile impact test data

Performance of the modified design method was also evaluated using the larger-scale missile impact tests. Perforation velocities for the SC wall specimens in the five test groups were calculated using the modified design method and marked on the larger-scale missile impact tests data in Figure 7-20 through Figure 7-24. Perforation resistance curves obtained from the original three-step design method were also presented in the figures for comparison.

The modified design method yielded somewhat conservative results in test group 1 as depicted in Figure 7-20. Estimated perforation velocity by the modified design method was less than the perforation velocity range observed from the experimental tests results. That is, the perforation velocity from the experimental tests is located in a range from 16.2% to 26.8% greater than the perforation velocity estimated by the modified design method. Nonetheless, it was found that conservatism was reduced over the original three-step design method. Perforation velocity ranges according to the two design methods are summarized in Table 7-6 to compare their conservative aspects.

In Figure 7-21, the modified design method shows somewhat conservative results in the experimental test results of test group 2. Perforation velocity estimated by the modified design method was less than the perforation velocity range observed from the experimental tests results. The perforation velocity from the experimental tests is in the range from 9.4% to 23.8% greater than the perforation velocity estimated by the modified design method. Conservatism was reduced significantly in the modified design method compared to the original three-step design method. Details of the comparison between the two design methods are summarized in Table 7-6.

In Figure 7-22, the modified design method shows equivalent results to the original three-step design method. The estimated perforation velocity using the modified design method was less than the perforation velocity range observed from the experimental tests results of group 3. That is, the perforation velocity from the experimental tests was in a range from 16.2% to 31.8% greater than the perforation velocity estimated by the modified design method.

In Figure 7-23, the modified design method shows conservative results for test group 4. A perforation velocity range is not found in this test group, because there is no test case in which perforation damage mode occurred. Estimated perforation velocity by the modified design method is less than the impact velocities of the projectiles which were stopped by the SC wall specimens. Thus, it is not possible to evaluate the conservative aspect of the modified design method quantitatively. The modified design method did, however, provide improved results with conservatism reduced over the original three-step design method.

In Figure 7-24, the modified design method is in a good agreement with the experimental tests results of test group 5. Estimated perforation velocity by the modified design method is located in the perforation velocity range observed from the experimental tests data. The perforation velocity from the experimental tests is located in the range from -16.7% to 7.7% greater than the perforation velocity estimated by the modified design method. Conservatism was reduced in the modified design method compared to the original three-step design method. Details of the comparison between the two design methods are summarized in Table 7-6.

## 7.6 Conclusions

Previously, the three-step design method for SC walls has been experimentally proven to have a considerable conservative aspect. Its conservatism was inherited by a statistical variation coefficient ( $\beta$ ) to ensure a high level of confidence which was 95%. This level of confidence was

measured based on the experimental test database which consisted of 58 test cases of SC wall missile impact tests. The value of  $\beta$  was mainly influenced by the deviation of the penetration depth of a projectile into the concrete core obtained from experimental tests results and manually calculated results by using the modified NDRC equations.

In this chapter, a modified three-step design method was proposed using the combined experimental tests database. Then, the performance of the modified three-step design method was evaluated and verified based on the experimental test data as well as numerical parametric analysis data. New features of the modified design method compared to the original three-step design method are as follows:

- 1) Modification factor equation,  $K_{sc}$ , was proposed.  $K_{sc}$  adjusts the penetration depth value of a projectile into concrete calculated by the modified NDRC equations to fit for SC walls.

- 2) Updated local failure mechanism (proposed in CHAPTER 4) was incorporated. Geometric properties in the cross-section of SC walls associated with concrete frustum formation were revised from the original three-step design method, based on the observation of the experimental investigations on the small-scale missile impact tests.

- 3) The modified design method was developed for use in the BDBA. Best estimate approach was adopted with the level of confidence of 50%. The original three-step design method has the level of confidence of 95% which is appropriate for the design basis accident (DBA).

The proposed modified design method provided reasonable results for both experimental tests data and numerical parametric analyses data of the small-scale missile impact tests. The modified design method generated a perforation resistance curve in which the perforation velocities were increased by an average of 17.5% for 1.0 in. diameter projectile and 8.7% for 1.5 in. diameter projectile, respectively, over the original three-step design method.

The proposed modified design method was also evaluated based on the larger-scale missile impact tests from Korea. These comparisons verified the improved performance of the modified design method over the original three-step design method. This method provided perforation velocities increased by an average of 5.1% for all test groups with considerably reduced conservatism.

Table 7-1 Summary of penetration depth values from experimental tests and manual calculations

<i>Test group &amp; No.</i>	<i>Test case identifier</i>	<i>V<sub>imp</sub></i> (ft/s)	<i>Experimental test</i>		<i>Manual calculation</i>		<i>Ratio</i> $x_{c\_calc}/x_{c\_test}$
			$x_{c\_test}$ (in)	$x_{c\_test}/T_c$	$x_{c\_calc}$ (in)	$x_{c\_calc}/T_c$	
<i>Gr. 1</i>	1 3.7-0.37-50-1.0-1.3-554	593	2.06	0.54	1.90	0.49	0.92
	2 3.7-0.37-50-1.0-1.3-677	674	3.06	0.80	2.14	0.56	0.70
	3 3.7-0.37-50-1.0-2.0-430	424	1.56	0.41	1.66	0.43	1.06
	4 3.7-0.37-50-1.0-2.0-525	513	3.16	0.82	1.97	0.51	0.62
	5 3.7-0.53-50-1.5-1.3-660	667	1.38	0.36	1.71	0.44	1.24
	6 3.7-0.53-50-1.5-1.3-750	760	2.00	0.52	1.92	0.50	0.96
	7 3.7-0.53-50-1.0-2.0-513	640	-	-	-	-	-
	8 3.7-0.53-50-1.0-2.0-626	710	-	-	-	-	-
	9 3.7-1.23-50-1.5-3.5-380	550	4.00	1.04	2.38	0.62	0.60
	10 3.7-1.23-50-1.5-3.5-465	489	1.91	0.50	2.15	0.56	1.13
<i>Gr. 2</i>	1 5.2-0.48-50-1.0-2.0-445	467	2.09	0.55	1.81	0.48	0.86
	2 5.2-0.48-50-1.0-2.0-544	549	3.31	0.87	2.09	0.55	0.63
	3 5.2-0.48-50-1.5-3.5-408	410	1.34	0.35	1.90	0.50	1.41
	4 5.2-0.48-50-1.5-3.5-498	484	2.41	0.63	2.21	0.58	0.92
<i>Gr. 3</i>	1 3.7-0.37-65-1.0-2.0-443	539	3.16	0.82	2.10	0.55	0.67
	2 3.7-0.37-65-1.0-2.0-541	634	-	-	-	-	-

Table 7-2 Comparison between the three-step design method and the proposed modified design method

	<b><i>Original three-step design method</i></b> (Bruhl et al. 2015)	<b><i>Modified design method</i></b>
<b><i>Step 1</i></b>	<u>Tentative sizing of the concrete wall thickness</u>	
	<ul style="list-style-type: none"> <li>- 70% of the conventional RC walls (NEI 07-13, DOE-STD-3014)</li> <li>- Or other design restrictions</li> </ul>	- Same
<b><i>Step 2</i></b>	<u>Determine residual velocity of projectile and concrete frustum upon impact</u>	
	<ul style="list-style-type: none"> <li>- Modified NDRC equations to determine perforation velocity, <math>V_p</math>, of the concrete wall</li> <li>- Statistical variability factor, <math>\beta</math>, to secure a level of confidence</li> </ul>	<ul style="list-style-type: none"> <li>- Proposed modification factor equation, <math>K_{sc}</math>, combined with the modified NDRC equations to determine <math>V_p</math></li> <li>- Proposed a new failure mechanism</li> </ul>
<b><i>Step 3</i></b>	<u>Determine required rear steel plate thickness to prevent perforation</u>	
	- Equations from Borvik et al. (2009)	- Same
<b><i>Failure mechanism</i></b>		

Table 7-3 Comparison of perforation velocity ranges obtained from experimental tests

<i>Group 1</i>							<i>Group 2</i>					
<i>1.0 in. diameter Proj.</i>				<i>1.5 in. diameter Proj.</i>			<i>1.0 in. diameter Proj.</i>			<i>1.5 in. diameter Proj.</i>		
$W_p$ (lbs)	$V_{imp}$ (ft/sec)	$V_{imp}/V_{m\_des}$	$V_{m\_des}/V_{des}$	$V_{imp}$ (ft/sec)	$V_{imp}/V_{m\_des}$	$V_{m\_des}/V_{des}$	$V_{imp}$ (ft/sec)	$V_{imp}/V_{m\_des}$	$V_{m\_des}/V_{des}$	$V_{imp}$ (ft/sec)	$V_{imp}/V_{m\_des}$	$V_{m\_des}/V_{des}$
1.3	-	-	-	-	-	-	-	-	-	-	-	-
2.0	513 - 640	0.888 - 1.107	1.192	-	-	-	-	-	-	-	-	-
2.7	-	-	-	-	-	-	-	-	-	-	-	-
3.5	-	-	-	-	-	-	-	-	-	-	-	-

<i>Group 3</i>						
<i>1.0 in. diameter Proj.</i>				<i>1.5 in. diameter Proj.</i>		
$W_p$ (lbs)	$V_{imp}$ (ft/sec)	$V_{imp}/V_{m\_des}$	$V_{m\_des}/V_{des}$	$V_{imp}$ (ft/sec)	$V_{imp}/V_{m\_des}$	$V_{m\_des}/V_{des}$
1.3	-	-	-	-	-	-
2.0	539 - 634	0.917 - 1.078	1.176	-	-	-
2.7	-	-	-	-	-	-
3.5	-	-	-	-	-	-

Table 7-4 Comparison of perforation velocity ranges obtained from numerical analyses

<i>Group 1</i>							<i>Group 2</i>					
<i>1.0 in. diameter Proj.</i>				<i>1.5 in. diameter Proj.</i>			<i>1.0 in. diameter Proj.</i>			<i>1.5 in. diameter Proj.</i>		
$W_p$ (lbs)	$V_{imp}$ (ft/sec)	$V_{imp}/V_{m\_des}$	$V_{m\_des}/V_{des}$	$V_{imp}$ (ft/sec)	$V_{imp}/V_{m\_des}$	$V_{m\_des}/V_{des}$	$V_{imp}$ (ft/sec)	$V_{imp}/V_{m\_des}$	$V_{m\_des}/V_{des}$	$V_{imp}$ (ft/sec)	$V_{imp}/V_{m\_des}$	$V_{m\_des}/V_{des}$
1.3	745 - 770	1.016 - 1.050	1.196	912 - 950	1.125 - 1.171	1.108	-	-	-	-	-	-
2.0	540 - 558	0.934 - 0.965	1.192	690 - 710	1.075 - 1.106	1.103	528 - 549	0.903 - 0.938	1.161	690 - 710	1.030 - 1.060	1.072
2.7	475 - 495	0.967 - 1.008	1.189	-	-	-	475 - 495	0.956 - 0.996	1.159	-	-	-
3.5	413 - 430	0.969 - 1.009	1.187	465 - 477	0.979 - 1.004	1.100	-	-	-	506 - 528	1.020 - 1.065	1.067

<i>Group 3</i>						
<i>1.0 in. diameter Proj.</i>			<i>1.5 in. diameter Proj.</i>			
$W_p$ (lbs)	$V_{imp}$ (ft/sec)	$V_{imp}/V_{m\_des}$	$V_{m\_des}/V_{des}$	$V_{imp}$ (ft/sec)	$V_{imp}/V_{m\_des}$	$V_{m\_des}/V_{des}$
1.3	-	-	-	-	-	-
2.0	558 - 568	0.949 - 0.966	1.176	-	-	-
2.7	475 - 495	0.952 - 0.992	1.174	-	-	-
3.5	-	-	-	-	-	-

Table 7-5 Summary of test matrix and results of larger-scale missile impact tests

<i>Test group /No.</i>	<i>Specimen ID</i>	$T_{sc}$ (mm)	$t_p$ (mm)	$f'_c$ (MPa)	$f_y^{pl}$ (MPa)	$\rho$ (%)	$\rho_t$ (%)	$W_p$ (Kgf)	$V_{imp}$ (m/s)	$V_{des}$ (m/s)	$V_{imp}/V_{des}$	$V_{m\_des}$ (m/s)	$V_{imp}/V_{m\_des}$	$V_{m\_des}/V_{des}$	<i>Test result</i> *	<i>Damage mode</i> **
Gr. 1	SC-T320-3.8-tie	320	6	34.2	400	3.75	0.24	60	165	136	1.213	142	1.162	1.044	Stop	S
1 2	SC-T320-3.8-tie	320	6	32.6	400	3.75	0.24	60	180	136	1.324	142	1.268	1.044	Perf.	P
Gr. 1	SC-T480-3.8	480	9	37.3	370	3.75	-	80	198	163	1.215	181	1.094	1.110	Stop	B
2 2	SC-T480-3.8	480	9	35.4	370	3.75	-	80	224	163	1.374	181	1.238	1.110	Perf.	P
Gr. 1	SC-T240-5.0	240	6	29.7	400	5.00	-	40	179	154	1.162	154	1.162	1.000	Stop	B
3 2	SC-T240-5.0	240	6	34.5	400	5.00	-	40	203	154	1.318	154	1.318	1.000	Perf.	P
Gr. 1	SC-T360-5.0	360	9	37.1	370	5.00	-	60	180	161	1.118	167	1.078	1.037	Stop	B
4 2	SC-T360-5.0	360	9	31.2	370	5.00	-	60	198	161	1.230	167	1.186	1.037	Stop	B
Gr. 1	SC-T360-5.0-HSA	360	9	32.5	510	5.00	-	80	130	152	0.855	156	0.833	1.026	Stop	B
5 2	SC-T360-5.0-HSA	360	9	32.9	510	5.00	-	80	168	152	1.105	156	1.077	1.026	Perf.	P

\* Stop: The specimen stopped the projectile  
 Perf.: The specimen was perforated by the projectile

\*\* B: Bulging, S: Splitting, P: Perforating

Table 7-6 Comparison of perforation velocity ranges obtained from experimental tests - Larger-scale missile impact tests

<i>Group 1</i>					<i>Group 2</i>				<i>Group 3</i>			
$W_p$ (Kg)	$V_{imp}$ (m/sec)	$V_{imp}/V_{des}$	$V_{imp}/V_{m_{des}}$	$V_{m_{des}}/V_{des}$	$V_{imp}$ (m/sec)	$V_{imp}/V_{des}$	$V_{imp}/V_{m_{des}}$	$V_{m_{des}}/V_{des}$	$V_{imp}$ (m/sec)	$V_{imp}/V_{des}$	$V_{imp}/V_{m_{des}}$	$V_{m_{des}}/V_{des}$
40	-	-	-	-	-	-	-	-	179 - 203	1.162 - 1.318	1.162 - 1.318	1.000
60	165 - 180	1.213 - 1.324	1.162 - 1.268	1.044	-	-	-	-	-	-	-	-
80	-	-	-	-	198 - 224	1.215 - 1.374	1.094 - 1.238	1.110	-	-	-	-

<i>Group 4</i>					<i>Group 5</i>			
$W_p$ (Kg)	$V_{imp}$ (m/sec)	$V_{imp}/V_{des}$	$V_{imp}/V_{m_{des}}$	$V_{m_{des}}/V_{des}$	$V_{imp}$ (m/sec)	$V_{imp}/V_{des}$	$V_{imp}/V_{m_{des}}$	$V_{m_{des}}/V_{des}$
40	-	-	-	-	-	-	-	-
60	-	-	-	-	-	-	-	-
80	-	-	-	-	130 - 168	0.855 - 1.105	0.833 - 1.077	1.026

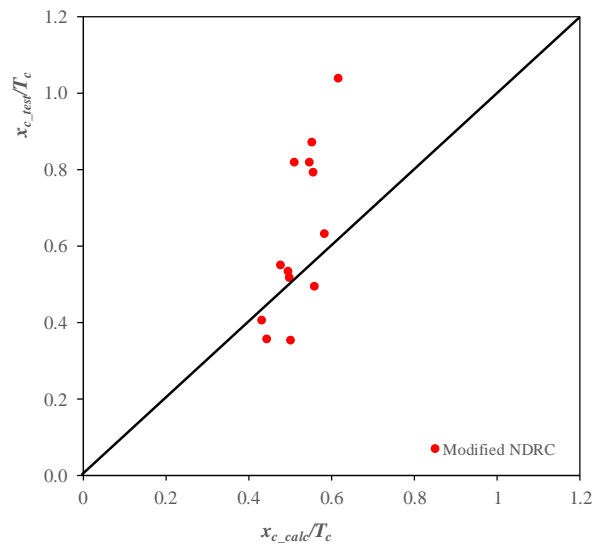


Figure 7-1 Comparison of penetration depth between measured values and calculated values

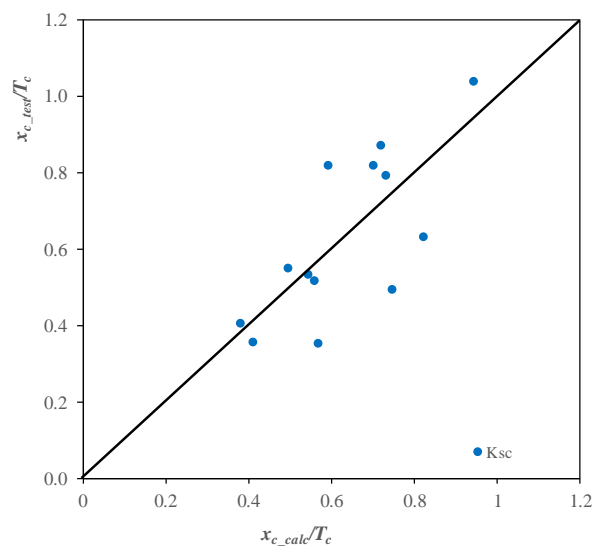


Figure 7-2 Comparison of penetration depth between measured values and calculated values by using the modification factor equation  $K_{SC}$

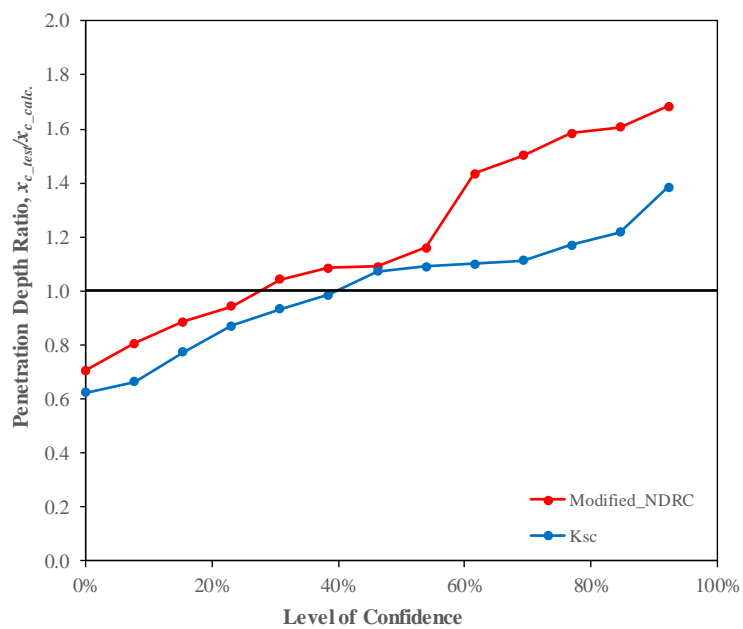
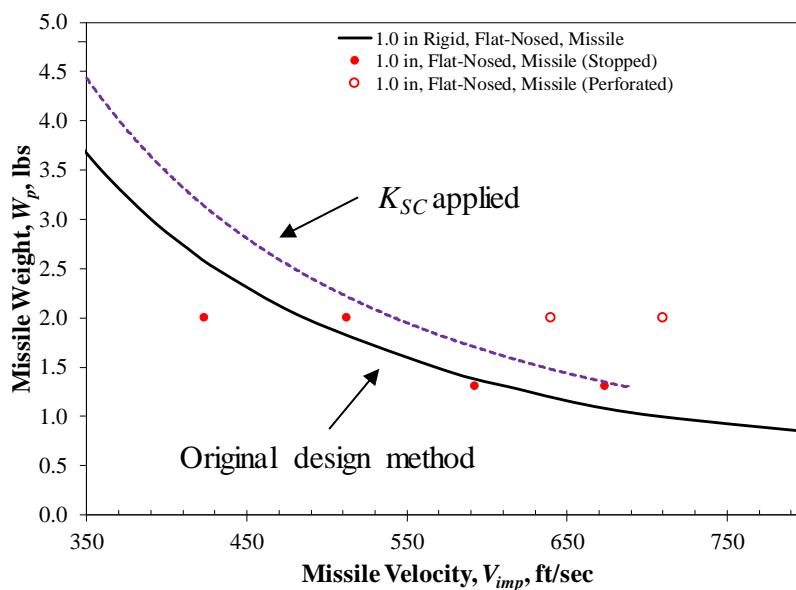
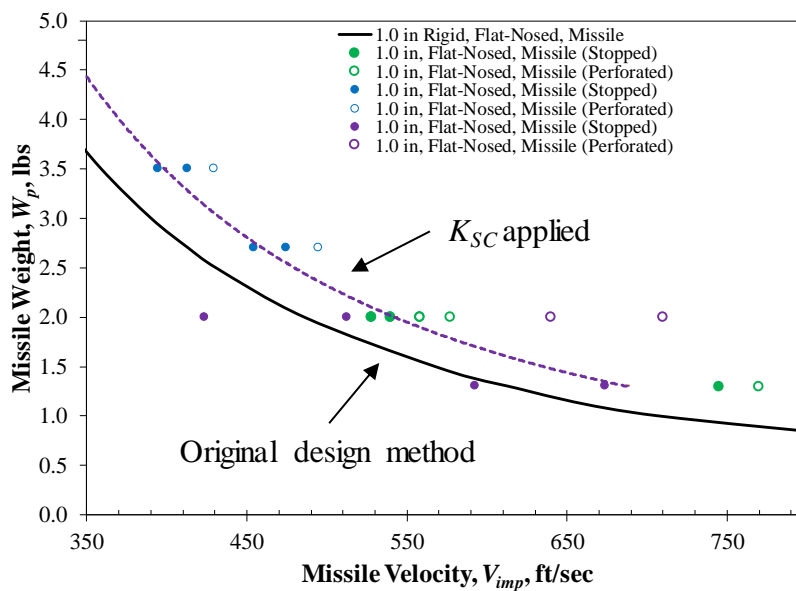


Figure 7-3 Degree of conservatism in modification factor equation  $K_{SC}$  and modified NDRC equations in estimating penetration depth in terms of level of confidence

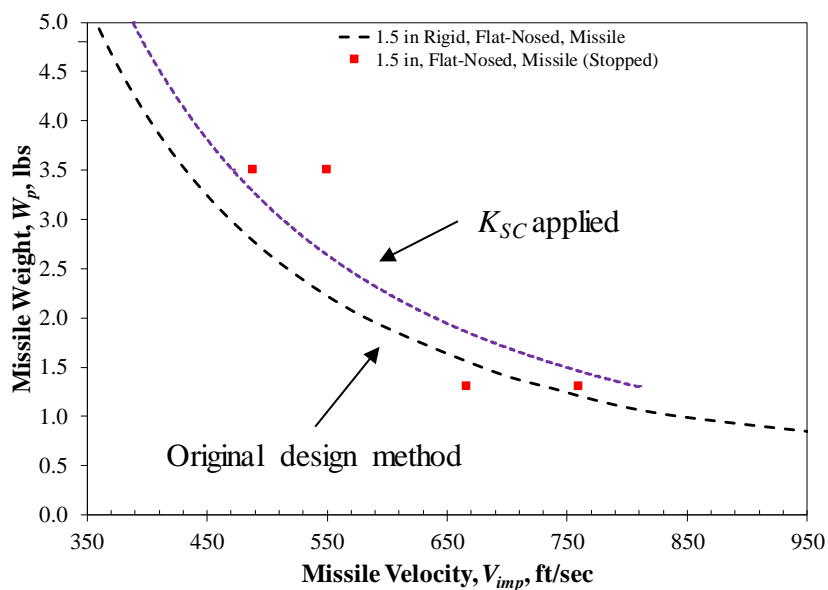


(a) On experimental tests data

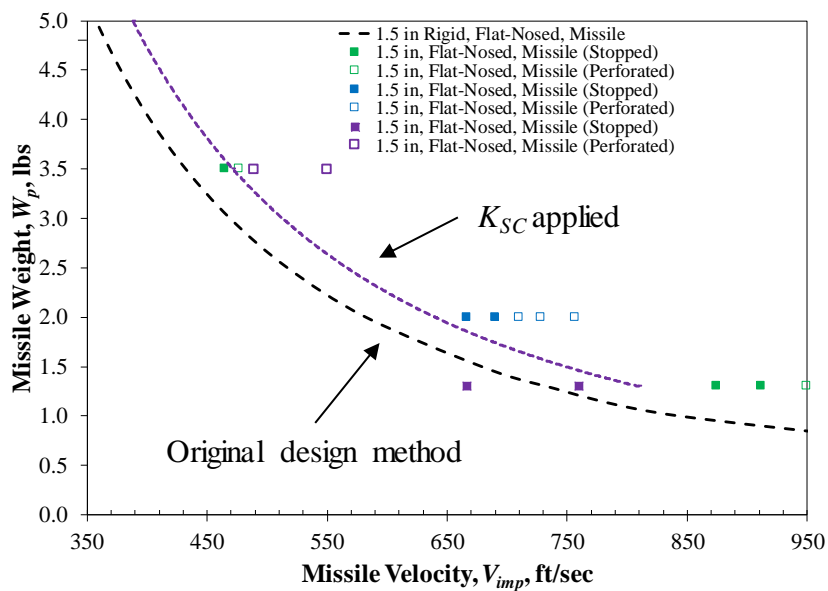


(b) On numerical parametric analyses data

Figure 7-4 Perforation resistance curves on the small-scale missile impact tests data: for 1.0 in. diameter projectile in Gr. 1

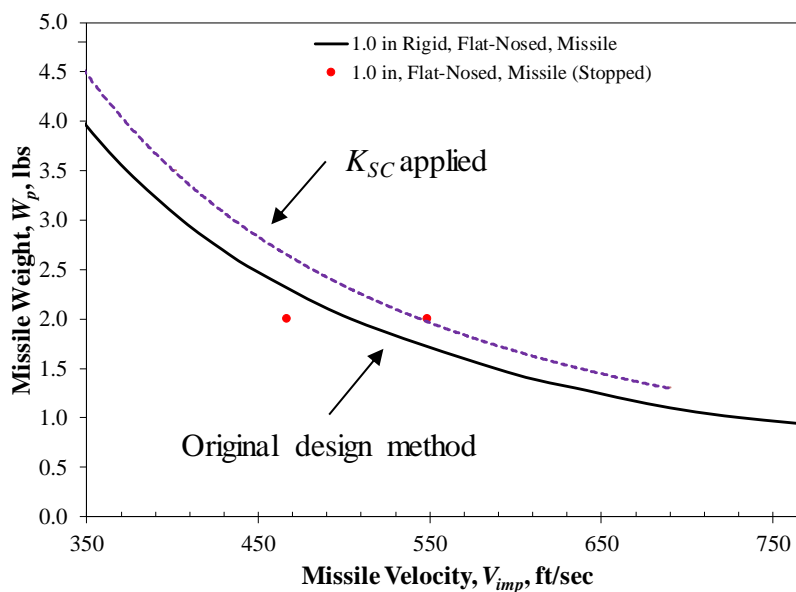


(a) On experimental tests data

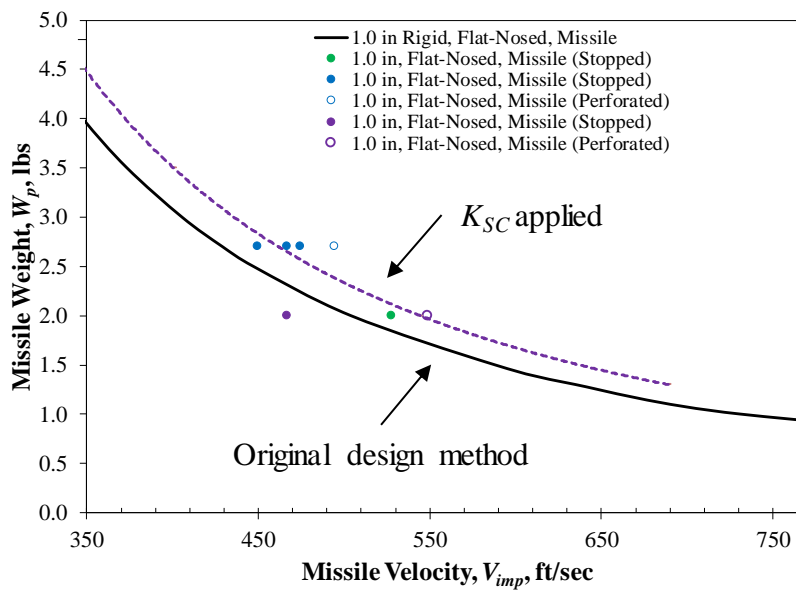


(b) On numerical parametric analyses data

Figure 7-5 Perforation resistance curves on the small-scale missile impact tests data: for 1.5 in. diameter projectile in Gr. 1

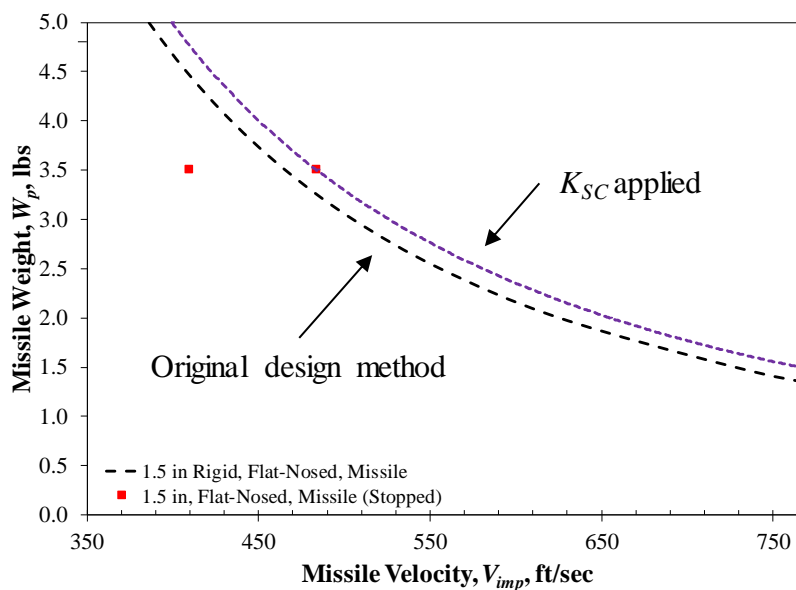


(a) On experimental tests data

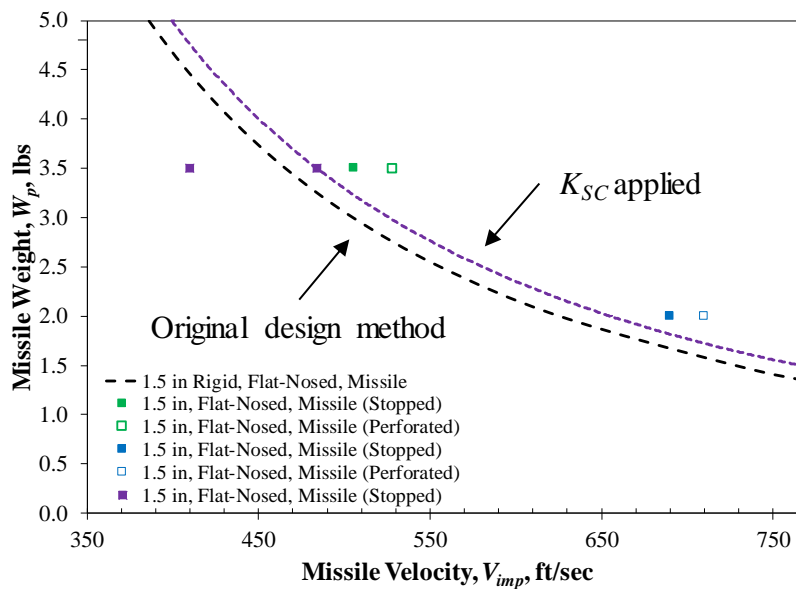


(b) On numerical parametric analyses data

Figure 7-6 Perforation resistance curves on the small-scale missile impact tests data: for 1.0 in. diameter projectile in Gr.2

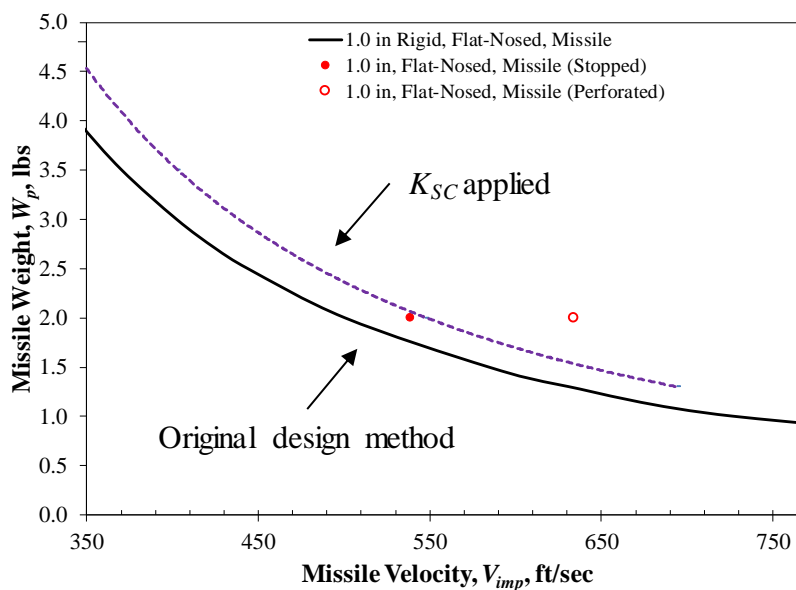


(a) On experimental tests data

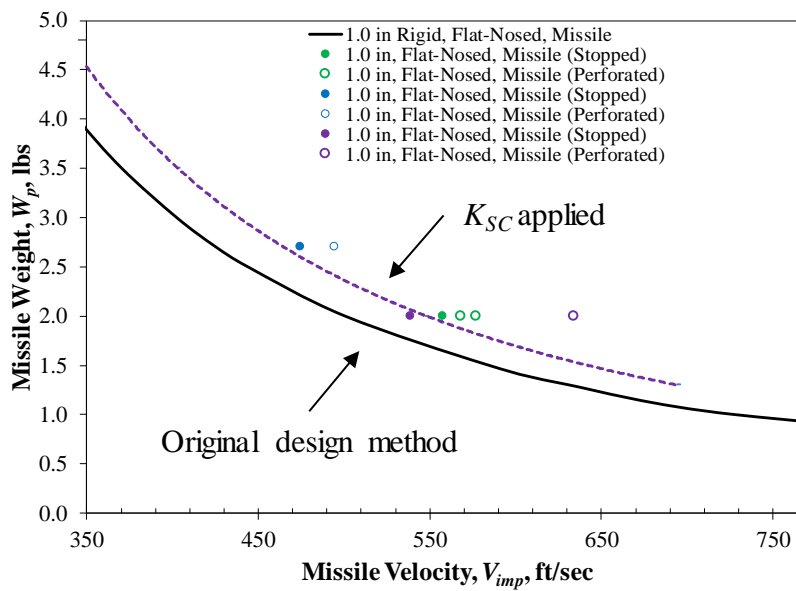


(b) On numerical parametric analyses data

Figure 7-7 Perforation resistance curves on the small-scale missile impact tests data: for 1.5 in. diameter projectile in Gr.2

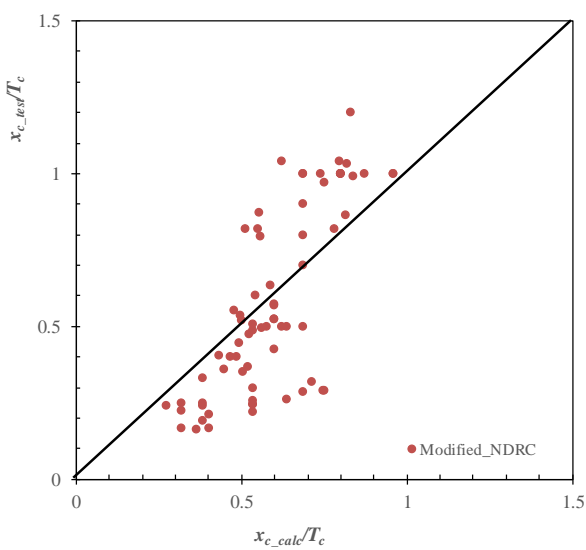


(a) On experimental tests data



(b) On numerical parametric analyses data

Figure 7-8 Perforation resistance curves on the small-scale missile impact tests data: for 1.0 in. diameter projectile in Gr.3



(a) Modified NDRC

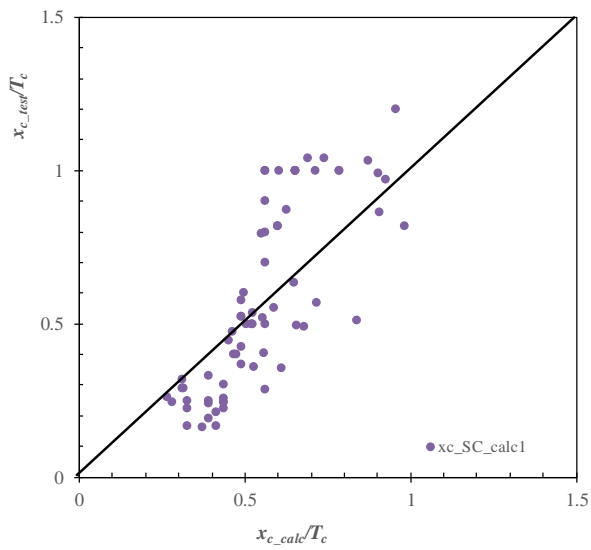
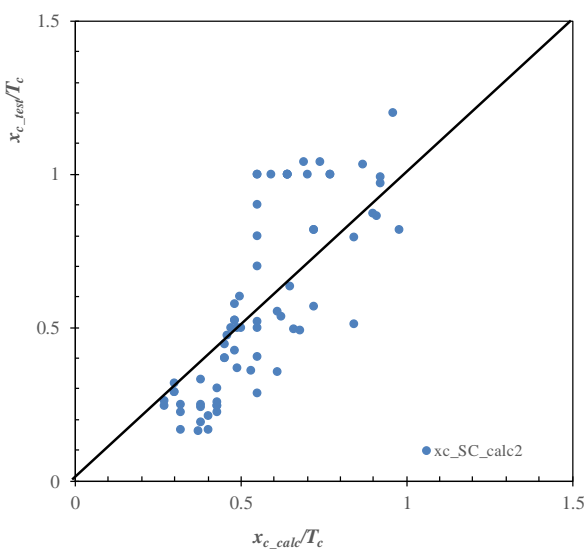
(b)  $x_{c\_SC\_calc1}$ (c)  $x_{c\_SC\_calc2}$ 

Figure 7-9 Comparison of penetration depth between measured value and calculated value by the modified NDRC equations and  $x_{c\_SC\_cal}$  equations

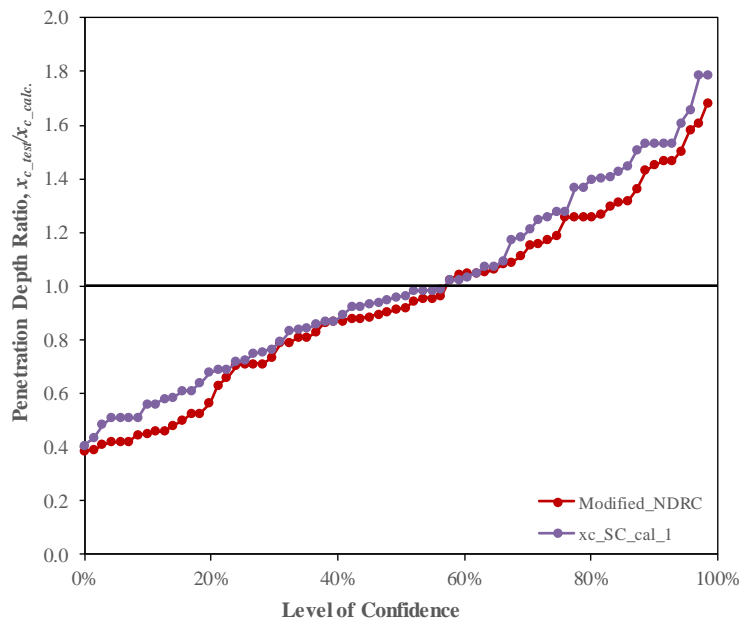
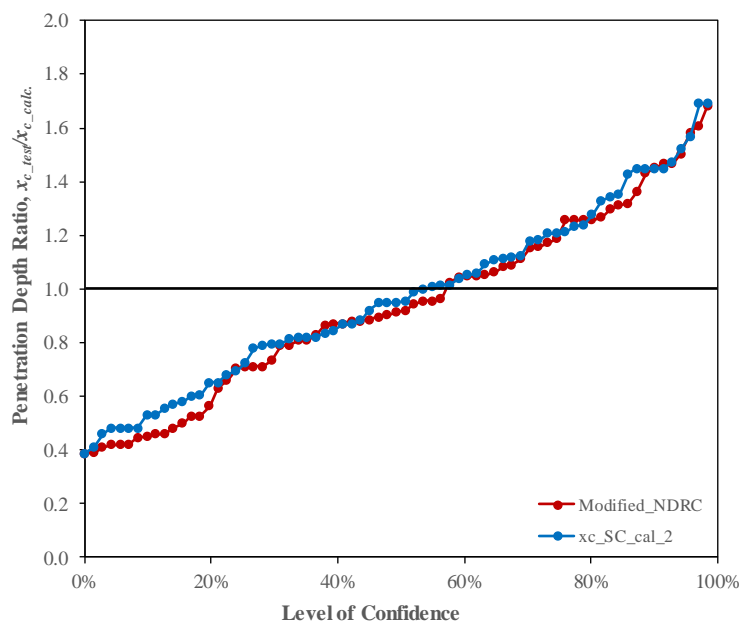
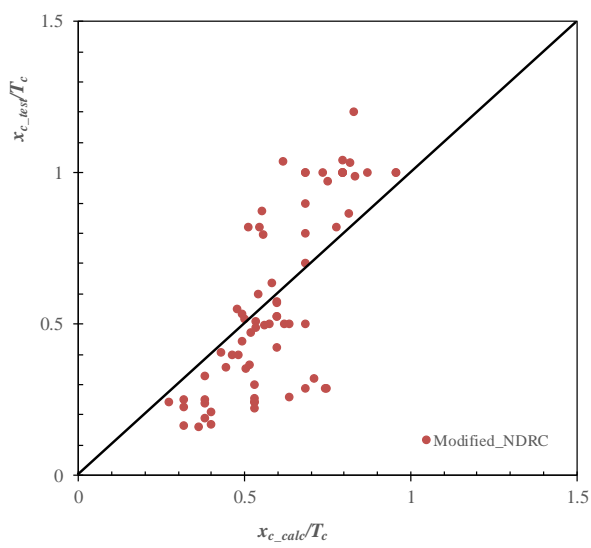
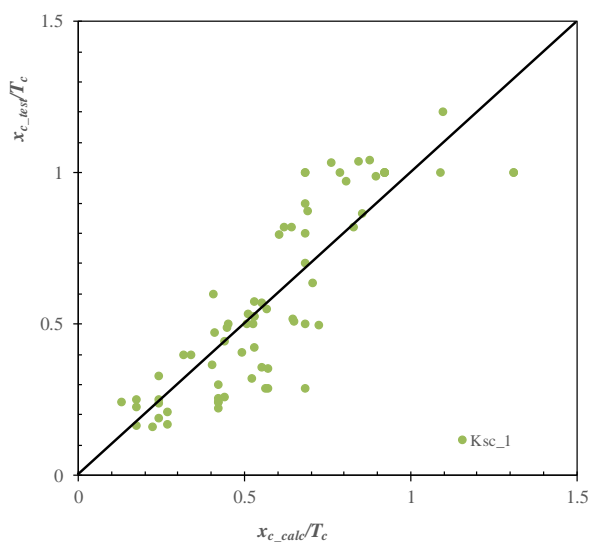
(a)  $x_{c\_SC\_calc1}$ (b)  $x_{c\_SC\_calc2}$ 

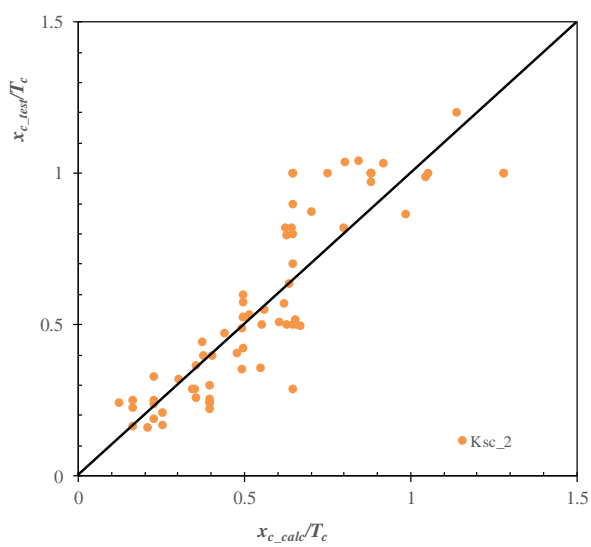
Figure 7-10 Comparison of the degree of conservatism of each penetration depth estimating equation in terms of the level of confidence



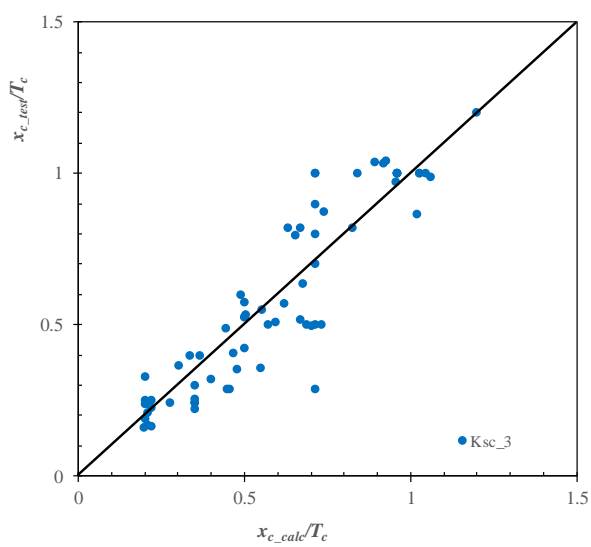
(a) Modified NDRC



(b) Ksc\_1



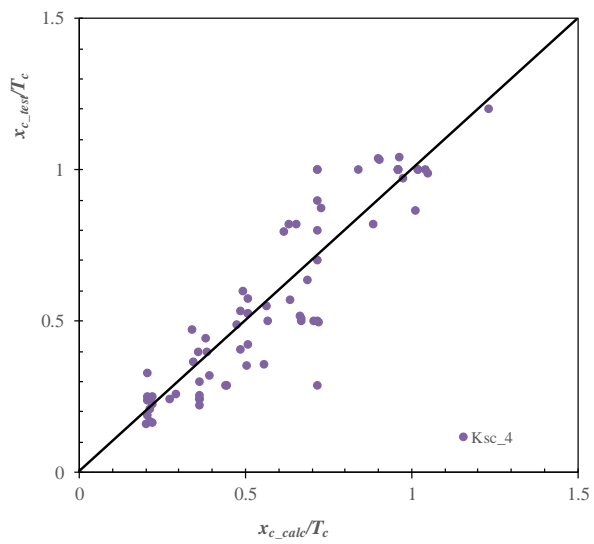
(c) Ksc\_2



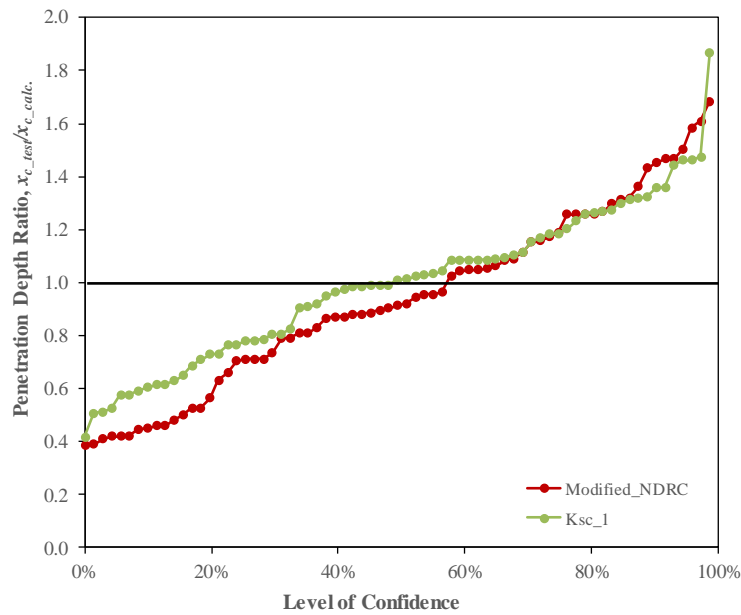
(d) Ksc\_3

Figure 7-11 Comparison of penetration depth between measured value and calculated value by using the modification factor equation,  $K_{SC}$

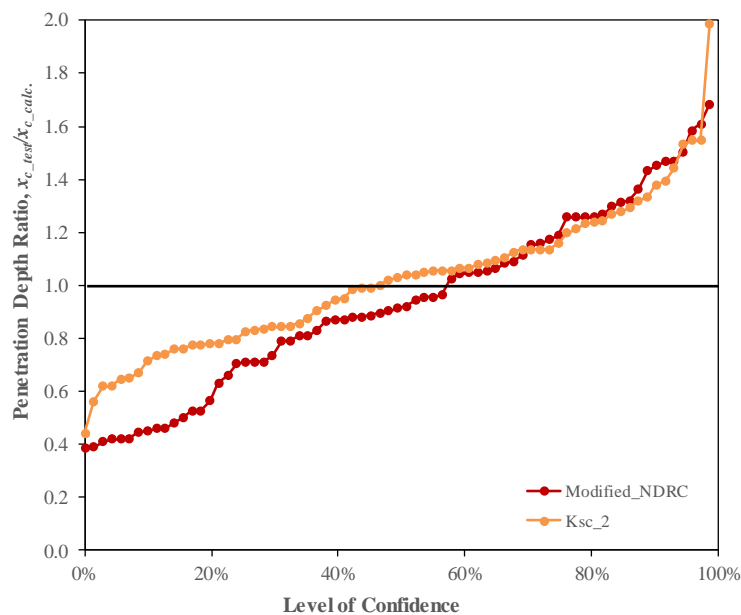
Figure 7-11 continued



(e) Ksc\_4



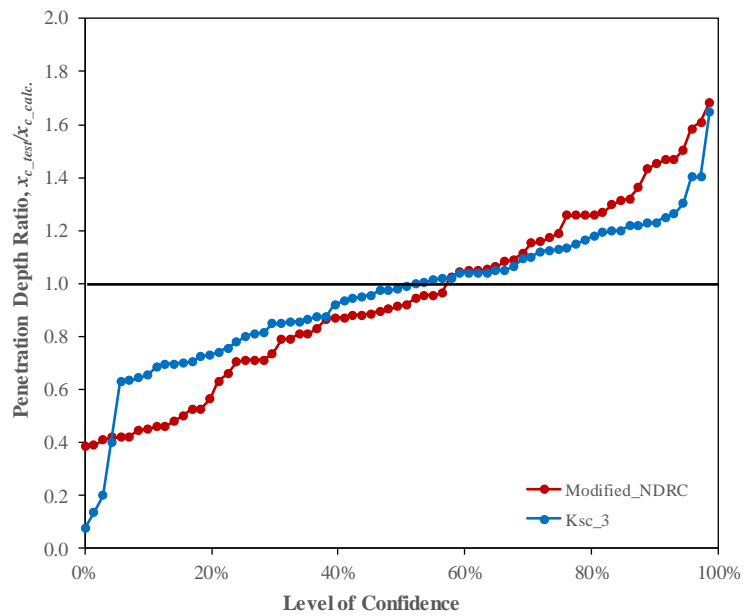
(a) Ksc\_1



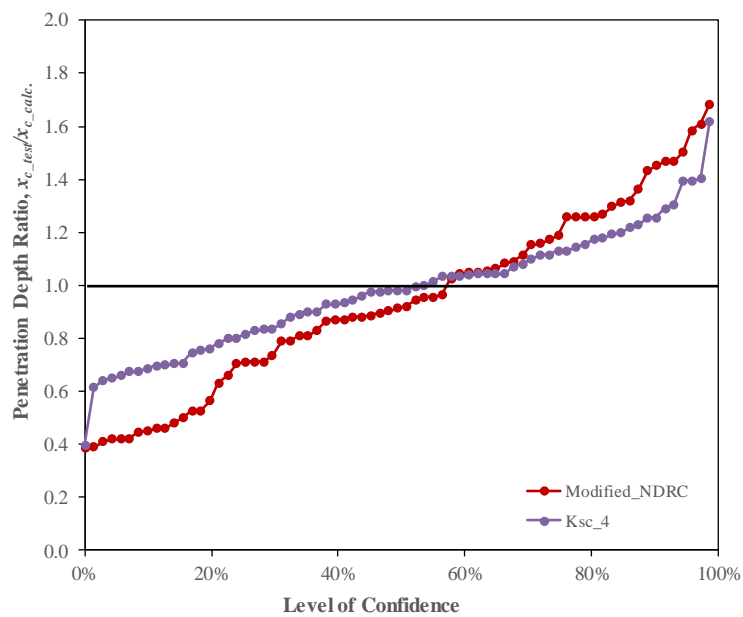
(b) Ksc\_2

Figure 7-12 Comparison of the degree of conservatism of each modification factor equation in estimating penetration depth in terms of the level of confidence

Figure 7-12 continued



(c) Ksc\_3



(d) Ksc\_4

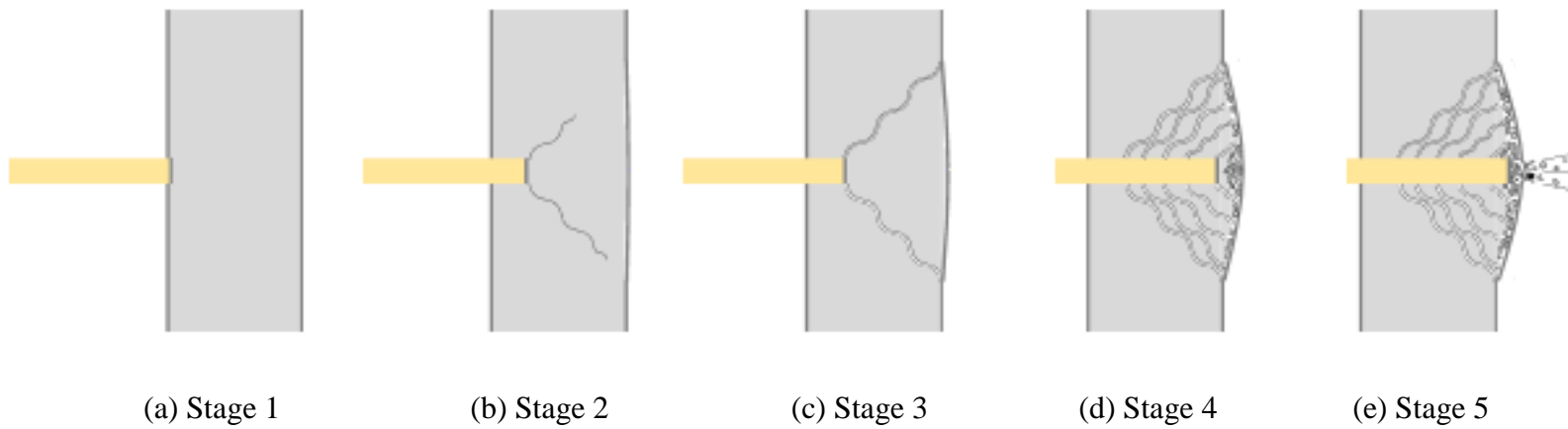


Figure 7-13 A failure mechanism proposed based on the experimental investigations on the small-scale missile impact tests results (from Figure 4-47)

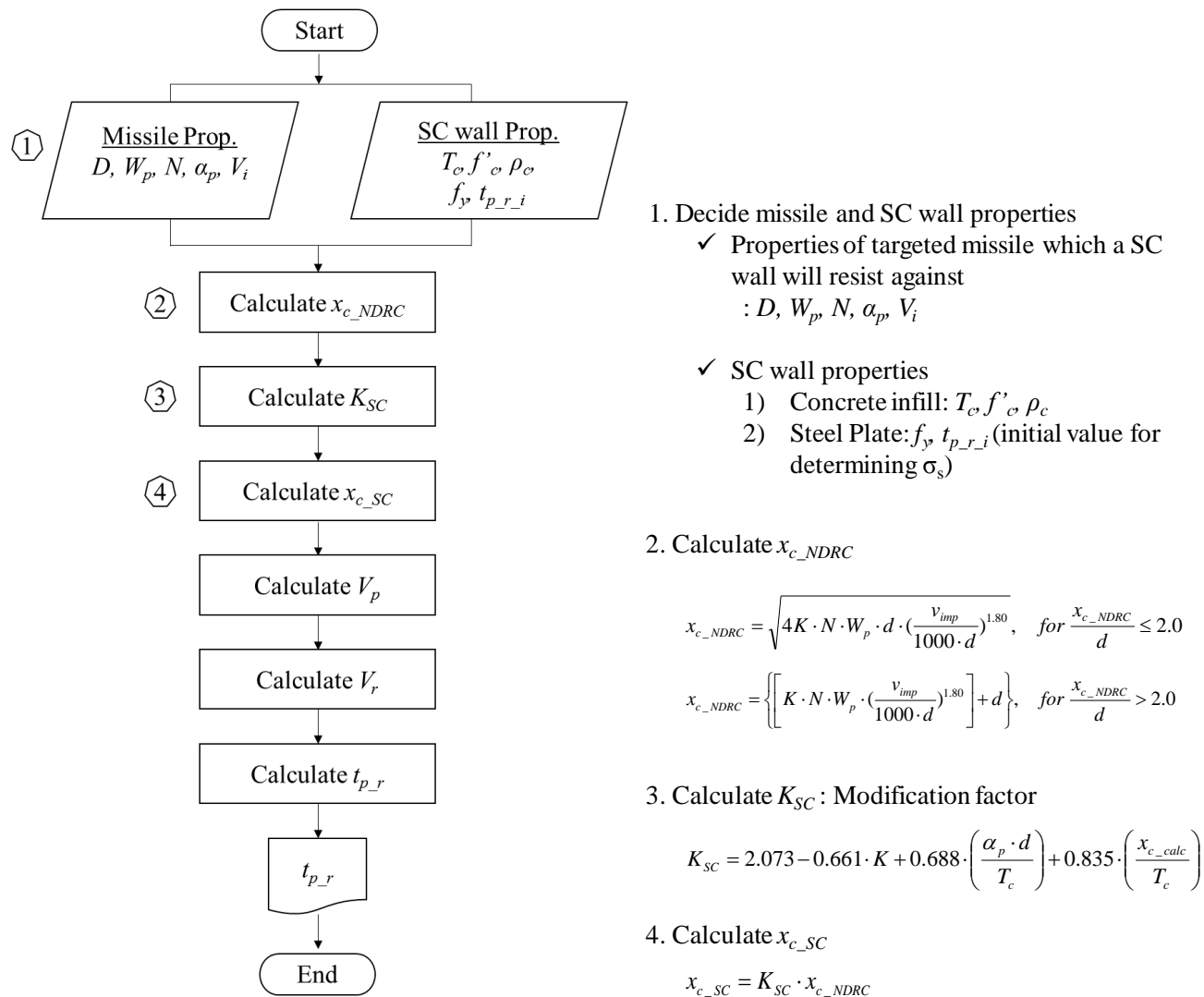
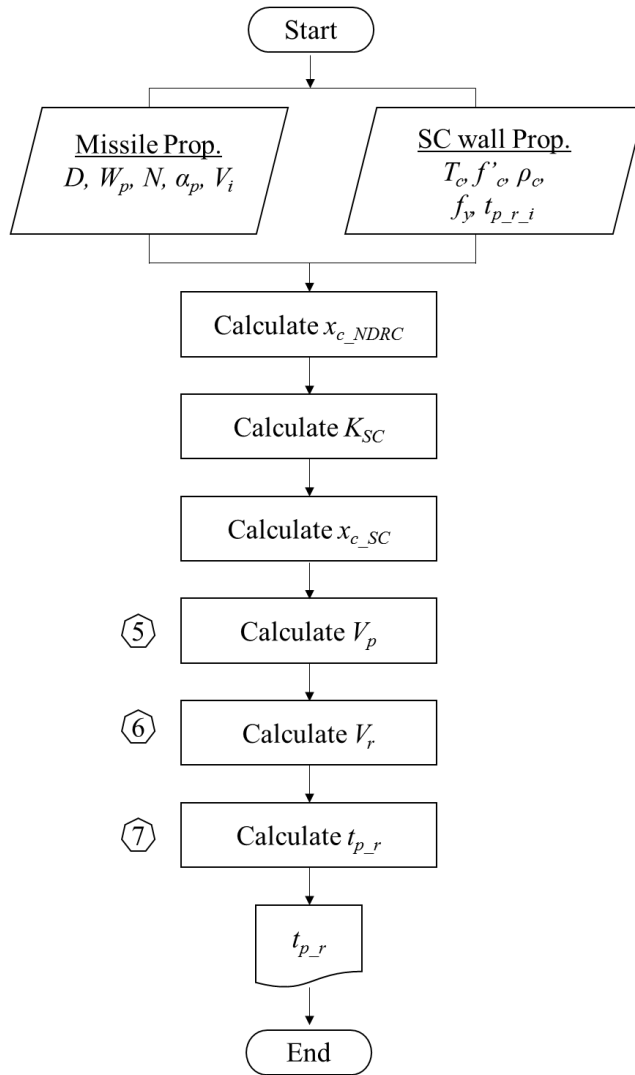


Figure 7-14 Calculation procedures of the proposed modified design method

Figure 7-14 continued



5. Calculate  $V_p$

$$V_p = 1000 \cdot d \cdot \left( \frac{d}{1.44 \cdot K \cdot W \cdot N \cdot K_{SC}^2} \left( 2.2 \pm \sqrt{4.48 - 1.2 \left( \frac{T_c}{\alpha_p d} \right)^2} \right) \right)^{5/9} \quad \text{for } 2.65 < \frac{T_c}{\alpha_p d} < 3.27$$

$$V_p = 1000 \cdot d \cdot \left( \frac{d}{4 \cdot K \cdot W \cdot N \cdot K_{SC}^2} \left( \frac{T_c}{1.29 \alpha_p d} - 0.53 \right) \right)^{5/9} \quad \text{for } 2.65 < \frac{T_c}{\alpha_p d} < 3.27$$

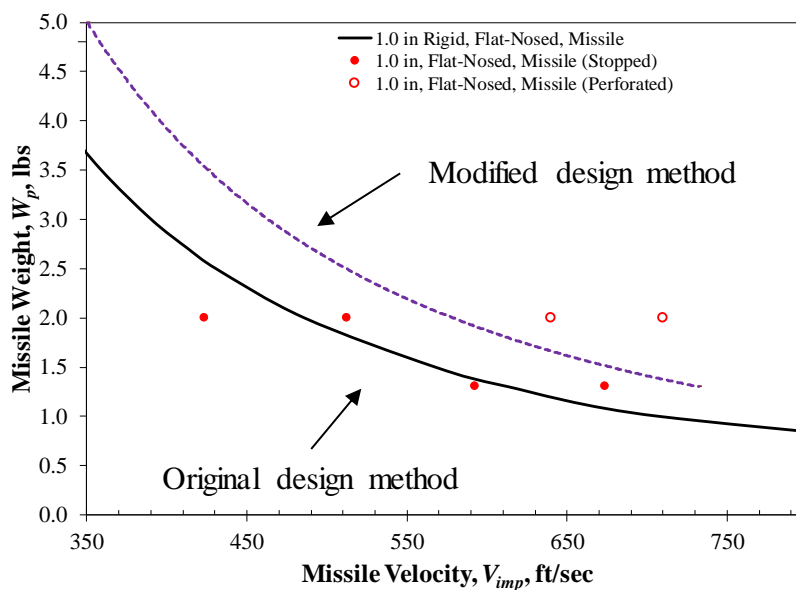
$$V_p = 1000 \cdot d \cdot \left( \frac{d}{K \cdot W \cdot N \cdot K_{SC}} \left( \frac{T_c}{1.29 \alpha_p d} - (0.53 + K_{SC}) \right) \right)^{5/9} \quad \text{for } \frac{T_c}{\alpha_p d} \geq 3.27$$

6. Calculate  $V_r$

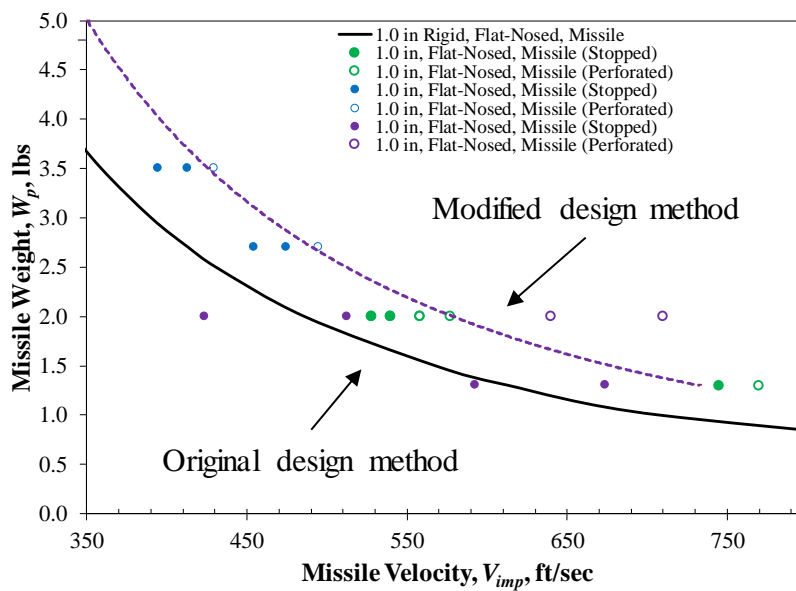
$$V_r = \sqrt{\left( \frac{W_p}{W_p + W_{cf}} \right) \cdot (V_i^2 - V_p^2)}$$

7. Calculate  $t_{p_r}$

$$t_{p_r} = 0.72 \cdot \left( \frac{(12 \cdot V_r)^2 \cdot m_t}{\pi d^2 \cdot \sigma_s} \right)$$

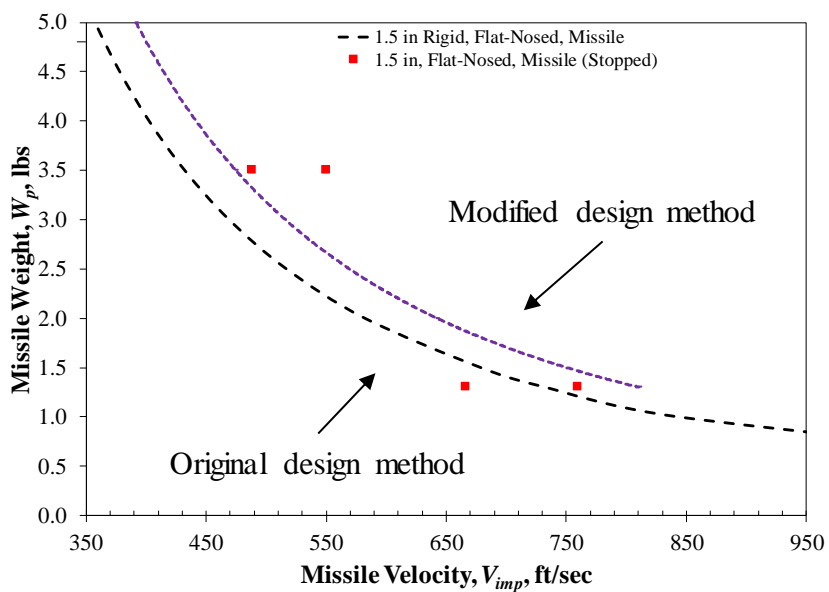


(a) On experimental tests data

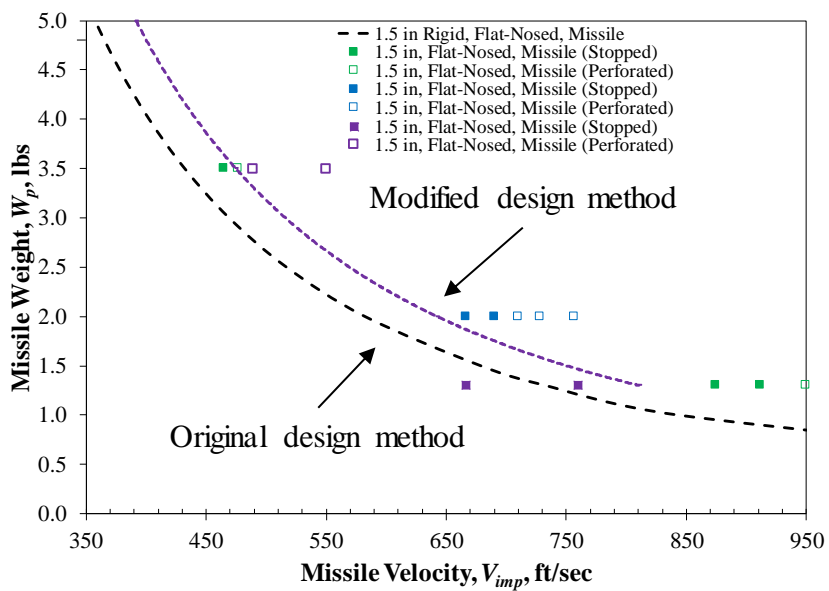


(b) On numerical parametric analyses data

Figure 7-15 Perforation resistance curves on the small-scale missile impact tests data: for 1.0 in. diameter projectile in Gr.1

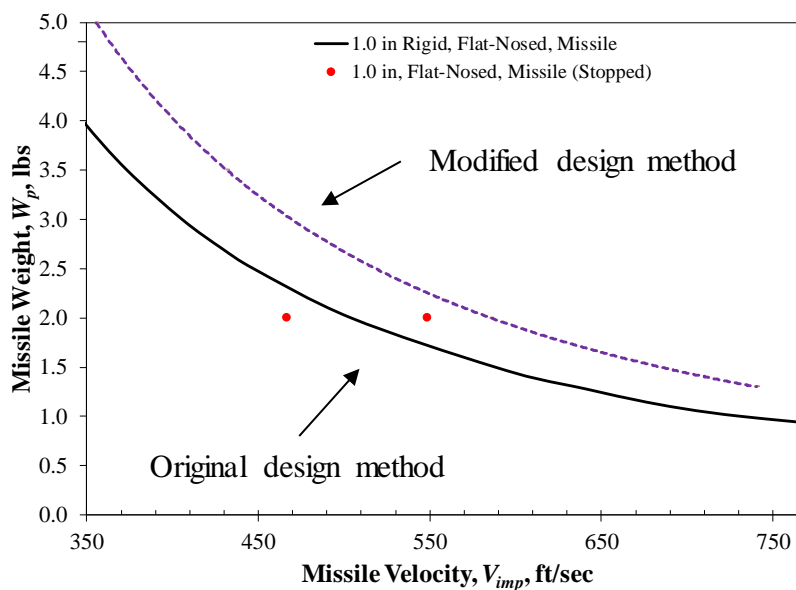


(a) On experimental tests data

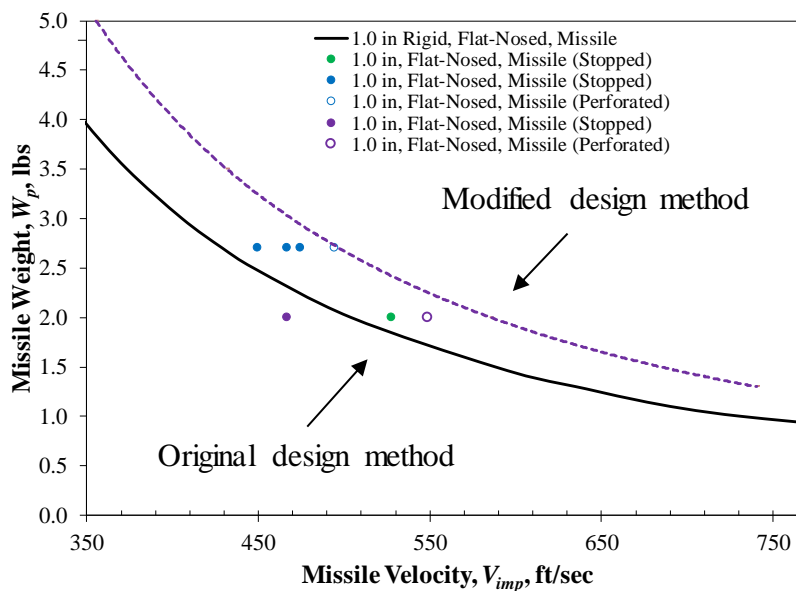


(b) On numerical parametric analyses data

Figure 7-16 Perforation resistance curves on the small-scale missile impact tests data: for 1.5 in. diameter projectile in Gr.1

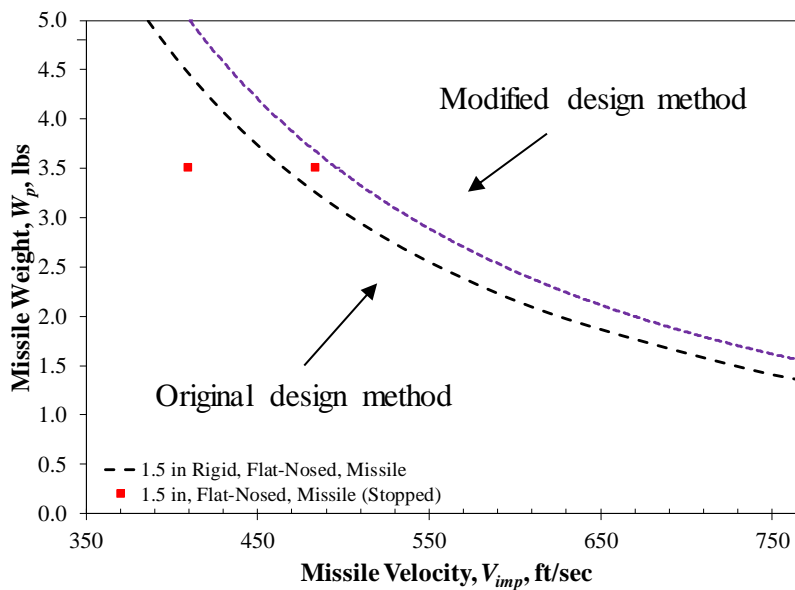


(a) On experimental tests data

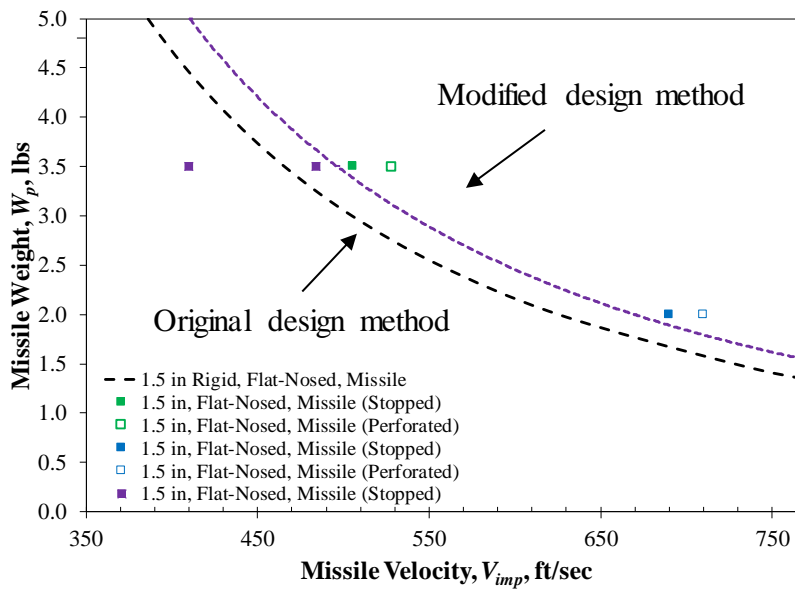


(b) On numerical parametric analyses data

Figure 7-17 Perforation resistance curves on the small-scale missile impact tests: for 1.0 in. diameter projectile in Gr.2

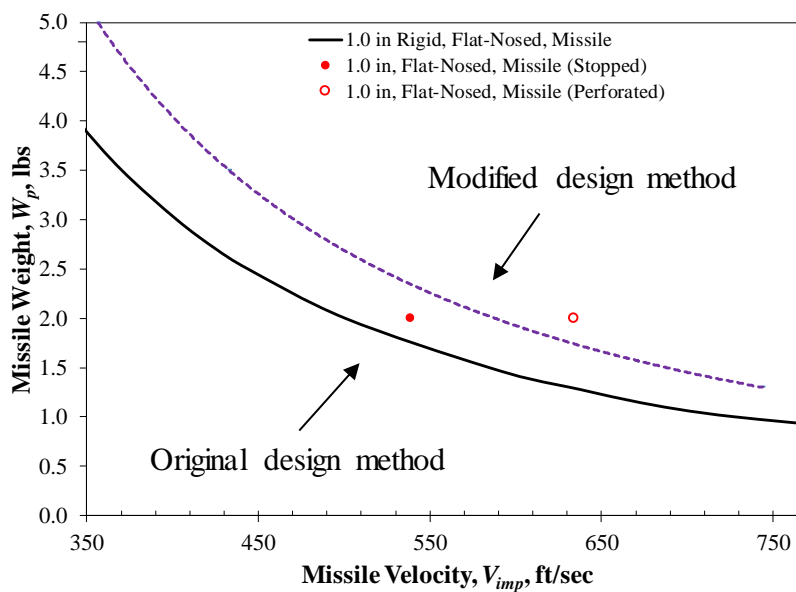


(a) On experimental tests data

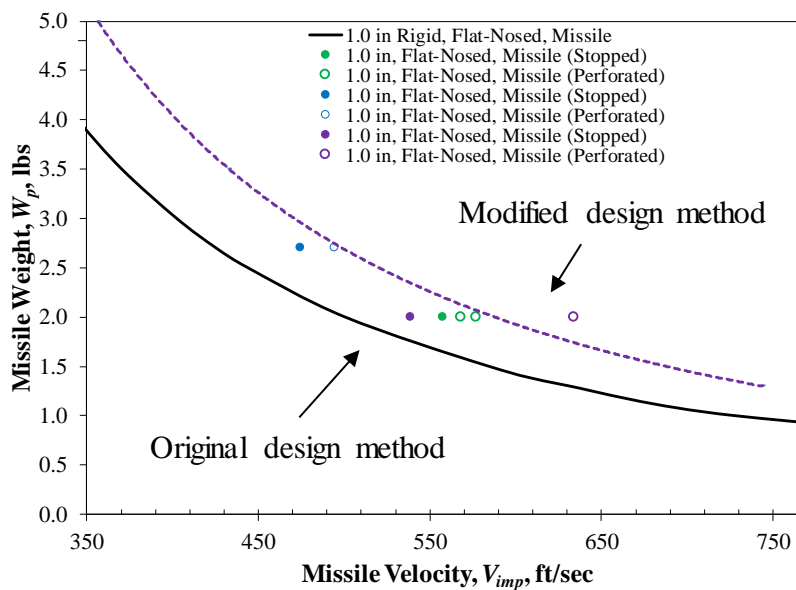


(b) On numerical parametric analyses data

Figure 7-18 Perforation resistance curves on the small-scale missile impact tests data: for 1.5 in. diameter projectile in Gr.2



(a) On experimental tests data



(b) On numerical parametric analyses data

Figure 7-19 Perforation resistance curves on the small-scale missile impact tests data: for 1.0 in. diameter projectile in Gr.3

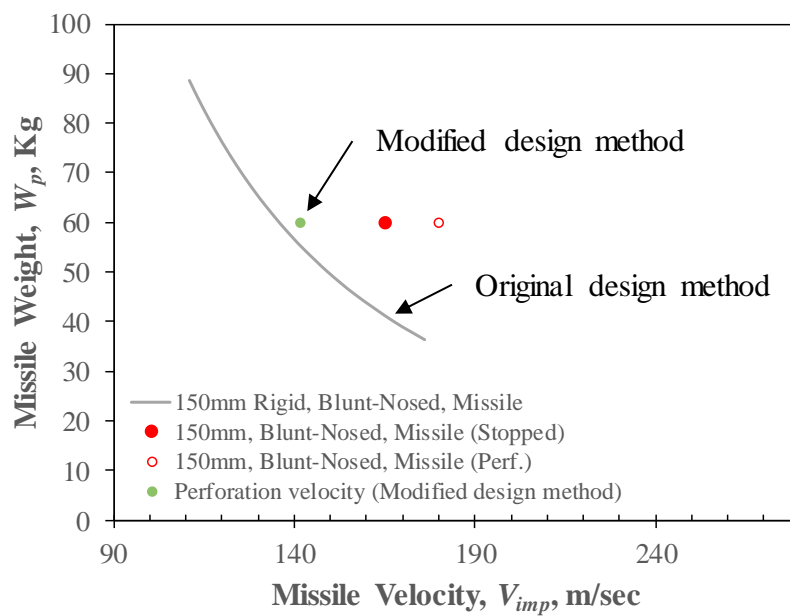


Figure 7-20 Perforation resistance curve and perforation velocity on the larger-scale missile impact tests data of group 1

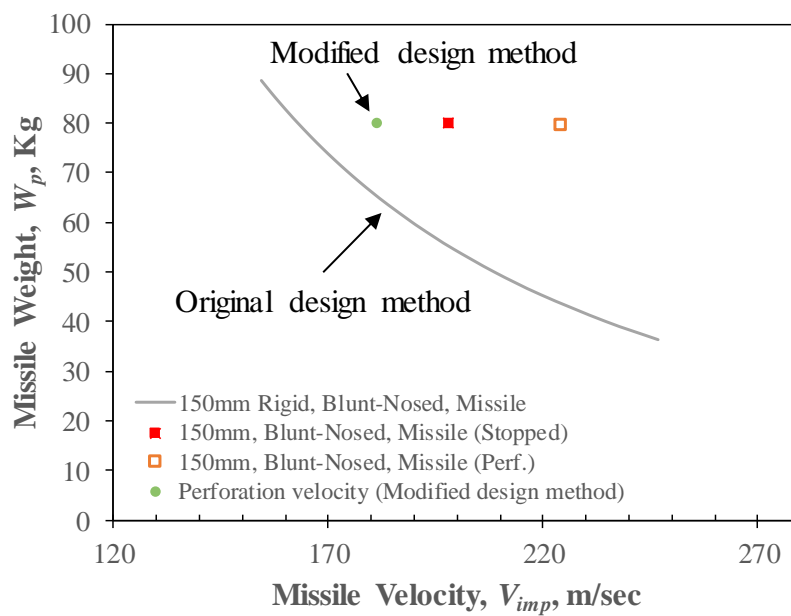


Figure 7-21 Perforation resistance curve and perforation velocity on the larger-scale missile impact tests data of group 2

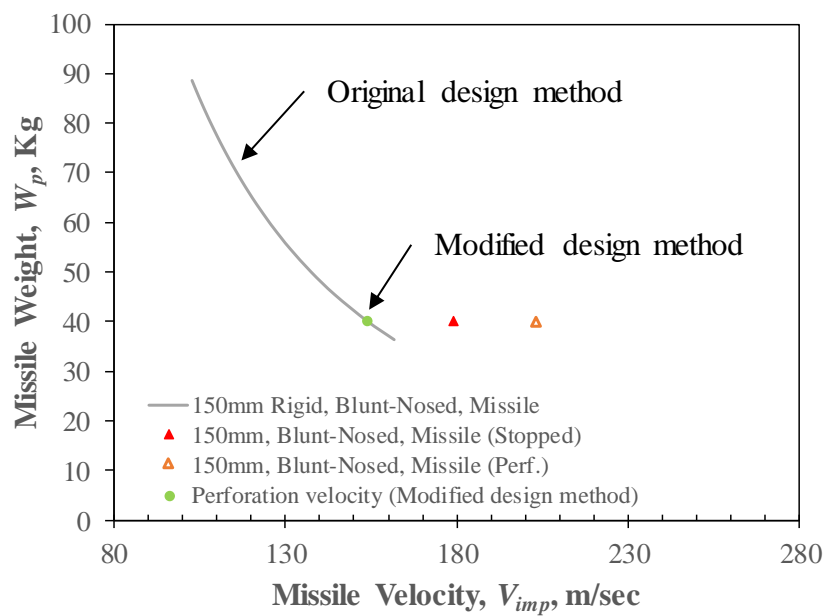


Figure 7-22 Perforation resistance curve and perforation velocity on the larger-scale missile impact tests data of group 3

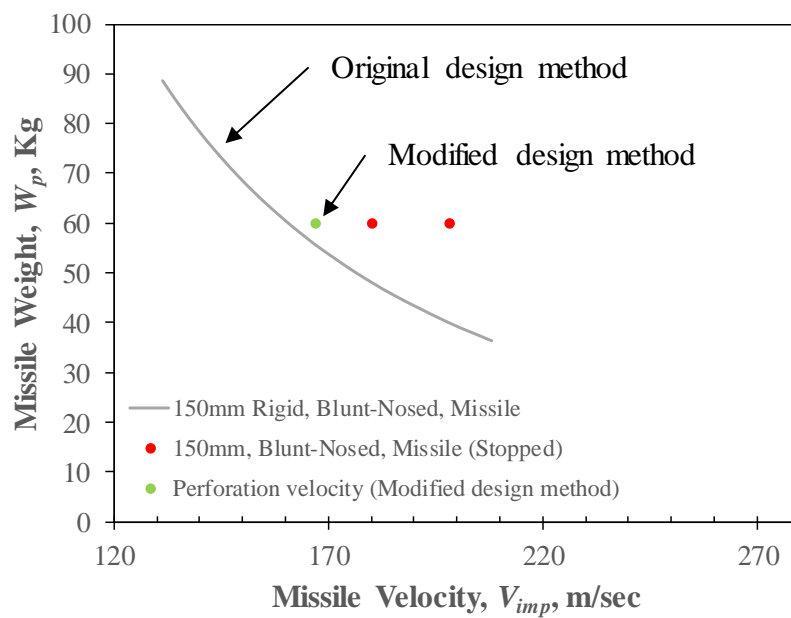


Figure 7-23 Perforation resistance curve and perforation velocity on the larger-scale missile impact tests data of group 4

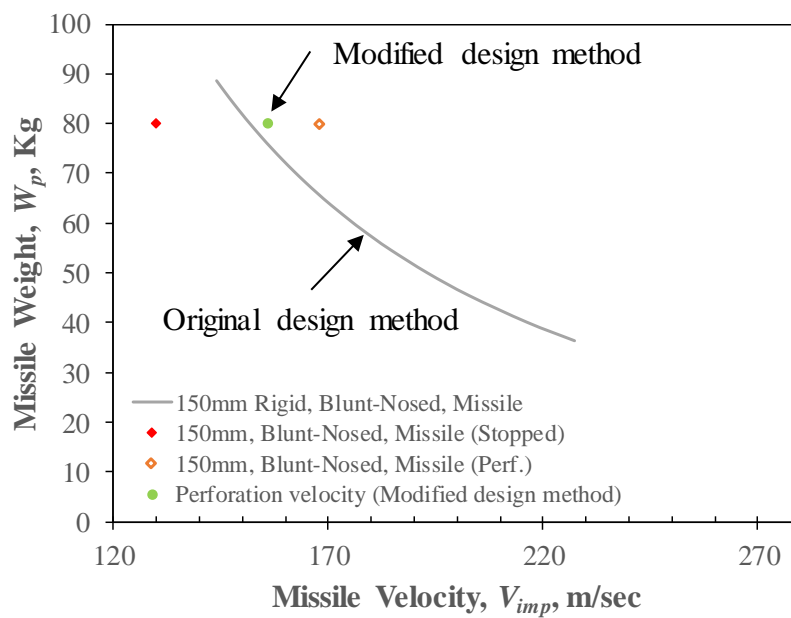


Figure 7-24 Perforation resistance curve and perforation velocity on the larger-scale missile impact tests data of group 5

## CHAPTER 8. LOCAL FAILURE MODES OF SC WALLS

### 8.1 Introduction

So far, we have discussed a methodology to design SC walls to prevent perforation due to missile impactive loading. An experimental study on local damage of SC walls was conducted through a series of small-scale missile impact tests in chapter 3 and 4. A numerical study was carried out to simulate experimental tests and to further evaluate local behavior of SC walls with varied design parameters in chapter 5 and 6. In chapter 7, a design method was proposed modifying the three-step design method based on findings from the experimental and numerical studies for this research project.

Even though the perforation of SC walls was prevented, potential failure modes such as punching shear, steel plate rupture, and excessive deflections should be taken into account as a design consideration.

In this chapter<sup>1)</sup>, numerical studies were carried out to evaluate local failure modes of SC walls against missile impact, especially when the perforation is prevented. In addition, a novel approach to obtain a static resistance function is proposed for use in SDOF or TDOF analysis to estimate the maximum deflection of SC walls subjected to missile impact.

### 8.2 Development of Numerical Models

A finite element analysis approach was adopted to carry out the studies to evaluate local failure modes and static resistance function of SC walls subjected to missile impactive loading. LS-DYNA, which is a general purpose commercial software, was used for finite element analyses.

---

1) Some results in this chapter were presented at a conference as follows: Varma, A., Kim, J. M., Seo, J., and Bruhl, J. (2017). "Local Failure Modes of SC Walls Subjected to Impactive Loading" *Transactions of the 24th International Conference of Structural Mechanics in Reactor Technology (SMiRT-24)*, Busan, South Korea

Finite element models were developed based on the methodology in the literature (Bruhl et al. 2015b). The methodology was benchmarked to the experimental tests conducted by other researchers (Sener and Varma 2014a) and its applicability was already verified.

The configuration of SC walls were the same as described in chapter 5: steel faceplate, tie bars, steel-headed shear stud anchors, and concrete. However, there are a few differences in finite element modeling strategies as follows. First, no projectile was used to apply impactive loading. It was found that very localized deformation occurred on the steel faceplate surface contacting the circumference of a projectile, which did not conform to the experimental test results. Thus, the projectile was replaced by a circular area which pressure loading was applied to. Second, a quarter model of SC wall was used for the analysis. Due to the full scale of SC walls considered in these studies, significantly large system memories and calculation time are required. Thus, quarter models were applied considering analysis efficiency with corresponding boundary conditions; fixed support conditions for two faces of the SC wall, and symmetric restrained boundary conditions for the other faces. Figure 8-1 shows a representative quarter model of the SC wall used for the studies. Third, no strain-rate effect was applied to the materials. This study investigated the structural behavior of SC walls after the perforation was prevented. Thus, quasi-static analysis was performed and strain-rate effect on the materials was not considered. Forth, element erosion criteria for concrete model was not defined. Because there is no interest in the behavior of concrete related with the perforation or the penetration damage of SC walls caused by the projectile impact.

### 8.2.1 Steel faceplate modeling

Modeling approach of steel faceplate was the same as described in chapter 5 with one exception; dynamic increase factor (DIF) was not applied.

### 8.2.2 Tie bar and steel-headed shear stud anchor modeling

Modeling approach of tie bar and steel-headed shear stud anchor was the same as described in chapter 5.

### 8.2.3 Concrete modeling

Modeling approach of concrete core was the same as described in chapter 5 with a couple of exceptions as follows.

Although the same Winfrith concrete model was used, a different form of the model named MAT\_85 was chosen instead of MAT\_84 used in chapter 5, since the strain-rate effect was neglected. For this case, the parameter of FE takes a crack width as an input, at which tensile normal stress across the crack becomes zero, instead of the fracture energy for MAT\_84. Simplified linear strain softening curve shown in Figure 8-2 was implemented in this form of Winfrith concrete model (MAT\_85). Once fracture energy is calculated, the crack width,  $w$ , at zero tensile strength can be obtained by Equation 8-1.

$$w = \frac{2 \cdot G_f}{f_t'} \quad \text{Equation 8-1}$$

MAT\_ADD\_EROSION to define erosion criteria was not used so that concrete element deletion was not implemented, which was different from the modeling strategy described in chapter 5.

#### 8.2.4 Other modeling details

Fixed support condition was applied to the quarter model of an SC wall. This was implemented by restraining degree of freedom for the nodes translationally and rotationally along the supported edges. Symmetric boundary condition was applied to the quarter model accordingly.

Pressure load was applied monotonically at the center of the SC wall with `LOAD_SEGMENT_SET` command. Diameter of the circular region for applying the pressure load was determined to be one fourth of the SC wall span according to the literature (Johnson et al. 2014).

`ERODE_SURFACE_TO_SURFACE` and `AUTOMATIC_BEAM_TO_SURFACE` commands were not used in the modeling approach herein compared to that of chapter 5.

### 8.3 Numerical Parametric Studies

A total of 10 numerical analyses were conducted to investigate local failure modes and effects of failure criteria for the components of SC walls on their structural behavior. Table 8-1 shows the details of numerical models employed for the parametric studies. Global dimensions of all the analysis models were the same; SC wall thickness,  $T_{sc}$ , was 36 in., and span-to-wall thickness ratio,  $L/T_{sc}$ , was 10. Steel faceplate thickness,  $t_p$ , of 0.75 in. was used so that the flexural reinforcement ratio,  $\rho$ , was constant at 4.2%. Shear stud anchor spacing-to-steel faceplate thickness ratio,  $s/t_p$ , was 12. Shear stud anchor diameter-to-steel faceplate thickness ratio,  $d_s/t_p$ , was 1.33. Tie bar spacing-to-wall thickness,  $S/T_{sc}$ , was 0.5. Shear reinforcement ratio,  $\rho_t$ , was varied ranging from 0.14 to 0.85. Concrete compressive strength,  $f'_c$ , was 5 ksi. Yield strength,  $f_y$ , of all the steel materials used was 50 ksi. All the analysis cases had a fixed support condition. Model identifier consisted of up to four terms depending on the analysis case, for example, “SC-0.38-H-N”. First term, “SC”, explains the model is for an SC wall. Second term indicates a corresponding shear

reinforcement ratio. Third term explains which hour glass control option was applied; “H” is included when Flanagan-Belytschko stiffness form (TYPE 4) is used. Fourth term presents if failure criteria were applied; “N” is included when there are no failure criteria defined.

For analysis numbers 1 to 8, shear reinforcement ratio was varied from 0.14% to 0.85% while flexural reinforcement ratio was constant at 4.2%. Failure strain value of 0.1 was input for the numerical model of the steel faceplates and the tie bars. Maximum tensile slip displacement of 0.335 in. was input for the numerical model of the shear stud anchors. Belytschko-Bindeman hourglass control option (TYPE 6) with default coefficient value was applied.

Analysis number 9 had the same SC wall configuration as analysis number 4 with a couple of exceptions: i) No failure criteria were applied for the steel faceplates, the tie bars, and the shear stud anchors; ii) Flanagan-Belytschko stiffness form (TYPE 4) hourglass control option was used to resolve numerical stability issues.

Analysis number 10 also had the same SC wall configuration as analysis number 4 with the exception of hourglass control option; Flanagan-Belytschko stiffness form (TYPE 4), which was the same as analysis number 9, was applied. The purpose was to verify any possible influence from different hourglass control options.

#### *8.4 Influence of Shear Reinforcement Ratio on Local Failure Mode*

Analysis numbers 1 to 8 were investigated to evaluate potential local failure modes of SC walls according to their shear reinforcement ratio. Figure 8-3 shows the resultant load-displacement responses for the analysis cases.

When the shear reinforcement ratio is less than or equal to 0.19%, shear failure occurred and “SF” was annotated on the load-displacement curve at its maximum load carrying capacity in Figure 8-3. Figure 8-4 shows a representative local failure behavior when the punching shear

failure occurred. It is observed that a tie bar, which is shear reinforcement for out-of-plane direction, was fractured before the steel faceplates yields. In the figure, concrete core was removed for clarity and deformed shape of the steel faceplates is seen clearly.

When the shear reinforcement ratio is greater than or equal to 0.64%, plastic mechanism formation was presented and “MF” was annotated on the load-displacement curve at its maximum load carrying capacity in Figure 8-3. In the figure, load carrying capacity of the corresponding curves almost reaches the flexural capacity obtained from the yield line analysis. Figure 8-5 illustrates a representative local failure behavior when the plastic mechanism was formed in the steel faceplates. The steel faceplates were deformed severely. Stress distribution indicates that the steel faceplates has already passed their yield strength approaching the ultimate strength level, however, there are no tie bars fractured.

When the shear reinforcement ratio is ranging from 0.24% and 0.55%, flexural yielding failure mode occurred and “FY” was annotated on the load-displacement curve at its maximum load-carrying capacity in Figure 8-3. Figure 8-6 illustrates a representative local failure behavior when the flexural yielding of the steel faceplates occurred. Tie bars were observed to be fractured after the steel faceplates yielded, however, the plastic mechanism in the steel faceplates was not developed.

### *8.5 Influence of Failure Criteria Definition on SC Wall Resistance Function*

Analyses result from model number 4, 9, and 10 were investigated to evaluate i) the effect of the hourglass control option between TYPE 6 and TYPE 4, and ii) the influence of the failure criteria for each component of SC walls. Figure 8-7 illustrates the comparison of resultant load-displacement responses from the analyses.

Load-displacement responses from model number 4 and 10 show a reasonable agreement in Figure 8-7. They have almost the same value of yield displacement at 1.4 in., and slightly different value of yield load at 5700 kips and 6000 kips, respectively. They also have almost the same value of ultimate displacement at 11.0 in., and maximum load carrying capacity at 9800 kips. No significant difference is found in pre- (less than 6%) and post-yield stiffness between these two analysis cases. Thus, it can be said that the effect of the different hourglass options on the structural behavior of SC walls is negligible.

Load-displacement responses from model number 4 and 9 show a great comparison in Figure 8-7. They present almost identical pre- and post-yield stiffness. Yield displacement and yield load agree favorably with the value of 1.4 in. and 6000 kips, respectively. However, ultimate displacement and maximum load carrying capacity do not agree well. Analysis result from model number 9 shows much larger ductility in the load-displacement response. Maximum load carrying capacity was comparable to that of analysis cases when the plastic mechanism formation occurred.

Plastic strain history data of the steel faceplates and the tie bars, and slip displacement history data of the shear stud anchors are pulled out from the analysis result of model number 9 and presented in Figure 8-8 for a better understanding of the influence of the failure criteria for the components of SC walls. From Figure 8-8 (a), plastic strain value of the steel faceplates indicates 0.05 when the displacement reaches at 9 in. which corresponds to the applied load value of approximately 13000 kips. If a design engineer considers this is an appropriate failure criterion for the steel faceplates, then the resistance function will follow the load-displacement curve and terminate at this point. The resistance function can be determined based on the failure criterion for the tie bars as well. For example, from Figure 8-8 (b), the tie bars point out plastic strain value of 0.10 when the displacement reaches 7 in. which corresponds to the applied load value of

approximately 9000 kips. If a design engineer judges this is a proper failure criterion for the tie bars, the resistance function will follow the load-displacement curve and terminate at this point. Failure criterion of the shear stud anchors also contributes to determining the resistance function of SC walls. From Figure 8-8 (c), slip displacement value indicates 0.42 in. at the displacement of 12.8 in. corresponding to the applied load value of approximately 11500 kips. In the same way, if a design engineer considers this is a reasonable failure criterion for the shear stud anchors, the resistance function will follow the load-displacement curve and terminate at this point.

A representative resistance function for an SC wall (model number 9) is proposed in Figure 8-9, on which three critical limit states (or events) marked. Plastic strain value of 0.10 for the tie bars is marked as point A; Slip displacement value of 0.42 in. for the shear stud anchors is marked as point B; Plastic strain value of 0.05 for the steel faceplates is marked as point C. These points are the same values as described above and drawn from Figure 8-8. Design engineers may decide to terminate the load-displacement curve corresponding to specific failure criteria and use it as the static resistance function accordingly. Doing so, permits the engineer to better understand governing failure mode and the corresponding available ductility as indicated on the horizontal axis at the top of Figure 8-9;  $U_y$  indicates the yield displacement. For this representative resistance function, the available ductility is 4.5 for point A, 9 for point B, and 13 for point C. It is important to note that points B and C infer that other components have a certain capacity. That is, to achieve point C in this example, the tie bars must be able to accommodate plastic strains of 0.18 and the stud anchors must permit 0.60 inches of slip displacement. Depending on the ductility demand required in the design, the engineer can use this to inform design decision such as specifying a tie bar or faceplate material with a required minimum fracture strain.

## 8.6 *Summary and Conclusions*

Local failure modes of SC walls were identified through a series of numerical analyses; especially when the perforation of the wall from missile impact was prevented against missile impact. Punching shear, flexural yielding, and plastic mechanism formation failure modes were observed successively as the shear reinforcement ratio increased for a constant flexural reinforcement ratio (Kim et al. 2017b).

For punching shear failure mode, it was shown that the ductility ratio was small (less than 5), and the load carrying capacity was underdeveloped (less than half of the load from the yield line analysis). The tie bars were fractured before the steel faceplates yielded.

Plastic mechanism formation failure mode resulted in a large ductility ratio greater than 10 and a well (fully)-developed load carrying capacity comparable to the value from the yield line analysis. The steel faceplates yielded with severe deformation, however, the tie bars were not fractured.

Flexural yielding failure mode occurred when the shear reinforcement ratio was between the values from punching shear failure mode and plastic mechanism formation failure mode. Ductility ratio ranged between 5 and 10, and load capacity was greater than half, but less than the full value of the yield line analysis. Tie bars were fractured after the steel faceplates yielded, however, no plastic mechanism in the steel faceplates was developed.

An innovative approach was proposed to generate the static resistance function of SC walls for use in SDOF or TDOF analysis. A Fully developed load-displacement response of an SC wall (model number 9) was presented from a finite element model in which no failure criteria were defined. Additional information from the analysis results such as plastic strain history data of the steel faceplates and the tie bars, and slip displacement of the shear stud anchors was utilized to evaluate the influence of failure criteria on the static resistance function of an SC wall. Final static

resistance function can be generated by terminating the load-displacement curve at the point determined based on appropriate failure criteria of constituent components of the SC wall. After all, design engineers can make a decision on design parameters to obtain a static resistance function required for ensuring the desired ductility and/or load capacity demands are satisfied.

Table 8-1 Parametric analyses matrix

<i>No.</i>	<i>Model identifier</i>	$t_{sc}$ (in)	$L/t_{sc}$	$t_p$ (in)	$\rho$ (%)	$s/t_p$	$d_s/t_p$	$S/t_{sc}$	$\rho_t$ (%)	$f'_c$ (ksi)	$f_y$ (ksi)	<i>Support condition</i>
1	SC-0.14	36	10	0.75	4.2	12	1.33	0.5	<b>0.14</b>	5	50	Fix
2	SC-0.19	36	10	0.75	4.2	12	1.33	0.5	<b>0.19</b>	5	50	Fix
3	SC-0.24	36	10	0.75	4.2	12	1.33	0.5	<b>0.24</b>	5	50	Fix
4	SC-0.38	36	10	0.75	4.2	12	1.33	0.5	<b>0.38</b>	5	50	Fix
5	SC-0.46	36	10	0.75	4.2	12	1.33	0.5	<b>0.46</b>	5	50	Fix
6	SC-0.55	36	10	0.75	4.2	12	1.33	0.5	<b>0.55</b>	5	50	Fix
7	SC-0.64	36	10	0.75	4.2	12	1.33	0.5	<b>0.64</b>	5	50	Fix
8	SC-0.85	36	10	0.75	4.2	12	1.33	0.5	<b>0.85</b>	5	50	Fix
9	SC-0.38-H-N	36	10	0.75	4.2	12	1.33	0.5	<b>0.38</b>	5	50	Fix
10	SC-0.38-H	36	10	0.75	4.2	12	1.33	0.5	<b>0.38</b>	5	50	Fix

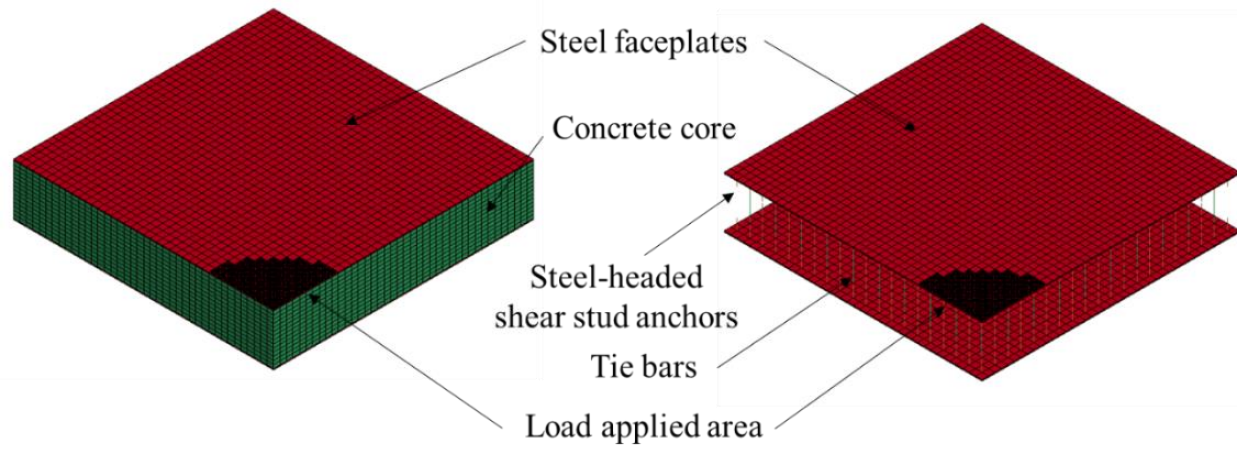


Figure 8-1 A representative quarter finite element model of SC walls

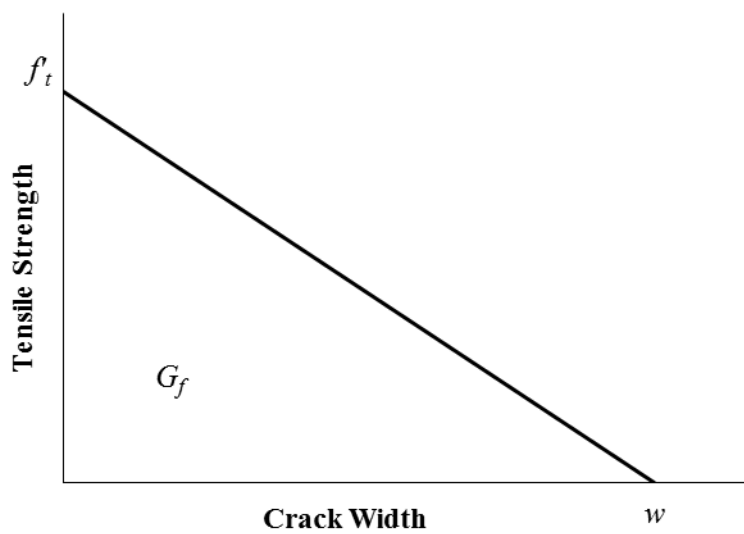


Figure 8-2 The linear strain softening response (Schwer 2011)

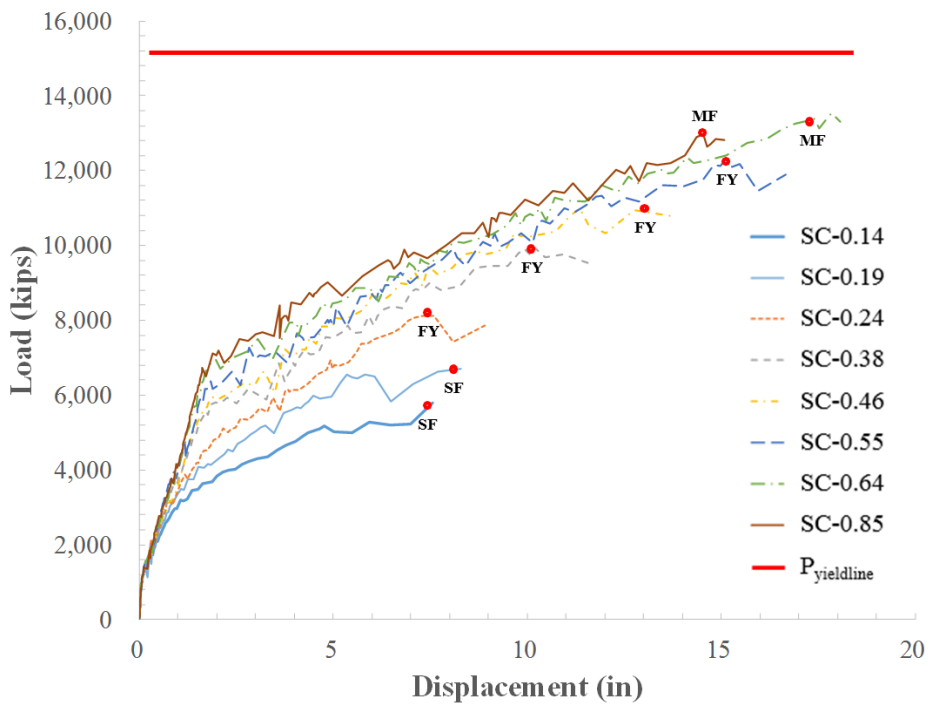


Figure 8-3 Load-displacement curves for analysis numbers from 1 to 8

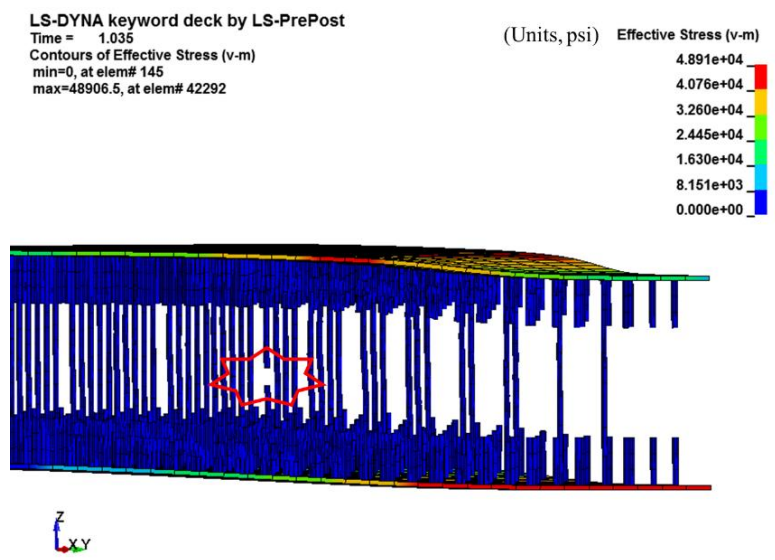


Figure 8-4 Detailed local failure behavior of analysis number 2: punching shear failure (concrete core was removed for clarity) (Varma et al. 2017)

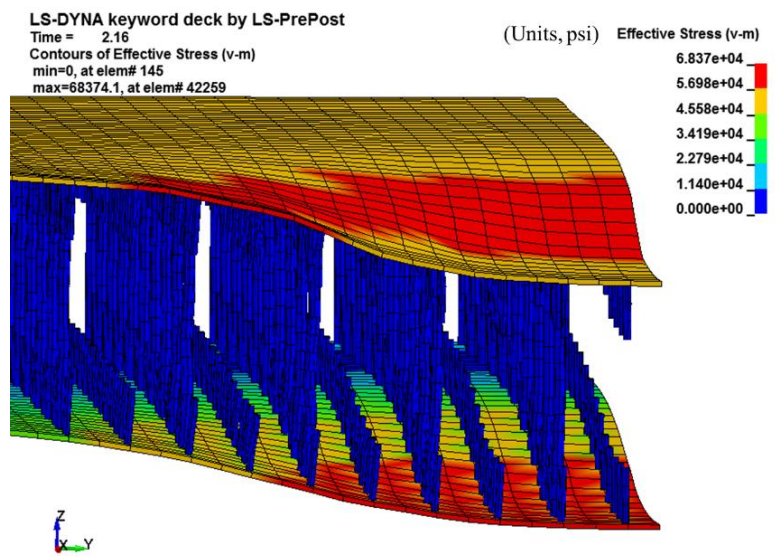


Figure 8-5 Detailed local failure behavior of analysis number 7: plastic mechanism formation (concrete core was removed for clarity)

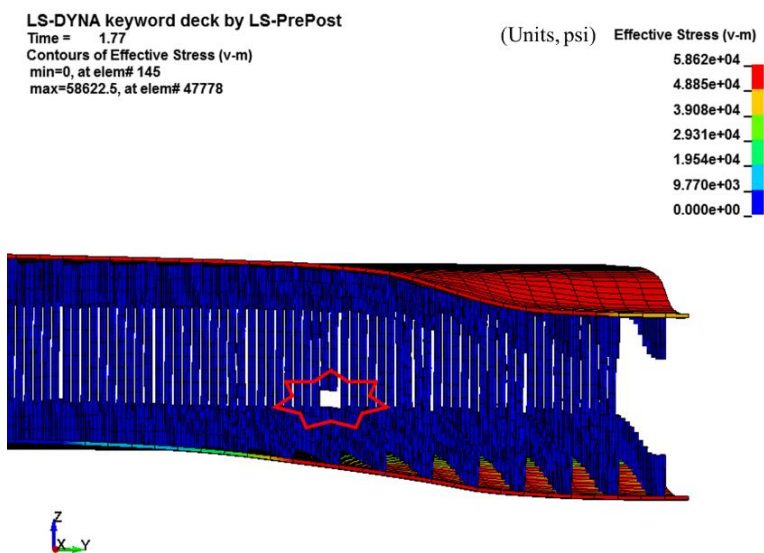


Figure 8-6 Detailed local failure behavior of analysis number 5: flexural yielding (concrete core was removed for clarity)

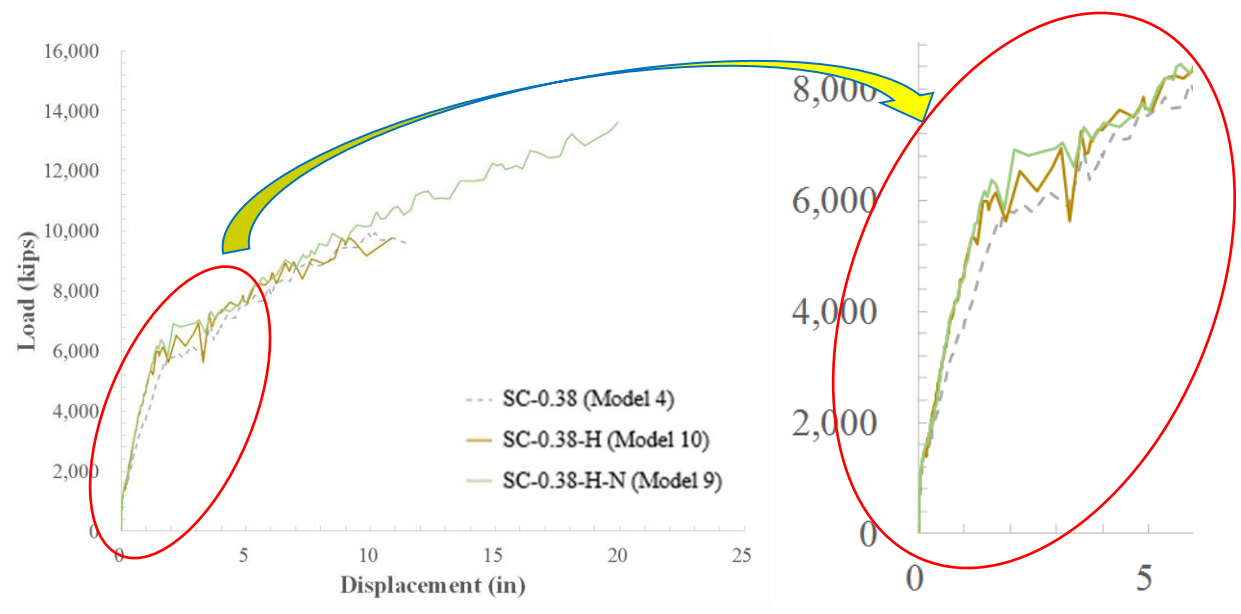
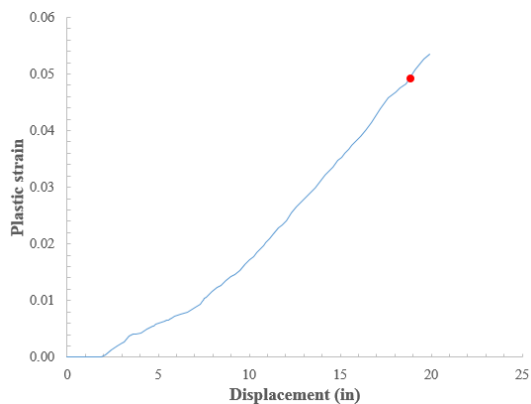
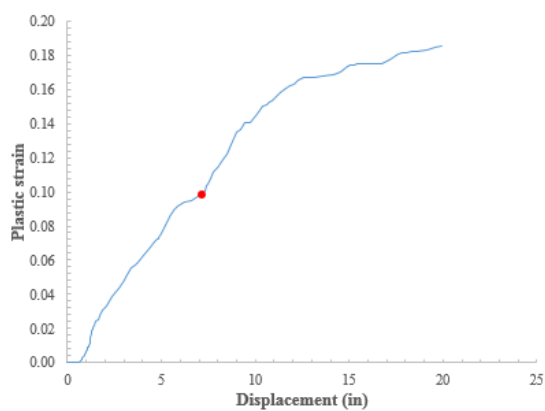


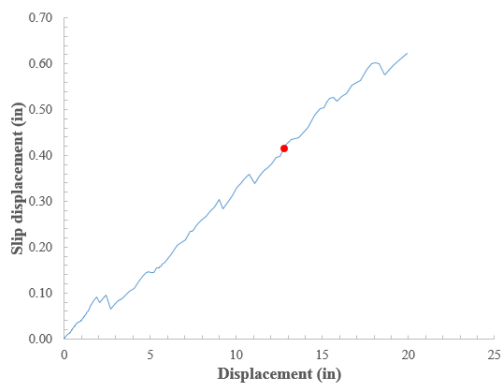
Figure 8-7 Load-displacement response from analysis cases of model number 4, 9 and 10



(a) Plastic strain of the steel faceplate



(b) Plastic strain of the tie bar



(c) Slip displacement of the stud anchors

Figure 8-8 Plastic strain and slip displacement history data for the components of SC walls

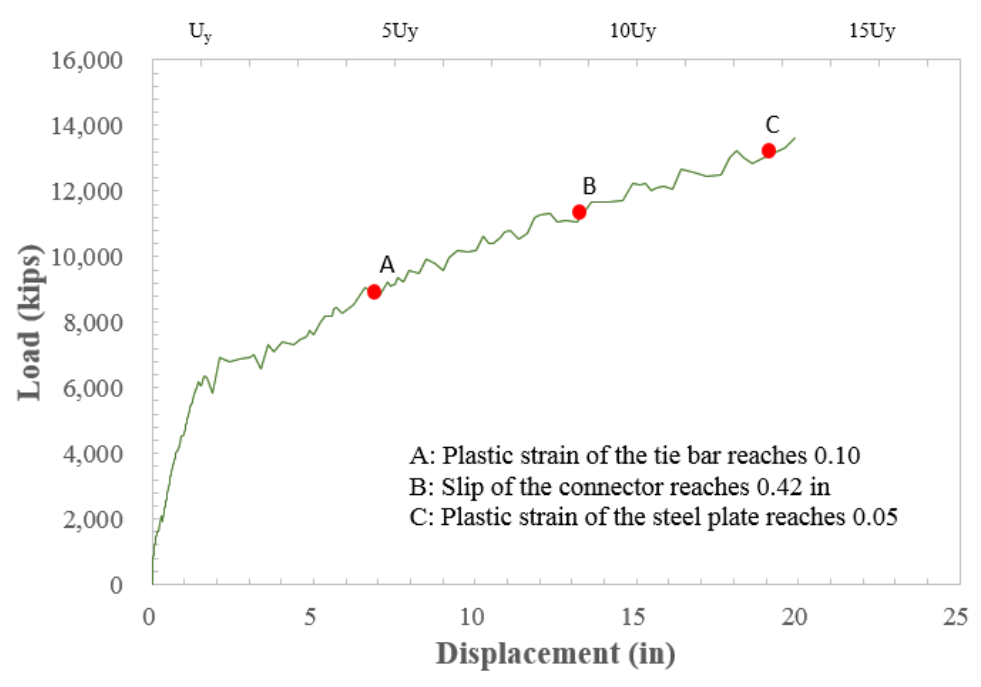


Figure 8-9 A representative resistance function on which critical events were marked

## CHAPTER 9. SUMMARY AND CONCLUSIONS

### 9.1 *Research Summary*

A series of sixteen missile impact tests of SC wall specimens were conducted as part of the experimental study for this research project. All test cases were categorized into three groups according to varying design parameters of SC walls. Within these three groups, special attention was paid to flexural reinforcement ratio, shear reinforcement ratio, steel faceplate strength, and parameters of projectiles including diameter and weight.

The SC wall specimens were designed in small-scale in accordance with AISC N690 s1, Appendix N9. Projectiles were fabricated from AISI 4340 rod stock with additional heat treatment. Sabots were prepared to secure sealing between the gun barrel and the projectiles, and to ensure the projectiles' flight was level. Test setup was designed and fabricated to allow the tests in indoor laboratory scale. Test setup consisted of a gas gun assembly, gun barrel, front chamber, main support structure, rear chamber, and catcher chamber. The impact instance could be observed through a view portal in the front chamber and was recorded using a high-speed video camera.

Experimental test data from all the sixteen test cases was analyzed carefully to investigate the local damage behavior of SC walls subjected to missile impact. Test results including impact velocity, primary test results (stopped or perforated), damage mode, penetration depth, and bulging depth were examined and measured, and values were summarized. After each test, external damage of the specimens was investigated and three different damage modes were identified: bulging, splitting and perforating damage mode. Internal damage observed in the cross-section of the post-test specimens, including tunneling zone and concrete frustum, was investigated, measured and summarized.

All test results were graphed in terms of impact velocity and weight of the projectiles so that the velocity ranges in which the perforation velocity was located could be quantified. Test cases in which a projectile was stopped by the specimen were marked as solid shapes; Test cases in which a projectile perforated the specimen were marked as hollow shapes. On top of these, perforation resistance curves, calculated by using the three-step design method, were drawn and compared with the graphed test results to evaluate the accuracy of the design method. The comparison showed that the three-step design method has a considerable conservatism built in.

Performance of the modified NDRC equations, which were used in the three-step design method, were evaluated based on the experimental test results. It was found that the modified NDRC equations did not provide accurate estimations of the penetration depth of a projectile into the concrete of SC walls. This is likely due to the difference in damage modes between RC walls and SC walls.

Internal damage behavior presented in the cross-sections of the post-test SC wall specimens was examined carefully. Detailed dimensions of geometric features including tunneling zone and concrete frustum were summarized. Based on this examination, a local failure mechanism was proposed which consist of five stages.

Numerical models were developed to simulate the experimental tests and better understand the local damage behavior of SC walls subjected to missile impact. LS-DYNA, a commercial finite element analysis software, was used to develop three-dimensional finite element models of SC wall specimens. In the finite element model, the steel faceplates and projectile were implemented using solid elements with piecewise linear plasticity (MAT\_24) material model for their material properties. The concrete core was implemented using solid elements with the Winfrith concrete model (MAT\_84). Tie bars and shear stud anchors were modeled using beam elements with

MAT\_24 material model. Zero length discrete beam elements were used to represent the load-slip behavior of the shear stud anchors caused by the composite action between the steel faceplates and the concrete core. Contact and constraint commands were used appropriately for the physical interaction among the components of the SC wall model.

The developed finite element models were benchmarked to the experimental test results. Numerical analysis results including primary analysis result (stopped or perforated), damage mode, penetration depth, and bulging depth were compared with the experimental test results. Rear steel faceplate rupture patterns and the internal failure mechanism observed from the finite element models were also compared with the experimental test results. The comparison resulted in reasonable agreement thus the finite element models were proven to be acceptable for this research.

Two sets of numerical parametric studies were performed using the benchmarked finite element models. The purpose of the first set of the parametric studies was to generate additional data points for use in specifying perforation velocity ranges for the experimental test groups and evaluating the accuracy of the modified design method to be proposed later. A total of 40 numerical analyses were conducted with varying projectile parameters such as weight and velocity. The purpose of the second set of the parametric studies was to evaluate the influence of design parameters on the local damage behavior of SC walls. A series of 12 numerical analyses were conducted varying the flexural reinforcement ratio, shear reinforcement ratio and steel faceplate strength. The analyses results showed that flexural reinforcement ratio and steel faceplate strength are critical design parameters which affect the penetration depth of a projectile into the concrete core.

The three-step design method is employed as one of the rational tools to aid in preventing perforation failure of SC walls against missile impact. But, the test results in this research project

showed that there is room for improvement in terms of accuracy and conservatism aspects of the three-step design method. A modification factor equation,  $K_{sc}$ , was introduced to increase accuracy in estimating the penetration depth of a projectile into concrete core of SC walls. The modification factor equation was used with the modified NDRC equations and its effectiveness was verified. Next, a modified design method was proposed incorporating the modification factor equation and revised local failure mechanism which was obtained from the experimental investigations. The modified design method was verified using the small-scale missile impact test data and the larger-scale missile impact test data obtained from South Korean tests.

Up to this point, this research project focused on the design methodology to prevent perforation of SC walls against missile impact. All the results from the experimental tests, numerical model development & benchmarking, and parametric studies supported the need for the development of a modified design method. Next, this research project shifted to a focus on local failure modes when the perforation was prevented from missile impactive loading on SC walls. The research of this was performed numerically. Instead of using a finite element modeling approach for dynamic analysis, that for quasi-static analysis was chosen. Two sets of parametric studies were conducted. The purpose of the first set of parametric studies was to evaluate possible local failure mode of SC walls. A total of 8 numerical analyses were carried out and three local failure modes were identified. The purpose of the second set of parametric studies was to generate a static resistance curve of SC walls for use in SDOF or TDOF analysis. A total of 3 numerical analyses were conducted and an innovative approach was proposed to obtain a static resistance curve using failure criteria for different components of SC walls. With this approach, engineers will be able to generate static resistance curves by defining proper design parameters according to ductility and/or load capacity demands.

## 9.2 Conclusions

Based on the experimental investigation of the small-scale SC wall specimens subjected to projectile impactive loading, the following conclusions were drawn:

1. The experimental methodology used in this research project including test setup, specimen design, instrumentation, projectile and sabot design was proven to be appropriate to conduct missile impact studies on SC walls.
2. The three-step design method was evaluated using the test results and its accuracy was quantified. It was found that the method has a significant level of conservatism. This conservatism is likely attributed to the use of the statistical variability parameter ( $\beta$ ) in the design method and the incomplete assumed failure mechanism used in its development.
3. The modified NDRC equations, which were incorporated into the three-step design method, were evaluated to verify their effectiveness in estimating penetration depth of SC walls. Based on the observations, the calculated values were less than the test results when a projectile penetrated a concrete core more than two-thirds of its thickness, which means the calculation provided unconservative results. This is most likely due to the difference in the damage mode between RC and SC walls.
4. Three damage modes were observed throughout the experimental program: (i) bulging, (ii) splitting, and (iii) perforating.
5. Local failure mechanism was explained in five stages: (i) front steel faceplate damage, (ii) drilling damage (tunneling zone) in a concrete core, (iii) concrete frustum formation in the concrete core and deformation of the rear steel faceplate, (iv) crushing in the concrete frustum repeating its formation, and (v) rear steel faceplate rupture. Stage four and five

were SC wall specific characteristics caused by an attached rear steel faceplate, compared with the conventional RC walls.

Based on the numerical investigation of the small-scale SC wall specimens subjected to projectile impactive loading, the following conclusions were drawn:

1. Numerical models were developed using the three-dimensional finite element method in LS-DYNA, and benchmarked to the experimental test results.
2. In the model, steel faceplates and projectile were modeled using solid elements combined with the piecewise linear plasticity material model. Concrete core was modeled using solid elements combined with the Winfrith concrete model. Tie bars and steel-headed shear stud anchors were modeled with beam elements combined with the piecewise linear plasticity material model. Zero length discrete beam elements were used to implement the load-slip behavior of the shear studs caused by the composite action between concrete core and steel faceplate. Spacer plates were modeled using solid elements with the rigid material model. Various contact and constraint algorithms were applied to implement relationships between each component of the SC wall specimen and projectile.
3. Penetration depth was estimated reasonably with an average error of 6%. Bulging depth was estimated reasonably with an average error of 9%. Damage mode was predicted favorably in thirteen out of sixteen test cases.
4. Numerical analysis provided reasonable agreement between the predicted deformation or rupture patterns of the rear steel faceplate for each damage mode with the experimental test results. Internal failure mechanisms presented in the numerical models conformed to the experimental test results.

5. One numerical parametric study, consisting of 40 numerical analyses, was conducted using the benchmarked numerical models. This study yielded additional data points which were added to the experimental test results for use in specifying perforation velocity ranges for the experimental test groups and evaluating the accuracy of the modified design method to be proposed later.
6. A second numerical parametric study, consisting of 12 numerical analyses, was conducted to evaluate the influence of design parameters on local damage behavior of SC walls. This study showed that the flexural reinforcement ratio and steel faceplate strength were critical design parameters in regards to estimating penetration depth of a projectile into the concrete core.

Based on the development of a design method for SC walls to prevent perforation from missile impact, the following conclusions were drawn:

1. Modification factor equation,  $K_{sc}$ , was proposed.  $K_{sc}$  adjusts the penetration depth value of a projectile into concrete calculated by the modified NDRC equations to be applicable to SC walls.
2. The updated local failure mechanism was incorporated. Geometric properties associated with concrete frustum formation were revised from the original three-step design method, based on experimental investigations on the small-scale missile impact tests.
3. The modified design method was developed for use in the BDBA. Best estimate approach was adopted with a level of confidence of 50%.
4. Based on the small-scale missile impact test data, the modified design method generated perforation resistance curves in which the perforation velocities were increased by an

average of 17.5% for 1.0 in. diameter projectile and 8.7% for 1.5 in. diameter projectile, respectively, over the original three-step design method. It was found that the conservatism of the three-step design method was reduced significantly.

5. Based on the larger-scale missile impact test data, the modified design method provided perforation curve in which the perforation velocities were increased by an average of 5.1% for the entire test groups over the original three-step design method. It was found that the conservatism of the three-step design method was reduced reasonably yielding better estimation of the perforation velocities.

Based on the numerical investigations of SC walls under quasi-static loading, assuming perforation by missile impact is prevented, the following conclusions were drawn:

1. Local failure modes of SC walls including punching shear, flexural yielding, and plastic mechanism formation were identified through a series of numerical analyses.
2. For punching shear failure mode, it was shown that the ductility ratio was small (less than 5) and the load carrying capacity was underdeveloped (less than half of the load from the yield line analysis). The tie bars were fractured before the steel faceplates yielded.
3. Plastic mechanism formation failure mode resulted in a large ductility ratio of greater than 10 and a well-developed load carrying capacity comparable to the value from the yield line analysis. The steel faceplates yielded with severe deformation, however, the tie bars were not fractured.
4. For flexural yielding failure mode, the ductility ratio was between 5 and 10, and load capacity was greater than half of, but less than the full value from the yield line analysis.

Tie bars were fractured after the steel faceplates yielded, however, no plastic mechanism in the steel faceplates was developed.

5. An innovative approach was proposed to generate the static resistance function of SC walls for use in SDOF or TDOF analysis. According to this approach, a static resistance function can be generated by terminating the load-displacement curve at the point determined by proper failure criteria of constituent components of the SC wall.
6. Using this innovative approach, design engineers can make choices in design parameters to obtain a static resistance function required to ensure desired ductility and/or load capacity demands are satisfied.

### 9.3 *Recommendations for Future Work*

1. Currently, bulging depths of the rear steel faceplate of post-test SC wall specimens were measured manually using a contour gage after each test so that only final values of bulging depth were obtained. In the future, LVDTs could be applied to points around the center of the specimens so that time history data of bulging depths could be obtained for further understanding of the behavior of SC walls.
2. The test set up could be improved to investigate impact instances from the rear side of SC wall specimens. Installing another high-speed camera and equipping appropriate illuminations to the rear chamber of the test setup could yield valuable datasets including residual velocity of a missile, perforation sequences of the rear side of specimens, level of shrapnel scatter, and so on.
3. It has been observed that the Winfrith concrete model may produce unreliable results when strain-rate effect is applied (Schwer 2011). Thus, other available concrete models such as

CSCM (MAT\_159) and KCC (Mat\_72R3), could be used, instead of the Winfrith concrete model, for development and benchmarking of numerical models of SC walls.

4. There is some concern about the numerical models in this research project; especially when bigger tie bars and hex nuts were used. Bigger hex nuts interact with the steel faceplates and affect bulging or rupture patterns of the rear steel faceplate. Thus, further research will be suggested to conduct numerical analyses of SC wall specimens in which the tie bars and hex nuts are modeled with 3D solid elements.
5. CET (cavity expansion theory) was used to explain how missiles perforate the rear steel faceplate in the proposed design method and also the three-step design method. This approach is reasonable when the nose shape of the missile is conical and steel faceplate is relatively thick so that the hole in the steel faceplate can expand in a radial direction associated with true radial compressive stresses. However, experimental results in this research using flat nosed missile and relatively thin steel faceplates found the rupture pattern of the steel faceplate was horizontal or torn in four directions forming a cross shape. Thus, other steel faceplate perforation theories could be applied to further improve the accuracy of the proposed design method in this research.
6. The proposed design method is based on the mean value estimation, in which the level of confidence is 50%, aiming at the BDBA. Thus, further research could be conducted to accommodate a supplemental coefficient to adjust the level of confidence to be applied in the DBA cases.
7. Research for evaluation of local failure modes and for developing an innovative approach to generating static resistance functions was performed using only numerical parametric study results. Thus, an experimental study is recommended to verify each failure mode of

punching shear, flexural yielding, and plastic mechanism formation. Static resistance functions generated from the proposed method in CHAPTER 8 may need to be verified by an appropriate experimental program as well.

# APPENDIX

## COMBINED EXPERIMENTAL DATABASE

(partially after (Bruhl et al. 2015a))

No.	Source	Test #	Within Range of Parameters?	Missile Parameters										Slab Parameters										Test Outcome							
				Mass		Weight		Initial velocity		Type	Rigid?	Outer Diameter (D)		D/T <sub>c</sub>	Equivalent Diameter (d)		Nose	Concrete Thickness (T <sub>c</sub> )		Panel Length/Width		Reinf Ratio	Steel Plate Thickness		Concrete Strength		Steel Plate Strength		Damage	Penetration Depth	
				kg	lb*s <sup>2</sup> /in	N	lb	m/s	ft/s			cm	in		cm	in		mm	in	cm	in		%	mm	in	MPa	psi	MPa		ksi	cm
1	Abdel-Kader and Fouda (2014)	St-0-3-C	No	0.2	0.001	1.7	0.4	317	1040	hard-steel alloy blunt nose	Y	2.30	0.91	0.23	2.30	0.91	0.84	100	3.9	50.0	19.7	3.0	3.0	0.118	26.0	3771	360	52	Prf	6.0	2.4
2	Tsubota et al (1993)	13	Yes	0.4	0.002	4.2	0.9	170	558	rigid/hard missile	Y	3.50	1.38	0.58	3.50	1.38	0.72	60	2.4				0.8	0.031	24.5	3553			Split	6.0	2.4
3	Tsubota et al (1993)	22	Yes	0.4	0.002	4.2	0.9	170	558	rigid/hard missile	Y	3.50	1.38	0.58	3.50	1.38	0.72	60	2.4				1.2	0.047	24.5	3553			Split	6.0	2.4
4	Tsubota et al (1993)	30	Yes	0.4	0.002	4.2	0.9	170	558	rigid/hard missile	Y	3.50	1.38	0.70	3.50	1.38	0.72	50	2.0				1.6	0.063	24.5	3553			Split	5.0	2.0
5	Abdel-Kader and Fouda (2014)	St-0-2-A	No	0.2	0.001	1.7	0.4	336	1102	hard-steel alloy blunt nose	Y	2.30	0.91	0.23	2.30	0.91	0.84	100	3.9	50.0	19.7	2.0	2.0	0.079	26.0	3771	360	52	Bulg	5.0	2.0
6	Abdel-Kader and Fouda (2014)	St-0-2-B	No	0.2	0.001	1.7	0.4	359	1178	hard-steel alloy blunt nose	Y	2.30	0.91	0.23	2.30	0.91	0.84	100	3.9	50.0	19.7	2.0	2.0	0.079	26.0	3771	360	52	Bulg	5.0	2.0
7	Abdel-Kader and Fouda (2014)	St-0-2-C	No	0.2	0.001	1.7	0.4	367	1204	hard-steel alloy blunt nose	Y	2.30	0.91	0.23	2.30	0.91	0.84	100	3.9	50.0	19.7	2.0	2.0	0.079	26.0	3771	360	52	Bulg	5.0	2.0
8	Abdel-Kader and Fouda (2014)	St-0-3-A	No	0.2	0.001	1.7	0.4	270	886	hard-steel alloy blunt nose	Y	2.30	0.91	0.23	2.30	0.91	0.84	100	3.9	50.0	19.7	3.0	3.0	0.118	26.0	3771	360	52	Bulg	4.0	1.6
9	Abdel-Kader and Fouda (2014)	St-0-3-B	No	0.2	0.001	1.7	0.4	282	925	hard-steel alloy blunt nose	Y	2.30	0.91	0.23	2.30	0.91	0.84	100	3.9	50.0	19.7	3.0	3.0	0.118	26.0	3771	360	52	Bulg	4.0	1.6
10	Kojima (1991)	L-12-X	Yes	2.0	0.011	19.6	4.4	212	696	hard-nose missile	Y	6.00	2.36	0.50	4.50	1.77	0.84	120	4.7				3.2	0.126	27.0	3916	432	63	Pen	12.5	4.9
11	Kojima (1991)	L-18-X	Yes	2.0	0.011	19.6	4.4	206	676	hard-nose missile	Y	6.00	2.36	0.33	4.50	1.77	0.84	180	7.1				3.2	0.126	27.0	3916	432	63	Pen	6.6	2.6
12	Sugano et al (1993)	L6	Yes	1767	10.094	17334.3	3896.2	212	696	GE-J79 engine	N	76.00	29.92	0.66	33.0	13.0	0.72	1150	45.3				2.3	0.091	23.5	3408			Pen	30.0	11.8
13	Sugano et al (1993)	M23	Yes	100	0.571	981.0	220.5	216	709	MED	N	30.00	11.81	0.67	10.0	3.94	0.72	450	17.7				2.3	0.091	23.5	3408			Pen	13.0	5.1
14	Sugano et al (1993)	M24	Yes	100	0.571	981.0	220.5	217	712	MED	N	30.00	11.81	0.67	10.0	3.94	0.72	450	17.7				2.3	0.091	23.5	3408			Pen	13.0	5.1
15	Sugano et al (1993)	M25	Yes	100	0.571	981.0	220.5	210	689	MED	N	30.00	11.81	0.67	10.0	3.94	0.72	450	17.7				2.3	0.091	23.5	3408			Pen	14.4	5.7
16	Tsubota et al (1993)	14	Yes	0.4	0.002	4.2	0.9	170	558	rigid/hard missile	Y	3.50	1.38	0.50	3.50	1.38	0.72	70	2.8				0.8	0.031	24.5	3553			Bulg	7.0	2.8
17	Tsubota et al (1993)	15	Yes	0.4	0.002	4.2	0.9	170	558	rigid/hard missile	Y	3.50	1.38	0.44	3.50	1.38	0.72	80	3.1				0.8	0.031	24.5	3553			Bulg	4.6	1.8
18	Tsubota et al (1993)	16	Yes	0.4	0.002	4.2	0.9	170	558	rigid/hard missile	Y	3.50	1.38	0.39	3.50	1.38	0.72	90	3.5				0.8	0.031	24.5	3553			Bulg	2.3	0.9
19	Tsubota et al (1993)	17	Yes	0.4	0.002	4.2	0.9	170	558	rigid/hard missile	Y	3.50	1.38	0.35	3.50	1.38	0.72	100	3.9				0.8	0.031	24.5	3553			Bulg	2.5	1.0
20	Tsubota et al (1993)	18	Yes	0.4	0.002	4.2	0.9	170	558	rigid/hard missile	Y	3.50	1.38	0.33	3.50	1.38	0.72	105	4.1				0.8	0.031	24.5	3553			Pen	1.7	0.7
21	Tsubota et al (1993)	19	Yes	0.4	0.002	4.2	0.9	170	558	rigid/hard missile	Y	3.50	1.38	0.29	3.50	1.38	0.72	120	4.7				0.8	0.031	24.5	3553			Pen	2.7	1.1
22	Tsubota et al (1993)	20	Yes	0.4	0.002	4.2	0.9	170	558	rigid/hard missile	Y	3.50	1.38	0.25	3.50	1.38	0.72	140	5.5				0.8	0.031	24.5	3553			Pen	3.4	1.3
23	Tsubota et al (1993)	23	Yes	0.4	0.002	4.2	0.9	170	558	rigid/hard missile	Y	3.50	1.38	0.54	3.50	1.38	0.72	65	2.6				1.2	0.047	24.5	3553			Bulg	6.5	2.6
24	Tsubota et al (1993)	24	Yes	0.4	0.002	4.2	0.9	170	558	rigid/hard missile	Y	3.50	1.38	0.50	3.50	1.38	0.72	70	2.8				1.2	0.047	24.5	3553			Bulg	7.0	2.8
25	Tsubota et al (1993)	25	Yes	0.4	0.002	4.2	0.9	170	558	rigid/hard missile	Y	3.50	1.38	0.44	3.50	1.38	0.72	80	3.1				1.2	0.047	24.5	3553			Bulg	4.2	1.7
26	Tsubota et al (1993)	26	Yes	0.4	0.002	4.2	0.9	170	558	rigid/hard missile	Y	3.50	1.38	0.39	3.50	1.38	0.72	90	3.5				1.2	0.047	24.5	3553			Bulg	2.2	0.9
27	Tsubota et al (1993)	27	Yes	0.4	0.002	4.2	0.9	170	558	rigid/hard missile	Y	3.50	1.38	0.37	3.50	1.38	0.72	95	3.7				1.2	0.047	24.5	3553			Pen	2.0	0.8
28	Tsubota et al (1993)	28	Yes	0.4	0.002	4.2	0.9	170	558	rigid/hard missile	Y	3.50	1.38	0.35	3.50	1.38	0.72	100	3.9				1.2	0.047	24.5	3553			Pen	3.3	1.3
29	Tsubota et al (1993)	29	Yes	0.4	0.002	4.2	0.9	170	558	rigid/hard missile	Y	3.50	1.38	0.29	3.50	1.38	0.72	120	4.7				1.2	0.047	24.5	3553			Pen	2.0	0.8
30	Tsubota et al (1993)	31	Yes	0.4	0.002	4.2	0.9	170	558	rigid/hard missile	Y	3.50	1.38	0.64	3.50	1.38	0.72	55	2.2				1.6	0.063	24.5	3553			Bulg	5.5	2.2
31	Tsubota et al (1993)	32	Yes	0.4	0.002	4.2	0.9	170	558	rigid/hard missile	Y	3.50	1.38	0.58	3.50	1.38	0.72	60	2.4				1.6	0.063	24.5	3553			Bulg	6.0	2.4
32	Tsubota et al (1993)	33	Yes	0.4	0.002	4.2	0.9	170	558	rigid/hard missile	Y	3.50	1.38	0.50	3.50	1.38	0.72	70	2.8				1.6	0.063	24.5	3553			Bulg	4.9	1.9
33	Tsubota et al (1993)	34	Yes	0.4	0.002	4.2	0.9	170	558	rigid/hard missile	Y	3.50	1.38	0.44	3.50	1.38	0.72	80	3.1				1.6	0.063	24.5	3553			Bulg	3.4	1.3
34	Tsubota et al (1993)	35	Yes	0.4	0.002	4.2	0.9	170	558	rigid/hard missile	Y	3.50	1.38	0.39	3.50	1.38	0.72	90	3.5				1.6	0.063	24.5	3553			Bulg	2.7	1.1
35	Tsubota et al (1993)	36	Yes	0.4	0.002	4.2	0.9	170	558	rigid/hard missile	Y	3.50	1.38	0.37	3.50	1.38	0.72	95	3.7				1.6	0.063	24.5	3553			Pen	1.6	0.6
36	Tsubota et al (1993)	37	Yes	0.4	0.002	4.2	0.9	170	558	rigid/hard missile	Y	3.50	1.38	0.35	3.50	1.38	0.72	100	3.9				1.6	0.063	24.5	3553			Pen	1.9	0.7
37	Tsubota et al (1993)	38	Yes	0.4	0.002	4.2	0.9	170	558	rigid/hard missile	Y	3.50	1.38	0.29	3.50	1.38	0.72	120	4.7				1.6	0.063	24.5	3553			Pen	3.0	1.2
38	Tsubota et al (1993)	39	Yes	0.4	0.002	4.2	0.9	170	558	rigid/hard missile	Y	3.50	1.38	0.70	3.50	1.38	0.72	50	2.0				2.0	0.079	24.5	3553			Bulg	5.0	2.0
39	Tsubota et al (1993)	40	Yes	0.4	0.002	4.2	0.9	170	558	rigid/hard missile	Y	3.50	1.38	0.39	3.50	1.38	0.72	90	3.5				2.0	0.079	24.5	3553			Pen	2.0	0.8
40	Tsubota et al (1993)	42	Yes	0.4	0.002	4.2	0.9	170	558	rigid/hard missile	Y	3.50	1.38	0.50	3.50	1.38	0.72	70	2.8				0.8	0.031	24.5	3553			Bulg	3.5	1.4
41	Tsubota et al (1993)	43	Yes	0.4	0.002	4.2	0.9	170	558	rigid/hard missile	Y	3.50	1.38	0.44	3.50	1.38	0.72	80	3.1				0.8	0.031	24.5	3553			Bulg	4.2	1.7
42	Tsubota et al (1993)	44	Yes	0.4	0.002	4.2	0.9	170	558	rigid/hard missile	Y	3.50	1.38	0.58	3.50	1.38	0.72	60	2.4				1.2	0.047	24.5	3553			Bulg	6.0	2.4
43	Tsubota et al (1993)	45	Yes	0.4	0.002	4.2	0.9	170	558	rigid/hard missile	Y	3.50	1.38	0.50	3.50	1.38	0.72	70	2.8				1.2	0.047	24.5	3553			Bulg	5.6	2.2
44	Tsubota et al (1993)	46	Yes	0.4	0.002	4.2	0.9	170	558	rigid/hard missile	Y	3.50	1.38	0.50	3.50	1.38	0.72	70	2.8				1.6	0.063	24.5	3553			Bulg	6.3	2.5
45	Tsubota et al (1993)	47	Yes	0.4	0.002	4.2	0.9	170	558	rigid/hard missile	Y	3.50	1.38	0.39	3.50	1.38	0.72	90	3.5				1.6	0.063	24.5	3553			Bulg	2.2	0.9
46	Tsubota et al (1993)	48	Yes	0.4	0.002	4.2	0.9	170	558	rigid/hard missile	Y	3.50	1.38	0.35	3.50</																

No.	Source	Test #	Within Range of Parameters?	Missile Parameters											Slab Parameters										Test Outcome						
				Mass		Weight		Initial velocity		Type	Rigid?	Outer Diameter (D)		D/T <sub>c</sub>	Equivalent Diameter (d)		Nose	Concrete Thickness (T <sub>c</sub> )		Panel Length/Width		Reinf Ratio	Steel Plate Thickness		Concrete Strength		Steel Plate Strength		Damage	Penetration Depth	
				kg	lb*s <sup>2</sup> /in	N	lb	m/s	ft/s			cm	in		cm	in		N	mm	in	cm		in	%	mm	in	MPa	psi		MPa	ksi
48	Walter and Wolde-Tinsae (1984)	3	Yes	1475.7	8.430	14477.0	3254.0	132	432	turbine fragments	Y	75.21	29.61	0.55	54.0	21.3	1	1372	54.0				9.5	0.375	28.0	4058			Pen	61.0	24.0
49	Walter and Wolde-Tinsae (1984)	4	Yes	2099.8	11.995	20598.8	4630.0	115	377	turbine fragments	Y	87.15	34.31	0.64	59.2	23.3	1	1372	54.0				9.5	0.375	23.9	3465			Pen	65.0	25.6
50	Walter and Wolde-Tinsae (1984)	806	Yes	1.1	0.007	11.2	2.5	168	550	turbine fragments	Y	7.32	2.88	0.59	4.90	1.93	1	125	4.9				0.9	0.034	25.6	3718			Pen	6.1	2.4
51	Walter and Wolde-Tinsae (1984)	807	Yes	1.1	0.007	11.2	2.5	192	630	turbine fragments	Y	7.32	2.88	0.59	4.90	1.93	1	125	4.9				0.9	0.034	26.3	3815			Pen	7.1	2.8
52	Walter and Wolde-Tinsae (1984)	809	Yes	1.1	0.007	11.2	2.5	197	647	turbine fragments	Y	7.32	2.88	0.75	4.90	1.93	1	97	3.8				0.6	0.023	22.9	3320			Pen	8.4	3.3
53	Walter and Wolde-Tinsae (1984)	1-401-650	Yes	1.1	0.006	10.8	2.4	197	645	turbine fragments	Y	7.37	2.90	0.76	4.95	1.95	1	97	3.8				0.6	0.023	20.4	2952			Pen	10.0	4.0
54	Walter and Wolde-Tinsae (1984)	18-406-520	Yes	1.4	0.008	13.4	3.0	165	541	turbine fragments	Y	4.78	1.88	0.49	4.78	1.88	1	97	3.8				0.6	0.023	25.1	3637			Pen	9.4	3.7
55	Walter and Wolde-Tinsae (1984)	19-503-650	Yes	1.4	0.008	13.4	3.0	203	667	turbine fragments	Y	4.78	1.88	0.45	4.78	1.88	1	106	4.2				0.9	0.034	24.0	3479			Pen	10.5	4.2
56	Walter and Wolde-Tinsae (1984)	2-501-420	Yes	2.8	0.016	27.8	6.3	129	422	turbine fragments	Y	9.32	3.67	0.75	7.04	2.77	1	125	4.9				0.9	0.034	34.0	4932			Pen	6.4	2.5
57	Walter and Wolde-Tinsae (1984)	3-402-420	Yes	2.8	0.016	27.8	6.3	129	424	turbine fragments	Y	9.32	3.67	0.96	7.04	2.77	1	97	3.8				0.6	0.023	20.8	3013			Pen	8.0	3.1
58	Walter and Wolde-Tinsae (1984)	4-502-650	Yes	2.8	0.016	27.8	6.3	201	658	turbine fragments	Y	9.32	3.67	0.75	7.04	2.77	1	125	4.9				0.9	0.034	28.8	4175			Pen	15.0	5.9
59	Kim et al. (2017)	Gr1-1	Yes	0.6	0.003	5.8	1.3	181	593	rigid, flat nosed missile	Y	2.54	1.00	0.26	2.54	1.00	0.72	98	3.85			3.7	1.9	0.075	36.6	5310	386	56	Bulg	4.8	1.9
60	Kim et al. (2017)	Gr1-2	Yes	0.6	0.003	5.8	1.3	205	674	rigid, flat nosed missile	Y	2.54	1.00	0.26	2.54	1.00	0.72	98	3.85			3.7	1.9	0.075	36.6	5310	386	56	Bulg	5.4	2.1
61	Kim et al. (2017)	Gr1-3	Yes	0.9	0.005	8.9	2.0	129	424	rigid, flat nosed missile	Y	2.54	1.00	0.26	2.54	1.00	0.72	98	3.85			3.7	1.9	0.075	45.0	6520	386	56	Bulg	4.2	1.7
62	Kim et al. (2017)	Gr1-4	Yes	0.9	0.005	8.9	2.0	156	513	rigid, flat nosed missile	Y	2.54	1.00	0.26	2.54	1.00	0.72	98	3.85			3.7	1.9	0.075	45.0	6520	386	56	Bulg	5.0	2.0
63	Kim et al. (2017)	Gr1-5	Yes	0.6	0.003	5.8	1.3	203	667	rigid, flat nosed missile	Y	3.81	1.50	0.39	3.81	1.50	0.72	98	3.85			3.7	1.9	0.075	45.0	6520	386	56	Bulg	4.3	1.7
64	Kim et al. (2017)	Gr1-6	No	0.6	0.003	5.8	1.3	232	760	rigid, flat nosed missile	Y	3.81	1.50	0.39	3.81	1.50	0.72	98	3.85			3.7	1.9	0.075	45.0	6520	386	56	Bulg	4.9	1.9
65	Kim et al. (2017)	Gr1-9	Yes	1.6	0.009	15.6	3.5	168	550	rigid, flat nosed missile	Y	3.81	1.50	0.39	3.81	1.50	0.72	98	3.85			3.7	1.9	0.075	43.3	6280	386	56	Split	6.0	2.4
66	Kim et al. (2017)	Gr1-10	Yes	1.6	0.009	15.6	3.5	149	489	rigid, flat nosed missile	Y	3.81	1.50	0.39	3.81	1.50	0.72	98	3.85			3.7	1.9	0.075	41.9	6080	386	56	Bulg	5.5	2.2
67	Kim et al. (2017)	Gr2-1	Yes	0.9	0.005	8.9	2.0	142	467	rigid, flat nosed missile	Y	2.54	1.00	0.26	2.54	1.00	0.72	96	3.79			5.2	2.7	0.105	45.0	6530	400	58	Bulg	4.6	1.8
68	Kim et al. (2017)	Gr2-2	Yes	0.9	0.005	8.9	2.0	167	549	rigid, flat nosed missile	Y	2.54	1.00	0.26	2.54	1.00	0.72	96	3.79			5.2	2.7	0.105	45.0	6530	400	58	Split	5.3	2.1
69	Kim et al. (2017)	Gr2-3	Yes	1.6	0.009	15.6	3.5	125	410	rigid, flat nosed missile	Y	3.81	1.50	0.40	3.81	1.50	0.72	96	3.79			5.2	2.7	0.105	36.6	5310	400	58	Bulg	4.8	1.9
70	Kim et al. (2017)	Gr2-4	Yes	1.6	0.009	15.6	3.5	148	484	rigid, flat nosed missile	Y	3.81	1.50	0.40	3.81	1.50	0.72	96	3.79			5.2	2.7	0.105	36.6	5310	400	58	Bulg	5.6	2.2
71	Kim et al. (2017)	Gr3-1	Yes	0.9	0.005	8.9	2.0	164	539	rigid, flat nosed missile	Y	2.54	1.00	0.26	2.54	1.00	0.72	98	3.85			3.7	1.9	0.075	41.2	5980	503	73	Bulg	5.3	2.1

## REFERENCES

- ALCO Products Inc. (1955). *Hazard Summary Report for the Army Package Power Reactor*.
- American Institute of Steel Construction. (2011). *Steel Construction Manual 14th Edition*. American Institute of Steel Construction.
- American Institute of Steel Construction. (2015). *Specification for Safety-Related Steel Structures for Nuclear Facilities Including Supplement No. 1 (ANSI/AISC N690s1-15)*.
- American Society of Civil Engineers. (1980). *Structural Analysis and Design of Nuclear Plant Facilities (ASCE Manuals and Reports on Engineering Practice No. 58)*. New York, NY.
- Bhardwaj, S. R., and Varma, A. H. (2017). *Steel Design Guide 32-Design of Modular Steel-Plate Composite Walls for Safety- Related Nuclear Facilities*.
- Børvik, T., Forrestal, M. J., Hopperstad, O. S., Warren, T. L., and Langseth, M. (2009). “Perforation of AA5083-H116 aluminium plates with conical-nose steel projectiles – Calculations.” *International Journal of Impact Engineering*, Elsevier Ltd, 36(3), 426–437.
- Broadhouse, B. J. (1995). “SPD/D(95)363. AEA Technology. Winfrith Concrete Model in LS-DYNA3D.”
- Broadhouse, B. J., and Attwood, G. J. (1993). “Finite Element Analysis of the Impact Response of Reinforced Concrete Structures Using DYNA3D.” *Transactions of the 12th International Conference of Structural Mechanics in Reactor Technology (SMiRT-12)*.
- Broadhouse, B. J., and Neilson, A. J. (1987). “Modelling Reinforced Concrete Structures in DYNA3D.” *DYNA3D User Group Conference, London (UK)*.
- Bruhl, J. C. (2015). “BEHAVIOR AND DESIGN OF STEEL-PLATE COMPOSITE (SC) WALLS FOR BLAST LOADS.” Purdue University.
- Bruhl, J. C., Varma, A. H., and Johnson, W. H. (2015a). “Design of composite SC walls to prevent perforation from missile impact.” *International Journal of Impact Engineering*, Elsevier Ltd, 75, 75–87.
- Bruhl, J. C., Varma, A. H., and Kim, J. M. (2015b). “Static resistance function for steel-plate composite (SC) walls subject to impactive loading.” *Nuclear Engineering and Design*, 295.
- ERIN Engineering & Research Inc. (2011). “Methodology for Performing Aircraft Impact Assessments for New Plant Designs (NEI 07-13 Revision 8P).”

- Forrestal, M. J., Brar, N. S., and Luk, V. K. (1991). "Penetration of Strain-Hardening Targets With Rigid Spherical-Nose Rods." *Journal of Applied Mechanics*, 58(March 1991), 1989–1992.
- Forrestal, M. J., Luk, V. K., and Brar, N. S. (1990). "Perforation of aluminum armor plates with conical-nose projectiles." *Mechanics of Materials*, 10(1–2), 97–105.
- Forrestal, M. J., Tzou, D. Y., Askari, E., and Longcope, D. B. (1995). "Penetration into ductile metal targets with rigid spherical-nose rods." *International Journal of Impact Engineering*, 16(5–6), 699–710.
- Grisaro, H., and Dancygier, A. N. (2014). "Assessment of the perforation limit of a composite RC barrier with a rear steel liner to impact of a non-deforming projectile." *International Journal of Impact Engineering*, Elsevier Ltd, 64, 122–136.
- Hallquist, J. (2006). *LS-DYNA® theory manual*. Livermore Software Technology Corporation.
- Hashimoto, J., Takiguchi, K., Nishimura, K., Matsuzawa, K., Tsutsui, M., Ohashi, Y., Kojima, I., and Torita, H. (2005). "Experimental Study on Behavior of RC Panels Covered with Steel Plates Subjected to Missile Impact." *18th International Conference on Structure Mechanics in Reactor Technology (SMiRT 18)*, Beijing, China, 2604–2615.
- Johnson, W., Bruhl, J., Reigles, D., Li, J., and Varma, A. (2014). "Missile Impact on SC Walls: Global Response." *Structures Congress 2014*, 58(58), 1403–1414.
- Kar, A. K. (1979). "Residual velocity for projectiles." *Nuclear Engineering and Design*, 53(1), 87–95.
- Kim, J. M., Bruhl, J., Seo, J., and Varma, A. (2017a). "An overview of missile impact tests on Steel-plate Composite (SC) walls." *Structures Congress 2017: Blast, Impact Loading and Response of Structures - Selected Papers from the Structures Congress 2017*.
- Kim, J. M., Bruhl, J., Seo, J., and Varma, A. (2017b). "Preliminary Investigation of Local Failure Modes in Steel-Plate Composite Walls Subjected to Missile Impact." *Proceedings of Structures Congress 2017, Denver, Colorado*.
- Kim, J. M., Bruhl, J., and Varma, A. (2015). "Design of SC Walls Subjected to Impactive Loading for Local and Global Demands." *Transactions of the 23rd International Conference of Structural Mechanics in Reactor Technology (SMiRT-23)*.

- Kim, J. M., Varma, A., Seo, J., Bruhl, J., Lee, K., and Kim, K. (2017c). “Resistance of SC Walls Subjected to Missile Impact: Part 3. Small-Scale Tests.” *Transactions of the 24th International Conference of Structural Mechanics in Reactor Technology (SMiRT-24)*, Busan, South Korea.
- Malushte, S. R., and Varma, A. H. (2015). “Rethinking Steel-Plate Composite (SC) Construction for Improved Sustainability and Resiliency of Nuclear Power Plant Structures.” *Nuclear Power International Magazine*, 8(4), 17–22.
- Mizuno, J., Sawamoto, Y., Yamashita, T., Koshika, N., Niwa, N., and Suzuki, A. (2005a). “Investigation on Impact Resistance of Steel Plate Reinforced Concrete Barriers Against Aircraft Impact Part 1: Test Program and Results.” *18th International Conference on Structure Mechanics in Reactor Technology (SMiRT 18)*, Beijing, China, 2566–2579.
- Mizuno, J., Tanaka, E., Nishimura, I., Koshika, N., Suzuki, A., and Mihara, Y. (2005b). “Investigation on Impact Resistance Of Steel Plate Reinforced Concrete Barriers against Aircraft Impact Part 3: Analyses of Full-Scale Aircraft Impact.” *18th International Conference on Structure Mechanics in Reactor Technology (SMiRT 18)*, Beijing, China, 2591–2603.
- Morikawa, H. (1997). “Evaluation Method of Local Damages to Reinforced Concrete Plates with Steel Liners subjected to High-Velocity Impact of Projectile.” *Journal of Structural Construction Engineering (AIJ)*.
- Ollgaard, J. G., Slutter, R. G., and Fisher, J. W. (1971). “Shear Strength of Stud Connectors in Lightweight and Normal-Weight Concrete.” *AISC Engineering Journal*, 55–64.
- Ozaki, M., Akita, S., Osuga, H., Nakayama, T., and Adachi, N. (2004). “Study on steel plate reinforced concrete panels subjected to cyclic in-plane shear.” *Nuclear Engineering and Design*, 228(1–3), 225–244.
- Park, H. (2011). “Crack propagation through adhesive interface in glass driven by dynamic loading.” *Purdue University*.
- Piekutowski, A. J., Forrestal, M. J., Poormon, K. L., and Warren, T. L. (1996). “Perforation of aluminum plates with ogive-nose steel rods at normal and oblique impacts.” *International Journal of Impact Engineering*, 18(96), 877–887.

- Rosenberg, Z., and Dekel, E. (2009). "On the deep penetration and plate perforation by rigid projectiles." *International Journal of Solids and Structures*, Elsevier Ltd, 46(24), 4169–4180.
- Rosenberg, Z., and Dekel, E. (2010). "Revisiting the perforation of ductile plates by sharp-nosed rigid projectiles." *International Journal of Solids and Structures*, Elsevier Ltd, 47(22–23), 3022–3033.
- Rosenberg, Z., and Forrestal, M. J. (1988). "Perforation of Aluminum Plates with Conical-Nosed Rods-Additional Data and Discussion." *Journal of Applied Mechanics*, 55(March 1988), 236–238.
- Schlaseman, C. (2004). "Application of Advanced Construction Technologies to New Nuclear Power Plants (MPR-2610, Revision 2)." 132.
- Schwer, L. (2011). "The Winfrith Concrete Model : Beauty or Beast ? Insights into the Winfrith Concrete Model." (May).
- Sener, K. C., and Varma, A. H. (2014a). "Steel-plate composite walls: Experimental database and design for out-of-plane shear." *Journal of Constructional Steel Research*, Elsevier Ltd, 100, 197–210.
- Sener, K. C., and Varma, A. H. (2014b). "Steel-plate composite walls: Experimental database and design for out-of-plane shear." *Journal of Constructional Steel Research*, Elsevier Ltd, 100, 197–210.
- Sener, K. C., Varma, A. H., and Ayhan, D. (2015). "Steel-plate composite (SC) walls: Out-of-plane flexural behavior, database, and design." *Journal of Constructional Steel Research*, Elsevier Ltd, 108, 46–59.
- Seo, J., Varma, A. H., Sener, K., and Ayhan, D. (2016). "Steel-plate composite (SC) walls: In-plane shear behavior, database, and design." *Journal of Constructional Steel Research*, Elsevier Ltd, 119, 202–215.
- Shim, C. S., Lee, P. G., and Yoon, T. Y. (2004). "Static behavior of large stud shear connectors." *Engineering Structures*, 26(12), 1853–1860.
- Sugano, T., Tsubota, H., Kasai, Y., Koshika, N., Itoh, C., Shirai, K., von Riesemann, W. A., Bickel, D. C., and Parks, M. B. (1993). "Local damage to reinforced concrete structures caused by impact of aircraft engine missiles Part 2. Evaluation of test results." *Nuclear Engineering and Design*, 140(3), 407–423.

- Tsubota, H., Kasai, Y., Koshika, N., Morikawa, H., Uchida, T., and Ohno, T. (1993). “Quantitative Studies on Impact Resistance of Reinforced Concrete Panels with Steel Liners under Impact Loading Part 1: Scaled Model Impact Tests.” *12th International Conference on Structure Mechanics in Reactor Technology (SMiRT 12)*, Stuttgart, Germany, 169–174.
- U.S. Department of Defense. (2008). “Unified Facilities Criteria (UFC) Structures to Resist the Effects of Accidental Explosions.”
- U.S. Department of Energy. (2006). “DOE Standard: Accident Analysis For Aircraft Crash Into Hazardous Facilities.” *U.S. Department of Energy*, (May).
- URS Energy and Construction Inc. (2011). “MUAP-11019 Containment Internal Structure: Design Criteria for SC Walls for US-APWR Standard Plant (Report CIS-13-05-160-006).” 04, 106.
- Varma, A. H. (2000). “SEISMIC BEHAVIOR, ANALYSIS, AND DESIGN OF HIGH STRENGTH SQUARE CONCRETE FILLED STEEL TUBE (CFT) COLUMNS.” Lehigh University.
- Varma, A., Kim, J. M., Seo, J., and Bruhl, J. (2017). “Local Failure Modes of SC Walls Subjected to Impactive Loading.” *Transactions of the 24th International Conference of Structural Mechanics in Reactor Technology (SMiRT-24)*.
- Walter, T. A., and Wolde-Tinsae, A. M. (1984). “Turbine Missile Perforation of Reinforced Concrete.” *Journal of Structural Engineering*, 110(10), 2439–2455.
- Warren, T. L., Hanchak, S. J., and Poormon, K. L. (2001). “Penetration of limestone targets by ogive-nosed VAR 4340 steel projectiles at oblique angles: Experiments and simulations.” *International Journal of Impact Engineering*, 25, 993–1022.
- Wittmann, F. H. (2002). “Crack formation and fracture energy of normal and high strength concrete.” 27(August), 413–423.

## VITA

Joo Min Kim received his Bachelor of Science in Mechanical Engineering from Sungkyunkwan University, Seoul, South Korea and his Master of Science in Mechanical Engineering from the Korea Advanced Institute of Science and Technology (KAIST), Daejeon, South Korea. Upon graduation, he worked for eight years as a mechanical engineer for Doosan Heavy Industries and Construction Co., Ltd. in Changwon, South Korea.

In 2012, Joo Min Kim started his graduate studies in Structural Engineering at Purdue University, West Lafayette, Indiana, USA. He received his Master of Science in Structural Engineering in 2014 and began to pursue a Doctor of Philosophy in Structural Engineering. He has conducted experimental and numerical research on the behavior of steel-plate composite (SC) wall structures subjected to impactive loading.